Human-based Computational Investigations into Cardiac Electromechanical Alterations Caused by Drugs and Hypertrophic Cardiomyopathy

Francesca Margara

Keble College



Department of Computer Science

University of Oxford

Trinity Term 2021

This thesis is submitted to the Department of Computer Science, University of Oxford, for the degree of Doctor of Philosophy. This thesis is entirely my own work, and, except where otherwise indicated, describes my own research.

***

To Andrea

***

Francesca Margara
Keble College

Doctor of Philosophy
Trinity Term 2021

Human-based Computational Investigations into Cardiac Electromechanical Alterations Caused by Drugs and Hypertrophic Cardiomyopathy

Abstract

The assessment of drug safety and efficacy remains one of the biggest challenges in preclinical and clinical drug development. The prediction of drug action on cardiac contraction and electrophysiology is especially complex and diseased cardiac substrates are at a higher risk of developing potentially lethal reactions to pharmacological therapy. A deep mechanistic understanding of drug action in the context of specific cardiac pathophysiology is needed to guide the development and administration of effective and safe patient-specific therapies. These mechanistic understandings are still unknown for many cardiac diseases in particular cardiomyopathies. Most cardiomyopathy treatments focus on symptom relief, which do not specifically target disease pathophysiology. Therefore, defining key mechanisms in inherited cardiomyopathies due to specific genetic mutations is needed to develop novel effective pharmacological interventions that are patient specific.

Human-based modelling and simulation can accelerate the mechanistic understanding of cardiac pathophysiology and the development and evaluation of therapeutic interventions through human in-silico trials. Thus, the overall goal of this thesis is to develop computational methodologies integrated

with experimental and clinical data to investigate the mechanisms explaining the cardiac safety and efficacy of pharmacological therapies in health and hypertrophic cardiomyopathy.

To achieve this goal a novel in-silico human electromechanical ventricular modelling and simulation framework was developed, and mechanistic simulations conducted to assess drug-induced pro-arrhythmia and inotropic risk in healthy cardiac function. Next, a novel software tool was developed to provide automated high-throughput analysis of calcium transients in cardiomyocytes. This was used to phenotype primary and induced pluripotent stem cell-derived cardiomyocytes under pharmacological action and hypertrophic cardiomyopathy variants. Analysed data was used to inform a computational investigation into the pathophysiology of three different hypertrophic cardiomyopathy-causing mutations and their response to the novel pharmacological compound Mavacamten. To conduct in-silico trials of Mavacamten, the cellular electromechanical model was extended to include representation of myosin sequestration and release from the energy-conserving state SRX.

Overall, this thesis contributes towards a better understanding of how cardiac electromechanical substrates are affected by disease and pharmacological action and holds both preclinical and translational potential for precision medicine in inherited cardiomyopathies.

Publications

The publications resulting from the work described in this thesis are listed below.

Journal papers:

- **Margara F**, Psaras Y, Rodriguez B, Toepfer* CN and Bueno-Orovio* A. Human-based computational and experimental investigation of disease mechanisms and pharmacological action in mutation-specific hypertrophic cardiomyopathy. *In preparation*.
- Psaras* Y, **Margara* F**, Cicconet M, Sparrow AJ, Repetti G, et al. CalTrack: High Throughput Automated Calcium Transient Analysis in Cardiomyocytes. *Circ Res*. 2021.
- **Margara F**, Wang ZJ, Levrero-Florencio F, Santiago A, Vazquez M, et al. In-silico human electro-mechanical ventricular modelling and simulation for drug-induced pro-arrhythmia and inotropic risk assessment. *Prog Biophys Mol Biol*. 2021;159:58-74.

Conference proceedings:

- **Margara F**, Rodriguez B, Toepfer* CN and Bueno-Orovio A. Mavacamten Efficacy in Mutation-specific Hypertrophic Cardiomyopathy: an In-silico Approach to Inform Precision Medicine. *Submitted to Computing in Cardiology 2021.*
- **Margara F**, Wang ZJ, Bueno-Orovio A and Rodriguez B. Human Ventricular Modelling and Simulation of Drug Action on Electrophysiology and Contraction. *Computing in Cardiology*. 2020:1-4.

Journal abstracts:

- **Margara F**, Psaras Y, Rodriguez B, Toepfer CN and Bueno-Orovio A. Human-based computational and experimental investigation of disease mechanisms in mutation-specific hypertrophic cardiomyopathy. *EP Europace*. 2021;23:euab116.537.
- **Margara F**, Psaras Y, Rodriguez B, Toepfer* CN and Bueno-Orovio* A. Combining Human-based in Silico and in Vitro Models of Inherited Cardiac Diseases for Drug Safety and Efficacy Evaluation. *To appear in the Journal of Pharmacological and Toxicological Methods in September 2021.*
- **Margara F**, Passini E, Levrero-Florencio F, Bueno-Orovio A and Rodriguez B. Simultaneous assessment of drug-induced effects on contractility and electrophysiology using human in silico trials. *Journal of Pharmacological and Toxicological Methods*. 2020;105:106803.

A list of publications resulting from collaborative work during my DPhil is reported below.

- Wang ZJ, Santiago A, Zhou X, Wang L, **Margara F**, et al. Human biventricular electromechanical simulations on the progression of electrocardiographic and mechanical abnormalities in post-myocardial infarction. *Europace*. 2021;23:i143-i152.
- Corral-Acero J, **Margara F**, Marciniak M, Rodero C, Loncaric F, et al. The 'Digital Twin' to enable the vision of precision cardiology. *Eur Heart J*. 2020;41:4556-4564.
- Levrero-Florencio F, **Margara F**, Zacur E, Bueno-Orovio A, Wang ZJ, et al. Sensitivity analysis of a strongly-coupled human-based electromechanical

cardiac model: Effect of mechanical parameters on physiologically relevant biomarkers. *Comput Methods Appl Mech Eng*. 2020;361:112762.

- Passini E, **Margara F** and Rodriguez B. Computational investigation of drug-induced effects on human cardiac electro-mechanics. *EP Europace*. 2021;23.
- Smith HJ, **Margara F** and Rodriguez B. Unravelling the Mechanistic Links between Pro-Arrhythmia and Mechanical Function. *2020 Computing in Cardiology*. 2020:1-4.
- Riebel LL, Passini E, **Margara F**, Paci M, Biasetti J and Rodriguez B. In silico Identification of the Key Ionic Currents Modulating Human Pluripotent Stem Cells towards an Adult Cardiomyocyte Phenotype. *Submitted to Computing in Cardiology 2021.*
- Folkmanaite M, Zhou Z, **Margara F**, Zaccolo M and Rodriguez B. In-Silico Human Induced Pluripotent Stem Cell Derived Cardiomyocyte Electro-Mechanical Modelling and Simulation. *Submitted to Computing in Cardiology 2021.*
- "Advanced morpho-functional analysis reveals impaired cross-bridge kinetics and energetics in patients with a myosin binding protein C founder mutation causing hypertrophic cardiomyopathy". Collaboration with the Department of Clinical and Experimental Medicine, Division of Physiology, University of Florence, Italy.

Conference presentations

The work described in this thesis was presented at the following conferences:

- [Talk] **European Heart Rhythm Association (EHRA) and associated ESC Working Group on Cardiac Cellular Electrophysiology (EWGCCE) 45th meeting.** April 23-25, 2021, virtual conference.
- [Talk] **6th Annual International Living Heart Symposium.** December 8-9, 2020, virtual conference.
- [Talk] **PIC Winter School.** November 30-December 2, 2020, virtual conference.
- [Poster] **Safety Pharmacology Annual Meeting**. September 14-17, 2020, virtual conference.
- [Talk] **Computing in Cardiology.** September 13-16, 2020, virtual conference.
- [Poster] **Safety Pharmacology Annual Meeting**. September 23-26, 2019, Barcelona (Spain).
- [Poster] **Mechano-Electric Coupling and Arrhythmias workshop**. September 4-7, 2019, Freiburg (Germany).
- [Poster] **4th Barcelona VPH Summer School**. June 10-14, 2019, Barcelona (Spain).
- [Poster] **Oxford 3Rs (Replacement, Refinement and Reduction of Animals in Research) day**. April 8, 2019, Oxford (UK).
- [Poster] **Gordon Research Seminar and Conference on Cardiac Arrhythmia Mechanisms** (GRS/GRC). March 30-April 5, 2019, Lucca (Italy).

Prizes

The work described in this thesis was awarded the following prizes:

- **Best abstract award - category live abstracts** at the ESC Working Group on Cardiac Cellular Electrophysiology (EWGCCE) 45th meeting, 2021.
- **Semi-finalist** of the Rosanna Degani Young Investigators' Award competition at the international Computing in Cardiology conference, 2020.
- **Student travel award recipient** at the Safety Pharmacology Annual Meeting, 2019.

The work presented in this thesis will be further expanded thanks to the award of a **Doctoral Impact Scheme**, funded by the EPSRC Impact Acceleration Account (IAA), in which I am Co-Investigator together with my supervisor Prof Alfonso Bueno-Orovio. This project, entitled "In silico clinical trials for precision medicine in genetic heart disease: Evaluation study" will commence after my DPhil viva and will be conducted in collaboration with MyoKardia - Bristol Myers Squibb, a biopharmaceutical company discovering and developing targeted therapies for the treatment of cardiovascular diseases including hypertrophic cardiomyopathy.

Acknowledgements

First of all, I would like to thank my supervisors, Prof Alfonso Bueno-Orovio, Prof Blanca Rodriguez, and Dr Christopher Toepfer, for all their support over the past years. I honestly could not have asked for a better supervisory team, not only for the science I have learnt from you but also because you have been there to help me every step of the way. Alfonso, thank you for everything you have taught me but also for always supporting, reassuring, and making me feel valued from my very first day in Oxford. Blanca, thank you for always guiding me, motivating and pushing me beyond my limits when I needed it, and believing in me. I really look up to you. Chris, thank you for welcoming me in your lab, for your invaluable advice and ideas, and for your enthusiasm about my DPhil project.

The work presented here would not exist without the help and support of many people. Big thank you to Dr Jenny Wang. Jenny, thank you for being always available and your important contribution to my DPhil project. Thank you to Dr Yiangos Psaras. It has been great fun developing CalTrack together and I have learnt a lot about biology from you! Thanks to Dr Alexander Sparrow, Dr Paul Robinson, Manuel Schmid M.D., and everyone who contributed to the CalTrack project.

Thank you to Dr Francesc Levrero-Florencio, Dr Mariano Vázquez, and Dr Alfonso Santiago for fruitful discussions and help with the 3D simulations.

Thank you to Prof Peter Kohl, Dr Hua Rong Lu, Prof Esther Pueyo, and Mr Cristobal Rodero Gomez for being part of my progress review committee. All your feedback and suggestions have greatly contributed to improve my research!

A huge thank you to Prof Pablo Lamata for creating the PIC network and for always being in our corner. I'm grateful for the incredible opportunities the PIC network has provided me. PIC fellows, thank you all guys, it's been great fun to share this journey with you!

A big thank you to all the members at the Computational Cardiovascular Science Team and Toepfer Lab for such a great work environment, especially to Dr Elisa Passini and Dr Cristian Trovato. Ely, Cristian thank you for your friendship and support!

Thank you to the Department of Computer Science and Keble college community. Thank you to the European Union's Horizon 2020 research and Innovation programme for funding my DPhil.

Finally, a special thank you from the bottom of my heart to my family. Thank you because I know you are always there for me. I have missed you so much in past year and a half and I can't wait to hug you again!

Thank you, Andrea. I could not have done this without you.

Table of Contents

1 Introduction 18

1.1 Motivation 18

1.2 Thesis goal 20

1.3 Thesis outline 21

2 Biomedical and experimental background 23

2.1 The human heart 23

2.1.1 The structure and function of the human heart 23

2.1.2 Cardiac excitation-contraction coupling of human cardiomyocytes 27

2.1.3 The structure and function of cardiac myofilaments 31

2.2 Hypertrophic cardiomyopathy (HCM) 35

2.2.1 Disease overview 35

2.2.2 The genotype-phenotype relationship in human hypertrophic cardiomyopathy 39

2.2.3 Medical treatments 41

2.3 Drug cardiac safety and efficacy assessment in preclinical research 45

3 Computational background 50

3.1 Human-based cardiac modelling and simulation – overview 50

3.1.1 Human cardiac action potential models 51

3.1.2 Human cardiac contractility models 55

3.1.3 Multiscale human electromechanical modelling and simulation 61

3.1.4 Computational approaches to inter-subject variability 66

3.2 The Digital Twin in precision cardiology 69

3.2.1 Digital Twins for hypertrophic cardiomyopathy 71

3.3 Human in-silico drug trials for cardiac safety and efficacy assessment 75

4 In-silico human electromechanical ventricular modelling and simulation for drug-induced pro-arrhythmia and inotropic risk assessment 80

4.1 Introduction 81

4.2 Methods 82

4.2.1 Experimental data 82

4.2.2 Description of the electromechanical coupling of human-based models 86

4.2.3 Recalibration of the active tension model 91

4.2.4 Evaluation of the human electromechanical models and transmural heterogeneity 93

4.2.5 Simulations of drug-induced effects on human electromechanical function 94

4.2.6 Single cell implementation and stimulation protocols 95

4.2.7 Fully-coupled electromechanical simulations in 3D tissue slabs 96

4.3 Results 97

4.3.1 Evaluation of the human electromechanical cellular models 97

4.3.2 Cellular simulations of transmural heterogeneity in human cardiac electromechanics 102

4.3.3 Simulation of inotropic effects of multichannel action reference compounds 104

4.4 Discussion 114

4.4.1 Human electromechanical cell models 115

4.4.2 Transmural heterogeneity in cellular electromechanical properties 117

4.4.3 In-silico predictions of inotropic and pro-arrhythmic liabilities 119

4.4.4 Electromechanical coupling and repolarisation 122

4.4.5 Limitations and future work 123

4.4.6 Conclusion 124

5 CalTrack: open source and high throughput automated analysis of calcium transients in primary and iPSC derived cardiomyocytes 125

5.1 Introduction 126

5.2 Methods 129

5.2.1 Mathematical basis of CalTrack calcium transient analysis 129

5.2.2 Production of synthetic calcium transients for CalTrack benchmarking 134

5.2.3 Generation of WT and TNNI3$^{R21C/+}$ missense iPSC-CMs for calcium transient analyses 135

5.2.4 Guinea pig cardiomyocyte isolation and manipulation. 135

5.2.5 Statistical analysis 136

5.3 Results 136

5.3.1 CalTrack pipeline overview and applications 136

5.3.2 CalTrack robustly detects cardiomyocytes in low magnification image stacks ..139

5.3.3 CalTrack corrects for linear and exponential baseline drift in calcium transient acquisitions.....139

5.3.4 CalTrack provides analysis of irregular calcium transients including early afterdepolarisations and delayed afterdepolarisations 141

5.3.5 Assessment of quantitative calcium concentrations using CalTrack.....142

5.3.6 Benchmarking of CalTrack with synthetic simulated calcium transient data 144

5.3.7 Quantitative calcium analyses in adult TnnI3$^{R145G/+}$ cardiomyocytes with benchmarking comparison between automated CalTrack analysis and manual user-driven IonWizard analysis 146

5.3.8 CalTrack detects calcium transient responses to pharmacological agents Levosimendan and Isoproterenol in adult cardiomyocytes 149

5.3.9 CalTrack detects abnormal calcium transients in guinea pig cardiomyocytes expressing the TnnI3$^{R145G/+}$ hypertrophic cardiomyopathy variant 151

5.3.10 CalTrack detects basal and drug-induced calcium changes in iPSC-CMs with TNNI3$^{R21C/+}$ hypertrophic cardiomyopathy variant 152

5.4 Discussion 157

6 Human-based modelling and simulation of myosin sequestration changes due to pathogenic variants and Mavacamten 163

6.1 Introduction 163

6.2 Methods 165

6.2.1 Model construction 165

6.2.2 Model calibration 169

6.3 Results 171

6.4 Discussion 179

7 Human-based computational and experimental investigations of disease mechanisms and pharmacological action in mutation-specific hypertrophic cardiomyopathy 182

7.1 Introduction 182

7.2 Methods 184

7.2.1 Experimental characterisation of mutation-specific hypertrophic cardiomyopathy cellular phenotypes 184

7.2.2 The in-silico population of human models approach to investigate mutation-specific hypertrophic cardiomyopathy pathophysiology 186

7.2.3 Human in-silico trials of Mavacamten 191

7.3 Insights into mutation-specific pathophysiological mechanisms and their modulation of Mavacamten's efficacy 191

7.3.1 The pathogenic β-myosin heavy chain variant $MYH7^{R403Q/+}$ 191

7.3.2 The pathogenic troponin T variant $TNNT2^{R92Q/+}$ 197

7.3.3 The pathogenic troponin I variant $TNNI3^{R21C/+}$ 205

7.3.4 Comparison of Mavacamten's efficacy on $MYH7^{R403Q/+}$ $TNNT2^{R92Q/+}$ and $TNNI3^{R21C/+}$ variants. 211

7.4 Discussion 213

8 Conclusions 224

8.1 Summary of the thesis 224

8.2 Key contributions and main findings 226

8.3 Future Directions 229

Appendix I. Summary table for comparisons of currently available software for calcium transient assessments 231

Bibliography 233

Nonstandard Abbreviations and Acronyms

AP – action potential

APD – AP duration

ATP – adenosine triphosphate

ATPase – adenosine triphosphatase

CaT – calcium transient

DAD – delayed afterdepolarisation

DRX – myosin disordered relaxed state

EAD – early afterdepolarisation

HCM – hypertrophic cardiomyopathy

hiPSC – human induced pluripotent stem cell

hiPSC-CM – human induced pluripotent stem cell-derived cardiomyocyte

IC50 – concentration for 50% channel inhibition

iPSC – induced pluripotent stem cell

MYH7 – β-myosin heavy chain gene

ORd – O'Hara-Rudy dynamic model

ORd+Land – electromechanical model obtained by coupling the ORd model with the Land model.

SRX – myosin super relaxed state

TNNI3 – cardiac troponin I gene

TNNT2 – cardiac troponin T gene

ToR-ORd – Tomek-Rodriguez following ORd model

ToR-ORd+Land – electromechanical model obtained by coupling the ToR-ORd model with the Land model.

1 Introduction

1.1 Motivation

The assessment of the safety and efficacy of candidate drugs remains one of the biggest challenges in preclinical and clinical drug development [1]. The potential occurrence of drug-induced adverse outcomes often limits the development of new promising compounds. Specifically, cardiotoxicity is a major concern during drug development [2] and may emerge in the clinic even though it did not occur in early stages of drug development [3]. Its occurrence varies widely across the population, yet diseased cardiac substrates are at a higher risk of developing adverse reactions [4], including potentially lethal arrhythmias [5] and heart failure [6]. Thus, a deep mechanistic understanding of drug action in the context of specific cardiac pathophysiology is needed to guide the development and administration of effective and safe patient-specific therapies. These mechanistic understandings are still unknown for many cardiac diseases, in particular cardiomyopathies.

Cardiomyopathies are a heterogeneous group of heart disorders that can cause heart failure or sudden death, with an overall estimated prevalence of at least 3% in the general population worldwide [7]. Over the past decades, substantial progress has been made in defining the causative role and mechanisms of single gene mutations in primary cardiomyopathies [8-15] such as hypertrophic cardiomyopathy. Nevertheless, most cardiomyopathy

treatments focus on symptom relief, which do not specifically target disease pathophysiology [16].

Hypertrophic cardiomyopathy is a highly heterogeneous disorder, associated to more than 1500 genetic mutations [17]. Pharmacological treatment is often required in hypertrophic cardiomyopathy patients, yet this is based on the empirical use of long-standing drugs that do not target disease mechanisms and independently of patients' genotype. Accumulating evidence shows that hypertrophic cardiomyopathy pathophysiology and response to treatment depend on the underlying gene mutation [18]. Thus, hypertrophic cardiomyopathy is an emblematic example of the need for a precision medicine approach in which inter-subject variability, including genotype, is integrated in clinical decision making. To this end, defining key mechanisms in genetic cardiomyopathies due to specific genetic mutations is recognised as an important need for the development of novel effective pharmacological interventions that are patient specific.

Human-based computational methodologies are a powerful set of tools that can be used to accelerate the mechanistic understanding of cardiac pathophysiology [19-23], and to develop and evaluate therapeutic interventions through human in-silico trials [24-30]. Human-based modelling and simulation offer the opportunity to integrate detailed biophysical information on cardiac electrophysiology and mechanics and improve the understanding and prediction of drug safety and efficacy in humans [31]. Thus, in this thesis I develop and describe novel experimentally-informed in-silico methodologies to study alterations in human electromechanical ventricular

function caused by pharmacological therapies and hypertrophic cardiomyopathy.

1.2 Thesis goal

The overall goal of my thesis is to investigate the mechanisms explaining the cardiac safety and efficacy of pharmacological therapies in health and hypertrophic cardiomyopathy through modelling and simulation of human ventricular electromechanical function.

The specific goals of my thesis are:

1. To develop, calibrate, and evaluate a human-based mechanistic framework for the simulation of the ventricular cellular electromechanical function.
2. To perform in-silico evaluations of drug-induced effects on human ventricular electrophysiology, calcium dynamics, and active contraction.
3. To combine human-based in-silico and in-vitro models of hypertrophic cardiomyopathy to investigate mutation-specific pathophysiology.
4. To evaluate therapeutic efficacy of pharmacological interventions in mutation-specific hypertrophic cardiomyopathy.

The work presented in this thesis is based on the hypotheses that (i) the integration of the electrical and mechanical function of human cardiomyocytes in a single framework advances our capability of investigating cardiac diseases and drug action, and (ii) similar hypertrophic cardiomyopathy cellular phenotypes are generated through different pathways, and therefore specific

pathogenic mechanisms should be targeted by pharmacological intervention to achieve patient benefit.

The human ventricular modelling and simulation framework constructed in this thesis opens new avenues for future investigations into the complex interplay between electrical and mechanical cardiac substrates. It allows the investigation of how these substrates are affected by disease and pharmacological action. This approach holds both preclinical and translational potential with the goal of advancing precision medicine in inherited cardiomyopathies.

1.3 Thesis outline

The present chapter, **Chapter 1,** introduces the thesis, presents the main aims of the work, and provides the outline of this thesis.

Chapter 2 and 3 introduce background information on the main topic of the thesis. Chapter 2 focuses on the biomedical and experimental background whereas Chapter 3 describes the associated computational methodologies. Specifically, Chapter 2 introduces (i) the human heart, (ii) the inherited heart disease hypertrophic cardiomyopathy, (iii) the current experimental approaches and related challenges to assess drug safety and efficacy in preclinical development, including the use of human induced pluripotent stem cell-derived cardiomyocytes. Chapter 3 reviews state-of-the-art computational methodologies developed to (i) model the human ventricular electromechanical function in the context of inter-subject variability; (ii) build a Digital Twin of the human heart for precision cardiology, in particular to investigate hypertrophic cardiomyopathy; and (iii) evaluate drug safety and

efficacy through human in-silico drug trials. The description of the Digital Twin in precision cardiology provided in this chapter is based on our recent position paper published in the journal *European Heart Journal* [32].

Chapter 4 presents the development, calibration, and validation of an in-silico human electromechanical ventricular modelling and simulation framework for drug-induced pro-arrhythmia and inotropic risk assessment in healthy cardiac function. This study was recently published in the journal *Progress in Biophysics and Molecular Biology* [33].

Chapter 5 presents the development of CalTrack, a MatLab based algorithm, to analyse fluorescent calcium transients in living cardiomyocytes. It shows the performance of CalTrack in phenotyping primary and induced pluripotent stem cell-derived cardiomyocytes under pharmacological action and hypertrophic cardiomyopathy variants. This study was recently published in the journal *Circulation Research* [34].

Chapter 6 describes the extension of the modelling and simulation framework presented in Chapter 4 to include the representation of myosin sequestration and release from the energy-conserving state SRX in response to pathogenic variants and the pharmacological compound Mavacamten.

Chapter 7 features an experimentally-informed computational investigation into the pathophysiology of three different hypertrophic cardiomyopathy-causing mutations and their response to Mavacamten. It exploits the modelling and simulation framework presented in Chapter 4, and extended in Chapter 6, and the CalTrack-enabled data analysis presented in Chapter 5.

Chapter 8 summarises the key findings of the thesis, discusses the main contributions, and proposes directions for future work.

2 Biomedical and experimental background

In this chapter I present background information on the main topics of the thesis. I first briefly introduce the human heart, its structure and function, the excitation-contraction coupling of human ventricular myocytes, and the cardiac contractile machinery. I then introduce the inherited heart disease hypertrophic cardiomyopathy. I describe its genetic basis and available medical treatments. Finally, I conclude the chapter by presenting the current approaches used to assess cardiac safety and efficacy of therapeutic compounds in preclinical research, including the use of human induced pluripotent stem cell-derived cardiomyocytes.

This chapter presents the thesis topics from a biomedical and experimental point of view. Chapter 3 describes human-based computational methodologies to investigate cardiac pathophysiology, and to conduct in-silico drug trials with the goal of advancing toward precision medicine.

2.1 The human heart

2.1.1 The structure and function of the human heart

The human heart is in the thorax underneath the sternum located medially between the lungs. The heart dimensions are approximately equal to those of a fist. The heart consists of four chambers (Figure 2.1A), two upper chambers known as the atria, which are separated by the interatrial septum, and two lower chambers known as the ventricles, which are separated by the

interventricular septum. The atrioventricular septum separates the atria from the ventricles and contains the tricuspid valve in the right heart and the mitral valve in the left heart. A fibrous sac containing serous fluid, called the pericardium, covers the heart, protects it from infection, and lubricates its movement. The ventricular walls are made of three distinct layers of tissue, the exterior layer is known as the epicardium, which is divided from the internal endocardium by the central myocardium.

The heart is a dual circulatory pump and is the central organ of the cardiovascular system. Its most important function is to circulate blood to the periphery. In doing so it carries oxygen and nutrients to the organs and tissues of the body (Figure 2.1A). During each cardiac cycle, the right heart pumps blood through the pulmonary semilunar valve into the pulmonary arteries and onwards to the lungs to be oxygenated and carried back to the left heart. The left heart receives this oxygen-rich blood and pumps it into the body through the aortic semilunar valve and aorta.

Each cardiac cycle is characterised by a phase of diastole (relaxation) and a phase of systole (contraction), as illustrated in Figure 2.1B. During diastole, blood builds up in the atria and creates a pressure gradient. This forces the atrioventricular valves to open. Most blood passes into the ventricles through passive filling causing a gradual increase in ventricular diastolic pressure (Figure 2.1B, point A). The remaining blood is propelled into the ventricles by the contraction of the atria (Figure 2.1B, point B). Mechanical systole begins with the contraction of the ventricles further increasing ventricular pressures and forcing the atrioventricular valves to close (Figure 2.1B, point C). When

ventricular pressure exceeds the pressure in the pulmonary artery and aorta, the semilunar valves open (Figure 2.1B, point D) and ejection occurs.

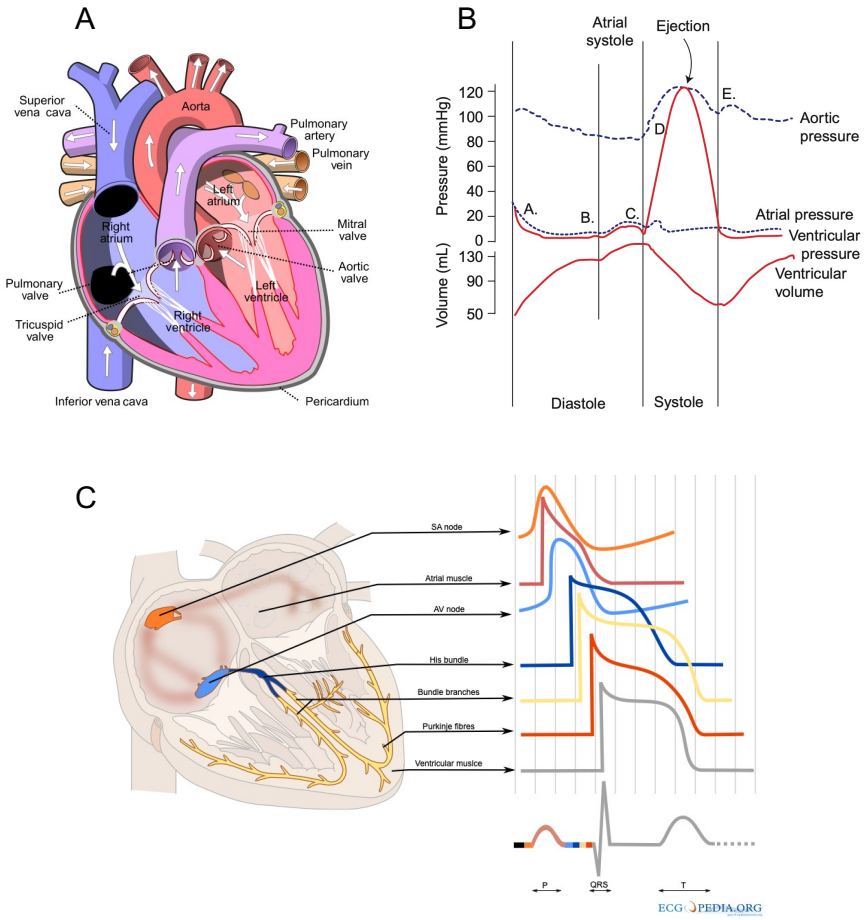

Figure 2.1. Schematic representation of the human heart structure and function. A: The human heart structure (reproduced from https://commons.wikimedia.org/w/index.php?curid=830253 under Open Access Licence). B: Pressure and volume changes during the cardiac cycle (reproduced from [35] with permission). C: The human heart electrical activity represented by the cellular action potentials from various cardiac regions and the associated body surface electrocardiogram (reproduced from https://en.ecgpedia.org/index.php?title=Conduction under Open Access Licence).

When ventricular pressure falls below that of the pulmonary artery and aorta, the blood in the pulmonary artery and aorta pushes back on the semilunar valve forcing it closed (Figure 2.1B, point E), completing the cardiac cycle.

Cardiac function depends on its chronotropic (cardiac frequency), inotropic (cardiac contractility), and lusitropic (cardiac relaxation) characteristics. Cardiac chronotropy ensures adequate heart rate changes to match metabolic demand. Myocardial inotropy represents the intrinsic force-generating ability of cardiac contractile proteins, while lusitropy represents the rate of myocardial relaxation, and it is linked to the reuptake into the sarcoplasmic reticulum and extrusion from the cell of calcium ions [36].

Cardiac function is also influenced by cardiac loads generated by the flow conditions in the veins and arteries, known as pre- and after-load. The preload is exerted on the myocardium by venous return and corresponds to the end-diastolic pressure that stretches the ventricular wall prior to contraction [37]. The afterload is the resistance against which the ventricle works and represents the load that needs to be overcome to expel blood [37].

The haemodynamic function of the heart is generated and coordinated by its electrical activity. Cardiac tissue is a syncytium of cardiac muscle cells, the cardiomyocytes, which are excitable and contractile. The electrical activity of the heart is initiated at the sinoatrial node, a collection of cells located on the right atrium that act as autonomous oscillators. The electrical signal generated here propagates through the atria to reach the atrioventricular node, located at the base of the atria. The septum that divides the atria and the ventricles is composed of non-excitable cells, and electrical excitation can continue propagation only through the atrioventricular node. From here, the electrical

signal propagates towards the ventricles through specialised fibres called Purkinje fibres that spread throughout the interior of the ventricles, ending on their endocardial surface. Electrical signals then emerge from the Purkinje fibre-muscle junctions, activate the ventricular muscle, and propagate through the ventricular wall towards to the epicardial surface (Figure 2.1C).

The electrical potential field generated by the electrical activity of the heart can be measured on the body surface and the acquired signal is called the electrocardiogram. The electrocardiogram describes the succession of electrical waves (the action potentials, see below) from the sinoatrial node to the ventricles in a complete cardiac cycle from contraction to relaxation (Figure 2.1C). It is composed of three main waveforms: the P wave, representing the depolarisation of the atria, the QRS complex, representing the depolarisation of the ventricles, and the T wave, representing ventricular repolarisation. The electrocardiogram is one of the most important tools to detect cardiac rhythm abnormalities in the clinic.

2.1.2 Cardiac excitation-contraction coupling of human cardiomyocytes

Cardiomyocytes are excitable cells which respond to electrical stimuli. If the electrical stimulus does not surpass the threshold for depolarisation, the potential difference across the cell membrane will quickly return to its resting value. On the other hand, if the stimulus is above threshold to trigger cellular depolarisation, the cell transmembrane potential rapidly increases precipitating an action potential (AP) [38]. The AP triggers contraction through the process of excitation-contraction coupling [39].

The AP describes the overall change in the membrane potential that results from changes in the activity of specific ionic currents, and it is characterised by a rapid depolarisation followed by a slower repolarisation (Figure 2.2A). The shape of a healthy cardiomyocyte AP is usually composed of the following different phases (Figure 2.2A) [40]. Phase 0 is the depolarisation phase, associated to the rapid influx of sodium ions in the cell that generates the fast sodium current (I_{Na}), and corresponds to the initial upstroke of the AP. Phase 1 initiates the repolarisation phase of the AP (early-repolarisation), and it is associated with the cessation of the I_{Na} current. Membrane repolarisation is driven by the transient outward potassium current (I_{to}). This phase corresponds to the first deflection (notch) of the AP trace. Phase 2 is the plateau phase, mediated by several currents. It is mostly maintained by the L-type calcium current (I_{CaL}), counteracting the fast and slow delayed rectifying potassium currents (I_{Kr} and I_{Ks}). In this phase, calcium ions enter the cell, and potassium ions leave the cell. Phase 3 is the repolarisation phase associated with potassium ions leaving the cell through the I_{Ks} and I_{Kr} currents. Finally, Phase 4 is the resting phase, where cardiomyocytes are back in the resting state characterised by a membrane voltage of approximately -85mV. The inward potassium rectifier (I_{K1}) and the sodium/potassium adenosine triphosphatase (ATPase) (I_{NaK}) currents play a key role in maintaining the resting membrane potential during this phase.

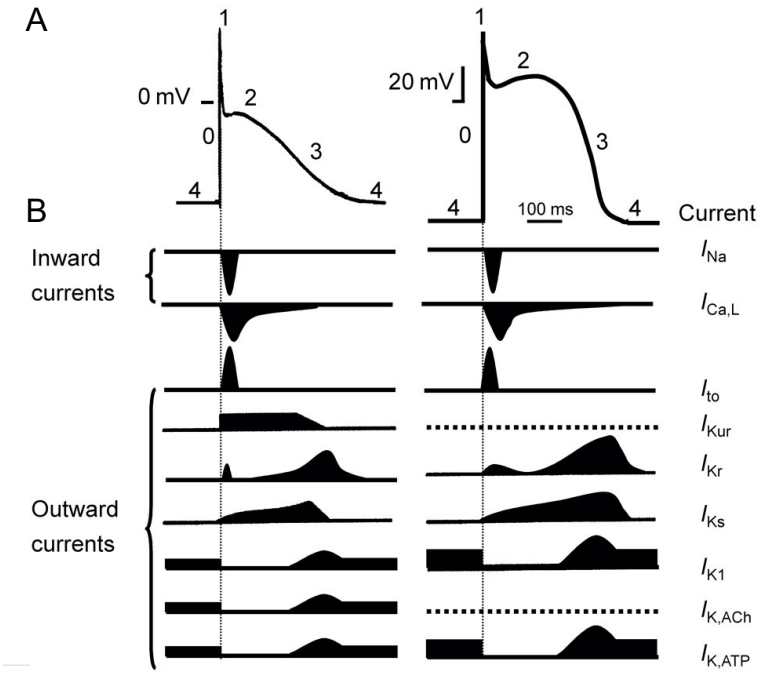

Figure 2.2. Inward (depolarising) and outward (repolarising) currents that underlie the different phases of the atrial (left) and ventricular (right) action potentials. Please see text for details. Adapted from [41] under Open Access Licence.

The dynamic changes of the AP waveform are due to a complex balance of ion fluxes across the cellular membrane, which separates the intracellular and extracellular spaces and creates a transmembrane electrochemical gradient. The electrochemical gradient drives AP dynamics and it is a combination of the concentration gradient due to differences in ionic concentrations across the membrane, and the electrical field between the two sides of the membrane. The ionic fluxes that generate the AP are facilitated by the proteins embedded in the cell membrane which are selectively permeable to ions under specific conditions. These include ion channels, ion exchangers, and ion pumps. The gating activity of each of these proteins regulates their dynamics and responds to changes in membrane voltage or ionic concentrations, among other factors [40].

Calcium is considered one of the most important ions that crosses the cell membrane because of its key contribution to the excitation-contraction coupling process, enabling cardiac contraction and relaxation [39]. Calcium ions enter the cell during the AP mainly through the L-type calcium channels, which are voltage-gated and therefore activated by depolarisation. This triggers an additional release of calcium ions from the sarcoplasmic reticulum via ryanodine receptors through the calcium-induced calcium-release (CICR) process. L-type calcium channels are located at the sarcolemmal-sarcoplasmic reticulum junctions in close proximity to the ryanodine receptors. It is the combination of influx and release of calcium that creates a sufficiently large calcium signal to activate contraction. When calcium ions bind to the myofilament protein troponin, they initiate a chain of events involving dynamic and structural changes in troponin and tropomyosin, thereby activating the thin filament by unearthing the myosin binding sites on actin, which promotes cyclical acto-myosin interactions and force generation (details provided in the next section). Myofilament relaxation occurs when the sarcoplasmic reticulum calcium-ATPase, sarcolemmal sodium-calcium exchange, sarcolemmal calcium-ATPase, and mitochondrial calcium uniport transporters transport calcium away from the cytosol [39]. This reduces the intracellular calcium concentration and facilitates myofilament inactivation.

The development of contraction force depends on intracellular calcium in a complex dynamic non-linear manner, which is a result of the cooperative behaviour of the myofilaments [39]. Force production at the myofilament is very sensitive to calcium, which facilitates rapid and synchronous myofilament activation by producing significant changes in force from small changes in

intracellular calcium. This is well represented by the steep force-calcium relationship observed in permeabilised cardiac muscle cells. This relationship can be accurately described by a Hill equation:

$$F = \frac{1}{1 + 10^{n_H(pCa - pCa_{50})}}$$

where free calcium is usually expressed on a logarithmic scale as $pCa = -log_{10}[Ca^{2+}]$ and the Hill coefficient (n_H) is a convenient measurement of the steepness of the curve. The high values of n_H observed in demembranated and intact trabeculae indicate myofilament cooperativity [42]. pCa_{50} represents the calcium value corresponding to half-maximum force. Myofilament calcium sensitivity can be altered by several factors including stretch, β-adrenergic activation, inotropic drugs, and also disease-causing mutations [18].

In intact cardiac cells, force generation is driven by the AP and thin filaments are not fully activated by the intracellular calcium transient, which has a small amplitude and short duration, and also raises and decays faster than the force generated from these calcium transients. In fact, peak calcium in a twitch is typically 0.5-1.0 μM whereas ~30 μM calcium is needed to elicit peak force in permealised myocardium [42]. Due to this, the instantaneous force-calcium relationship varies during the time course of the twitch. The twitch contractile waveform is therefore driven by the properties of the steady-state force-calcium relationship and the dynamics of the mechanisms that govern force generation within myofilaments [42].

2.1.3 The structure and function of cardiac myofilaments

Within cardiac myocytes, there is an abundance of myofibrils, which contain the cardiac sarcomeres, the functional unit of contraction. Sarcomeres are distinct, repeating units of overlapping thick and thin myofilaments (Figure 2.3A) which extend between Z-discs. The sarcomere is divided into A-, I-, and H-bands. The darker A-band contains thick and thin filaments whereas the lighter I-band is composed of thin filaments only. The H-band occupies the central portion of the A-band and contains only thick filaments without overlapping thin filaments [43]. Thick filaments are interconnected in the middle via the M-band and are held in place by titin. Thick filaments consist of myosin, myosin binding protein C, and myosin essential and regulatory light chains. Myosin is an actin-based molecular motor protein that hydrolyses adenosine triphosphate (ATP) to generate force. Cardiac myosin II molecules consist of two myosin heavy chains and two sets of light chains, the essential light chain (ELC) and the regulatory light chain (RLC). Myosin sub-fragment 1 (S1), contains the globular head of the myosin with the ATP- and actin-binding sites, followed by an ELC- and RLC-bound α-helix (lever arm), as illustrated in Figure 2.3B. Thin filaments are anchored in the Z-discs and contain actin and regulatory proteins including the troponin complex (troponin I, C and T) and tropomyosin.

During the cardiac cycle, sarcomere length changes as a result of thick and thin filaments sliding past one another. Calcium-based activation of the thin filament occurs when calcium binds to troponin C and enhances troponin C-troponin I interactions, which in turn weakens the troponin I attachment to actin, increases tropomyosin mobility on the surface of actin, and exposes myosin-binding sites on actin previously blocked by tropomyosin [44]. Myosin can then

bind actin to form crossbridges while undergoing energy-dependent conformational changes typified by the chemo-mechanical cycle of myosin. The actin-activated myosin chemo-mechanical cycle is presented in Figure 2.3C [45]. In step 1, the strongly-bound myosin head dissociates from actin upon ATP binding. In step 2, the weakly-bound head is locked into a pre-stroke configuration by ATP hydrolysis. Next, the rebinding of the head to actin in a strongly-bound state is associated with phosphate release (Step 3a and 3b). Step 4 is the powerstroke phase that follows strong binding. Finally, in step 5 adenosine diphosphate (ADP) is released, allowing rapid ATP binding, and the cycle starts once again (Figure 2.3C).

Cyclical interactions between actin and myosin in the presence of ATP drive sarcomeric contraction and generates power. This can be estimated by multiplying the ensemble force generated by myosin heads on actin and the maximal velocity of actin filaments driven by myosin heads [45].

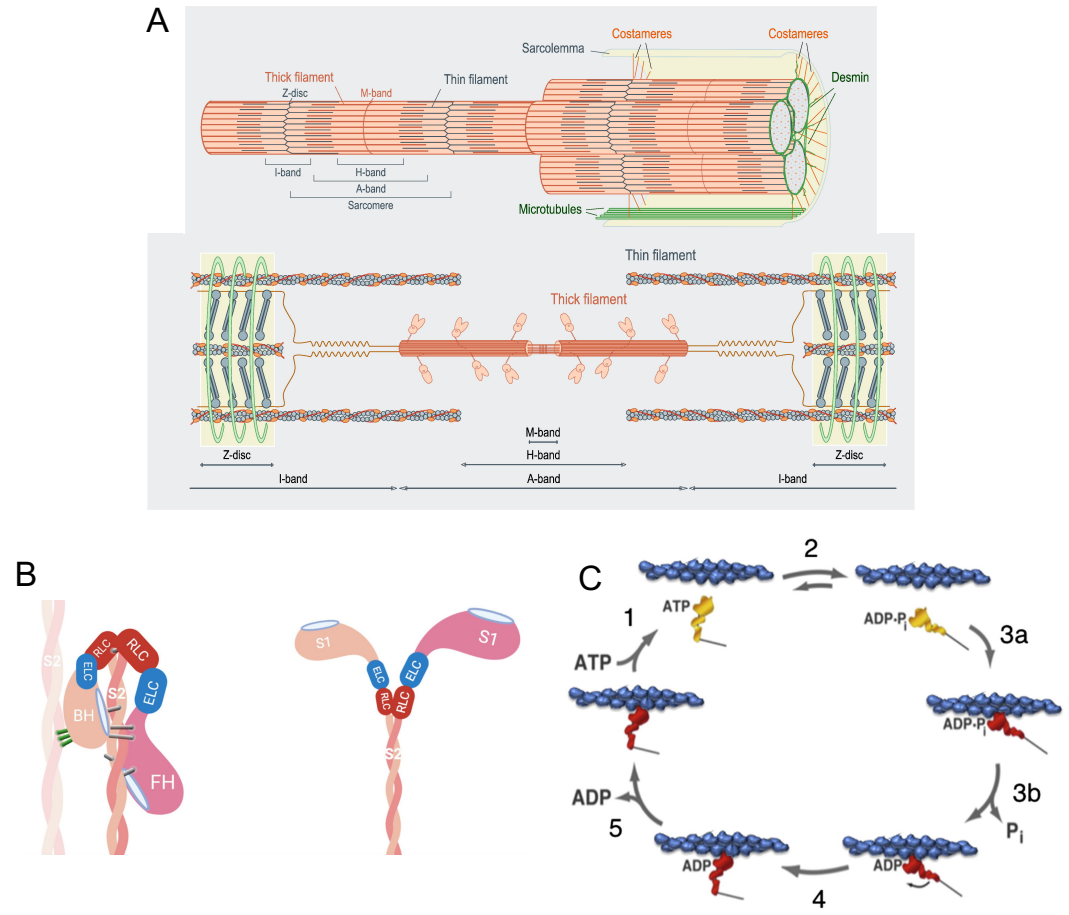

Figure 2.3. Force generation in cardiac sarcomeres. A: Schematic representation of cardiac muscle and individual sarcomere (reproduced from [46] under Open Access Licence). B: Myosin state conformations. Left: Folded back conformation. The blocked head (BH) is prevented from binding to actin by interacting with the free head (FH). Intermolecular (green) and intramolecular (grey) interactions highlighted. Right: The open on-state. S2: myosin subfragment 2, myosin neck region; ELC: myosin essential light chain; RLC: myosin regulatory light chain. Reproduced from [47] under Open Access Licence. C: The actin-activated myosin chemo-mechanical cycle. See text for details (reproduced from [45] under Open Access Licence).

Myosin ensemble force is the product of the intrinsic force generated by a single myosin head, the duty ratio (the fraction of time a myosin molecule

remains bound to actin), and the total number of functionally accessible myosin heads available for interaction with the actin filaments [45].

Recently, a new state of myosin that regulates contractile function by tuning myosin head availability was observed in myocardium [48]. This myosin state is termed the super relaxed state (SRX), where myosin heads are sequestered away from the actin thin filament. Broadly myosin SRX exists in a balance with the disordered relaxed state (DRX), which defines myosins that are available to drive contraction [49]. Myosin SRX is a biochemical and likely structural state primarily characterised by a decreased ATPase activity, where myosin heads interact with one another and the thick filament backbone [50], as illustrated in Figure 2.3B. By sequestering myosin heads away from the thin filament, myosin SRX modulates the constant representing accessible myosin heads (termed N in Huxley's model of force production [51]) and determines force production based on mechanical and metabolic demands [9]. Myosin SRX dysregulation has been observed as a central mechanism of hypertrophic cardiomyopathy pathophysiology [9, 13, 52] and it may have an important contribution to pathogenesis in a variety of human diseases [47]. The therapeutic efficacy of myosin SRX modulation is under investigation and has the potential for providing targeted pharmacological interventions in genetic cardiomyopathies [53].

2.2 Hypertrophic cardiomyopathy (HCM)

2.2.1 Disease overview

Hypertrophic cardiomyopathy (HCM) is a common inherited cardiac disease with a range of potential outcomes including more serious conditions such as

heart failure, and sudden cardiac death [54]. HCM is a highly clinically and genetically heterogeneous disease with a prevalence of about 1 in 500 [54]. HCM is defined by the presence of increased left ventricular wall thickness that is not solely explained by abnormal loading conditions [55]. In up to 60% of HCM patients, the disease is an autosomal dominant trait caused by mutations in cardiac sarcomeric protein genes [55]. Over 1500 mutations have been associated with HCM, and in the majority of patients these reside in the genes encoding β-myosin heavy chain (*MYH7*) and myosin-binding protein C (*MYBPC3*). Mutations are also found in other genes, including cardiac troponin I and T (*TNNI3*, *TNNT2*) each accounting for a small proportion of patients (1% to 5%) [17]. Recent analyses showed that HCM patients with pathogenic or likely pathogenic mutations are at a higher risk of developing heart failure and arrhythmias, compared to sarcomeric negative HCM patients [56].

HCM is diagnosed upon detection of increased left ventricular wall thickness by echocardiography, cardiac magnetic resonance imaging, or computed tomography, yet myocardial fibrosis, morphologic abnormalities of the mitral valve and apparatus, abnormal coronary microcirculatory function, and electrocardiographic abnormalities can also represent signs of the disease [55].

Since the landmark discovery that HCM is a genetic disease and with the recent advances in genetic testing, the number of patients with sarcomeric mutations that do not fulfil HCM diagnostic criteria has grown steadily. These are often called genotype-positive phenotype-negative individuals and, despite not having increased left ventricular wall thickness, they may present with a variety of cardiac abnormalities, including myocardial fibrosis, subclinical

diastolic dysfunction, and electrocardiographic abnormalities, which need more advanced screening methodologies to be detected, such as contrast-enhanced magnetic resonance imaging [54].

In spite of relatively low mortality rates, life-threatening complications due to HCM can occur, including sudden death in asymptomatic or mildly symptomatic patients, progressive heart failure with preserved systolic function with or without outflow tract obstruction, and systolic dysfunction [54]. HCM remains one of the most common causes of death in young people under 35 years of age. The identification of patients at high risk of sudden cardiac death is crucial to decide on prophylactic implantation of cardioverter defibrillators, yet diagnosis remains challenging [57]. An improved understanding of the complex multifactorial pathophysiology of HCM is needed to better risk stratify patients.

Cellular phenotype

Several cellular abnormalities have been identified in the myocardium of HCM patients which play an important role in disease development. These cellular abnormalities include ion channel and calcium handling changes, increased myofilament calcium sensitivity, blunted length-dependent myofilament activation, and increased amount of ATP used during force development (increased tension cost), as reviewed in [18]. Intracellular calcium handling is impaired in human HCM cardiomyocytes and associated with a prolonged action potential duration [58]. It was proposed that sarcomeric mutations cause a primary sustained increase in intracellular calcium through multiple mechanisms triggering a complex remodelling process involving alterations of

calcium/calmodulin kinase II (CaMKII). Increased phosphorylation of CaMKII downstream targets may be responsible for the abnormalities observed in HCM cardiomyocytes, and further contribute to abnormal calcium handling, thus setting up a pathological positive feedback loop [58]. Intracellular calcium handling abnormalities may also be exacerbated by increased calcium sensitivity at the myofilament, another key cellular hallmark of HCM.

In HCM the increased myofilament calcium sensitivity increases force generation and impairs relaxation with profound effects on ATP consumption. Increased myofilament calcium sensitivity has been observed in several systems, including human cardiac tissue obtained from HCM patients [59-62]. In HCM patients, length-dependent myofilament activation also appears to be blunted [62]. Length-dependent myofilament activation is an important cellular mechanism to modulate cardiac performance, and in HCM cardiomyocytes the increase in maximal force-generating capacity and myofilament calcium sensitivity upon stretch is smaller compared to healthy cardiomyocytes [62]. This can significantly impair diastolic function.

Tension cost is also usually increased in cardiac muscle preparations from HCM patients [63], meaning that the amount of ATP used during force development is higher than expected. Energetic alterations have been shown to be primarily related to the sarcomere mutation, with tension cost being higher in sarcomere positive compared with sarcomere negative HCM patients [63]. Recent studies have shown that physiological shifts between low- and high-energy myosin conformations are key for balancing energy consumption [9], and the thick filament mutations that disrupt the myosin low-energy conformation [9, 13, 52] lead to increased contractility and high energy usage.

2.2.2 The genotype-phenotype relationship in human hypertrophic cardiomyopathy

Remarkable progress has been made in the understanding of the genetic and molecular basis of HCM. It was first described in 1958 by Robert Donald Teare, who reported autopsy findings of patients with asymmetrical hypertrophy of the heart [64]. The first underlying genetic cause of HCM was reported in 1989 [3], when a gene responsible for familial HCM was mapped to its chromosome location. The first missense variant in exon 13 of the *MYH7* gene, that substituted an arginine residue (403) with glutamine in all affected, but no unaffected, HCM family members was discovered in 1990 [65]. Multiple research teams then confirmed the finding that sarcomere mutations cause HCM [66-70] and disease-causing mutations are now identified in ~60% of all HCM individuals [55]. However, despite the growing knowledge about the different causal genes, our understanding of the relationship between genotype and phenotype in HCM is still incomplete, and the notion of mutation-specific clinical outcomes has also been disputed [71]. Connecting genotype to phenotype in HCM is extremely challenging because of the wide phenotypic variability of disease manifestation and underlying pathogenesis, as well as multiple confounding factors including epigenetics and environmental causes [72]. Nevertheless, accumulating evidence shows that HCM pathophysiology and response to treatment depend on the underlying sarcomeric gene mutation [18], paving the way for a personalised approach to HCM therapy.

Lopes et al. [73] reviewed the literature on genotype-phenotype associations in patients with HCM and reported that in the 18 publications (corresponding to a total of 2459 patients) considered, the presence of any sarcomere gene

mutation was associated with a younger age at presentation, a family history of HCM, a family history of sudden cardiac death, and greater maximum left ventricular wall thickness. There were no differences when the two most frequently affected genes, *MYBPC3* and *MYH7*, were compared [73]. Recent analyses from the SHaRe registry (Sarcomeric Human Cardiomyopathy Registry) on 4591 HCM patients confirmed that the presence of a sarcomere mutation, together with a young age at diagnosis, is a predictor of adverse outcomes [56].

Sedaghat-Hamedani et al. [74] analysed 51 studies with 7675 HCM patients with mutations in the *MYBPC3*, *MYH7*, *TNNT2*, and *TNNI3* genes. They reported an earlier age of onset of disease in HCM patients carrying an *MYH7* variant, which also predicted a more severe phenotype than in patients without such mutations. Cardiac conduction disease, ventricular arrhythmia, and heart transplantation rate were higher in HCM patients with *MYH7* mutations in comparison to *MYBPC3*, and patients with sarcomeric mutations were more susceptible to sudden cardiac death.

Coppini et al. [75] compared thick (*MYBPC3*, *MHY7*, *MYL2*) and thin (*TNNT2*, *TNNI3*, *TPM1*, *ACTC*) filament gene mutations in adult HCM patients. Thin-filament mutations were associated with increased likelihood of advanced left ventricular dysfunction and heart failure compared with thick filament disease, whereas arrhythmic risk in thick and thin filament variant carriers was comparable [75]. Thin filament mutations, particularly in *TNNI3* and *TNNT2*, were also found to be associated with a risk of lethal arrhythmic events in paediatric-onset HCM patients [76].

A gene-specific response to pharmacological treatment in HCM has been reported [77, 78]. In a placebo-controlled clinical trial of preclinical HCM carriers harbouring different sarcomeric gene mutations, treatment with the L-type calcium channel blocker Diltiazem was safe and improved early left ventricular remodelling. However, while left ventricular wall thickness and mass, diastolic filling, and cardiac troponin I levels improved in *MYBPC3* patients, they did not improve in *MYH7* mutation carriers [77].

In non-obstructive HCM patients with sarcomere gene mutations treated with the angiotensin II type 1 receptor antagonist Candesartan, the drug-induced remodelling of the left ventricular mass was gene-specific. A marked decrease in the left ventricular mass was observed in *MYH7* patients, a moderate decrease was observed in *MYBPC3* patients, and no regression was observed in patients with a *TNNI3* mutation [78].

Gene-specific cellular pathology has also been described in cardiac samples obtained from HCM patients, and may underlie the gene-specific differences in clinical phenotype and response to treatment as reviewed by [18]. This included gene- and mutation-specific changes in myofilament calcium sensitivity and length-dependent activation [62], energetic cost of contraction [63], and associated proportions of myosin conformation states [9]. Particularly, in [9] it was shown that *MYH7* variants that altered motifs important for SRX formation had higher rates of adverse clinical outcomes, including heart failure and atrial fibrillation.

2.2.3 Medical treatments

According to the 2014 ESC guidelines on the diagnosis and management of HCM [55], pharmacological management of patients should focus on improving functional capacity, reducing symptoms, and preventing disease progression. In symptomatic patients with left ventricular outflow tract obstruction, the aim is to improve symptoms by using drugs, surgery, alcohol ablation or pacing. Therapy in symptomatic patients without left ventricular outflow tract obstruction should aim at arrhythmia management, reduction of left ventricular filling pressures, and treatment of angina. Patients with progressive left ventricular systolic or diastolic dysfunction refractory to medical therapy may be candidates for cardiac transplantation [55]. However, such symptom-based approaches may decrease patient morbidity, but they do not target disease pathophysiology [79].

Relieving left ventricular outflow tract obstruction in HCM is of particular importance given its role in disease pathogenesis [80]. Left ventricular outflow tract obstruction is present in ~75% of patients with HCM [17] and may be due to septal hypertrophy and narrowing of the left ventricular outflow tract. This can lead to abnormal blood flow vectors that dynamically displace the mitral valve leaflets anteriorly, or anatomical alterations in the mitral valve apparatus that make the valve more susceptible to abnormal flow vectors [17]. For symptomatic obstructive HCM, current medical therapy consists of administering drugs with negative inotropic and chronotropic effects, such as beta blockers, non-dihydropyridine calcium channel blockers (e.g. Verapamil, Diltiazem), or Disopyramide. Septal myectomy is the gold-standard strategy in case of drug-refractoriness [17].

More recently, advances in DNA sequencing and a deeper mechanistic understanding of underlying pathogenesis of the HCM disease has paved the way for precision medicine, which aims to overcome the symptom-based approaches. The precision medicine approaches favour a more discretely targeted strategy to prevent onset or alter progression of HCM, prior to the development of end-stage remodelling [16]. Novel therapies may target the disease-causing gene directly [53] or intervene with cellular pathogenic pathways that play a role in disease progression, such as alterations of myosin conformations [81], myofilament calcium sensitivity [60], ion channel remodelling [77, 82, 83], and perturbations in energetics [84]. Among these, Mavacamten is a particularly promising novel small molecule for the treatment of HCM pathophysiology [79].

Mavacamten

Mavacamten was first described in 2016 by Green et al. [81] as a small molecule that reduces contractility by decreasing the ATPase activity of cardiac myosin. Early, chronic administration of Mavacamten suppressed the development of ventricular hypertrophy, cardiomyocyte disarray, and myocardial fibrosis, and attenuated hypertrophic and profibrotic gene expression in mice harbouring heterozygous patient specific mutations in the myosin heavy chain [81]. Further analyses [85] revealed that Mavacamten modulates multiple steps of the myosin chemo-mechanical cycle. This study confirmed that the primary mechanism of action of Mavacamten is its ability to slow phosphate release from β-cardiac myosin-S1. A secondary mechanism of Mavacamten treatment has been identified whereby the number of cross-

bridges transitioning from the weakly to the strongly bound states is decreased [85].

Mavacamten was later shown to relieve many of the biochemical, energetic, and cellular disease hallmarks in thick filament models of HCM [9, 50, 52, 86], alongside clinically relevant disease features [79]. It was shown that certain mutations that cause HCM destabilise the low-energy super-relaxed state of cardiac myosin (Section 2.1.3), while the small molecule Mavacamten promotes it [9, 50, 86], thereby correcting the HCM cellular contractile and metabolic phenotypes [9]. Mavacamten was also shown to partially salvage some cellular abnormalities of two thin filament HCM variants [87]. However, the incomplete rescue of the phenotype suggests that a more targeted approach should be adopted to address thin filament mutation pathophysiology [47].

Since the hypercontractile state is recognised as a final common endpoint in HCM independently of genotype, and based on the promising results obtained in pre-clinical models of thick filament HCM, Mavacamten has progressed to clinical trials. In the proof-of-concept phase 2 PIONEER-HCM trial, treatment with Mavacamten in obstructive HCM was generally well tolerated and improved post-exercise left ventricular outflow tract gradients and exercise capacity and symptoms [88]. In the multicentre, phase 3, randomized, double blind, placebo-controlled trial EXPLORER-HCM [79], involving 251 obstructive HCM patients, Mavacamten led to clinically meaningful improvements in haemodynamic status, functional capacity, and subjective wellbeing. These results were achieved at the expense of a small average reduction in ejection fraction. Severely symptomatic patients were excluded from this trial but have

now been included in the VALOR-HCM trial (A Study to Evaluate Mavacamten in Adults with Symptomatic Obstructive HCM Who Are Eligible for Septal Reduction Therapy; NCT04349072). In the EXPLORER-HCM cardiac magnetic resonance sub-study, Mavacamten treatment was shown to favourably impact HCM cardiac remodelling in terms of absolute intracellular myocardial mass index, left ventricular mass index and wall thickness, left atrial volume index, reduced hypertrophy and left atrial volume, and reduced levels of plasma biomarkers of myocardial stress and injury [89]. Mavacamten is also under investigation for non-obstructive HCM (phase 2 MAVERICK-HCM trial), and exploratory analyses showed a significant reduction in N-terminal pro B-type natriuretic peptide, although only one third of patients with a more severe phenotype improved in terms of New York Heart Association class and peak oxygen consumption [90].

2.3 Drug cardiac safety and efficacy assessment in preclinical research

Drug safety and efficacy is one of the biggest challenges in both preclinical and clinical drug development [1, 91, 92]. Predicting the effect of a drug on cardiac function is especially complex, and cardiotoxicity is one of the major reasons limiting drug progression to the clinic, or its withdrawal from the market [2]. Therefore, predicting the cardiac safety profile of a drug in specific patient populations is essential for both safety and pre-clinical development efficiency. Regulatory guidance issued in 2005 mandates the non-clinical and clinical investigation of the effects of all new chemical entities on cardiac electrophysiology, specifically those that may delay ventricular repolarisation [93, 94]. Drug-induced effects on cardiac contractility is only part of follow-

up/supplementary studies (see below). These documents were issued in response to the recognised link between drug treatment, delayed repolarisation, and the life-threatening Torsades de Pointes (TdP) ventricular arrhythmias [95]. They focus on the non-clinical (ICH S7B) and clinical (ICH E14) assessment of the risk of heart rate-corrected QT interval (QTc) prolongation on the electrocardiogram as a surrogate marker of TdP arrhythmia. The three core assays associated with the regulatory guidance include the in-vitro hERG, in-vivo QT assays, and the clinical thorough QT (TQT) studies. The hERG assay is particularly important as it evaluates the propensity of a drug to block the rapid delayed rectifier potassium current I_{Kr} (carried by hERG channels), a major determinant of ventricular repolarisation. In fact, the majority of compounds that can induce TdP are known to also block I_{Kr}, although I_{Kr} block alone is not always predictive of pro-arrhythmic risk [96]. Since this guidance was issued no newly approved drugs have been removed from the market because of TdP risk. However, this guidance has also unintentionally prevented the development of otherwise safe and effective drugs [97]. In fact, it is now well recognised that the prolongation of the QTc interval is a sensitive but not specific endpoint to predict pro-arrhythmia, and the current approaches are suitable to predict QTc prolongation but are inadequate to assess the risk of TdP [98].

Based on these findings, a new strategy was proposed in 2013 by the US Food and Drug Administration among others, the Comprehensive in-vitro Proarrhythmia Assay (CiPA) [99]. The CiPA approach shifts the focus from the hERG assay towards a mechanistic assessment of pro-arrhythmia risk by means of (i) multiple cardiac ion channel screening, (ii) in-silico models of the

human ventricular AP for the mechanistic prediction of drug-induced repolarisation abnormalities based on the drug ion channel profile, and (iii) confirmation of the results from ion channel screening and in-silico modelling with human stem cell-derived cardiomyocytes (hiPSC-CMs) [98]. Such an approach aims at the early mechanistic detection of potential pro-arrhythmia liabilities with the aim of avoiding costly failures in drug development.

A novel key feature of the CiPA approach is the use of hiPSC-CMs, together with the use of in-silico models (as reviewed in the next chapter).

hiPSC-CM technology is based on the discovery by Yamanaka and colleagues that induced pluripotent stem cells can be generated from adult human fibroblasts [100] and then differentiated into functional cardiomyocytes. hiPSC-CMs present several key features that make them a valuable tool for mechanistic investigation of drug-induced cardiotoxicity in safety pharmacology and precision medicine [101]: large-scale production of hiPSC-CMs can be achieved efficiently and cost-effectively; they do not involve the use of human embryos, thereby avoiding ethical concerns; they express human cardiac ion channel and sarcomere genes, allowing them to overcome the shortcomings of species-related differences in physiology and gene expression profiles that confound the translation of results from animal models to human; they can be patient- and disease-specific. The potential of hiPSC-CMs for the prediction of both drug-induced pro-arrhythmia [102, 103] and changes in cardiomyocyte contraction [104] has already been shown, despite the well-known limitations of this experimental model related to hiPSC-CM immaturity when compared to adult cardiomyocytes [105].

Compared to the assessment of drug-induced pro-arrhythmic risk, the routine evaluation of drug-induced changes in cardiac inotropy (the force of cardiac contraction) has not yet been rigorously formulated and there is no consensus on whether this should be mandatory or not [106]. Nevertheless, the inotropic risk evaluation is an essential part of the drug development process to determine the safety profile of a candidate compound. Drug-induced alterations in cardiac contractility can have little or no effect in healthy volunteers, but can also increase metabolic demand, risking myocardial hypoxia or inducing heart failure symptoms in certain patient populations [106]. Current measurements of drug-induced changes in contractility are conducted by means of phenotypic assays, typically involving in-vivo studies or isolated whole heart models [107, 108], despite the limited throughput. More recently, in-vitro models, with higher throughput, have gained momentum. These include freshly isolated adult cardiomyocytes [109-112] and hiPSC-CMs [104, 113-115].

Current strategies for the assessment of drug-induced pro-arrhythmia and inotropic risk assessment share some common challenges, including the need to tackle inter-subject variability in drug response and the translation of findings from the animal models extensively used in drug testing to humans.

Several factors can modulate the safety and therapeutic efficacy of pharmacological interventions such as gender, age, genetic background, disease, and life-style [116, 117]. These cannot be studied in animal models, which also present significant pathophysiological differences compared to humans [118].

The need of a human-based approach that provides mechanistic prediction and understanding of drug safety and efficacy is evident. This approach must extend to modelling modulation of drug effects by genetic background, comorbidities and environmental factors that have been identified in specific patient populations [31, 119]. Human-based computational methodologies have already begun to prove their potential in this regard, as discussed in further detail in the next chapter.

3 Computational background

In this chapter, I present the available computational methodologies to investigate cardiac pathophysiology and conduct in-silico drug trials using human-based modelling and simulation. I first provide an overview of human cardiac modelling and simulation, including state-of-the-art human cardiac electrophysiology and contractility models. I then introduce the concept of the Digital Twin and the vision of precision medicine. Next, I review computational studies of HCM. Finally, I conclude the chapter by presenting the available methodologies to conduct in-silico drug trials and evaluate drug cardiac safety and efficacy using human-based modelling and simulation.

3.1 Human-based cardiac modelling and simulation – overview

In the last six decades, biophysically detailed information on human cardiac pathophysiology has been successfully integrated into computational modelling and simulation frameworks. At the basic science level, this has facilitated and augmented mechanistic investigations of cardiac function and disease [32], paving the way for a new era of personalised care in cardiovascular medicine. Population- and patient-specific cardiac modelling and simulation offer the opportunity to define the optimal therapy choice for each individual patient, which can be extended to patient populations. Industrial and regulatory bodies have already shown interest in such tools for

the evaluation of the safety and efficacy of new or existing therapeutic interventions [120].

This is now possible thanks to the ground-breaking research that led to the development of the first models of cardiac APs and force generation. This was achieved through an iterative process employing experimental findings and theoretical principles [121]. The early theoretical work on cardiac electrophysiology and contractility models has been instrumental in guiding experimental research, and represents the base for the biophysically-detailed models of cell- and species-specific electrophysiology, calcium handling, and force generation that are now available. These models can now represent ion channel, buffer, pump, transporter, and myofilament protein dynamics, while including physiological processes such as pH regulation, β-adrenergic stimulation, and calcium homeostasis, and relating these processes to the modulation of cellular and organ level function [122].

3.1.1 Human cardiac action potential models

The initial modelling studies of the cardiac AP (1960-1980) were based on the seminal work by Hodgkin & Huxley on the giant squid nerve AP [123]. In their 1952 paper, Hodgkin & Huxley provided measurements of sodium and potassium ion channel kinetics and formulated differential equations whose solution yielded accurate predictions of the nerve AP and conduction velocity. Denis Noble [124] then developed the first cardiac AP model, characterised by a longer AP than the neuronal one and automaticity, by refitting the formulation for the fast sodium and inward rectifier currents, I_{Na} and I_{K1}, to electrophysiological recordings obtained in mammalian cardiac Purkinje fibres.

In addition to I_{K1}, Noble included in his model a new potassium current, representing the delayed potassium rectifier current, whose conductance slowly increases during the depolarisation phase, thereby prolonging AP duration.

The extension of the voltage clamp technique to the heart [125] facilitated the discovery of several different ion channels, including multiple delayed rectification channels, calcium channels, and the sodium-potassium and sodium-calcium exchangers, whose contribution were then included in the subsequent models. The McAllister-Noble-Tsien [126] model included the multiple slow potassium ion channels and the calcium ion channels. Beeler-Reuter [127] developed the first model of ventricular cells. The DiFrancesco-Noble [128] model incorporated the hyperpolarising-activated mixed sodium-potassium cation channel I_f [129], and, for the first time, changes in intracellular and extracellular ionic concentrations, and the intracellular calcium signalling system. This was the most significant departure from the Hodgkin & Huxley formulation [130]. The modelling of calcium movements was then incorporated into subsequent models including the Earm-Noble [131] model, the first model based on single cell experiments rather than multicellular cardiac tissue.

Nowadays there exist multiple cardiac cell models, covering different cell types and species. Each model has its own strength and limitations and should be carefully chosen based on the research question of interest. Among all human cellular ventricular models, some of the most recent and popular ones are the ten Tusscher-Panfilov model [132], the Grandi et al. model [133], the Carro et al. model [134], the O'Hara et al. model [135], and the ToR-ORd model [136]. The most relevant for the research conducted in this thesis is the human ToR-

ORd model (Tomek-Rodriguez - following ORd) developed from the ORd (O'Hara-Rudy dynamic) model.

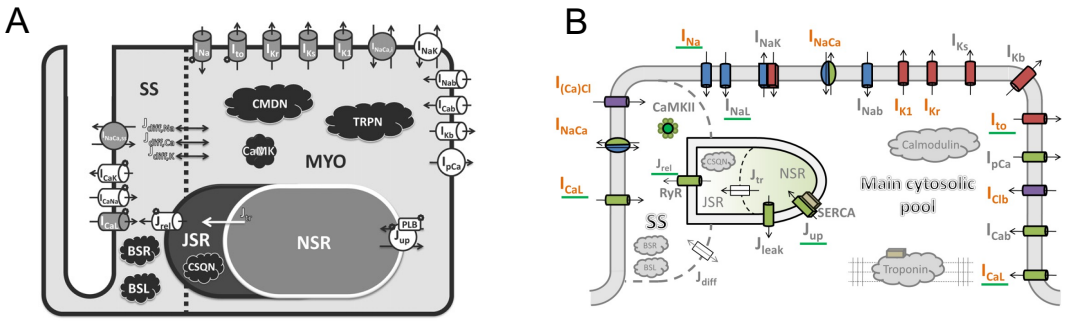

Figure 3.1. ORd (left) and ToR-ORd (right) model diagrams (reproduced from [135, 136] under Open Access Licence).

The ORd human ventricular AP model (Figure 3.1, left panel, [135]) was developed in 2011 using novel un-diseased human ventricular data and well replicated calcium/calmodulin-dependent protein kinase II signalling, arrhythmia precursors such as alternans and early afterdepolarisation, and responses to simulated drug block and disease remodelling. The ToR-ORd model (Figure 3.1, right panel, [136]) was then developed from the ORd model to overcome its shortcomings. In fact, the comparison of simulation outputs, mainly the AP and calcium transient, obtained with the ORd model against human ventricular experimental data had revealed important inconsistencies, related to the AP plateau, the dynamics of accommodation of the AP duration to heart rate acceleration, and the positive inotropic effect of sodium current block on calcium transient amplitude. Thus, the authors focused on an in-depth re-evaluation of the L-type calcium current I_{CaL} formulation and re-assessment of the rapid delayed rectifier current I_{Kr}, among other model modifications.

Importantly, they adopted a development strategy based on strictly separated model calibration and validation, which led to the design, development, calibration, and validation of a novel model of human ventricular electrophysiology and excitation contraction coupling. The resulting model reproduced all key depolarisation, repolarisation and calcium dynamic properties in healthy ventricular cardiomyocytes under drug block and in key diseased conditions, such as hyperkalemia and HCM [136]. Particularly, the validated model exhibited an AP and calcium transient morphology in agreement with human data, responded well to drug block, and could replicate arrhythmia precursors such as early afterdepolarisations and alternans. When embedded in whole-heart simulations it generated physiological conduction velocities and realistic electrocardiogram signals.

The ToR-ORd and the other human models mentioned above are all biophysically-detailed and describe, through mathematical equations, the main biophysical cellular processes (e.g. ion currents and fluxes) of human ventricular myocytes separately, allowing for connection between sub-cellular and cell level phenomena. They usually include three main compartments (the bulk cytoplasm, where most ionic currents enter or exit the cell; a cytoplasmic subspace representing the space near the T-tubules; and one or more compartments representing the sarcoplasmic reticulum) and many ionic currents (usually the sodium current I_{Na}, sometimes divided into fast and late components; L-type calcium current I_{CaL}; the transient outward potassium current I_{to}; the rapid and slow delayed rectifier potassium currents I_{Kr} and I_{Ks}; the inward rectifier potassium current I_{K1}; the sodium-calcium exchange

current I_{NaCa}; the sodium-potassium pump current I_{NaK}) as illustrated in Figure 3.1.

From a mathematical point of view, such models for cardiac electrophysiology are based on systems of ordinary differential equations (ODEs):

$$C_m \frac{dv}{dt} + i_{ion}(v, \boldsymbol{w}, \boldsymbol{c}) = i_{app}(t),$$

$$i_{ion}(v, \boldsymbol{w}, \boldsymbol{c}) = \sum_{k=1}^{P} g_k(\boldsymbol{c}) \prod_{j=1}^{M} w_j^{p_{jk}}\big(v - v_k(\boldsymbol{c})\big) + I_0(v, \boldsymbol{c}),$$

$$\frac{d\boldsymbol{w}}{dt} = m_w(v, \boldsymbol{w}, \boldsymbol{c}), \qquad \frac{d\boldsymbol{c}}{dt} = m_c(v, \boldsymbol{w}, \boldsymbol{c}).$$

Following the formalism presented [137], v denotes the local transmembrane potential between the intra- and extra-cellular fluid, C_m is the local membrane capacitance, i_{app} is the applied external current. The ionic currents usually follow a Hodgkin-Huxley type description for P different ionic species with v_k being the reversal potential of the k-th ionic species; w_j are the so-called gating variables, taking values in [0, 1] and regulating the transmembrane currents and the intracellular concentrations c_k of the different ionic species.

3.1.2 Human cardiac contractility models

Similar to models of cardiac electrophysiology, the development of models of cardiac mechanics has evolved significantly over the past decades, and has been tightly connected to the growing availability of experimental data. This has allowed the translation of the initial seminal studies in skeletal muscle, into cardiac-, species-, human- and finally patient-specific modelling frameworks

[138] with the aim of improving our mechanistic understanding into cardiac physiology and ultimately inform clinical/regulatory decision making.

The complexity of myocardial mechanics and the experimental protocols needed to accurately describe them fuels the ongoing debate about the fundamental biophysical mechanisms of this system and its appropriate mathematical representation [138, 139]. Multiple frameworks have been proposed to test and generate new hypothesis that explain mechanisms, which are important to advance our mechanistic understanding alongside experimental [140-142] and clinical [143-145] findings.

Early theoretical frameworks were mostly based on the work of A.V. Hill [146] and A.F. Huxley [51]. These frameworks continue to inform computational and experimental studies into cardiac muscle physiology to this day. In 1938, Hill developed a phenomenological ‘rheological’ model that linked the release of energy by muscle, the mechanical work performed by the muscle, the force of contraction, and the velocity of shortening. In 1957 Huxley developed the first model of tension generation by crossbridges based on protein dynamics and recent electron microscopy data. This model recapitulated Hill's force-velocity relationship by modelling only two crossbridge states, attached and detached. The relative position of the actin-binding site to the equilibrium position of the nearest crossbridge was the key factor influencing the rate constants for crossbridges attachment and detachment. The force of an attached crossbridge was assumed to be a linear function of the distortion from the equilibrium position. Despite the very simplistic representation, modified versions of this two-state crossbridge model continue to be used [139].

Together with crossbridge cycling, calcium-based activation and thin filament cooperativity are the other key components of the cardiac mechanical system, and these have been usually modelled by means of discrete elements called functional units. Each functional unit is composed of a troponin-tropomyosin complex (called regulatory unit), spanning seven actin molecules, and one nearby crossbridge. In this modelling approach, the regulatory unit binds calcium, which in turn allows the crossbridge formation. Cooperative activation can also be integrated into the models to describe the high sensitivity of cardiac muscle to calcium. Cooperativity has been traditionally attributed to the following (combination of) mechanisms [147]: crossbridge-regulatory unit interactions, where cycling of crossbridges has been shown to increase the calcium affinity of troponin; regulatory unit-regulatory unit interactions, where cooperative interactions are generally thought to arise from nearest-neighbour regulatory units along the thin filaments; crossbridge-crossbridge interactions, where many cooperative interactions may occur between neighbouring crossbridges [139].

The evolution of the early theoretical frameworks into crossbridge-based models with cooperative calcium-based activation has led to a multitude of models of different level of complexity, as reviewed by [138, 139]. Among them, here I mention the most recent ones: Rice 2008 [148]; Campbell 2010 [149]; Land 2012 [150]; Mijailovich 2017 [151]; Land 2017 [152]; Campbell 2018 [141]; Balakina-Vikulova 2020 [153]; Lyon 2020 [142]; Mijailovich 2021 [154]. Among these, only the Land 2017, the Balakina-Vikulova 2020, and the Lyon 2020 provided a human-specific model parameterisation.

Given the relevance for the studies presented in this thesis, I provide below a detailed description of the recent Land model of human cardiac contraction.

The Land et al. model [152] recapitulates contraction and passive viscoelasticity in human myocytes, including troponin C and tropomyosin kinetics, a three-state crossbridge model that accounts for the distortion of crossbridges, and the cellular viscoelastic response (Figure 3.2). Each component was parametrised using a new comprehensive set of experimental data, characterising the passive tension and active contractile properties of skinned human cardiac myocytes at body temperature. More in detail, the passive response is modelled using a three-parameter model similar to a standard linear solid, consisting of a dashpot and spring in series, in parallel with another spring. Despite its simplicity, the model was able to capture the passive and viscoelastic response shown in the experimental data.

For the active tension model, they considered a relatively simple and phenomenological representation of cooperative activation, where thin filament kinetics is described by the interactions of calcium ions, troponin C, and tropomyosin to regulate availability of myosin binding sites on actin. Specifically, given a calcium transient, the fraction of troponin C units with calcium bound to its regulatory binding sites (Ca_{TRPN}) is computed as:

$$\frac{dCa_{TRPN}}{dt} = k_{TRPN}\left(\left(\frac{[Ca^{2+}]_i}{[Ca^{2+}]_{T50}}\right)^{n_{TRPN}}(1 - Ca_{TRPN}) - Ca_{TRPN}\right)$$

where k_{TRPN} represents the unbinding rate (also called k_{off}), n_{TRPN} the cooperativity of the calcium-troponin C binding rate, and $[Ca^{2+}]_{T50}$ the half-

activation point (also called $Ca50$). In this model, the troponin concentration Ca_{TRPN} drives the unblocking of tropomyosin, as represented by the fraction of blocked myosin binding sites on actin B:

$$\frac{dB}{dt} = k_b * Ca_{TRPN}^{-n_{Tm}/2} * U - k_u * Ca_{TRPN}^{n_{Tm}/2} * B$$

where *U* is the fraction of unblocked myosin binding sites without crossbridges bound, k_b and k_u represent transition rates, and n_{Tm} is the Hill coefficient of the steady-state relationship between Ca_{TRPN} and the fraction of unblocked binding sites 1−*B*. Crossbridge binding and force generation are modelled using a three-state crossbridge cycle with unbound (*U*), pre-powerstroke (*W*) and post-powerstroke (*S*) states, and a distortion-decay model which tracks the average distortion of crossbridges in the *W* and *S* states:

$$\frac{dW}{dt} = k_{uw} * U - k_{wu} * W - k_{ws} * W - \gamma_{wu} * W$$

$$\frac{dS}{dt} = k_{ws} * W - k_{su} * S - \gamma_{su} * S$$

$$U = (1 - B) - S - W$$

where $k_{uw}, k_{wu}, k_{ws}, \gamma_{wu}, k_{su}, \gamma_{su}$ represent transition rates. Active tension can then be computed as:

$$T_a = h(\lambda)\frac{T_{ref}}{r_s}\left((\zeta_s + 1)S + \zeta_w W\right)$$

where λ is the extension ratio given by the ratio of sarcomere length divided by sarcomere length at rest, $h(\lambda)$ describes the length-dependent contribution to maximal tension at resting length T_{ref}, r_s represents the duty ratio, ζ_s and ζ_w describe the distortion of the S and W states. Of note, in this model λ is a model input. In the isometric condition when $\lambda = 1$, as considered in the studies conducted in this thesis, active tension is given by:

$$T_a = \frac{T_{ref}}{r_s}S.$$

In fact, under these conditions, $h(\lambda) = 1$, $\zeta_w = 0$, and $\zeta_s = 0$. This is because total distortion is given by the distortion induced by the powerstroke and the distortion induced by imposed changes in cell length, and ζ_s and ζ_w are given relative to the powerstroke distortion, therefore $\zeta_w = 0$ indicates no distortion, and $\zeta_s = 0$ indicates no additional distortion to that given by the powerstroke [152].

Overall, this is a model of active contraction in the human heart with a level of complexity that reflects the available experimental data, and which can be efficiently used in multi-scale cardiac mechanics models (low-dimensional set of ODEs). For these reasons, it was chosen for the computational studies conducted in this thesis.

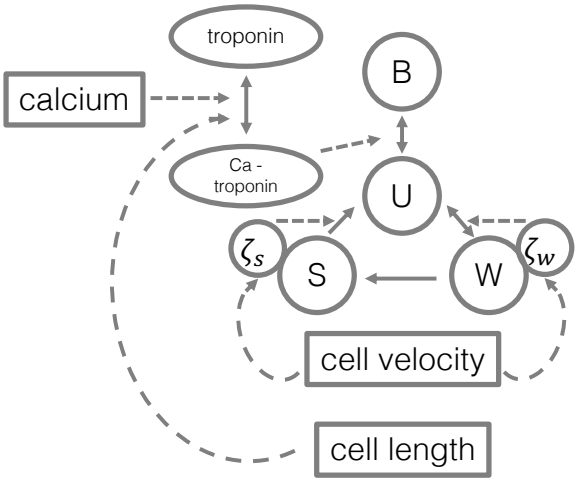

Figure 3.2. Overview of Land et al. active tension model (redrawn from [152]).

3.1.3 Multiscale human electromechanical modelling and simulation

The cellular models described in the previous sections represent separate descriptions of the electrical and mechanical activity of human cardiomyocytes. These can be combined, as shown in chapter 4, to obtain a coupled model of human cardiac electromechanical function. Moreover, cellular models can be integrated in higher scale frameworks for the simulation of cardiac function at the tissue and whole organ level.

Figure 3.3 illustrates the process of multiscale integration of experimental and clinical data into computational models of cardiac electrophysiology at the cellular, tissue, and organ levels [31]. It shows the tight coupling of modelling, simulation science, and experimental/clinical data [155] that is needed to construct and validate the models. Figure 3.3 also exemplifies some of the applications where this approach has been successful, including the simulation of the action potential and electrolyte concentrations in health, disease, and under drug treatment [156-159], the high-resolution investigation of mechanisms underlying arrhythmia based on clinical electrophysiology studies

[160, 161], or the interpretation and identification of arrhythmic-risk biomarkers at the surface potential level [162-165]. Each step of the diagram presented in Figure 3.3 can be also extended to include its mechanical and electromechanical counterpart [144, 145, 166, 167] constructed through a similar process of data integration and iterative validation.

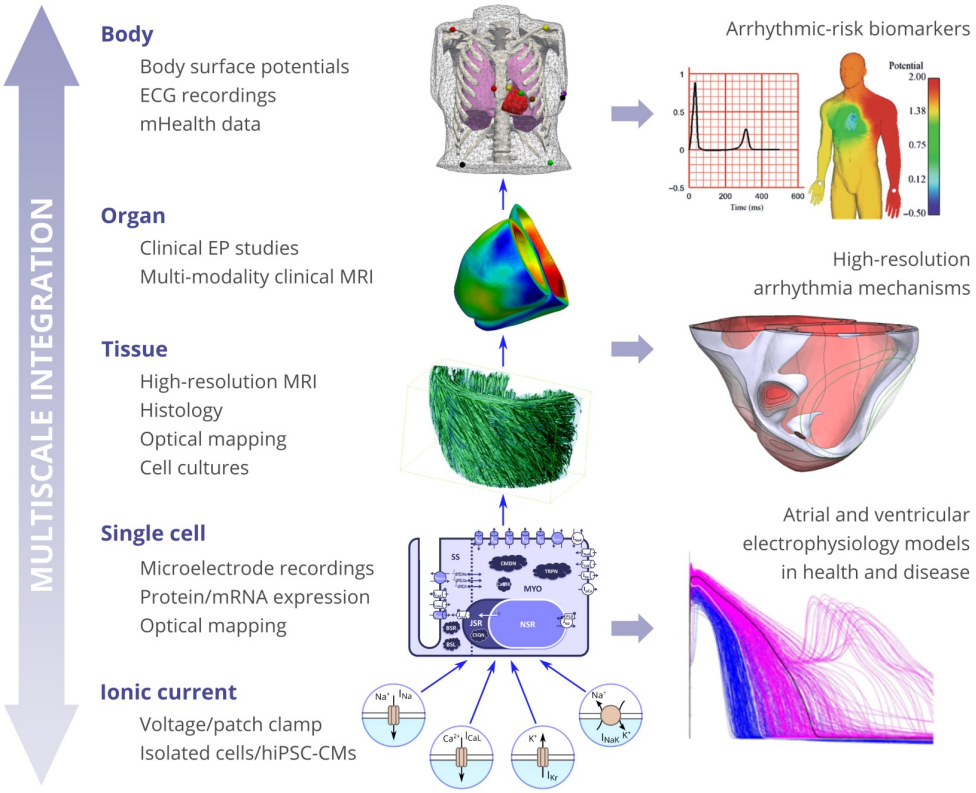

Figure 3.3. Multiscale integration of biomedical data into computational models of cardiac electrophysiology (from [31] under Open Access Licence).

In tissue and organ models, the diffusion through the cardiac tissue of the electrical depolarisation wave generated by cellular activity can be simulated by means of the bidomain equations [168], a coupled system of partial differential equations describing the intracellular and extracellular potential fields through the cardiac tissue, coupled with a system of ODEs representing

cellular activity. Under the assumption that the anisotropy of the intracellular and extracellular spaces is the same [169] (i.e., that the extracellular conductivity tensor is proportional to the intracellular one), the bidomain model reduces to the simpler formulation called the monodomain formulation, used in this thesis. This is a single partial differential equation coupled to the equations of the cellular model, which yields the system:

$$\chi\left[C_m \partial_t v + i_{ion}(v, \boldsymbol{w}, \boldsymbol{c}) - i_{app}(t)\right] = \frac{1}{J} \nabla \cdot (\boldsymbol{D_o} \nabla v), \qquad in\ \Omega_E^0 \times (0,T]$$

$$\frac{d\boldsymbol{w}}{dt} = m_w(v, \boldsymbol{w}, \boldsymbol{c}), \qquad in\ \Omega_E^0 \times (0,T]$$

$$\frac{d\boldsymbol{c}}{dt} = m_c(v, \boldsymbol{w}, \boldsymbol{c}), \qquad in\ \Omega_E^0 \times (0,T]$$

where C_m is the membrane capacitance per unit area, χ is the ratio of membrane area per tissue volume, J is the determinant of the deformation gradient tensor (see below), D_o is the conductivity tensor, and Ω_E^0 is the region where the electrophysiological problem is solved [137]. Supposing that the tissue is electrically isolated from the surrounding matrix, zero-flux boundary conditions are applied on the whole boundary for the transmembrane voltage v:

$$\boldsymbol{D_o} \nabla v \cdot \boldsymbol{n}_s = 0, \qquad on\ \partial\Omega_E^0 \times (0,T].$$

The deformation of the ventricles that result from the active tension generated within each cardiomyocyte can be simulated using the equations of continuum mechanics [137] and assuming the myocardium an orthotropic, hyperelastic,

and (quasi-)incompressible material with passive properties defined by exponential strain-energy functions [170]. These mathematical models describe the deformation of a body from the reference configuration $\Omega_0(\boldsymbol{X})$ to the current configuration $\Omega_t(\boldsymbol{x})$ through the deformation gradient $\boldsymbol{F}$:

$$F_{ij=}\frac{\partial x_i}{\partial X_j}, \qquad i,j = 1,2,3.$$

The mechanical behaviour of cardiac tissue is usually described by the stationary equilibrium (or by a dynamic formulation if inertial contributions are included), given as [171]:

$$-Div[\boldsymbol{FS}(\boldsymbol{U},\boldsymbol{X})] = \boldsymbol{b_0}(\boldsymbol{X}), \qquad for\ \boldsymbol{X} \in \Omega_0$$

where $\boldsymbol{U}(\boldsymbol{X},t)$ is the unknown deformation, $\boldsymbol{S}(\boldsymbol{U},\boldsymbol{X})$ is the second Piola-Kirchhoff stress tensor, $\boldsymbol{b}_0(\boldsymbol{X})$ are the body forces and Div denotes the divergence operator in the reference configuration. This should be completed with appropriate boundary conditions. For the hyperelastic cardiac tissue, the stress tensor can be derived from a pseudo strain-energy function that accounts for the microstructural composition of the tissue [170].

In the active stress formulation, as used in this thesis, the total stress $\boldsymbol{S}$ is additively decomposed considering the action of both external loads (such as intracavitary and pericardial pressures) and active stresses intrinsically generated during contraction [171]:

$$\boldsymbol{S} = \boldsymbol{S_p} + \boldsymbol{S_a}$$

where $\boldsymbol{S_p}$ and $\boldsymbol{S_a}$ are the passive and active stresses, respectively. The formulation of passive stresses derives from the constitutive equation:

$$\boldsymbol{S_p} = 2\frac{\partial \Psi(\boldsymbol{C})}{\partial \boldsymbol{C}}$$

where Ψ is the strain-energy function and $\boldsymbol{C} = \boldsymbol{F}^T\boldsymbol{F}$ is the right Cauchy-Green tensor. The active stress can be defined considering that the stresses due to active contraction act along the fibre orientation $\boldsymbol{f_0}$ in the reference configuration:

$$\boldsymbol{S_a} = S_a\,(\boldsymbol{f_0}\cdot\boldsymbol{C}\boldsymbol{f_0})^{-1}\,\boldsymbol{f_0}\otimes\boldsymbol{f_0}$$

where S_a is the scalar active stress induced in the fibre direction. Most physiological models of active stress generation are based on sets of ODEs (for example the Land model [152] introduced above) of the form:

$$\frac{\partial \boldsymbol{\zeta}}{\partial t} = \boldsymbol{h}\left(\boldsymbol{\zeta}, \boldsymbol{\eta}, \lambda, \dot{\lambda}\right)$$

$$S_a = f\left(\boldsymbol{\zeta}, \boldsymbol{\eta}, \lambda, \dot{\lambda}\right).$$

The state vector $\boldsymbol{\zeta}$ represents the cellular mechanisms of active stress generation, and depends on the electrophysiological state $\boldsymbol{\eta}$, stretch ratio λ, and stretch rate $\dot{\lambda}$.

The key connection between the electrical and mechanical subsystems is given by the intracellular calcium released during electrical activation that leads to myofilament activation and force generation.

Several different anatomical models have been used in recent modelling studies to simulate cardiac electromechanical function, from simple tissue blocks [137], to truncated ellipsoids of the left ventricle [150, 172], up to anatomically accurate bi-ventricular or whole-heart geometries from histological sectioning or patient-specific clinical images [145, 171, 173]. Anatomically-accurate models include the representation of the cardiac fibre organisation as obtained from rule-based methods, histological sectioning information, or from diffusion tensor magnetic resonance data [174].

3.1.4 Computational approaches to inter-subject variability

One of the biggest challenges in the understanding and prediction of cardiac function, especially in diseased conditions and under medical treatment, is variability. Physiological variability can be determined by different sources and mechanisms related to, for example, sex, age, nutrition, lifestyle, and circadian rhythm [116, 117, 175, 176], and usually it does not affect overall cardiac function. However, it is under disease conditions or pharmacological interventions, that the underlying differences in the cardiac substrate may favour pro-arrhythmic abnormalities or pump dysfunction [4]. Thus, the investigation of the sources and modulators of variability, from the sub-cellular to the body level, is essential to understand the high-risk conditions an individual is exposed to and what the underlying mechanisms determining this

risk are. This is an important concept in shaping the vision of personalised medicine, as discussed in the next section.

Variability can express itself at all different scales, from the protein up to the body, and has been traditionally considered a problem in both experimental and clinical studies, which predominantly focus on the 'mean' behaviour of the population. However, the 'mean' behaviour may not accurately represent any specific scenarios, and as mentioned variability can significantly impact the response to disease and medical treatments.

The importance of the information carried by variability is now recognised [177-179] and computational approaches have been developed, mainly for cardiac electrophysiology, to account for this variability when building models of cardiac function. These can be broadly divided into population-based modelling and sensitivity analysis, and sample-specific modelling (Figure 3.4). The overall idea behind these approaches is to start with a baseline model that describes the average data. Then, in population-based and sensitivity analysis approaches, model parameters are varied to generate model variants of the baseline model. The varied parameters are those identified or assumed to be the primary source of variability as defined by the scope of the investigation. In the experimentally-calibrated population of models approach it is important to ensure that the behaviour of the generated models is in agreement with experimental evidence. The sensitivity analysis approach mostly focuses on establishing how model parameters' variation affect model output [172, 180, 181]. Population of models studies can identify key modulators of cardiac function and generate new insights and hypothesis concerning variability [157, 182, 183]. These have been extensively used in recent years, especially for

drug safety and efficacy assessment [27, 184, 185] and for arrhythmia risk stratification in healthy and diseased populations [22, 23, 157]. In a sample-specific modelling approach, a baseline model is instead reparametrised to fit specific datasets. Thus, through optimisation and statistical techniques, the baseline model can be tailored to describe a specific cell/patient population [186, 187].

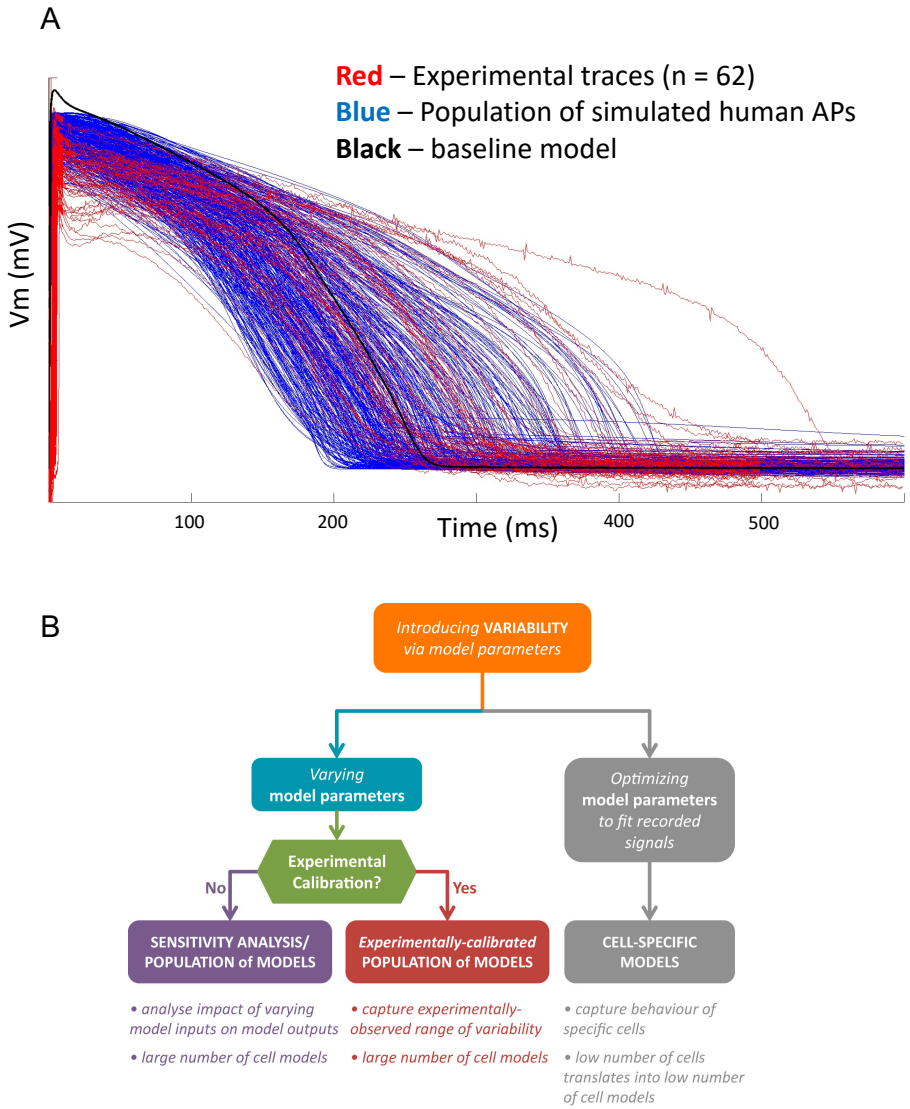

Figure 3.4. Computational approaches to investigate physiological variability. A: AP traces from experiments, baseline computational model, and a population of models

calibrated to experimental data [182]. B: Summary of different approaches to study physiological variability (reproduced from [177] under Open Access Licence).

3.2 The Digital Twin in precision cardiology

The medical field is entering a new era of personalised medicine to provide patients with patient specific diagnosis and treatment [188]. This has been facilitated by the capture of extensive individualised data through advanced imaging technologies and genetic profiling. The need for personalised medicine is rapidly evolving and emerging in every field of medicine including cardiology. The vision for personalised medicine is of a highly interconnected need for incorporating inter-subject variability with clinical decision making, and also recognising the role of lifestyle, environmental, and biomedical factors in modulating patient's response to treatment.

In this context, the 'Digital Twin' describes a quantitative framework where the data from an individual patient, or a specific population, acquired over time can be comprehensively integrated in a coherent and dynamic manner. This can be accurately and cost-effectively achieved through mechanistic and statistical modelling techniques [32]. Digital Twins are well positioned to exploit the increasing data available to provide a mechanistic understanding of multiscale pathophysiology and its modulators. In our recent position paper [32] we argued that precision medicine will be enabled by the synergetic combination of induction and deduction, from, respectively, the statistical models learnt from the data and the mechanistic modelling and simulation constructed from biophysical knowledge (Figure 3.5). We illustrated the synergies between mechanistic and statistical models in accelerating cardiovascular research

towards precision cardiology through a series of successful examples that can be broadly divided in (i) model synergy for improving clinical decision, and (ii) model synergy to accelerate evidence generation. In the first category we can place the contribution of models to diagnosis, for example by inferring clinical biomarkers that cannot be directly measured or require invasive procedures [189, 190]. A Digital Twin may also indicate whether a certain medical intervention is appropriate for a patient, or specific patient populations, by simulating responses to a therapy before it is selected [26, 143, 191] thus guiding treatment decision making. Furthermore, while statistical modelling allows for categorising patients based on the probability of various outcomes, mechanistic modelling provides an explanation for this categorisation [192]. In relation to the generation of evidence, digital evidence can play a key role in the regulatory process. Digital evidence is already part of a sub-set of regulatory submissions [120].

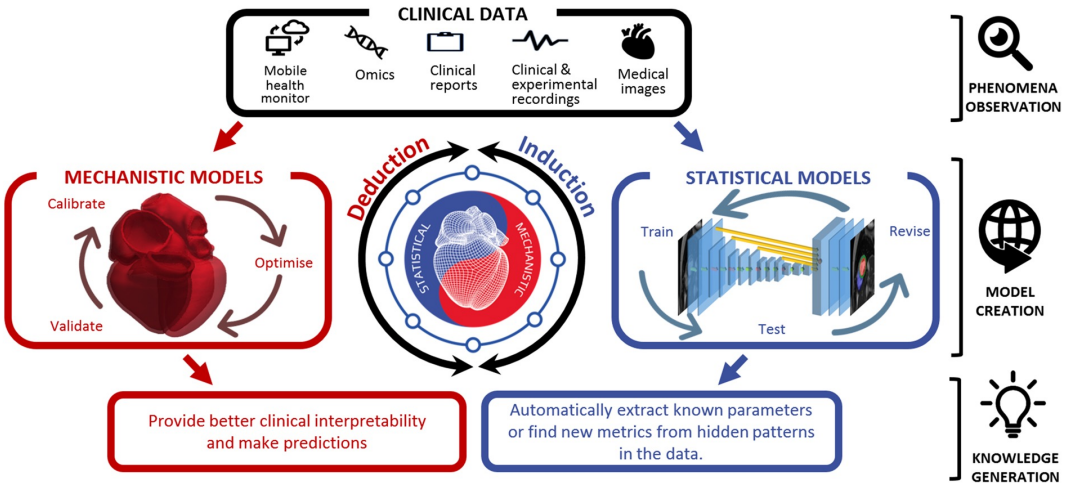

Figure 3.5. Synergetic combination of computer-enhanced induction (using statistical models learnt from data) and deduction (mechanistic modelling and simulation

integrating multi-scale knowledge) in the Digital Twin for precision cardiology (reproduced from [32] under Open Access Licence).

Although the current usage of certain components of the Digital Twin are still limited and fragmented in clinical/regulatory practice, in our position paper we envisioned that the concept of the Digital Twin may be fully adopted in the next 5 to 10 years, depending on the coordinated effort from scientific, clinical, industrial, and regulatory stakeholders in building the necessary evidence and tackling the organisational and societal challenges involved in the process [32].

3.2.1 Digital Twins for hypertrophic cardiomyopathy

The concept of the Digital Twin is related to the need to account for inter-subject variability when we investigate cardiac function under disease conditions and drug treatments to determine the most appropriate course of action. As illustrated in Section 2.2, HCM is a genetically and clinically highly heterogeneous disease and thus can be considered an emblematic example of the need for personalised medicine. A few computational studies have investigated the sources and modulators of HCM heterogeneity and have adopted a Digital Twin approach for risk stratification and its mechanistic explanation.

As reviewed in [193, 194], computational models spanning different scales, from molecule to organ, and integrated with experimental data, can provide new information about the processes governing HCM and potential therapies. At the lowest scale, both molecular dynamics [195, 196] and computational modelling of the actomyosin ATPase cycle [151, 197] and thin filaments [198] have been used to investigate and predict the effects of point mutations on

sarcomere contractility. Recently, a spatially explicit model of sarcomeres has also been used to investigate the role of variable amounts of incorporation of mutant troponin C on cardiac muscle twitch contraction [199].

To investigate how sarcomeric mutations in HCM may contribute to arrhythmogenesis, Zile and Trayanova [200] used a human cellular electromechanical model under reduced repolarisation reserve and altered thin filament activation. They demonstrated that myofilament protein dynamics can play an important role in early afterdepolarisation formation (as important arrhythmia precursors) through troponin C buffering of cytoplasmic calcium.

An hiPSC-CM electromechanical model has also been used by Prondzynski et al. [201] to further explain experimental findings on a rare sarcomeric mutation in an HCM patient. They showed that hiPSC-CMs obtained from the patient recapitulated several hallmarks of HCM, including prolonged AP duration and enhanced L-type calcium current. The computational model was used to prove that increased L-type calcium current could explain the observed AP duration prolongation.

Passini et al. [157] used a synergistic approach that tightly couples modelling and simulation with experimental data, in the context of biological variability. They did this to unravel the key mechanisms underlying arrhythmia precursors in HCM and identify effective pharmacological targets. Particularly, they used populations of models of human ventricular cellular electrophysiology informed by a comprehensive experimental dataset of APs, calcium transients, ionic currents and mRNA data obtained in human HCM cardiomyocytes [58]. They identified the reactivation of the overexpressed L-type calcium current, favoured by a decreased repolarisation reserve, as a key mechanism driving

repolarisation abnormalities in HCM. Moreover, through human in-silico drug trials, they identified potentially-efficacious anti-arrhythmic strategies specific to the HCM phenotype. They found that selective L-type calcium current block had high efficacy in the suppression of pro-arrhythmic abnormalities, but also markedly compromised calcium transient amplitude in human HCM. On the contrary, the multichannel block of sodium-calcium exchanger, late sodium, and L-type calcium currents exhibited a better efficacy profile than the respective single blocks, without the deleterious effect on systolic calcium [157].

Expanding on these results, in a subsequent study on the electrophysiological and contractile effects of Disopyramide in patients with obstructive HCM, Coppini et al. [82] investigated the cellular mechanisms of Disopyramide action on dispersion of repolarisation with a similar population of models approach as described above. Cellular findings were then integrated into a cardiac magnetic resonance-based anatomical model of a patient with obstructive HCM. This allowed them to investigate the mechanisms of dispersion at the whole ventricular level. They showed that Disopyramide markedly decreased dispersion of repolarisation times in the region of septal hypertrophy and slightly prolonged repolarisation in the non-hypertrophic epicardium. Because of this differential effect on distinct ventricular regions, a QT shortening in septal precordial electrocardiogram leads along with modest QT prolongation in the lateral ones was observed in-silico. Thus, the modelling and simulation study provided an explanation for the apparent discrepancy between observed AP shortening and the clinical QTc prolongation observed in patients with HCM following Disopyramide administration [82].

Ventricular arrhythmias are a major cause of sudden cardiac death in young HCM patients, yet the relationship between heterogeneous cardiac substrate, its manifestation on the electrocardiogram, and arrhythmic risk remains unclear. To address this, Lyon et al. [202] exploited computational clustering and mathematical modelling to first classify patients into distinct phenotypic subgroups based on their electrocardiogram, and then characterise the associated clinical risk factors and anatomical features of each group. Interestingly, patients with primary T wave inversion not secondary to QRS abnormalities had increased risk scores and coexisting septal and apical hypertrophy, suggesting that primary T wave inversion may increase sudden cardiac death risk in HCM, rather than T wave inversion secondary to depolarisation abnormalities [202]. Next, in order to mechanistically explain the distinct electrocardiogram phenotypes, Lyon et al. [192] constructed heart-torso anatomical models from the cardiac magnetic resonance images of HCM patients, representative of the identified phenotypes. Through mechanistic simulation they were able to explain the electrocardiogram phenotype of the two identified groups with higher sudden cardiac death risk score. The differential influence of different mechanisms, including hypertrophy, tissue microstructure alterations, abnormal conduction system, and ionic remodelling, was tested. The two high risk phenotypes were explained by different mechanisms. Specifically, ionic remodelling and AP prolongation in hypertrophied apical and septal areas explained the T wave inversion with normal QRS phenotype, whereas abnormal Purkinje-myocardial coupling explained the abnormal QRS morphology phenotype [192].

The combination of the studies by Lyon and colleagues represents a clear example of the Digital Twin approach where statistical and mechanistic modelling, informed by clinical data, are combined to suggest novel strategies to risk-stratify patients based on a fundamental understanding of the underlying determinants of risk.

3.3 Human in-silico drug trials for cardiac safety and efficacy assessment

Through a broad range of mathematical models, with varying complexity and predictive power, modelling and simulation are expected to improve and accelerate the cost-effectiveness of the drug development process [203]. Simulations have demonstrated that they are a valuable tool for fast and rational decision making, and can be (and have already been) used to predict how a compound influences human electrophysiology for arrhythmogenic risk prediction, accounting also for biological variability [27]. In the work presented in this thesis I also show how these computational methodologies can be applied to investigate the effect of pharmacological intervention on cardiac contractility (Chapter 4 and [33]).

Recently, the use of in-silico models of human ventricular AP for drug testing has been sponsored by regulators through the new cardiac safety paradigm CiPA [98], as explained in Section 2.3. Within this framework, the use of in-silico models will inform the mechanistic prediction of potentially lethal drug-induced forms of ventricular tachycardia (TdP). Computational frameworks for TdP risk assessment present several advantages, including the possibility of exploring a wide range of clinically-relevant drug concentrations at different

pacing frequencies and in different pathophysiological conditions, and computing several cell-based metrics for risk evaluation.

Computational frameworks encompassing a broad range of spatial and temporal scales have been used to assess drug action, from atomic and molecular scale modelling of ion channel gating and drug-channel interactions [204, 205] to cellular level computational frameworks [29]. Mechanistic models have been successfully applied to the study of drug-induced arrhythmias, both in terms of risk score prediction and mechanistic explanations. See, for example, Moreno et al. [206] for the prediction of class I anti-arrhythmic drug action; Sarkar and Sobie [24] for understanding the role of repolarisation reserve in the variability of response to proarrhythmic drugs; Lancaster and Sobie [207] for the development of a computational approach that combines simulations of drug effects on dynamics with statistical analysis and machine-learning; Mirams et al. [208] for simulations of multiple ion channel blocks; Grandi and Maleckar [25] for anti-arrhythmic strategies in atrial fibrillation; Yang et al. [26] for drug therapy in catecholaminergic polymorphic ventricular tachycardia; Martinez-Navarro et al. [209] on the role of sodium current availability and electrophysiological and anatomical factors determining arrhythmic risk in acute ischaemia.

Importantly, mechanistic models can also be exploited to investigate drug efficacy. Passini and colleagues [157] used this methodology to identify the key ionic mechanisms driving repolarisation abnormalities in HCM and suggest the blocking of a combination of currents as an effective antiarrhythmic therapy, as explained in the previous section.

A very important and challenging point from a regulatory perspective is the possibility of making decisions on risk reliably and objectively. When the risk of drug-induced TdP is assessed using an in-silico methodology, the input information usually comes from in-vitro pharmacology data from multiple ion channels. Such data are known to include a relevant amount of variability that needs to be taken into account within the in-silico framework. Risk assessment must also consider an additional complicating but essential factor: the pathophysiological variability that exhibits itself both within and between individuals. This has been modelled through population-based approaches to allow the prediction of the response of specific sub-populations, as described in Section 3.1.4 [27, 182, 184, 210, 211].

Other statistical methods, e.g., logistic regression, have also been used to assess proarrhythmic risk [212]. Gong and Sobie [213], developed a population-based approach combining mechanistic mathematical modelling and statistical analyses to simulate metrics in heterogeneous populations of models containing adult ventricular myocytes and those derived from induced pluripotent stem cells. These simulated measurements were used to predict adult myocyte drug responses from stem cells behaviours.

Network simulations have been used to mechanistically study tyrosine kinase inhibitors-induced cardiotoxicity by constructing and validating a computational model of cardiomyocyte apoptosis, integrating intrinsic apoptotic and tyrosine kinase signalling pathways [214]. Network modelling has also been used to predict and understand how drugs modulate cardiac fibrosis through simulations of the fibroblast signalling network [30].

Moving to higher dimensions, computational frameworks have also been developed for 2D/3D tissue representations and, even more importantly, for biophysically-detailed reconstructions of the human ventricles [162, 209, 215-217]. This enabled the possibility of investigating emergent phenomena (e.g. re-entrant arrhythmias, pump disfunction) of the cardiac system that can only be observed and studied at tissue and organ levels [206].

Very recently, computational approaches have also been used to investigate the cardiac proarrhythmia risk of pharmacological therapies used against COVID-19. Delaunois et al. [218] applied a set of in silico and in-vitro assays compliant with the CiPA paradigm to assess the risk of chloroquine (CLQ) or hydroxychloroquine (OH-CLQ)-mediated QT prolongation and TdP. They combined patch clamp assays on seven cardiac ion channels, in-silico models of healthy and high-risk human ventricular electrophysiology, and hiPSC-CMs. The integrated approach confirmed the proarrhythmia risk of CLQ and OH-CLQ. Varshneya et al. [219] explored the potential effects on cardiac electrophysiology of 4 drugs, and their combination, proposed to treat COVID-19. Through simulations of pharmacokinetics and a quantitative systems pharmacology approach for the modelling of ventricular myocytes, they showed that drug combinations can lead to greater cellular AP prolongation compared with drugs given in isolation, and that females with pre-existing heart disease are more susceptible to drug-induced arrhythmias.

In conclusion, all the studies presented above, even if just a subset of all published studies, point to the benefits of using computational frameworks in drug safety and efficacy evaluations as tools to (i) reveal fundamental biological principles and mechanisms, (ii) model interactions between drugs

and system components, and (iii) predict emergent treatment effects [220]. They also highlight that in addition to the ability of cellular models to explore the impact of ion current changes on the AP or calcium cycling, we also need to upscale investigations to the whole organ and body levels to increase our understanding of how ion channel effects translate to electrocardiogram changes, and to phenomena such as re-entry and arrhythmia [203].

However, although in-silico models of cardiac cellular contractility have been successfully used to investigate, for example, the effects of mechano-electric feedback [153, 221], β-adrenergic simulation [142, 222], and transmural heterogeneity [223, 224] on cardiac function, they have not been used to address the preclinical assessment of drug-induced inotropic risk. Drug-induced effects on cardiac contractility can lead to potentially life-threatening adverse outcomes due to heart failure. Thus, in this thesis I developed a computational framework to investigate the effect of pharmacological intervention simultaneously on both electrophysiology and contractility.

4 In-silico human electromechanical ventricular modelling and simulation for drug-induced pro-arrhythmia and inotropic risk assessment

This chapter describes the computational investigation "In-silico human electro-mechanical ventricular modelling and simulation for drug-induced pro-arrhythmia and inotropic risk assessment", as published in 2021 in the journal Progress in Biophysics and Molecular Biology [33].

In this chapter, I describe the development, calibration, and evaluation of a novel human-based model of integrated ventricular cellular electrophysiology, calcium dynamics, and active contraction. First, I describe the electromechanical coupling of electrophysiology and contractility models, and the re-calibration of the active tension model based on human data. Next, I investigate the effects of the electromechanical coupling on the heterogeneous healthy ventricular function and its modulation by pharmacological action using multiscale human-based modelling and simulation.

The modelling and simulation framework developed in this study will then be extended in Chapter 6 to include the representation of myosin SRX and DRX conformations and used to conduct the investigations presented in Chapter 7.

4.1 Introduction

As reviewed in Chapter 3, human-based computational approaches are now employed beyond academia, reaching clinical, industrial, and regulatory environments. They provide virtual tools, embedding our knowledge on human physiology, to investigate disease, and develop and evaluate therapeutic interventions. Over the last six decades, computational modelling and simulation have played a key role in cardiac science. They have accelerated the mechanistic understanding of cardiac pathophysiology, usually through separate paths for electrophysiology and contractility, through an essential iterative exchange between experimental data and modelling and simulation science, thereby enabling the development and validation of biophysical models. Technical advancement and availability of human tissue has increased the collection of human-specific datasets, characterising different aspects of ventricular electromechanics. These include excitation-contraction coupling and calcium dynamics [58, 135, 225], as well as contractile [82, 152, 226-228] and passive material properties [170, 229, 230]. Experimental data at different scales, from subcellular to whole-organ dynamics, have then been integrated into multiscale computer models of human physiology [152, 171, 172, 191].

Given the important contribution of the strong coupling between the cardiac electrical and mechanical activity in determining the response to disease and drug action, I here developed a human-based integrated pipeline for the simultaneous simulation of electrophysiology, calcium dynamics, and contractility in ventricular cardiomyocytes. I aimed to investigate the effects of electromechanical coupling on cellular function and its modulation by

pharmacological action using multiscale modelling and simulation. To address this goal, the most recent models of human ventricular electrophysiology (the ToR-ORd [136] and its predecessor ORd [135] models, described in Chapter 3) and active contraction (Land model [152], described in Chapter 3) were coupled and calibrated using experimental data. Simulations were conducted to quantify the effect of electromechanical coupling on the AP, calcium dynamics, and active contraction in healthy virtual human ventricular cardiomyocytes and tissue, and during drug exposure. The proposed modelling and simulation framework offers the opportunity to extend human-based investigations into the mechanisms of disease and drug action to incorporate heterogeneous electrical and mechanical features of cardiac function and their strong coupling.

4.2 Methods

4.2.1 Experimental data

Table 4.1 summarises the experimental recordings used in this study to calibrate and evaluate the human electromechanical models. Active tension data [226-228] obtained from isolated human preparations at body temperature were considered for the model calibration. A heterogeneous and comprehensive set of data was used for model validation, including human recordings of AP [231] and calcium transients [58], electrophysiology [225] and contractile [232] transmural heterogeneity data, and drug responses [112, 233]. Moreover, force [226], AP [135] and calcium transient [234] frequency dependence, and force length dependence [235, 236] data were considered.

Table 4.1. Description of the human experimental data used for model calibration and evaluation. tp: time to peak, rt50/rt90/rt95: time to 50/90/95% decay, APD50/APD90: action potential (AP) duration at 50/90% repolarisation. Data are reported as Median ± STD except for AP data from [231] which is reported as [min max]. Green: data used for model calibration. Blue: data used for model evaluation.

Reference	Tissue preparation	Data type	Biomarkers
Pieske et al. 1996 [227]	Left ventricular trabeculae from non-failing hearts (paced at 1 Hz, 37 °C)	Active Tension (muscles were gradually stretched along their length-tension curve in 0.05 mm steps until maximum isometric tension was reached)	amplitude (mN/mm^2): 13.7±1.8 tp (ms): 165±7 rt50 (ms): 116±6 rt95 (ms): 334±43
Mulieri et al. 1992 [226]	Biopsy strips of left ventricular myocardium of hearts from coronary artery bypass surgery (paced at 1.2 Hz, 37 °C)	Active Tension (muscles were gradually stretched in 0.05 mm increments to the length at which active twitch tension was maximum)	peak (mN/mm^2): 22.8±1.4 tp (ms): 157±10 rt50 (ms): 117±8 rt95 (ms): 477±31 (time to complete relaxation)
Rossman et al. 2004 [228]	Trabeculae from the right ventricular free wall of donor heart (paced at 0.5 or 2.5 Hz, 37 °C)	Active Tension (the final length was set at 80% of the difference between *L*max and *L*0, where an active developed force can first be identified)	developed force (mN/mm^2): 16.7±1.6 (0.5 Hz), 30.3±4.6 (2 Hz) tp (ms): 235±13.4 (0.5 Hz), 151±6.1 (2 Hz) rt50 (ms): 153±71 (0.5 Hz), 98±7.7 (2 Hz) rt95 (ms): 309±13.7 (0.5 Hz), 173±10.7 (2 Hz)
Britton et al. 2017 [231]	Right ventricular trabeculae and papillary tissue preparations from non-failing	Action Potential	tp (ms): [3.1 14.0] APD50 (ms): [106.6 349.4] APD90 (ms): [178.1 442.7]

	human hearts, perfused and paced at 1Hz		
Coppini et al. 2013 [58]	Viable single myocytes from septal specimens of control patients	Calcium Transient	tp (ms): 47.8±10 rt50 (ms): 151.1±89.2 rt90 (ms): 315.6±161.2
Lou et al. 2011 [225]	Isolated left ventricular wedge preparations from non-failing human hearts	Electrophysiological heterogeneity	AP repolarisation sequence: mid>endo>epi CaT repolarisation sequence: mid>endo>epi
Haynes et al. 2014 [232]	Permeabilised sub-epicardial, mid-myocardial, and sub-endocardial specimens from left ventricular free wall of non-failing human hearts	Contractile heterogeneity	Isometric tension distribution: higher at mid-myocardium
Nguyen et al. 2017 [112]	Adult human primary ventricular myocytes isolated from donor heart	Active Tension	Tension reduction under drug exposure
Guo et al. 2011 [237]	Isolated non-failing human ventricular endocardial myocytes	Action Potential	Early afterdepolarisations formation under drug exposure
Page et al. 2016 [233]	Human ventricular trabeculae from ethically consented organ donors	Action Potential	AP duration prolongation and early afterdepolarisations formation under drug exposure

O'Hara et al. 2011 [135]	Non-failing human hearts	Action Potential	AP frequency dependence
Schmidt et al. 1998 [234]	Non-failing human hearts	Intracellular Calcium Peak and Decay	CaT frequency dependence
Mulieri et al. 1992 [226]	Biopsy strips of left ventricular myocardium of hearts from coronary artery bypass surgery (paced at 1.2 Hz, 37 °C)	Active Tension (muscles were gradually stretched in 0.05-mm increments to the length at which active twitch tension was maximum)	Force frequency dependence
Vahl et al. 1997 [235]	Isolated intact human left ventricular myocardium from 8 normal donor hearts (paced at 1 Hz, 37 °C)	Developed Force (measured for L/Lmax between 0.8 and 1)	Length-dependence of developed force
Holubarsch et al. 1998 [236]	Human left ventricular non-failing preparations from 8 donor hearts (paced at 0.5 Hz, 37 °C).	Developed Force	Length-dependence of developed force

4.2.2 Description of the electromechanical coupling of human-based models

Previously published human electrophysiology, calcium dynamics and active tension models were coupled through forward (excitation-contraction coupling) and reverse (mechano-electric feedback) processes. Specifically, the new ToR-ORd model [136] and the modified version of the ORd model [135] published in [158] were considered for electrophysiology and excitation-contraction coupling. The Land model [152] was adopted for active tension generation. Descriptions of the original models are provided in Chapter 3.

The bidirectional electromechanical coupling was achieved as previously reported [172, 221]. The free intracellular calcium concentration computed in the electrophysiology models (ToR-ORd and ORd) served as the input for the Land model, and the amount of calcium bound to troponin C computed in the Land model was fed back into the ToR-ORd and ORd models and used to update the free intracellular calcium concentration.

The total calcium concentration present in the cell ($[Ca^{2+}]_{total}$) can be decomposed as the sum of intracellular free calcium ($[Ca^{2+}]_i$), calcium bound to calmodulin (CMDN, $[Ca^{2+}]_{CMDN}$), and to troponin C (TRPN, $[Ca^{2+}]_{TRPN}$), such that

$$[Ca^{2+}]_{total} = [Ca^{2+}]_i + [Ca^{2+}]_{CMDN} + [Ca^{2+}]_{TRPN}.$$

A time differentiation of the previous equation yields

$$\frac{d[Ca^{2+}]_{total}}{dt} = \frac{d[Ca^{2+}]_i}{dt} + \frac{d[Ca^{2+}]_{CMDN}}{dt} + \frac{d[Ca^{2+}]_{TRPN}}{dt}.$$

Equivalently, changes in total calcium are prescribed by the conservation of calcium ions through the membrane and the sarcoplasmic reticulum, given by:

$$\frac{d[Ca^{2+}]_{total}}{dt} = \left(-I_{pCa} - I_{Cab} + 2I_{NaCa,i}\right)\frac{A_{cap}}{2Fv_{myo}} - J_{up}\frac{v_{nsr}}{v_{myo}} + J_{diff,Ca}\frac{v_{ss}}{v_{myo}}.$$

In the original ToR-ORd and ORd models, the binding of calcium to calmodulin and troponin C buffers is modelled by the algebraic expressions

$$[Ca^{2+}]_{CMDN} = [\overline{CMDN}]\frac{[Ca^{2+}]_i}{[Ca^{2+}]_i + K_{CMDN}}$$

$$[Ca^{2+}]_{TRPN} = [\overline{TRPN}]\frac{[Ca^{2+}]_i}{[Ca^{2+}]_i + K_{TRPN}}$$

and therefore

$$\frac{d[Ca^{2+}]_{total}}{dt} = \frac{d[Ca^{2+}]_i}{dt} + \frac{d[Ca^{2+}]_{CMDN}}{dt} + \frac{d[Ca^{2+}]_{TRPN}}{dt}$$

$$= \frac{d[Ca^{2+}]_i}{dt}\left(1 + \frac{[\overline{CMDN}]K_{CMDN}}{([Ca^{2+}]_i + K_{CMDN})^2} + \frac{[\overline{TRPN}]K_{TRPN}}{([Ca^{2+}]_i + K_{TRPN})^2}\right)$$

yielding

$$\frac{d[Ca^{2+}]_i}{dt} = \beta_{Cai}\left(\left(-I_{pCa} - I_{Cab} + 2I_{NaCa,i}\right)\frac{A_{cap}}{2Fv_{myo}} - J_{up}\frac{v_{nsr}}{v_{myo}} + J_{diff,Ca}\frac{v_{ss}}{v_{myo}}\right)$$

where

$$\beta_{Cai} = \frac{1}{1 + \frac{[\overline{CMDN}]K_{CMDN}}{([Ca^{2+}]_i + K_{CMDN})^2} + \frac{[\overline{TRPN}]K_{TRPN}}{([Ca^{2+}]_i + K_{TRPN})^2}}.$$

In the ToR-ORd and ORd models, the amount of calcium bound to buffers is therefore described through a combined scheme that includes both troponin C and calmodulin and provides a steady-state approximation of the phenomenon. In order to implement the electromechanical coupling, the combined buffering scheme was separated, keeping an algebraic formulation for the calmodulin buffer and including a dynamic calcium buffering for troponin C. The amount of calcium bound to troponin C ($[Ca^{2+}]_{TRPN}$) is defined as the fraction of troponin C units with calcium bound to its regulatory binding site ($CaTRPN$) multiplied by a constant maximum concentration of calcium ions that can bind to troponin C ($[Ca^{2+}]_{TRPN,max}$ = 0.07 mM, as considered in [135]), leading to

$$\frac{d[Ca^{2+}]_{TRPN}}{dt} = [Ca^{2+}]_{TRPN,max} \frac{dCaTRPN}{dt}$$

I then adopted the formulation provided by Land et al. [152] to describe the dynamic binding of calcium to troponin C (Section 3.1.2):

$$\frac{dCaTRPN}{dt} = k_{TRPN} \left(\left(\frac{[Ca^{2+}]_i}{[Ca^{2+}]_{T50}} \right)^{n_{TRPN}} (1 - CaTRPN) - CaTRPN \right)$$

The final formulation for the transient of the free intracellular calcium then becomes:

$$\frac{d[Ca^{2+}]_i}{dt} = \beta^*_{Cai}\left(\left(-I_{pCa} - I_{Cab} + 2I_{NaCa,i}\right)\frac{A_{cap}}{2Fv_{myo}} - J_{up}\,\frac{v_{nsr}}{v_{myo}} + J_{diff,Ca}\,\frac{v_{ss}}{v_{myo}} - \frac{d[Ca^{2+}]_{TRPN}}{dt}\right)$$

where

$$\beta^*_{Cai} = \frac{1}{1 + \frac{[\overline{CMDN}]K_{CMDN}}{([Ca^{2+}]_i + K_{CMDN})^2}}$$

Figure 4.1 presents an illustration of the coupling between the ToR-ORd and Land models and the biomarkers considered in this study. It also illustrates the abnormalities in AP and active tension (early afterdepolarisations, EADs, and aftercontractions, respectively) that may arise under drug exposure. Specifically, the biomarkers computed after each electromechanical simulation were: time-to-peak (tp) response of AP, calcium transient (CaT), and active tension; AP duration (APD) at 50% and 90% of repolarisation (APD50 and APD90, respectively); and relaxation times of CaT and active tension at 50% and 90/95% decay (rt50 and rt90/rt95, respectively).

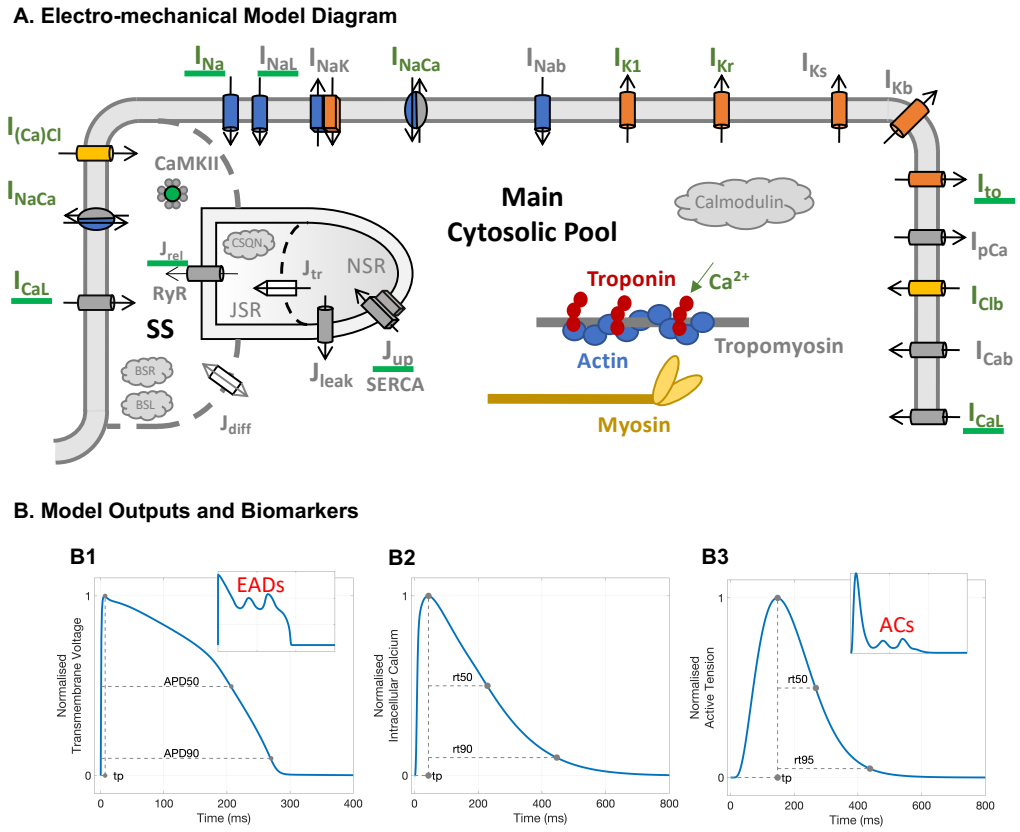

Figure 4.1. Human-based biophysical models and biomarkers of electromechanical function. A: Schematic representation of ionic currents, calcium dynamics, and contractile properties considered. Here the electrophysiology model diagram represents the ToR-ORd model (adapted from [136] under Open Access Licence). B: Biomarkers computed. B1: typical AP waveform and relative biomarkers (tp: time to AP peak; APD50/APD90: AP duration at 50/90% repolarisation). Inset: AP repolarisation abnormalities (early afterdepolarisations, EADs). B2: Typical CaT waveform and relative biomarkers (tp: time to CaT peak; rt50/rt90: time to 50/90% decay from CaT peak). B3: Typical active tension waveform and relative biomarkers (tp: time to active tension peak; rt50/rt95: time to 50/95% decay from active tension peak). Inset: Active tension abnormalities (aftercontractions, ACs).

Occurrences of EADs and aftercontractions were identified as a positive change in the slope of the AP repolarisation phase and of the contractility

relaxation transient, before the following stimulus-induced AP and contraction, respectively [112]. Occurrences of contractility escapes were identified as electrical stimuli that did not result in a contraction transient.

4.2.3 Recalibration of the active tension model

The coupled electromechanical models (from now on referred to as ToR-ORd+Land and ORd+Land) were calibrated against human experimental recordings to achieve physiological active tension. This was necessary because the CaT from the ToR-ORd and ORd models was in close agreement with human recordings [58] but was different from the transient used by Land to drive contraction (Figure 4.2B). Therefore, the Land model parameters had to be re-parameterised to achieve physiological active tension, when driven by the physiological CaTs from the ToR-ORd (and ORd) model. The calibrated Land model parameters were the Hill coefficient of cooperative activation and the tropomyosin rate constant (Table 4.2). As in Land, isometric twitch data in intact human preparations from the literature (Table 4.1) were used to extrapolate target active tension biomarkers.

In the calibration process, from each simulation with the electromechanical models, the active tension Ta was computed, and the biomarkers tp, rt50, rt95, and maximum and minimum tension values were extracted. Those were fed into the following cost function [152]:

$$d_t = d(tp, [147,172]) + d(rt50, [109,125]) + d(rt95, [291,377]) + 10d(\max(Ta), [15,25]) + 25\min(Ta)$$

where the distances d between each biomarker and the corresponding experimental ranges were computed and summed to obtain the total cost d_t, which was then minimised. The two weights in the cost function that multiply minimal (25) and maximal (10) active tension were chosen by the authors of the Land model to ensure good activation and relaxation as a first priority, and were kept unvaried in our study. The ranges of biomarkers chosen as target for this calibration procedure are [15-25] for active tension peak (mN/mm^2), [147-172] for tp (ms), [109-125] for rt50 (ms), and [291-377] for rt95, based on Table 4.1 and [152]. The cost function was minimised using the MatLab function *ga* (with default parameters), which finds the minimum of a function using a genetic algorithm.

The model parameters fitted in this procedure are reported in Table 4.2, and were chosen based on the following assumptions. Firstly, the active tension Land model parameters are 17 in total. Six of them are related to length changes and would not affect model outputs in our isometric setup. The Tref parameter, which is the tension developed at maximal activation for an extension ratio (λ) equal to 1, would only scale the model output. Therefore, it was not considered as a candidate in the sensitivity analysis. All the remaining parameters were varied one-at-a-time for a +/-10% variation to assess their impact on AP, CaT, and active tension. Those that significantly affected CaT were discarded (n_{TRPN} and Ca50). Of the remaining, k_{TRPN}, k_{uw}, k_{ws}, r_w, and r_s did not exert a significant effect on active tension to be included in the calibration. Of the three remaining parameters, I did not vary $TRPN_{50}$ as it is indicated by the Land model's authors to have an important length-dependant

effect. Since I was not testing length changes, I decided to leave that property unaffected.

Table 4.2. Model parameters fitted in the calibration process.

	ku	**nTm**
Parameter Meaning	blocked (B) to unbound (U) myosin binding sites on actin transition rate	Hill coefficient of the cooperative Hill curve between fraction of troponin C units with calcium bound (CaTRPN) and unblocked states 1-B
Parameter Range	0.01-1	1.5-2.5
Original Value	1	5
Calibrated ORd+Land	0.04	2.4
Calibrated ToR ORd+Land	0.021	2.036

The calibrated ToR-ORd+Land and ORd+Land models were then used to evaluate the various physiological effects of electromechanical coupling.

4.2.4 Evaluation of the human electromechanical models and transmural heterogeneity

I compared simulated APs and CaTs using the ToR-ORd+Land and ORd+Land models with human experimental data [58, 231], as in [136], to evaluate the electrophysiological consequences of electromechanical coupling. I then incorporated transmural heterogeneities in ionic properties to generate human mid-myocardial and epicardial cell models from the endocardial version described above. Changes to the ionic conductances describing mid-myocardial and epicardial cells were implemented following the publication of a dataset describing transmural differences [135, 136].

Additionally, the mid-myocardial L-type calcium permeability was scaled by 1.8 as is [238].

4.2.5 Simulations of drug-induced effects on human electromechanical function

I simulated drug-induced effects on cellular and tissue electromechanical function and compared the results with reported effects on human preparations. I focused on the following multichannel action reference compounds: Dofetilide (antiarrhythmic drug class III), Verapamil (antiarrhythmic drug class IV) and Quinidine (antiarrhythmic drug class Ia). Compounds' selection was based on preclinical [112, 239, 240] and clinical [215, 241, 242] data availability for electrophysiology and contractility in human subjects. The selected drugs were reference compounds with well-characterised clinical outcomes and different pro-arrhythmic profiles: Verapamil is considered safe with no Torsade de Pointes (TdP) risk, while both Dofetilide and Quinidine prolong the QT interval and are clearly associated with TdP risk (CredibleMeds® [243]).

Drug effects were incorporated in the electromechanical models using IC50 and Hill coefficient data [27], by means of simple pore-block models of drug action. The full list of compounds, IC50/Hill coefficients and the maximal effective free therapeutic concentrations used to simulate drug action can be found in Table 4.3. To estimate inotropic effects, the percentage of tension reduction relative to control was computed and summarised as Hill curves. Simulated active tension was compared to experimentally recorded sarcomere shortening in human cardiomyocytes [112] as a qualitative measurement of

drug-induced changes in cardiac inotropy. Drug-induced effects on AP were compared against AP recordings obtained in human trabeculae [233].

Table 4.3. List and short description of compounds considered in this study, clinical Torsade de Pointes (TdP) risk, inotropic effect, IC50 and Hill coefficients for the pore-block drug models, concentrations tested and maximal effective free therapeutic concentrations (EFTPCmax). I_{Naf}: fast sodium current, I_{to}: transient outward potassium current, I_{CaL}: L-type calcium current, I_{Kr}: rapid delayed rectifier potassium current, I_{Ks}: slow delayed rectifier potassium current.

	Dofetilide	**Verapamil**	**Quinidine**
Description	Antiarrhythmic Class III	Antiarrhythmic Class IV	Antiarrhythmic Class Ia
TdP risk	1	0	1
Inotropic effect	positive	negative	negative
EFTPCmax (μM)	0.0021	0.088	3.237
Concentrations tested (μM)	0.02 0.03 0.04 0.05 0.06 0.1	0.001 0.01 0.1 1 10	0.3 3 30 100
IC50(h) I_{Naf}	31.9(0.54)	32.5(1.33)	14.6(1.22)
IC50(h) I_{to}	300(1)		
IC50(h) I_{CaL}	201(1)	0.2(0.8)	6.4(0.68)
IC50(h) I_{Kr}	0.013(1.56)	0.25(0.89)	0.72(1.06)
IC50(h) I_{Ks}	135(1)		

4.2.6 Single cell implementation and stimulation protocols

Cellular simulations were conducted using MatLab (Mathworks Inc. Natick, MA, USA) using the ordinary differential equation solver *ode15s*. Stimulus currents of -53 μA/μF with 1 ms duration, and of -80 μA/μF with 0.5 ms duration were used, as in the original ToR-ORd and ORd models, respectively. The extension ratio (λ, sarcomere length over sarcomere length at rest) was set to 1, unless otherwise stated. For each baseline simulation, steady-state was reached at 1 Hz pacing before biomarkers were computed. For the in-silico

drug trials, after reaching steady-state at 1 Hz pacing frequency, drugs were applied, and the simulations ran for an additional 200 beats at 1 Hz pacing frequency (unless otherwise stated). The final beats were inspected for depolarisation/repolarisation abnormalities, aftercontractions, and contractility escapes.

4.2.7 Fully-coupled electromechanical simulations in 3D tissue slabs

To analyse the functional consequences of drug exposure on tissue-level cardiac electromechanics, the biophysically-detailed model of cellular electromechanical coupling was incorporated into the 3D framework of electrical propagation and tissue deformation recently described in [172], solved using the multi-physics computational code *Alya* [244]. This includes coupled anisotropic descriptions of the mechanical behaviour of ventricular muscle [170] and cardiac electrical propagation (monodomain formulation [168]).

Cuboid geometries were used to model the small tissue preparations that are often exploited in experimental investigations of cardiac contraction [226-228] and preclinical drug testing [233]. They offer the advantage of up-scaling investigations from cellular to 3D preparations, incorporating cell coupling effects, without the computational complexity that arises from more complex geometries.

Simulations were performed on a 1 cm cube made of endocardial cells with constant fibre directions along the z axis. Simulated tissue samples were electrically and mechanically transversely isotropic. Dirichlet boundary conditions were applied at the bottom face (z=0), fixing it in all directions. A

stimulus current of -100 μA/μF for 1 ms was applied to one of the fixed corners at 1 Hz pacing until steady-state was reached. Drug-induced effects were quantified through the computation of the longitudinal shortening together with the analysis of abnormalities in electrical conduction and mechanical contraction.

4.3 Results

4.3.1 Evaluation of the human electromechanical cellular models

Figure 4.2 illustrates the AP, CaT, and active tension time course for the novel ToR-ORd+Land and ORd+Land models, compared to the Land model. It shows the need for recalibration of the mechanical Land model in order to obtain physiological active tensions with the coupled models. In particular, Figure 4.2B shows the large amplitude and the delayed time-to-peak of the CaT used in the original Land model, compared to the new coupled models. Due to such differences, the active tensions simulated by the non-calibrated models were significantly lower (Figure 4.2C, dashed lines) than reported physiological values. This follows the well-known non-linear relationship between calcium and force. Such inconsistencies were corrected by the calibration process (Figure 4.2C, solid lines), which yielded simulated active tensions for both models in line with the experimental data considered in terms of amplitude, peak development, and relaxation kinetics. This procedure did not affect the morphology nor the kinetics of AP (Figure 4.2A) and CaT (Figure 4.2B), retaining good agreement with human experimental data [58, 231].

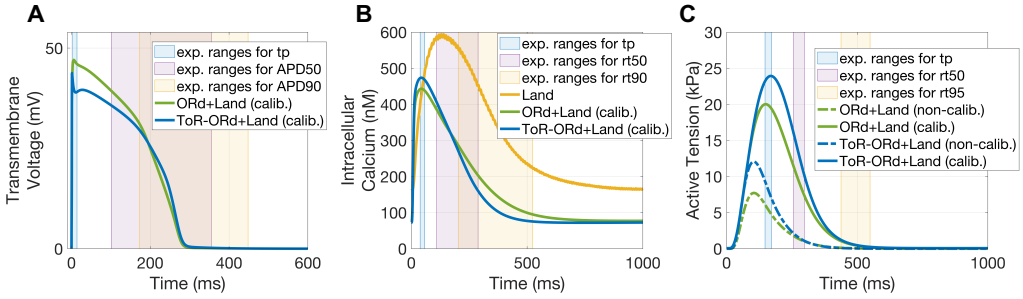

Figure 4.2. Human electromechanical model calibration and comparison with experimental data. Comparisons between the AP (A), CaT (B), and active tension (C) of the calibrated models and human experimental data (A: [231]; B: [58]; C: [226-228]). ToR-ORd+Land model in blue and ORd+Land model in green. Calibrated models have AP, CaT, and active tension biomarkers that are within experimental ranges. Panel B also shows the CaT used to drive contraction in the original Land model (yellow). Calibration does not affect the AP or CaT (A&B). Panel C shows how the simulated active tensions better replicate experimental data after calibration.

Following calibration, I analysed how all the state variables of the Land model changed due to the use of the fitted parameters and I investigated the changes in the steady-state calcium-force relationship. The effect of calibration on active tension was attained through changes in the time course of the fraction of blocked myosin sites on actin, with more sites becoming unblocked during one cycle. A small fraction of these sites (1%) also remains unblocked at steady-state, while previously they all returned to their blocked state, generating a significantly small residual tension (0.075 kPa, 0.3% of peak active tension). Importantly, this suggested that actomyosin interactions contribute to diastolic stress, as proposed by [245] in intact mouse cardiac myocytes. As a consequence of the modifications in the contractility model, the calibrated ToR-ORd+Land model resulted in a calcium sensitivity of 0.55

μM compared to the previous 0.60 μM, maximal active tension of 106.8 compared to the previous 119.1 kPa, and Hill coefficient of 2.9 compared to the previous 6.2.

Figure 4.3A illustrates the frequency dependence of the ToR-ORd+Land model in control conditions (similar results hold for the ORd+Land model), by reporting the simulated AP, CaT, and active tension at three different cycle lengths (500, 1000, 2000 ms) and relative biomarkers values. Figure 4.3A shows that, for increasing pacing frequencies, the time to peak of AP, CaT, and active tension slightly declined (Figure 4.3A4) while the time to 90% repolarisation/decay was significantly shorter (Figure 4.3A5). Peak values were larger for CaT and active tension, whereas AP peak was slightly lower at higher pacing frequencies (Figure 4.3A6). This is in agreement with experimental data [135, 226, 234].

The calibrated electromechanical models retained also good agreement with experimental data in terms of length-dependence properties (Figure 4.3B), despite direct comparison with experimental evidence being challenging due to differences between experimental and simulation setups.

Vahl et al. [235] reported an increase in developed force of a factor 5.5 in normal donor hearts going from a length of 0.8×Lmax to Lmax. At Lmax the time to peak was 175±23 ms and the time required from peak force to 90% relaxation was 240±25 ms. Holubarsch et al. [236] showed that, when muscle length was increased from 90% to 100% optimum length, peak developed force increased by 36% in non-failing human left ventricular myocardium.

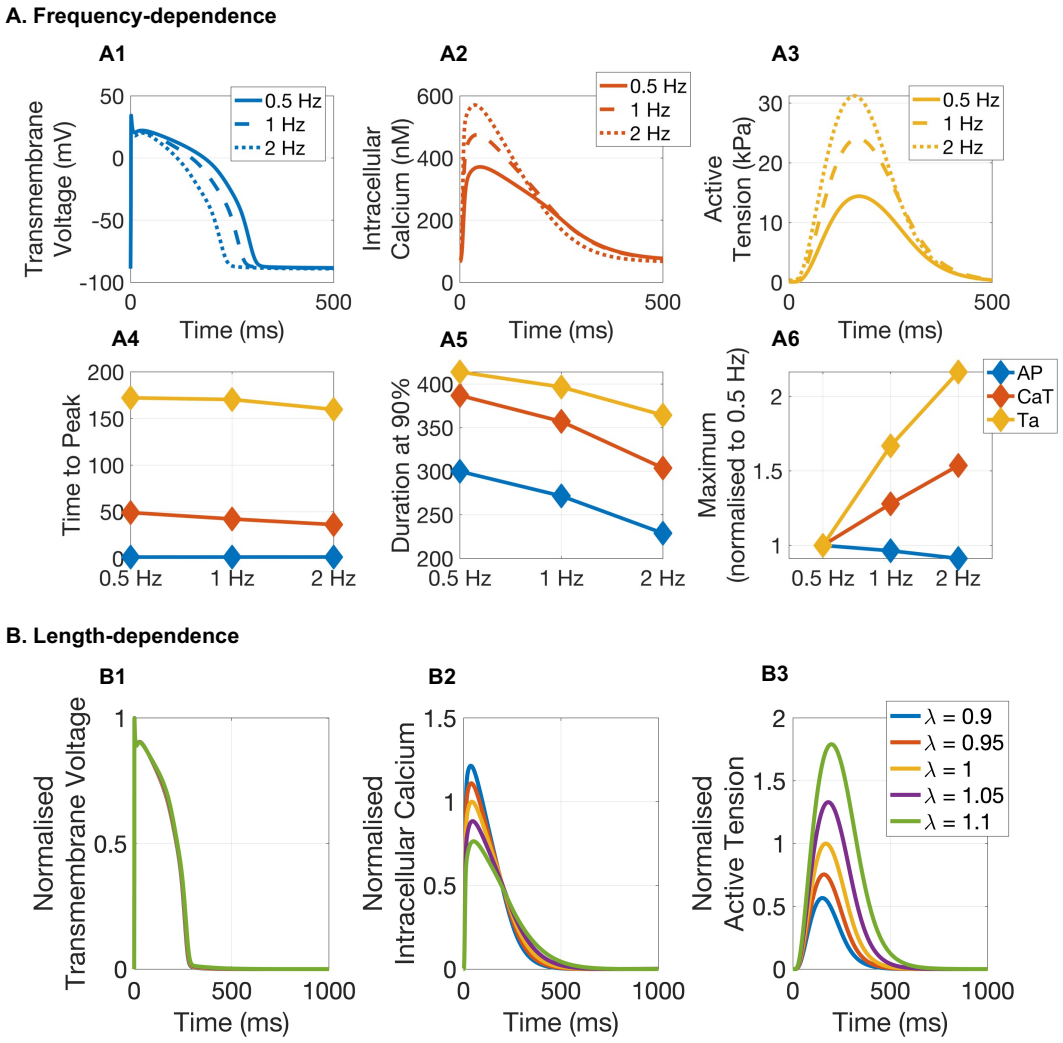

Figure 4.3. Frequency- and length-dependence of the ToR-ORd+Land model in control conditions. A: AP (A1), CaT (A2), and active tension (A3) waveforms and relative biomarkers (time to peak (A4), time to 90% repolarisation/decay (A5), and normalised peak value (A6)) for 0.5, 1, and 2 Hz pacing. B: Length-dependence of simulated action potential (B1), CaT (B2), and active tension (B3) for λ = 0.9, 0.95, 1, 1.05, and 2 (normalised to λ = 1).

I next analysed how the coupling with the contractility model affected cellular electrophysiology. The AP morphology and kinetics of the electromechanically coupled models perfectly resembled those of the purely electrophysiological models (Figure 4.4A&C). However, the CaT exhibited larger amplitudes and

faster kinetics (Figure 4.4B&D). Figure 4.4E displays the calcium transient biomarkers as obtained in experiments and simulation. The black box plots represent the experimental data [58] obtained in non-failing non-hypertrophic control cells through fluorescence imaging. The simulation results were obtained with the electromechanical models (circles) and their corresponding electrophysiology-only models (triangles).

The electromechanical coupling brought an improvement by better capturing the experimental data, especially for the calcium duration at 90% decay. The simulated biomarker values fell within the experimental range, even though in some cases outside of the 25-75 percentiles range.

The differences between the electrophysiology-only and the electromechanical models stem from the change in buffering scheme adopted: in the coupled formulation, the combined troponin-calmodulin buffering scheme of the ToR-ORd and ORd models was split up into its two components, and the Land dynamic formulation for troponin C was adopted. As a consequence, the coupled models predicted that less calcium bound to these buffers (Figure 4.4B&D, insets), increasing the free calcium availability inside the cell. Overall, the agreement of simulated behaviour and experimental data reported in this section provided a reliable basis for the credibility of the calibrated coupled models.

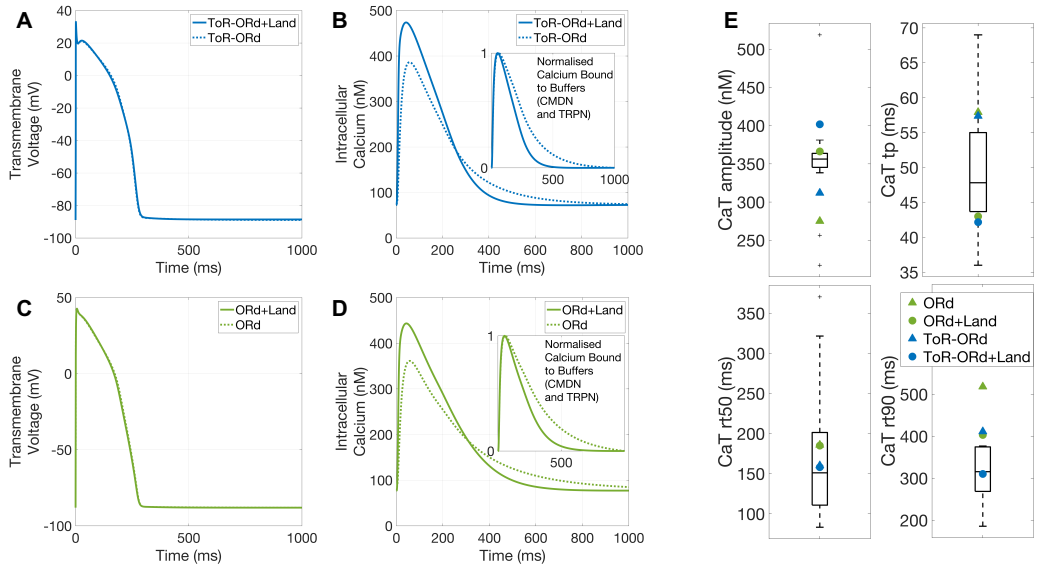

Figure 4.4. Electrophysiological consequences of dynamic calcium binding to troponin C. A&C: Electromechanical coupling does not affect AP waveforms. B&D: The dynamic calcium binding to troponin C formulation changes the time course of CaTs and predicts less calcium binding to troponin C compared with the previous steady-state approximation (insets). E: Quantification of the changes in CaT biomarkers induced by dynamic calcium binding to troponin C. Black box plots represent experimental data.

4.3.2 Cellular simulations of transmural heterogeneity in human cardiac electromechanics

Simulation results with the calibrated cellular electromechanical models, ToR-ORd+Land and ORd+Land, were both able to replicate the transmurally varying features of healthy human cardiac electromechanics in terms of AP repolarisation and CaT decay sequences (as reported by [225]), and isometric tension (as reported by [232]). These include the well-known transmurally heterogeneous behaviour of AP repolarisation (Figures 4.5A&B, first row) [246]. Mid-myocardial cells experience the longest APs, followed by

endocardial and epicardial cells. The same transmural heterogeneity was found in the CaTs (Figures 4.5A&B, second row), and consequently in the active tension transients (Figures 4.5A&B, third row).

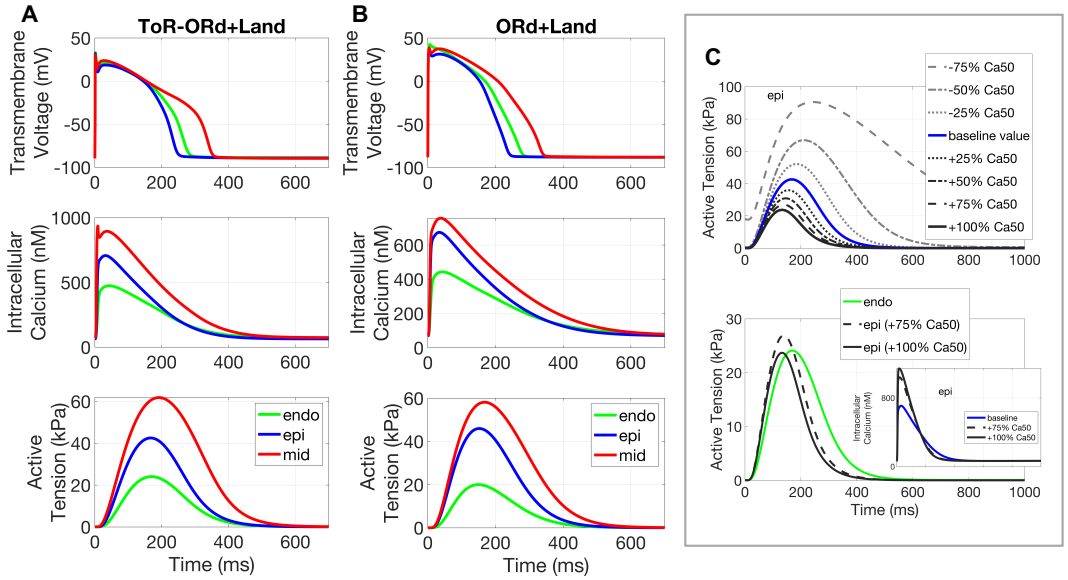

Figure 4.5. Transmural heterogeneity effects. Results of single cell simulations under heterogeneous electrophysiological transmural properties. A&B: Comparison between ToR-Ord+Land (A) and Ord+Land (B) models in AP, CaT, and active tension for endocardial, epicardial, and mid-myocardial cells. C: Active tension development in epicardial cells can be modulated by myofilament calcium sensitivity (Ca50 value). Sensitivity analysis results predict that epicardial calcium sensitivity in the range between 1.75x and 2x the baseline Ca50 value (i.e. reduced sensitivity) achieves a similar active tension for epicardial compared to endocardial cells, as experimentally reported by [232]. Inset: Changes in CaT induced by calcium sensitivity.

Simulation results showed a significantly higher tension in the mid-myocardium compared to the epicardial and endocardial cells, which is consistent with previous experimental findings [232]. However, the simulations also predicted a higher tension in the epicardium than in the endocardium (Figures 4.5A&B,

third row), while experimental data indicate similar values for both cell types. The experimental data by [232] also suggest that the endocardium may present a higher calcium sensitivity compared to the epicardium, which was not considered thus far in our simulations. To test this hypothesis, I performed a sensitivity analysis exploring the range of 0 to 2-fold changes in calcium sensitivity for the epicardial cells.

Results in Figure 4.5C indicate that a decrease in epicardial calcium sensitivity (between 1.75× and 2× the baseline Ca50 value) recovered a peak active tension in epicardial cells similar to that found in the endocardial ones, consistent with the experimental data. This also led to a faster epicardial onset of contraction, time to peak, and a faster relaxation rate compared to endocardium, as reported by [247] for canine samples. Such changes led to higher CaT amplitudes (Figure 4.5C, inset), as calcium sensitivity modulates the amount of calcium bound to troponin C.

4.3.3 Simulation of inotropic effects of multichannel action reference compounds

Dofetilide selectively blocks I_{Kr}. It induces a dose-dependent increase in the QT interval, and TdP is the most dangerous side effect of this therapy. In this study, Dofetilide concentrations were explored in the range of 0.02 to 0.1 μM, in correspondence with experimental investigations [112, 233, 237].

Simulations conducted with the cellular ToR-ORd+Land model at the lowest drug concentration (0.02 μM) showed that Dofetilide prolonged the AP, which in turn increased intracellular calcium, and therefore active tension (pacing frequency of 0.25 Hz, Figure 4.6B1). For higher concentrations, Dofetilide was

capable of inducing repolarisation abnormalities in the form of EADs due to L-type calcium current reactivation, resulting in the triggering of aftercontractions at the highest concentrations tested (0.06 and 0.1 μM, pacing frequency of 0.25 Hz, Figure 4.6B1). Dofetilide-induced EADs at 0.1 μM (0.25 Hz pacing) have been experimentally reported in human cardiomyocytes (Figure 4.6A2, [237]), and also at 1 Hz pacing in human trabeculae (Figure 4.6A1, [233]). Data from human cardiomyocytes have also shown aftercontractions at 0.06 μM at 1 Hz pacing frequency (Figure 4.6A3, [112]). Consistent with the ToR-ORd+Land model, simulations with the ORd+Land model also showed that APD prolongation induced a positive inotropic effect at the lowest concentration tested (pacing frequency of 0.25 Hz). Simulations with the ORd+Land model, however, predicted an earlier onset of Dofetilide-induced aftercontractions already at a low concentration of 0.05 μM. Complete repolarisation failure also occurred at higher Dofetilide doses in the ORd-Land model, highlighting the higher sensitivity of the ORd model to I_{Kr} current blockage compared to the more recent ToR-ORd model.

Dofetilide-induced EADs, as observed in isolated cells, were also replicated in tissue simulations, as shown in Figure 4.6B3 (0.01 μM Dofetilide, 1.25 Hz pacing). EAD formation in human trabeculae exposed to 0.1 μM Dofetilide at 1 Hz pacing have been previously reported (Figure 4.6A1, [233]). In tissue simulations, a significant portion of paced APs at the stimulus site (Figure 4.6B3, dashed traces) failed to propagate due to the formation of EADs and delayed repolarisations, causing contractility escapes (Figure 4.6B3, horizontal arrows).

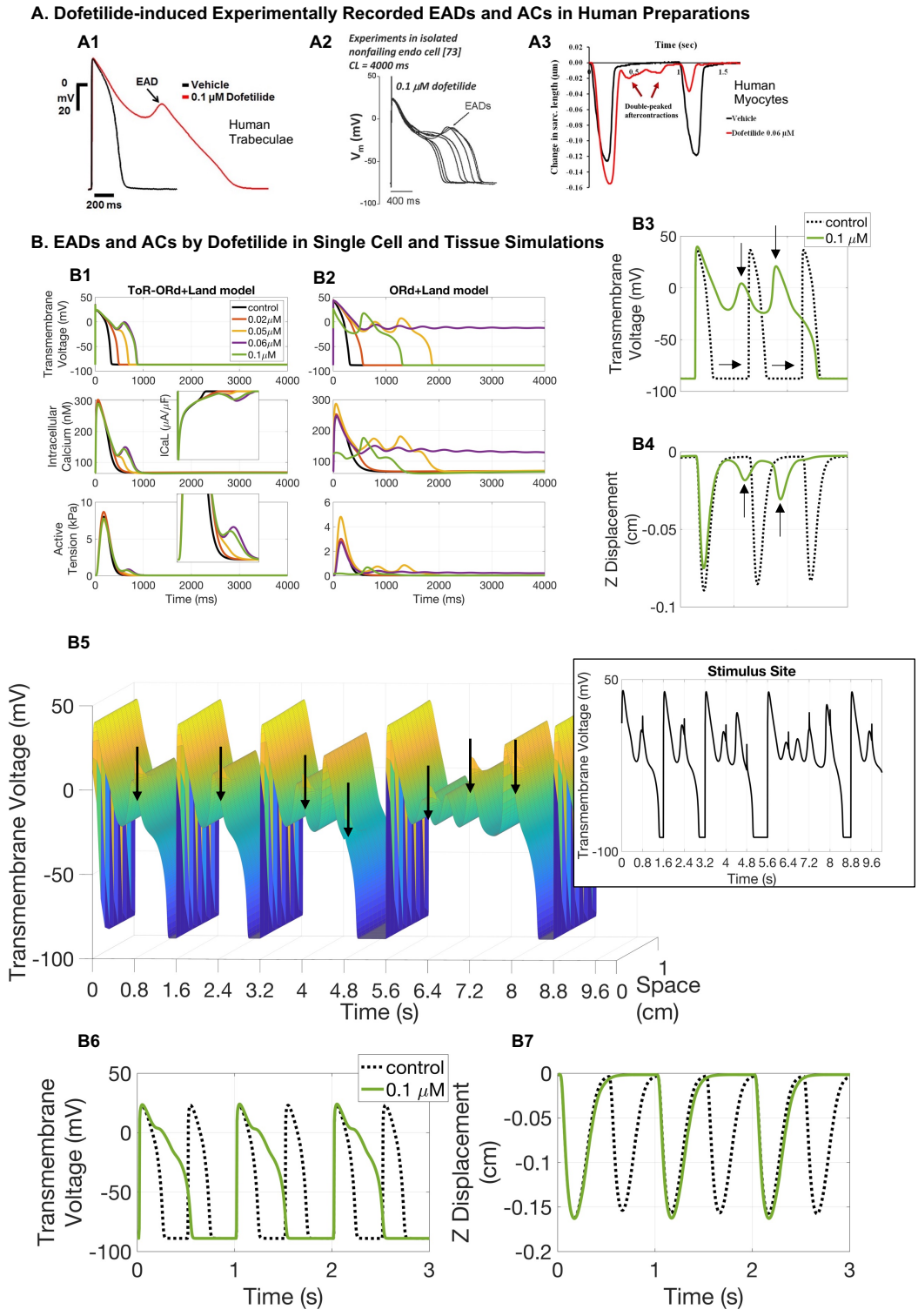

Figure 4.6. Dofetilide. A: Experimental evidence of Dofetilide-induced abnormalities recorded in human trabeculae at 1 Hz pacing (A1: EADs, figure reproduced with permission from [233]) and human myocytes paced at 0.25 Hz (A2: EADs, reproduced from [135] under Open Access Licence) and 1 Hz (A3: Aftercontractions, reproduced

from [112] under Open Access Licence). B: Single cell and tissue simulations of Dofetilide exposure. B1&B2: Single cell comparison between ToR-Ord+Land (B1) and Ord+Land (B2) model predictions. Dofetilide-induced AP prolongation favours a persistent calcium current, which mediates positive inotropic effects at low doses and EAD formation for the highest doses. B3-B5: 3D tissue simulations at 1.25 Hz pacing. 0.1 μM of Dofetilide induces EADs (B3) that trigger aftercontractions (B4). Contractility escapes indicated by horizontal arrows. AP and z displacements recorded at the free surface opposite stimulation. B5: AP time course in a line connecting two opposite corners. Arrows highlight APs propagation failure. The inset reports the AP time course at the stimulus site. Results in B3&B5 obtained with the Ord+Land model. B6&B7: Contractility escapes recorded in 3D tissue simulations using the ToR-ORd+Land model.

AP propagation failure is also illustrated in Figure 4.6B5, where I report the time course of the transmembrane voltage in a tissue line connecting two opposite corners of a tissue slab. Contractility escapes have been previously observed in 17% of recordings in human preparations exposed to high Dofetilide concentrations [112].

The simulation results allowed the identification of important electromechanical coupling consequences in the myocardial response to Dofetilide. Importantly, electromechanical coupling provided a more robust repolarisation compared to models that employed only electrophysiology (Figures 4.7A&B). Electromechanical coupling mitigated the APD prolongation induced by Dofetilide, and also raised the concentration required for the onset of EADs to 0.06 μM. These phenomena were stronger at lower pacing frequencies, but also present at 1 Hz pacing (Figure 4.7B).

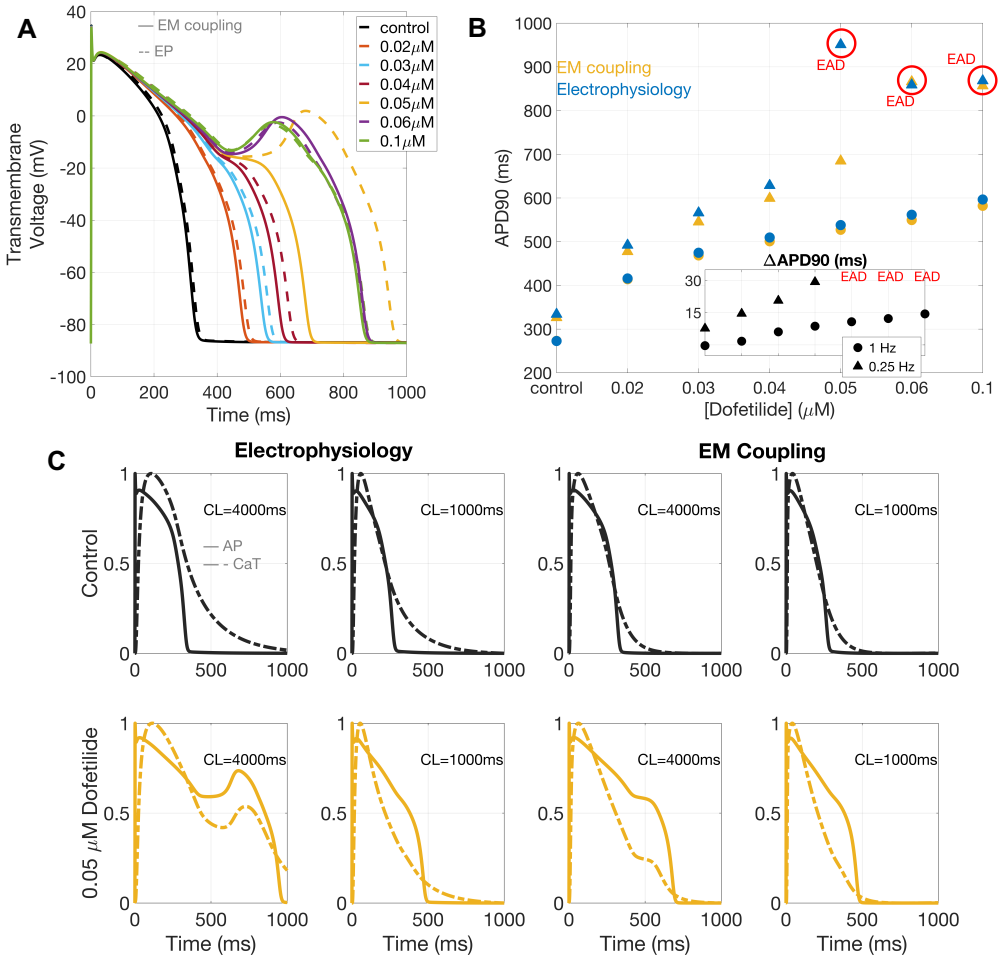

Figure 4.7. Electromechanical coupling and repolarisation. Electromechanical coupling (EM) mitigates the APD prolongation induced by Dofetilide, and delays EAD onset (A&B). This is mediated by a faster CaT decay under EM coupling (C), which recovers almost entirely during AP repolarisation. Results obtained with the ToR-Ord+Land model. CL: cycle length.

Dofetilide-induced APD90 prolongation in the electromechanical ToR-ORd+Land and its respective electrophysiology-only ToR-ORd models (for both 0.25 and 1 Hz pacing rates) is reported in Figure 4.7B. Computed differences in APD90 between the electromechanical ToR-ORd+Land and its

respective electrophysiology-only ToR-ORd models (for both 0.25 and 1 Hz pacing rates) are reported in the inset of Figure 4.7B.

The explanation for the more robust repolarisation under electromechanical coupling is presented in Figure 4.7C, which shows the AP and CaT with electrophysiology versus electromechanical models, at 0.25 and 1 Hz pacing, for control conditions and 0.05 μM Dofetilide. Under electromechanical coupling, the CaT decayed almost completely before the end of the AP repolarisation. For both coupled and uncoupled models, Dofetilide-induced AP prolongation increased calcium influx into the cell through a persistent L-type calcium current. However, in the presence of electromechanical coupling, this effect occurred when the CaT had decayed almost completely, resulting in a smaller chance of inducing additional AP prolongation or EADs.

Verapamil blocks both potassium (I_{Kr}) and calcium (I_{CaL}) currents, with minor effects on APD and QT interval. Verapamil has a TdP risk of 0 (not classified). Figure 4.8B1 illustrates simulated dose-response curves of peak active tension at different Verapamil concentrations (0.001, 0.01, 0.1, 1, 10 μM) at 1Hz pacing, using the ToR-ORd+Land and ORd+Land models. My simulated results correctly reproduced Verapamil-induced effects on contractility, in agreement with reports classifying it as a negative inotropic compound [112, 241]. Both models predicted a very similar negative inotropic response of human cardiomyocytes to Verapamil. Estimated IC50 and Hill coefficients for active tension reduction resulted in an equal IC50 of 0.05 μM for both models, and Hill coefficients of 1.1 and 1 for ORd+Land and ToR-ORd+Land, respectively. I qualitatively compared these results to experimental dose-

response curves of sarcomere shortening by Verapamil in human cardiomyocytes (Figure 4.8A1), which reported an IC50 of 0.04 μM. Simulations on tissue slabs allowed for the quantification of Verapamil-induced changes in longitudinal displacement (Figure 4.8B2) and showed further agreement with experimental data (Figure 4.8A2).

Despite the very similar inotropic response, mediated by a similar effect on CaT, the ToR-ORd+Land and the ORd+Land models provided different predictions in terms of APD prolongation (Figure 4.8C2). The ORd+Land model produced a much larger APD prolongation at the two highest drug concentrations (of 194 and 353 ms) than the ToR-ORd model (of 98 and 138 ms), see Figure 4.8C3. Disagreement between experimental [233] and in-silico predictions of Verapamil-induced APD prolongation have been reported before [210], and ascribed to an incorrect balance between the I_{Kr} and I_{CaL} currents in the ORd model, or an overestimation of the IC50 for I_{Kr} block measured in voltage clamp experiments. Thanks to its revised I_{Kr} and I_{CaL} formulations, the ToR-ORd+Land model predictions are closer to experimental data, which report no APD prolongation (Figure 4.8C1), than those of the ORd+Land model. However, the strong dependence of the in-silico predictions on the IC50 data used as input inevitably persists.

Additional analyses with the ToR-ORd+Land model showed that, in order to reproduce experimental data on APD, IC50 for I_{Kr} had to be one order of magnitude higher (considering the IC50 for I_{CaL} of 0.2 μM and Hill coefficient of 0.8, as done in this study).

A. Verapamil-induced Effects on Contractility: Single Cell In-vitro Experiments

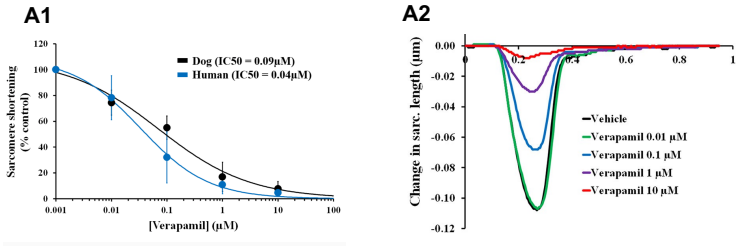

B. Verapamil-induced Effects on Contractility: Single Cell and Tissue In-silico Experiments

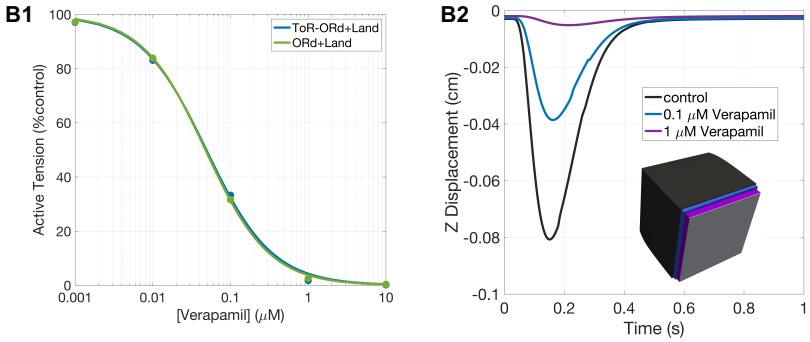

C. Verapamil-induced Effects on Electrophysiology: In-vitro and In-silico Experiments

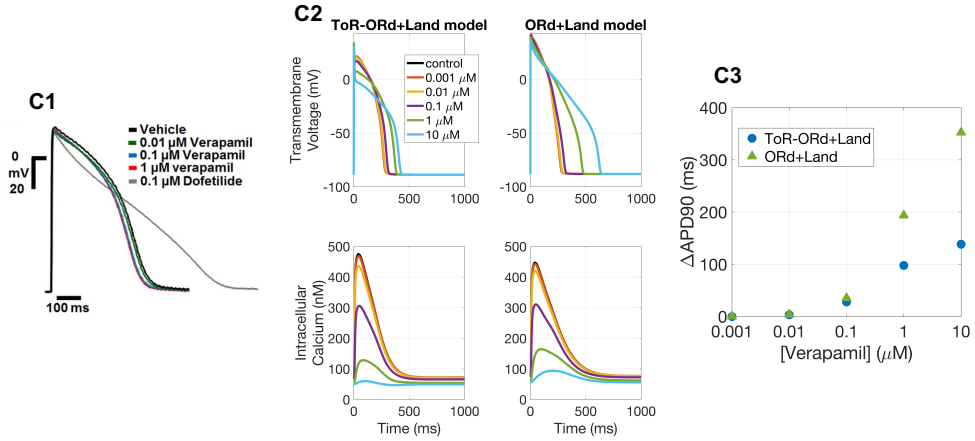

Figure 4.8. Verapamil. A: Experimental evidence of Verapamil-induced effects on cell shortening, reproduced from [112] under Open Access Licence. B: Single cell and tissue simulation of Verapamil effects. B1: Dose-response curves of peak active tension for Verapamil, using the ToR-Ord+Land and Ord+Land models. B2: Longitudinal displacement of the free face computed in tissue slabs exposed to different drug concentrations. Inset: Superimposed tissue slabs at maximal shortenings (undeformed tissue configuration in grey). C: In-vitro (C1) and in-silico (C2&C3) experiments of Verapamil-induced effects on electrophysiology. C1: Human

trabeculae (figure reproduced with permission from [233]). C2: Verapamil-induced effects on AP and CaT for ToR-Ord+Land and Ord+Land models. C3: APD90 prolongation under Verapamil exposure with respect to control APD90 for both models.

In that scenario, a mild APD shortening was observed (maximum shortening of 10 ms) for concentrations ranging between 0.001 and 1 μM, while 10 μM still yielded APD prolongation (76 ms). It is worth noting that such a high concentration of 10 μM (more than 100-fold the maximal effective free therapeutic concentration) has not been tested experimentally. However, prolonged QT and QTc intervals (from 375±24 ms to 469±54, and from 440±30 to 511±44ms, respectively) have been reported in cancer patients under high dose Verapamil infusion [248].

Quinidine is a class I antiarrhythmic agent that acts as a blocker of voltage-gated sodium channels, and is used to prevent ventricular arrhythmias despite safety concerns related to voltage-gated potassium channel block. Quinidine is known to have a negative inotropic effect [249]. Importantly, according to published IC50 data [239], Quinidine also significantly blocks I_{CaL}, leading to weaker contraction in cardiomyocytes. As shown both in-silico (Figure 4.9B2) and by experimental data from human cardiomyocytes (Figure 4.9A2), Quinidine generated a dose-dependent decrease in both active tension and sarcomere shortening, indicating a strong negative inotropic effect of the drug, which is already present at therapeutic doses. At 1 Hz pacing, IC50 for active tension was 1.7 μM with a Hill coefficient of 1.1 for the ORd+Land, and IC50

of 1.7 μM and Hill coefficient of 1 for ToR-ORd+Land, compared to an experimental IC50 for sarcomere shortening of 3.6 μM.

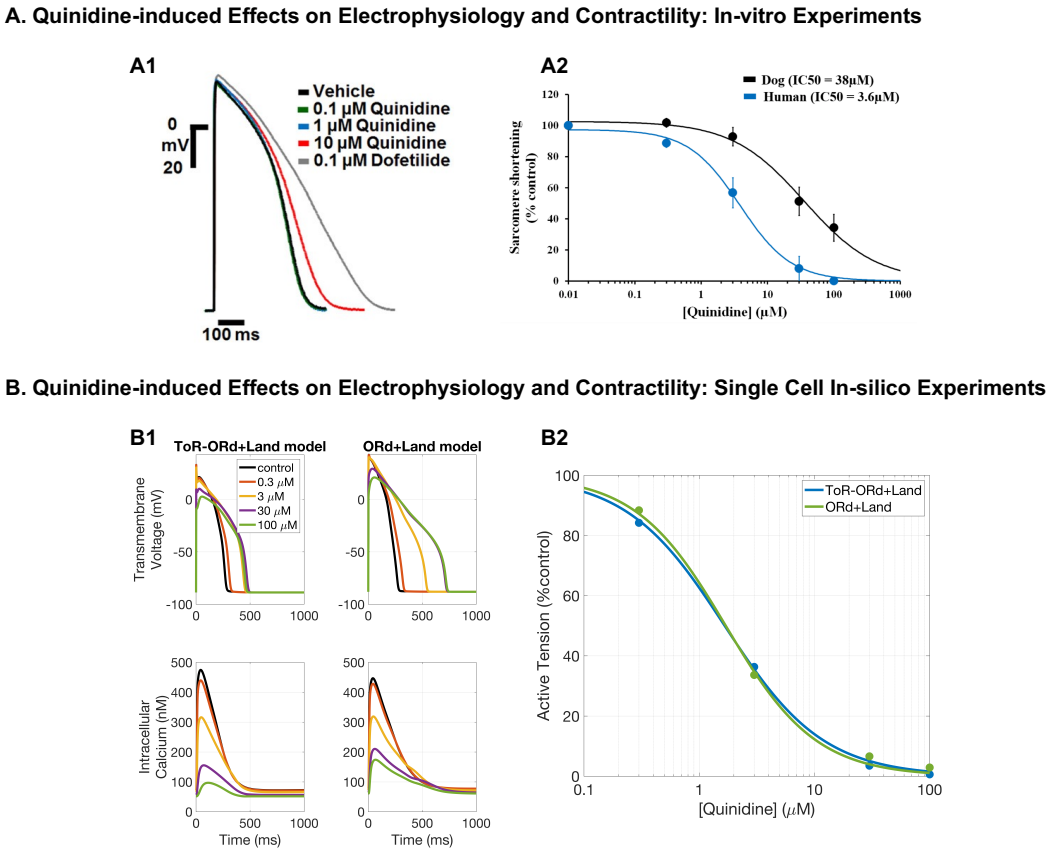

Figure 4.9. Quinidine. A: Experimental evidence on Quinidine-induced effects on human APs (A1, figure reproduced with permission from [233]) and cell shortening (A2, figure reproduced from [112] under Open Access Licence). B: Single cell simulations of Quinidine effects. B1: Comparison between the ToR-Ord+Land and Ord+Land models in response to Quinidine action in terms of APs and CaTs. B2: Quinidine dose-response curves for active tension reduction for both the ToR-Ord+Land and Ord+Land models.

The small differences in the in-silico predictions of Quinidine-induced inotropic effects can be ascribed to the differences between the ToR-ORd and ORd

models. In particular, one of the most relevant features of the recent ToR-ORd model compared to ORd is its capability of correctly reproducing the negative inotropic sodium block, mediated by reduced intracellular calcium [136]. In the context of Quinidine exposure, the negative inotropic effect associated with I_{CaL} inhibition is therefore further increased by sodium block, which explains the different predictions between the two coupled models (Figure 4.9B2).

As per Verapamil, disagreement in APD prolongation between model predictions and experimental results across different concentrations, IC50 datasets, and hERG block models has been previously noted [210]. Simulation results with the ToR-ORd+Land model showed an APD prolongation of 39, 169, 202, and 185 ms at Quinidine doses of 0.3, 3, 30, and 100 μM, respectively (Figure 4.9B1). Significant prolongation of APD has also been experimentally reported at high Quinidine doses, around 10 μM and higher (Figure 4.9A1). These differences can be ascribed to the reported IC50 of 0.72 μM (Hill coefficient of 1.06) for I_{Kr}, which implies very high I_{Kr} block at the doses considered, starting from 28% at 0.3 μM and 82% at 3 μM.

4.4 Discussion

In this study, I have presented strongly-coupled electromechanical models of human ventricular myocytes and myocardial tissue, by integrating existing human models of cellular electrophysiology and contractility. In particular, I have thoroughly compared the behaviour of the new ToR-ORd model with its predecessor ORd model, which have both been coupled with the Land model. The models are calibrated to yield physiological active contraction properties. Independent validation of the electromechanical behaviour of these models

show that they can reproduce the transmural heterogeneities of excitation-contraction coupling and force generation seen in human experimental data, and also correctly predict the inotropic response of different multichannel action reference compounds. The simulations that I have made can explain the partial mismatch between in-silico and in-vitro predictions of drug-induced APD prolongation for multichannel action compounds. My simulations also show that models with electromechanical coupling have a more robust cellular repolarisation when simulating drug exposure, especially when compared to models that account for electrophysiology alone. Electromechanical coupling mitigates the APD prolongation induced by Dofetilide, and also delays the onset of EAD formation. Overall, this study provides a human-based mechanistic framework for future investigations into the complex interplay between the electrical and mechanical substrates of cardiac function, and its modulation under pharmacological action. The work paves the way for future extension and translation of these results towards tissue- and organ-level computational studies of cardiac pathophysiology.

4.4.1 Human electromechanical cell models

The electromechanical simulations conducted in this study feature the use of two different human electrophysiology models, the ToR-ORd model, and its predecessor ORd. Both models are coupled with the Land model and provide descriptions of human cardiomyocyte electromechanical behaviours. Such descriptions are in agreement with the AP biomarkers [231] considered in this study (time to peak, APD50, and APD90). However, as explained in [136], the ToR-ORd model provides an improved description, compared to ORd, of

ventricular electrophysiology, in particular in terms of AP plateau, dynamics of accommodation of the APD to heart rate acceleration, and sodium-block induced changes in intracellular calcium. Calcium [58] and active tension [226-228] human data are also reproduced by the models. I have shown a strong agreement between the simulated CaT biomarkers with the new coupled models and the experimental data reported in [58]. However, such data differ from the ones presented in [250] and [251], especially for the time to peak. There is substantial experimental variability in the CaT characterisation shown in the aforementioned studies. Possible reasons behind that could be related to the type of preparations, the isolation procedure [252, 253], and the recording techniques.

The electromechanical models presented in this study are constructed from models featuring components either human-specific or reparametrised from animals. They are therefore the result of significant and ongoing research (as reviewed in Chapter 3). The human-relevant focus will facilitate future research on disease and drug-induced effects, where the translation from preclinical to clinical findings is particularly challenging due to species-specific differences [254].

Both coupled models feature a dynamic description of calcium binding to troponin C that links the electrophysiology and contractility subcomponents and allows a more accurate prediction of free intracellular calcium availability [58] compared to previous steady-state buffers used in the ToR-ORd and ORd models. The importance of modelling the dynamic intracellular calcium buffers in order to reproduce experimental data has been noted before [255].

However, when comparing the two models, we observe that the ToR-ORd model provides a more robust prediction of the drug-induced effects as demonstrated by our simulation results for Dofetilide and Verapamil, in addition to the previously reported model's improvements with respect to the ORd model [136]. The ToR-ORd model should therefore be preferred to the ORd model for future human-relevant drug and disease studies.

4.4.2 Transmural heterogeneity in cellular electromechanical properties

Numerous studies have addressed ionic heterogeneity within the human ventricular myocardium [256, 257], and heterogeneities of excitation-contraction coupling and force generation in animal hearts [247, 258, 259]. However, the role of spatial heterogeneities of excitation-contraction coupling, intracellular calcium handling, and force generation in the human heart remain unclear [225]. Potentially, the presence of those heterogeneities may imply that both physiological contractile properties and susceptibility to pathological remodelling during disease differ across the ventricular wall.

The electromechanical models presented in this study incorporate heterogeneous ionic currents, fluxes, and buffer distributions based on the datasets published in [135, 136]. I show that heterogeneous subcellular properties of electrophysiology are reflected by similar heterogeneities at the level of cellular function. Cellular AP and CaT transmural differences resemble the data presented in [225]. Such heterogeneities are known to be larger in isolated preparations compared to the electrotonically-coupled ventricular myocardium [260]. Heterogeneous CaTs translate into heterogeneous active tensions, in keeping with the well-known physiological relationship between

intracellular calcium and force development [42]. The prediction of active tension development in the mid-myocardial cell is consistent with experimental data, which show that they produce the highest tension. However, to fully recapitulate the experimental dataset across heterogeneous active tensions [232], myofilament calcium sensitivities also need to be taken into account as outlined by our sensitivity analysis. This is in accordance with the experimental report on non-failing human samples exhibiting a statistically significant increase in calcium sensitivity across sub-epicardial to sub-endocardial regions [232].

Khokhlova et al. [261] had already suggested the need to consider endo/epi differences in cooperativity of calcium activation of myofilaments to replicate experimental results on the distinct cellular responses to changes in mechanical load. They also suggested that mechano-calcium-electric feedback is a key factor in modulating the electrophysiological and contractile properties of myocytes across the ventricular wall [262].

Experimental data on transmural heterogeneity of CaTs and mechanical activity are controversial. Wan et al. [263] showed a lower amplitude of the CaT in the endo cells of guinea pig left ventricle than in the epi cells, consistent with our findings, whereas others reported no differences in cardiomyocytes from rabbit, dog, and human samples (as reviewed in [223]).

Several studies have linked cellular and sub-cellular heterogeneities to macroscopic functional endpoints and provide context to the heterogeneous mechanical functions observed in this study. There are clinical studies that have stated that transmural variation in the contractile function of the human myocardium may influence clinical endpoints [264, 265]. A few computational

studies demonstrated the importance of accounting for heterogeneous distributions of contractile properties to replicate experimental evidence [266-268]. A very recent study [269] has also shown that a thicker mid-myocardial layer may improve pumping efficiency and contractility.

Our study was designed to investigate the role of well-documented transmural electrophysiological heterogeneities in the human myocardium and their impact on contraction. I investigated whether such sub-cellular electrophysiological changes could explain the cellular level experimental data reported for human samples from different ventricular regions. Indeed, I have shown that the additional source of transmural heterogeneity was needed to fully recapitulate the experimental evidence. However, I did not investigate the effect of other sources of heterogeneity reported in the literature such as transmural distribution of fast and slow isoforms of myosin [270, 271].

4.4.3 In-silico predictions of inotropic and pro-arrhythmic liabilities

Pro-arrhythmic and inotropic liabilities are major concerns for the pharmaceutical industry [2], and it is important to test for potential changes in cardiac electrophysiology and contractility early in the drug discovery pipeline [112]. In-silico approaches represent a human-relevant system that is a fast and cheap way of conducting therapeutic safety screens, which have already shown their potential to accurately predict clinical risk [27, 184, 272]. However, there is still a lack of computational approaches for inotropic risk prediction. Here, I present a modelling and simulation framework to investigate simultaneous drug-induced effects on myocardial contractility and propensities for arrhythmia. The simulations of drug-induced effects on human

electromechanical function conducted in this study correctly classify negative and positive inotropic reference compounds and explain the mechanisms behind their observed effects on contractility. This part of my study also showed improved agreement between in-vitro and in-silico predictions on APD prolongation compared to previous studies [210].

The Dofetilide-induced inotropic response predicted by the models closely resembles the experimental data from [112], including the occurrence of aftercontractions at high Dofetilide concentrations. The mechanism underpinning this response is due to the APD prolongation driven by I_{Kr} block, and subsequent intracellular calcium increase. This is in good agreement with previous reports on the interaction between calcium handling and the APD [273]. The aftercontractions triggered in single cells by EADs were also replicated in tissue simulations. This is in further agreement with experimental recordings under Dofetilide action in both human cardiomyocytes [112] and trabeculae [233]. Contractility escapes, i.e. electrical stimuli that do not result in a contraction transient, are also present in both in-silico and in-vitro experiments [112].

My simulation results provide additional evidence on the key role of intracellular calcium in determining the magnitude of cardiac contraction with Verapamil and Quinidine treatment. For both compounds, simulations predict a concentration-dependent decrease in active tension, confirmed by a decrease in sarcomere shortening observed experimentally in human cardiomyocytes [112]. For this reason, Verapamil treatment is usually avoided in patients with severe left ventricular dysfunction, and our simulation results

confirmed this potential risk by demonstrating the drug's negative inotropic effects.

Both Verapamil and Quinidine are multichannel action compounds that block, among other currents, I_{Kr} and I_{CaL}. The I_{Kr} block, which is significant even for low concentrations of both drugs, determines the AP prolongation, while the I_{CaL} block affects primarily the CaT. Our simulations show that an I_{Kr}-only block leads to a mild increase in calcium followed by a positive inotropic effect. This is clearly counteracted by the direct calcium block under Verapamil or Quinidine exposure. On the other hand, an I_{CaL} block alone leads to a mild AP shortening which, for Verapamil and Quinidine, is opposed by the I_{Kr} block.

The prediction of APD changes for multi-channel action compounds is a very challenging task [210] due to concomitant effects on both inward and outward currents. I show that the new ToR-ORd+Land model is more robust against APD prolongation under Verapamil exposure, while still predicting a longer prolongation than experimental data [233]. This is an inevitable consequence of the reported IC50 values available, inducing very high levels of I_{Kr} block. To replicate experimental data, simulations predict that the IC50 for I_{Kr} has to be one order of magnitude bigger. This is particularly important in light of the recent heightened awareness of high variability in IC50 measurements [274]. Experimental data report both APD prolongation [275, 276] and shortening [233, 277] induced by Verapamil, and additional studies are needed to overcome such controversy.

In-vitro experiments employing Quinidine report no APD prolongation except for the highest dose of 10 μM [233]. Our simulation results predict APD

prolongation starting from 3 μM, because of the reported IC50 for I_{Kr}, with a significant reduction in peak potential.

4.4.4 Electromechanical coupling and repolarisation

The in-silico analyses of the effects of Dofetilide on electromechanical function (in both cardiomyocytes and trabeculae) show a more robust electrical repolarisation when using an electromechanical coupling model, when compared to electrophysiology-only models. While consistent for different pacing frequencies, this is more evident at slow pacing. I was able to explain such behaviour by detailed analyses of the time course of the simulated AP and CaT. Coupling-induced changes on the CaT allow for calcium to decay almost completely within the duration of the AP. Under such circumstances, the APD prolongation induced by drug exposure has less opportunity to translate into calcium abnormalities. This can also be seen in the electromechanical window (EMw), defined as the difference between the duration of electrical and mechanical systole, which has been computed in previous studies as the difference between the APD and CaT duration at 90% repolarisation/decay [184]. In baseline conditions, the EMw is shorter in electromechanical models than in electrophysiology-only models. However, the EMw shortening induced by Dofetilide, known to be a pro-arrhythmic effect of I_{Kr} blockers, is greater in electrophysiology-only models than in electromechanical ones. As shown in [184], the shortening of the EMw is an effective biomarker of TdP prediction, and it can be used to explain the higher propensity of electrophysiology-only models to develop repolarisation abnormalities.

4.4.5 Limitations and future work

While the models presented in this study have been able to recapitulate some of the transmurally varying electromechanical features of the healthy human myocardium, additional sources of heterogeneity have been reported in the literature. Inclusion of these aspects of heterogeneity in the models would provide a more comprehensive description of the heterogeneous cardiac substrates. As suggested in previous studies [270, 271] myosin expression may differ across the myocardium, and further simulations are needed to assess the impact of a transmural gradient in such properties on cardiac function.

Another key limitation of this study is the lack of after-load simulations. Contractile response is affected by pre-load and after-load conditions. The simulation of pre-load and after-load, together with isometric load, would provide a more exhaustive description of contraction modes. Further model development is needed to include a mathematical representation of the dynamic changes in sarcomere length. Evaluation of such simulation results would also require human-relevant data that is currently unavailable.

Finally, a key factor to consider for the comparisons reported in this study between experimental and simulation data is the differences between experimental setups. Experiments are often conducted at a fixed muscle length, which would allow some sarcomere shortening even in isometric contractions [278], whereas in these simulations one can only control sarcomere length by means of extension ratios. The 3D simulation framework presented in this study can be key in overcoming this limitation, combining

cellular active tension with tissue deformation, thus providing a closer representation of the experimental system.

4.4.6 Conclusion

In this study I integrated the most recent models of human ventricular electrophysiology and active contraction and calibrated them using human experimental data. This process yielded physiological simulated active tensions, APs, and CaTs in agreement with experiments in human preparations. Furthermore, the simulated electromechanical function reproduced the reported transmurally heterogeneous properties of human myocardium. I quantified the effect of the electromechanical coupling on electrophysiology and force generation in virtual human ventricular cardiomyocytes and myocardial tissue, both in control conditions and under drug exposure. My simulations correctly predicted the inotropic response of different multichannel action reference compounds. Furthermore, they generated additional evidence to explain the partial mismatch between in-silico and in-vitro predictions of drug-induced APD prolongation. Simulations demonstrated that cardiac electromechanical coupling provides a more robust repolarisation under drug exposure compared to electrophysiology-only models. The human-based mechanistic framework presented in this study will enable future investigations (such as the study presented in Chapter 6 and 7) into the complex interactions between electrophysiology and contractility, also allowing the simultaneous assessment of pro-arrhythmia and inotropic liabilities of pharmacological therapies.

5 CalTrack: open source and high throughput automated analysis of calcium transients in primary and iPSC derived cardiomyocytes

This chapter describes the investigation "CalTrack: High Throughput Automated Calcium Transient Analysis in Cardiomyocytes" as published in 2021 in the journal Circulation Research [34]. For this publication I share first authorship with Dr Yiangos Psaras. My contribution to the work presented here is related to: (i) the development of the mathematical basis of CalTrack, (ii) the experimental data analysis with CalTrack and statistical analysis with Prism software, and (iii) the design and the writing of the journal publication.

In this chapter I describe the development and use of a novel software tool, CalTrack, for the high throughput automated analysis of calcium transients from many cellular formats. First, I present the mathematical basis of the software and then its performance in phenotyping primary and induced pluripotent stem cell-derived cardiomyocytes (iPSC-CMs) in response to pharmacological compounds and HCM variants. The data analysis enabled by this novel tool will then be exploited in Chapter 7 to inform a computational investigation into the pathogenic mechanisms of HCM and their modulation by therapeutic intervention. In turn computational modelling and simulation of cardiac pathophysiology will be used to augment the experimental datasets

provided by CalTrack to enable a mechanistic understanding of cellular phenotypes.

5.1 Introduction

As reviewed in Section 2.1.2, the calcium transient of the cardiomyocyte is the primary driver of cardiac contraction and relaxation and can directly influence arrhythmogenicity. As such, dynamic calcium measurements are key to understanding cardiomyocyte physiology, pathology, and the therapeutic efficacy and safety of delivered compounds [211].

Investigations into cardiovascular biology employ fluorescent indicators of cellular calcium, including cell permeable fluorophores [279, 280] and viral delivery of genetically-encoded calcium sensors [281, 282] that may target sub-cellular structures such as sarcomeres [283, 284]. Despite the successful application of these strategies to primary cells derived from experimental models or explanted human tissues [285], there remains an unmet need for higher throughput calcium screening assays, in particular to address human immortalized embryonic stem cell and iPSC-CMs. Furthermore, computational approaches for the investigation of cardiac pathophysiology and drug action strongly rely on the availability of large quantities of high-quality data. With this goal, CalTrack, a suite of MatLab algorithms with the flexibility to analyse cellular calcium transients from many cellular formats in an automated, un-biased, and rapid analysis platform was developed. CalTrack uses high throughput fluorescent cellular imaging to enable analyses of wildtype (WT) and mutant iPSC-CMs, derived from patients or genetically engineered for

patient-specific variants using clustered regularly interspaced short palindromic repeats (CRISPR)/Cas-9 methodologies [286].

Phenotyping of iPSC-CMs has recently become easier with techniques that allow rapid automated assessments of contractile function [287, 288], which address the challenges of cellular heterogeneity in this system by increasing experimental throughput. While the development of more physiologically relevant models remains an important endeavour to overcome cellular immaturity, rapid phenotyping of iPSC-CMs by CalTrack can identify subtle changes that are critical to understanding pathogenic signals. Existing strategies with these capabilities typically require expensive hardware and skilled manual interventions (Appendix I).

CalTrack defines calcium transients in primary cardiomyocytes from animal models [283] and iPSC-CMs, including cells on patterned substrates [289, 290] or in engineered three-dimensional tissue systems [291] (Figure 5.1). The algorithm automates background subtraction, performs photobleach correction, uses masks to identify individual cells in image stacks with multiple cells per field of view, averages all identified transients, and performs transient fitting with parametric output. This code relies only upon providing a directory of video files (.avi, .vsi, .mov, .czi, .m4v, .mp4, and others) that can be converted to .tif stacks (Figure 5.2). Previously extracted fluorescence data in an excel file format can also be read by CalTrack. CalTrack is user friendly and computationally inexpensive, so that it can be run on a local computer. On average, the algorithm requires 140 seconds to convert 10 video files (250 frames) to .tif stacks and 55 seconds to analyse and export computed parameters into excel files. In comparison, manual conversion of similar videos

(120 seconds), extraction of calcium traces (200 seconds), and computation of the parameters is considerably slower. In addition, manual computation of average representative traces, with baseline correction, can impair standardisation. CalTrack is freely available using a MatLab pipeline or provided as a compiled version for users without MatLab access.

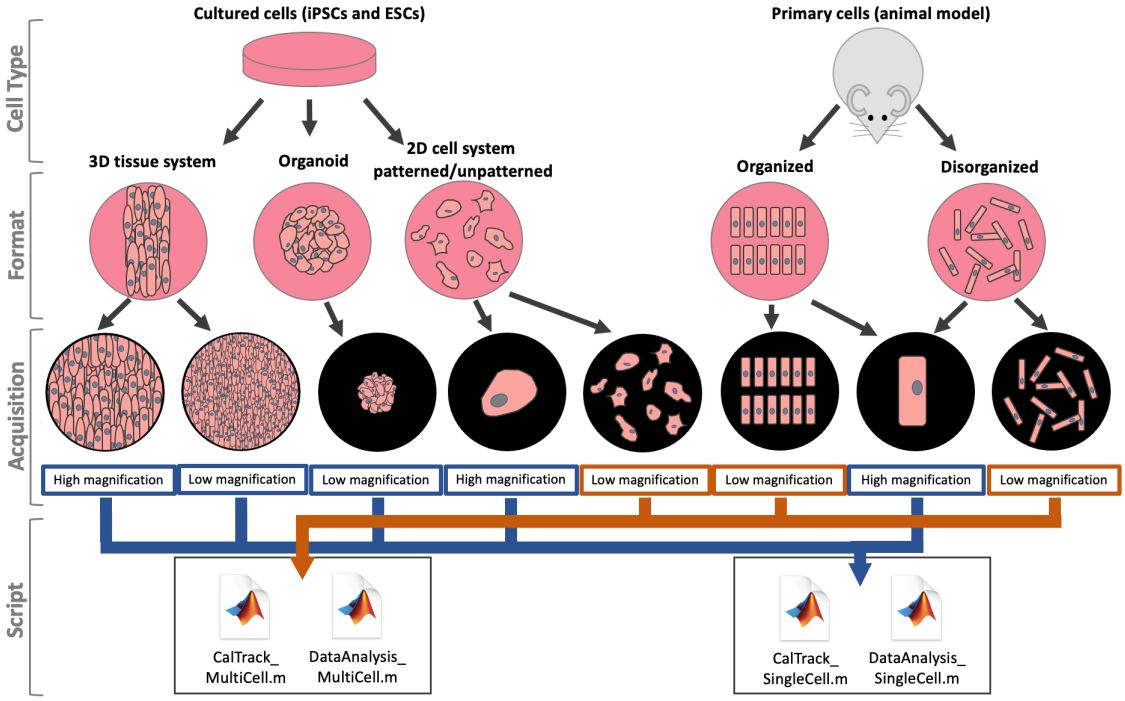

Figure 5.1. The variety of cardiovascular model systems and constructs that can be automatedly analysed using CalTrack.

This study shows that CalTrack's rapid automated analysis and fitting of hundreds of cells on a local computer provides robust statistical power for analysing changes in cellular calcium transients in comparison to a commercial software. As CalTrack only requires fluorescence microscopy, or extracted traces, to rapidly analyse large data sets, this platform may provide a critical

resource for the cardiac biology community to accelerate experimentation in physiology, pathology, and therapeutic screening.

5.2 Methods

5.2.1 Mathematical basis of CalTrack calcium transient analysis

To extract calcium traces, CalTrack relies on the Bio-Formats toolbox [292] for MatLab (Mathworks Inc. Natick, MA, USA). CalTrack initially reads all frames in the video stack and averages the value of all pixels to generate a mask. Where multiple cell segmentation is required the average image is subjected to a difference of Gaussians filter [293] to increase contrast in local boundaries. Contrast-limited adaptive histogram equalisation, and erosion-dilation enhance this to produce a segmented cell mask. This is applied to extract the raw fluorescence within each cell per frame, as the sum of all pixels in each cell (n):

$$N(t) = \sum_{i=1}^{n} p_i(t) = \ Fluorescent\ Trace$$

where p_i represents each pixel intensity.

First the software extracts the fluorescent traces from image stacks, and image processing is carried out and morphological operators are applied to segment the cells and exclude the background. Previously extracted traces can also be processed with CalTrack. Next, calcium traces that have successfully passed quality control and have either been corrected for photobleach or have been

deemed by the user not to require photobleach correction, are analysed as follows.

To select the beginning of each fluorescent transient and perform transient segmentation, the entire trace is converted to an array of the difference of each intensity value with its previous value:

$$D = diff(N) = [N(2) - N(1), N(3) - N(2), \dots, N(n) - N(n-1)].$$

The onsets of fluorescence increase, which corresponds to the start of calcium transients, match the peak values of D. Peaks in D (termed D_p) are selected as onsets of calcium-driven fluorescent transients by thresholding to a minimum prominence of 50%. The beginning of each transient is selected by subtracting an offset of 10% of the cycle length to D_p (e.g. 100 ms for 1 Hz pacing), in the original trace. Individual transients are cropped from the whole fluorescent trace by specifying their beginning and ending points at D_p-offset and D_{p+1}-offset respectively. Next, the transients are averaged to a single fluorescence intensity transient unless the option of measuring parameters on each individual transient is selected by the user, in which case the following is performed on every transient. When measuring parameters on each individual transient, a measurement of the standard deviation of all individual transients' parameters is provided as a quality control metric. As an alternative to automatic transient segmentation, CalTrack offers the user the option to perform this process by defining the beginning of the first calcium transient via event markers such as the time of electrical pacing, if known.

To characterise all temporal parameters of the obtained average transient, the baseline intensity must be determined. This is achieved by averaging the last points of the trace that correspond to a temporal window of 20% of the cycle length (e.g. 200ms for 1 Hz pacing). Subsequently, the peak of the trace is selected as the maximum intensity value and the transient magnitude is calculated as *max – baseline.* F_{max}/F_0 is calculated as the peak value divided by the baseline. Next, since fluorescent traces may have a lower baseline at the end of the trace than at the beginning, a more robust value for the baseline is defined as *baseline + (0.03 x magnitude).* This enables automated definition of the beginning and end of each transient in the fluorescent trace, and is the smallest change that can support automation, while minimally altering the measured temporal parameters (Figure 5.8). The redefined baseline value is used to calculate all temporal parameters via linear interpolation (i.e. interpolation of time at intensity values corresponding to 0%, 10%, 50% and 90% of the magnitude, which has been re-calculated with the re-defined baseline), with the exception of tau (and its fitting parameters), which is calculated by fitting the decaying arm of the fluorescent trace with an exponential decay curve with equation $y = ae^{bx} + c$, and calculating tau as $tau = -\frac{1}{b}$. The goodness-of-fit value is also calculated and reported for quality control. The complete list of parameters computed by CalTrack is reported below.

Baseline (AU): also called F_0, is the mean value of the last points of the average transient that correspond to a temporal window of 20% of the pacing period. Given as an arbitrary unit of total fluorescence unless the user selected

to convert fluorescence into calcium values by providing a calibration curve, in this case this is μM.

F_{max}/F_0: maximum fluorescence value (F_{max}) divided by baseline value (Baseline or F_0).

Magnitude: maximum fluorescence value (F_{max}) minus baseline value (Baseline or F_0).

For the remaining parameters, the re-computed baseline is adopted and used to compute a new magnitude.

t_0 (ms): obtained as the intersection between the signal (before peak) and baseline.

t_{end} (ms): obtained as the intersection between the signal (after peak) and baseline.

CD (ms): time of fluorescence (signifying calcium) above baseline, i.e. duration of the calcium transient.

CD90 (ms): time calcium is above 90% of the signal (defined as baseline + 0.1*magnitude).

CD50 (ms): time calcium is above 50% of the signal (defined as baseline + 0.5*magnitude).

CD10 (ms): time calcium is above 10% of the signal (defined as baseline + 0.9*magnitude).

T_{on} (ms): time at which calcium is maximal, computed from t_0.

T_{off} (ms): time from peak to tend.

$T10_{on}$ (ms): from t_0, time to 10% contraction (defined as baseline + 0.1*magnitude).

$T50_{on}$ (ms): from t_0, time to 50% contraction (defined as baseline + 0.5*magnitude).

$T90_{on}$ (ms): from t_0, time to 90% contraction (defined as baseline + 0.9*magnitude).

$T10_{off}$ (ms): from peak, time to 10% relaxation (defined as baseline + 0.9*magnitude).

$T50_{off}$ (ms): from peak, time to 50% relaxation (defined as baseline + 0.5*magnitude).

$T90_{off}$ (ms): from peak, time to 90% relaxation (defined as baseline + 0.1*magnitude).

tau (ms): generated from fitting signal y to $y = ae^{bx} + c$. tau = -1/b.

fit_a: parameter a of the fit.

fit_c: parameter c of the fit.

fit_rsquare: goodness-of-fit, coefficient of determination (R-squared).

BR (Hz): beat rate.

BBtime_mean (ms): average beat-to-beat time.

Nperiod: number of periods used to compute that average.

Signal to noise ratio: average transient value divided by the standard deviation of baseline.

For traces without uniform electrical pacing (i.e. more fluorescent transients are identified than the manually-input pacing frequency justifies) or traces that display aberrations reminiscent of irregular behaviour, such as early or delayed afterdepolarisations (Figure 5.4), additional information is reported as output. This includes the beat-to-beat time as the average time interval between

peaks, the number of intervals used to compute the beat-to-beat time, and the cell and beat number where early or delayed afterdepolarisations occurred. These traces may later undergo *post hoc* processing. Here an automated analysis of the regular events is carried out (i.e. excluding the irregular parts of the trace), and reported measurements include all of the above in addition to the number of total and irregular beats, as well as classifying irregular beats as an early or delayed afterdepolarisation.

5.2.2 Production of synthetic calcium transients for CalTrack benchmarking

I simulated synthetic calcium transients using the biophysically-detailed electromechanical model described in Chapter 4 [33]. Simulations were conducted in MatLab, using the numerical solver *ode15s* with solutions reported every 1 ms, corresponding to an acquisition frequency of 1000 frames per second (FPS). The model was stimulated at 0.5, 1, and 2 Hz for 200 beats, delivering a stimulus current of -53 μA/μF for 1 ms. The last 5 beats of each simulation were saved. For each pacing frequency, 20 5-beat traces were generated by scaling either the L-type calcium or the rapid delayed rectifier potassium currents' conductance. Calcium traces were down sampled to match experimental acquisition frequencies. Noise equivalent to 2.5 times the standard deviation of the final 300 ms of each calcium trace was added to each trace. Resemblance to commonly acquired experimental data was confirmed on all traces visually before analysing with CalTrack.

5.2.3 Generation of WT and TNNI3$^{R21C/+}$ missense iPSC-CMs for calcium transient analyses

Generation of the pathogenic *TNNI3*$^{R21C/+}$ [294] HCM missense iPSC line used for calcium transient analyses was performed by CRISPR/Cas-9 editing of the PGP1 cell line by Dr. Giuliana Repetti and Dr. Christopher Toepfer at the Seidman Lab [34, 286, 295-297]. The *TNNI3*$^{R21C/+}$ cell line was differentiated into iPSC-CMs via Wnt pathway modulation, and plated in a 2D assay plate by Dr. Yiangos Psaras at the Toepfer Lab [298]. Cells were subsequently treated with dimethylsulfoxide (DMSO) or Mavacamten 0.3-3 μM and imaged for calcium transients using RGECO by Dr. Psaras [34, 283].

5.2.4 Guinea pig cardiomyocyte isolation and manipulation.

Guinea pig cardiomyocyte isolation and manipulation was done at the Redwood Lab by Dr. Alexander Sparrow and Dr. Paul Robinson. Guinea pig studies were performed with protocols that were reviewed and approved by the Animal Welfare and Ethical Review Board at the University of Oxford and conform to the UK Animals (Scientific Procedures) Act, 1986. Adult left ventricular cardiomyocytes (adolescent male, 10-15 weeks in age) were isolated and immediately processed for ratiometric calcium analyses as previously described [15]. Paced Fura-2-loaded cells were studied using the Ionoptix (Waltham, MA) platform IonWizard, according to manufacturer's protocols, and by CalTrack. Alternatively, isolated cardiomyocytes were co-transduced for 48 hours with adenovirus carrying a red genetically encoded calcium indicator (RGECO) [283] and a cDNA encoding either WT *TnnI3* or R145G *TnnI3*, and cultured in plates for imaging [283]. Videos of 0.5 Hz

electrically paced cardiomyocytes at 37°C were acquired at 25 FPS. Pharmacologic effects were assessed in guinea pig cardiomyocytes that had been pre-treated with either DMSO or 10 μM Levosimendan for 15 minutes at 37°C prior to imaging.

5.2.5 Statistical analysis

Statistical analyses were performed using GraphPad Prism version 8.4.2 for macOS (GraphPad Software, San Diego California USA, www.graphpad.com). Normality in all data sets, defined as alpha < 0.05, was assessed by the D'Agostino-Pearson normality test. Single comparisons of data were assessed by a double tailed Student's *t* test or non-parametric Mann-Whitney, depending on data normality. Multiple comparisons were performed with a one-way ANOVA with Sidak post-hoc correction for multiple comparisons or Kruskal-Wallis with post-hoc Dunn's correction, depending on data normality. For multiple comparisons in paired data where the normality test was not satisfied, data was tested with a non-parametric Friedman's test with Dunn's multiple comparisons correction. In all instances a significance cut-off of $p < 0.05$ was used.

5.3 Results

5.3.1 CalTrack pipeline overview and applications

CalTrack analyses image stacks/videos acquired with fluorescent calcium reporters in iPSC-CMs or isolated adult cardiomyocytes (Figure 5.1). Alternatively, extracted traces (collected in excel files) that bypass the need to derive data from stacks/videos can also be analysed. After incubation with

chemical calcium dyes such as Fura-2, Fluo-4 [279] or following transduction with viruses carrying calcium probes (e.g., RGECOs/GCaMPs [299]), cells are imaged using a fluorescent microscope at a range of magnifications (typically 100X-10X) to provide image stacks of either single or multiple cells per field of view (Figure 5.2). Image acquisition rates should at minimum be 25 FPS, but ideally should be 40-100 FPS to allow the accurate capture of calcium transients. However, data acquired at up to 1000 data points per second can be analysed (Figure 5.5 and Figure 5.9). CalTrack applies a mask to these image stacks to identify either single or multiple cells in a field of view (Figure 5.2). In the case of imaging single iPSC-CMs at 100X or an equivalent optical magnification, CalTrack identifies the area that the cell occupies in the field of view and applies a fixed mask to the cell to measure fluorophore intensity in each frame of the acquisition (Figure 5.2A&B). Fluorophore intensity is therefore measured within the cell's boundary at maximum relaxation throughout each frame of the acquisition (Figure 5.2A-C). The individual transients can then be segmented and aligned to create a mean transient per cell (Figure 5.2D), which is used to determine the parameters that define the calcium transient. Examples of the CalTrack fitting and parametric determination are illustrated in Figure 5.2E.

For low magnification acquisitions where multiple cells are within a single field of view, CalTrack can distinguish cells by applying a mask that defines cells within a field of view (Figure 5.2F&G). This allows the simultaneous fluorescence intensity assessment of many cells from one image stack (Figure 5.2H). Each of the identified cells can then be individually segmented so that

a mean transient per cell can be computed (Figure 5.2I). The computed mean is then used for fitting and measurement of transient parameters (Figure 5.2J).

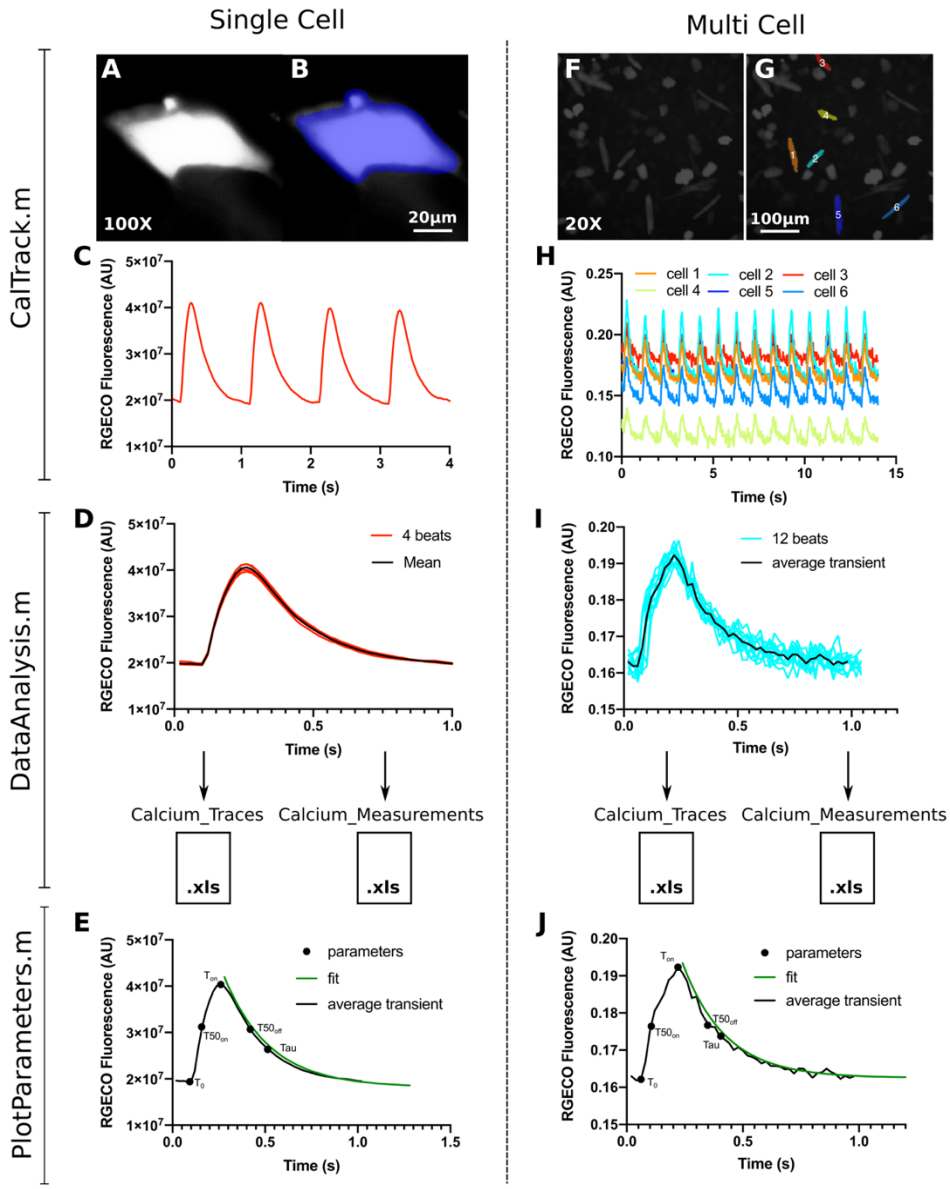

Figure 5.2. The CalTrack calcium analysis pipeline can be used for Single Cell or Multi Cell image stacks. A: A single iPSC-CM imaged using an 100X objective that has been masked (B) by CalTrack for segmentation and fluorescent trace extraction. C: From the masked iPSC-CM CalTrack extracts a raw calcium trace. D: CalTrack automatedly segments the beats (red lines) and averages them into one trace (black line). E: CalTrack provides all parameters from each individual transient or from the

mean transient of a single cell. F: The same analysis routine can be applied to low magnification (20X) image stacks with multiple cells per field of view. G: The CalTrack segmentation mask identifies single cells for transient analysis and provides raw fluorescent traces for each cell (H), which can then be individually segmented and averaged (I) for automatic parametric output (J).

5.3.2 CalTrack robustly detects cardiomyocytes in low magnification image stacks

Imaging calcium transients in multiple cells within a single field of view at low magnification can improve throughput. To enable the analysis of this data, CalTrack constructs a cell mask to identify individual cells, and excludes rounded dead cells by filtering out non-elongated cells. This strategy yielded a 1.36% false negative rate and 4.04% false positive rate. Cells detected by CalTrack are presented to the user for final quality control, and the end user can further exclude cells as false positives. As the predominance of false positives reflect overlapping cells within high plating densities, cultures should aim to minimise individual cellular overlap to reduce false positive detection of cells.

5.3.3 CalTrack corrects for linear and exponential baseline drift in calcium transient acquisitions

Baseline drift in fluorescent microscopy with calcium indicators can be caused by multiple events including photobleaching, loss of fluorophore from the cell, or cell damage.

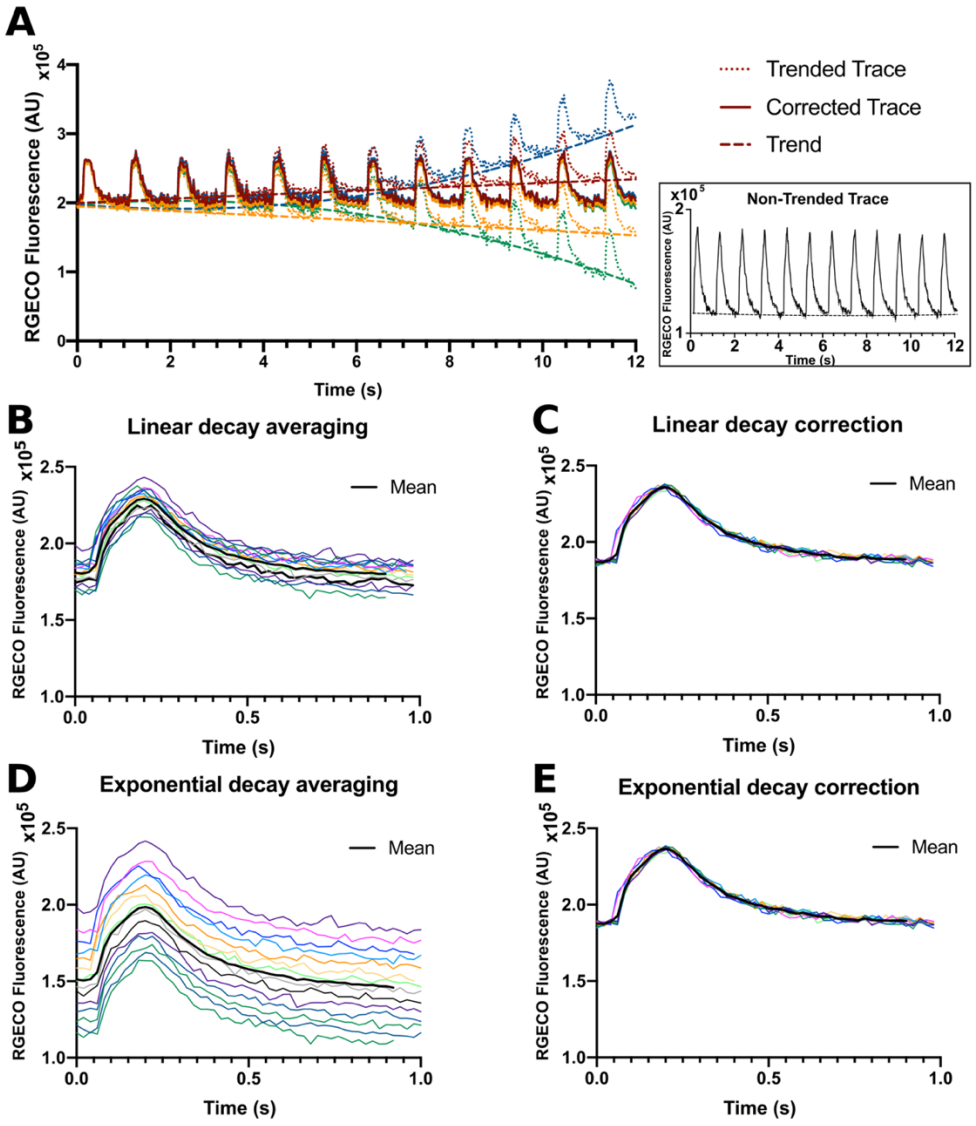

Figure 5.3. CalTrack successfully corrects linear and exponential photobleach events. A: Simulated linear and exponential baseline shifts are applied to a fluorescent calcium trace (inset). Coloured trend lines are fit to the baseline shifted data by CalTrack. These are used to correct shifts in baseline. B&D: Segmented individual transients from traces that need baseline correction due to baseline drift caused by linear decay (B) or exponential decay (D). CalTrack correction of baseline drift functions robustly for linear (C) or exponential (E) baseline shift.

CalTrack enables the investigator to select whether elimination from processing or correction of baseline drift is desirable. To correct baseline drift,

a second-degree polynomial, applicable for both linear and exponential drifts, is used to determine the baseline trend; this is subsequently subtracted from the original trace to detrend the data (Figure 5.3A). Data that lacks baseline drift remains unaffected (Figure 5.3A Inset). Prior to baseline correction, linear baseline drift would skew mean calcium transient segmentation (Figure 5.3B). Correction of the linear baseline drift reduces individual transient drift and provides a robust corrected mean transient (Figure 5.3C). The same applies to an exponential decay in baseline, which can be successfully modelled and removed from datasets with this approach (Figure 5.3D&E).

5.3.4 CalTrack provides analysis of irregular calcium transients including early afterdepolarisations and delayed afterdepolarisations

To account for irregular fluorescent transients, which cannot be analysed as part of the main automated analysis, CalTrack has additional *post hoc* analysis capabilities. These analyses require high signal to noise ratio in the extracted traces to allow robust detection of irregular transients. CalTrack classifies irregular traces as non-adherence to pacing and/or calcium spikes reminiscent of early and delayed afterdepolarisations (Figure 5.4).

CalTrack can exclude the irregular events from the multi-beat trace and measure parameters from the regular transients as it would usually in adherent transients. The irregular transients are subsequently analysed and CalTrack provides a count of the number of total transients, the number of excluded events, and the number of irregular events, including designation of events as early or delayed afterdepolarisations.

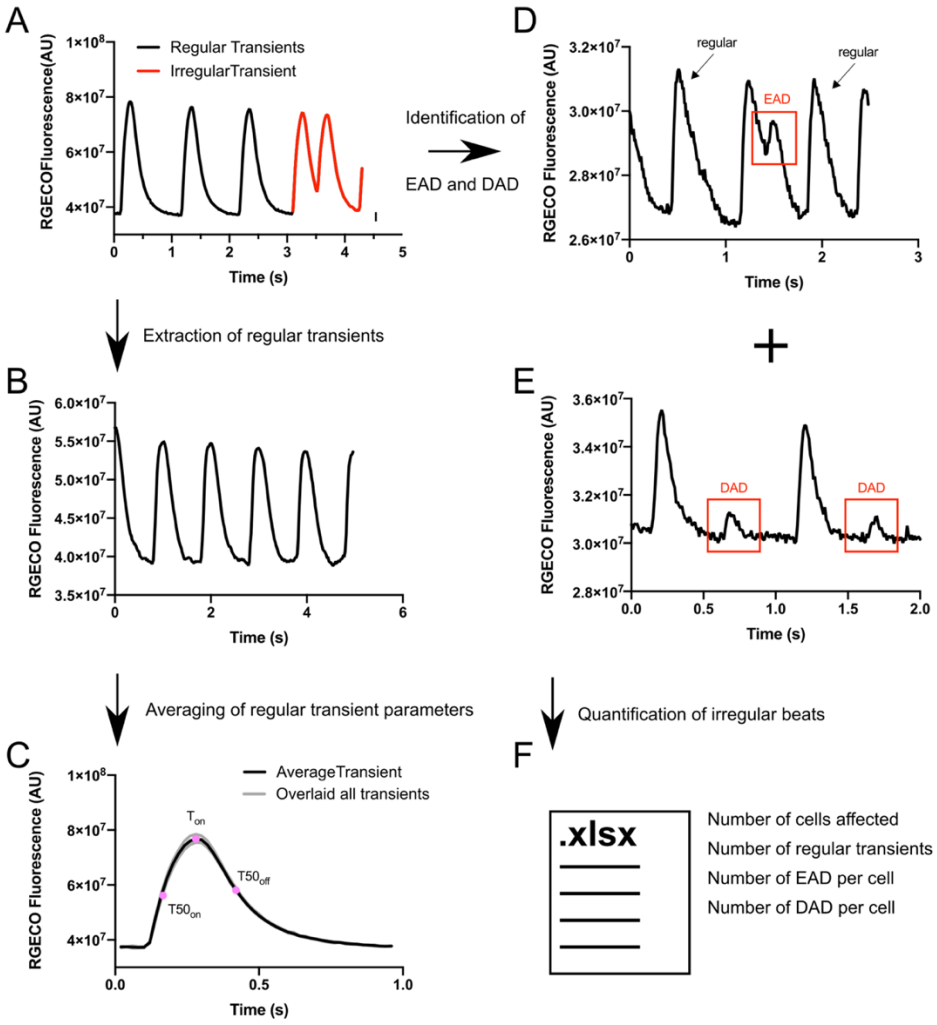

Figure 5.4. Post processing for irregular calcium traces. A: Representative example of an irregular trace. B: CalTrack separates the regular traces from the entire transient. C: Regular traces are averaged, and all parameters are measured as in the standard pipeline. Irregular traces are separated from the regular ones and recorded as EADs (early afterdepolarisations) if a second peak is detected before a transient reaches baseline (D), or DADs (delayed afterdepolarisations) if a smaller peak is detected after the transient reaches baseline (E). F: All data is collated and exported in an excel spreadsheet format.

5.3.5 Assessment of quantitative calcium concentrations using CalTrack

CalTrack can quantify intracellular calcium using the ratiometric indicator Fura-2 in WT adult guinea pig cardiomyocytes (Figure 5.5).

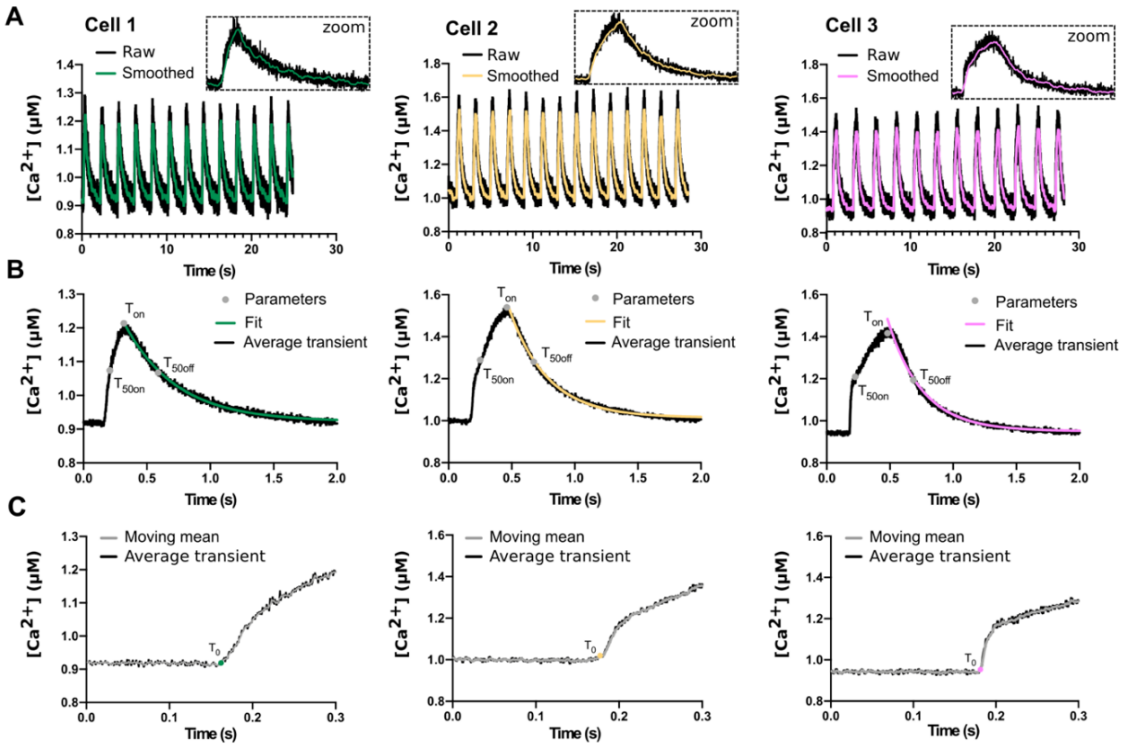

Figure 5.5. CalTrack processing of Fura-2 fluorescent traces acquired at 1000 FPS. A: Representative examples of three traces with distinctive steep (left), biphasic (right), and intermediate (middle) morphology. Raw fluorescence traces at 1000 FPS are smoothed down to 100 FPS for processing. Expanded view of single traces and their smoothed traces are shown in the insets. B: Average transients produced by reversion to 1000 FPS with parameter fitting. C: Expanded version illustrating robust detection of the initial point of calcium increase (T_0).

When running CalTrack the user can either provide a calibration curve for the ratiometric indicator or alternatively, a calibration curve is generated within CalTrack by inputting the fluorescence intensity values at known calcium concentrations for a specific ratiometric indicator. This calibration is then used with the fluorescence ratio of the ratiometric indicator to generate absolute raw and smoothed calcium concentration traces, demarcating T_0, providing profiles

with temporal parameters from baseline and peak calcium concentrations, and quantifying the baseline and peak concentration of intracellular calcium (Figure 5.5).

5.3.6 Benchmarking of CalTrack with synthetic simulated calcium transient data

CalTrack has been designed to function for multiple pacing frequencies, allowing the user to define the experimental pacing frequency.

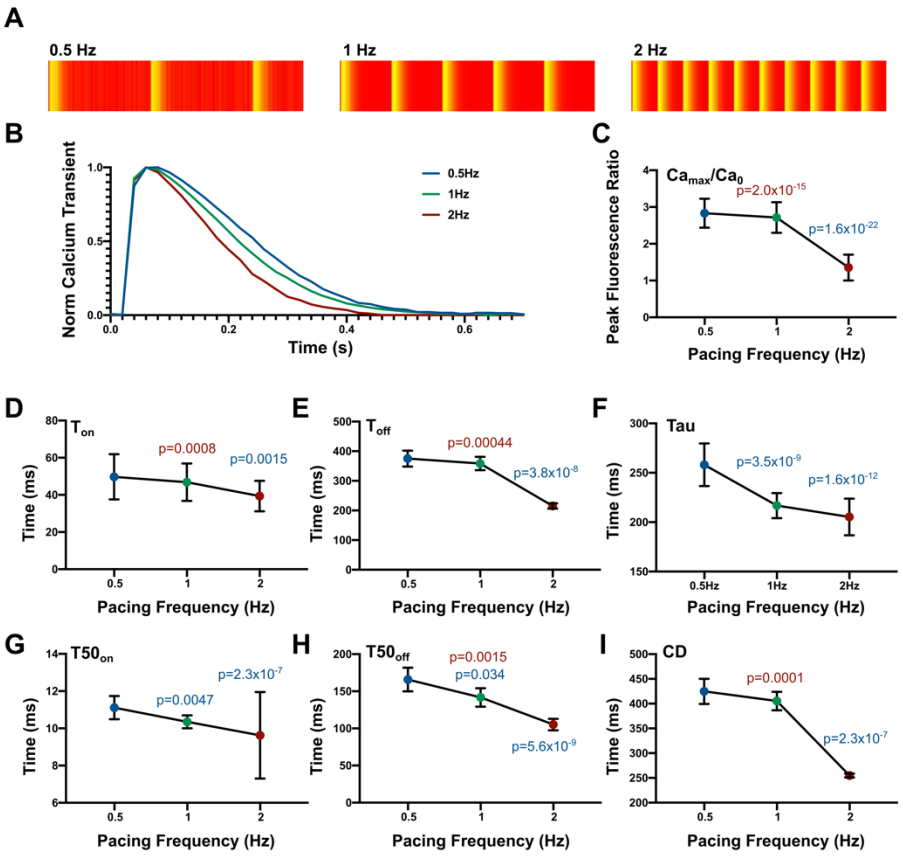

Figure 5.6. CalTrack analyses computationally simulated calcium transients at multiple beating frequencies with fidelity. A: 0.5-2 Hz kymographs produced by CalTrack. B: Average normalised calcium transients (n = 20 simulated traces for each pacing frequency). C-I: Normalised peak calcium concentration (equivalent to

F_{max}/F_0), T_{on}, T_{off}, tau, $T50_{on}$, $T50_{off}$ and CD for the different pacing frequencies. Data presented as mean and standard deviation. Statistical analysis performed by one-way ANOVA with a post-hoc Sidak correction or non-parametric Friedman test with Dunn's multiple comparisons correction, with a significance cut-off of $p<0.05$.

To test the fidelity of the underlying CalTrack code, simulated calcium transients obtained from 20 virtually generated human cardiomyocytes and several pacing frequencies from 0.5 Hz to 2 Hz were used (Figure 5.6). Variation of electrical pacing frequency affects simulated calcium transient parameters as expected (Figure 5.6A-I). When using CalTrack to analyse these data, the mean over 20 simulated calcium transients shows marked changes in calcium transient characteristics with pacing frequency (Figure 5.6B). Normalised calcium peak (equivalent to F_{max}/F_0 in experiments) decreases with increasing pacing frequency (Figure 5.6C). All kinetics parameters are faster at higher pacing frequencies (Figure 5.6D-I).

To determine the interference of noise with measurements, random noise was added to simulated calcium traces at 1 Hz pacing (Figure 5.7). Measurements of F_{max}/F_0, tau, T_{on}, T_{off}, $T50_{on}$, and $T50_{off}$ were unchanged at signal to noise ratio 15-70. However, the $T50_{on}$ was increased (Figure 5.7H) and T_{off} was decreased (Figure 5.7G) at low signal to noise ratio of 10. Therefore, data acquired below signal to noise ratio of 15 may be unreliable and should be closely scrutinized by the end user.

Simulated calcium data have been also used to assess the impact of the re-computed baseline on the estimation of the calcium parameters. Figure 5.8 shows that the redefined baseline minimally alters the measured temporal parameters while allowing for automated computation.

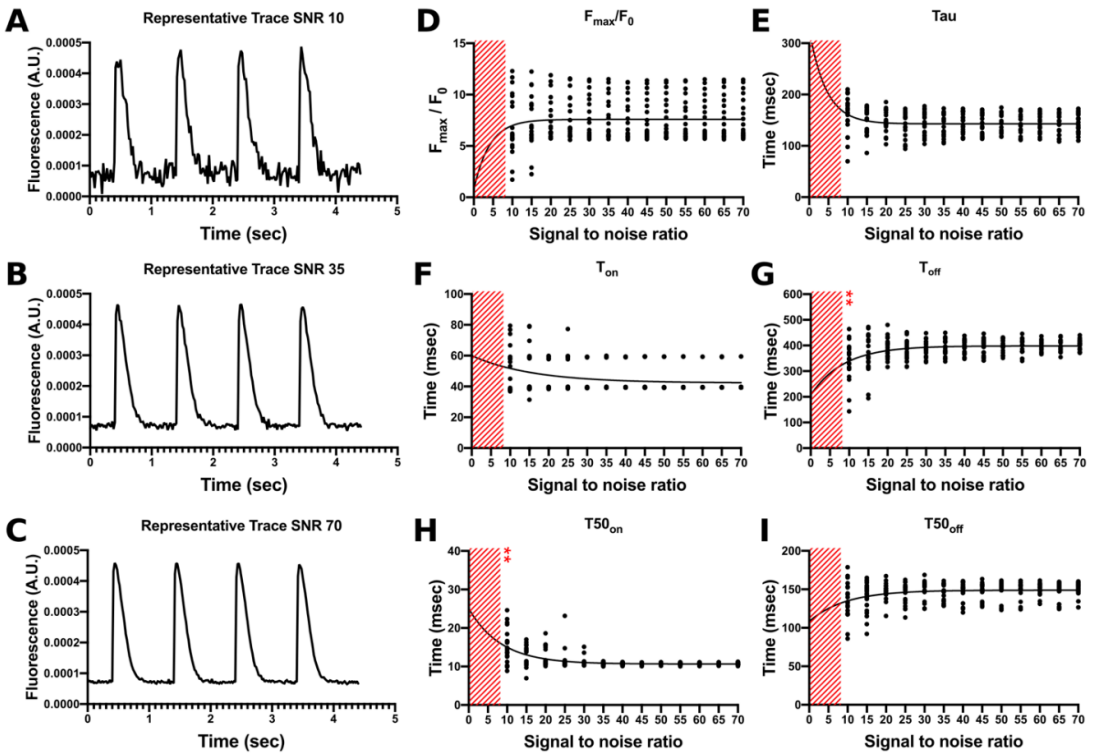

*Figure 5.7. The effect of decreased trace signal to noise ratio (SNR) on data measurement. A-C: Representative simulation of signal to noise ratios at 10, 35, and 70 respectively on the same initial trace. D-I: F_{max}/F_0, tau, T_{on}, T_{off}, $T50_{on}$, $T50_{off}$ for different SNR. N = 20 for each signal to noise ratio and p values are reported as follows: p = 0.0043 for T_{off} and p = 0.0054 for T_{50on}, ** for p ≤ 0.01 against SNR 70. Fitted lines represent nonlinear decay. Red shaded sections indicate traces that could not be analysed with CalTrack. Statistical analysis performed by one-way ANOVA with post-hoc Sidak correction for multiple comparisons or non-parametric Friedman test with Dunn's multiple comparisons correction, with a significance cut-off of p<0.05.*

5.3.7 Quantitative calcium analyses in adult Tnni3$^{R145G/+}$ cardiomyocytes with benchmarking comparison between automated CalTrack analysis and manual user-driven IonWizard analysis

A comparison between CalTrack and IonWizard software analysis was carried out for the ratiometric calcium data from adult guinea pig cardiomyocytes,

which had either been transfected with human *TnnI3*$^{+/+}$ [300] or with the R145G troponin I variant (*TnnI3*$^{R145G/+}$) [69, 283] and loaded with Fura-2 (Figure 5.9).

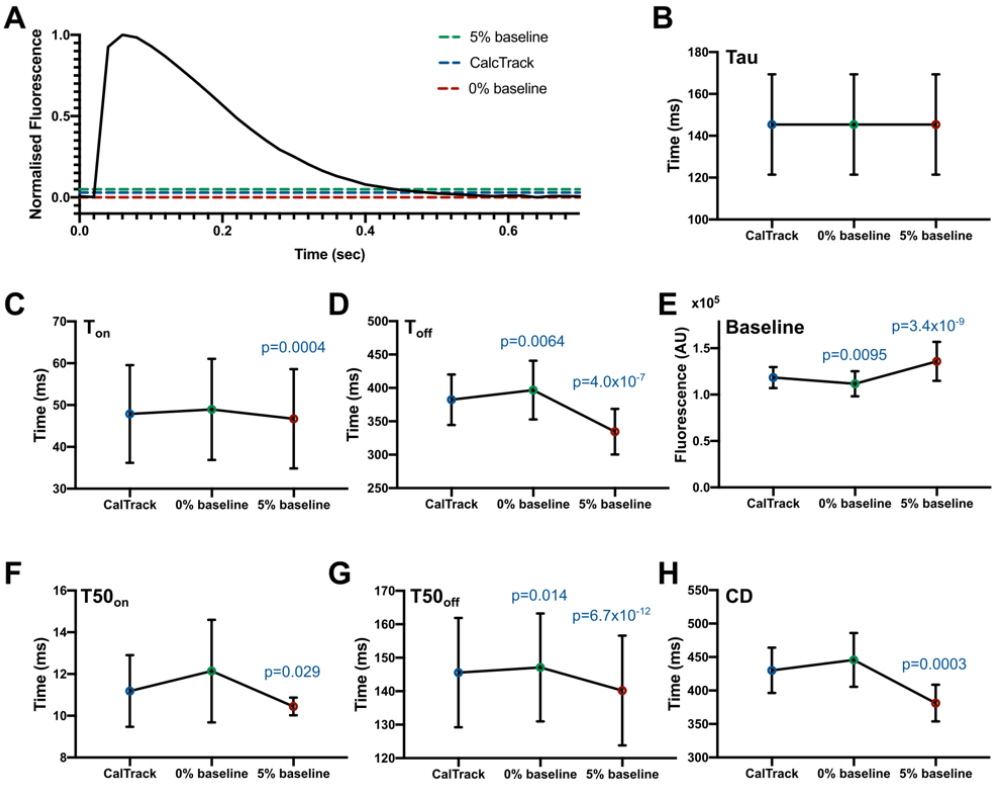

Figure 5.8: Effect of altering baseline fluorescence estimation 5% or CalTrack (3%) in comparison to hand-picked data. A: Simulated fluorescent calcium. Baseline fluorescence is denoted by hand measurement (0% baseline, n = 20), a 5% automated baseline can be applied (5% baseline, n = 20), and CalTrack analysis uses an intermediate 3% baseline (n = 20) to increase fidelity of automated baseline fitting in noisy traces. B-H: tau, T_{on}, T_{off}, Baseline, $T50_{on}$, $T50_{off}$, and CD for the different baseline values. Data presented as mean and standard deviation. Statistical analysis performed by one-way ANOVA with a post-hoc Sidak correction for multiple comparisons or non-parametric Friedman test with Dunn's multiple comparisons correction, with a significance cut-off of $p<0.05$.

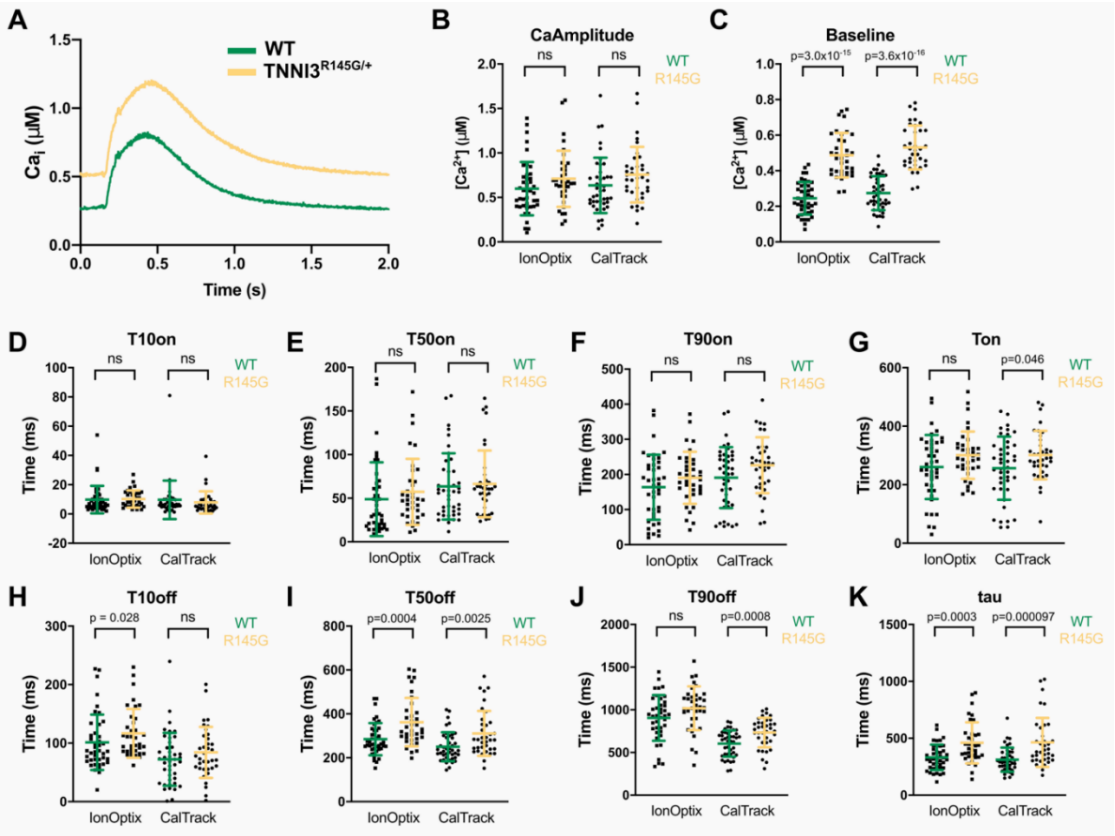

Figure 5.9. Automated CalTrack quantification of calcium concentration and kinetic parameters in guinea pig WT and TnnI3$^{R145G/+}$ cardiomyocytes is comparable to manual IonOptix IonWizard software analysis. A: Average calcium transients are identical by analysis via IonWizard or CalTrack analysis. Average traces are made of n = 42 WT and n = 36 for TnnI3$^{R145G/+}$ cells. B-H: Calcium amplitude, Baseline, T10$_{on}$, T50$_{on}$, T90$_{on}$, T$_{on}$, T10$_{off}$, T50$_{off}$, T90$_{off}$, and tau as estimated by IonOptix and CalTrack. Data presented as mean and standard deviation. Statistical analysis performed by a two-tailed Student's t-test or by nonparametric Mann-Whitney test with a significance cut-off of p > 0.05. No statistical comparisons are made between IonOptix and CalTrack.

Both algorithms detected significantly increased baseline and peak calcium concentrations without altering calcium amplitudes (Figure 5.9A-C). The times to 10%, 50% and 90% of peak calcium were not significantly different, although

CalTrack detected a modest increase in the time to peak calcium (Figure 5.9D-G). Both software detected abnormalities in calcium decay times, although not identically, and prolonged tau in the *Tnni3*$^{R145G/+}$ vs. WT cardiomyocytes (Figure 5.9H-K). While these analyses demonstrated comparable data acquisition and interpretation by both software platforms, the overall operator times for using IonWizard was 20-fold longer on average per cell analysed (CalTrack ~1 minute, IonWizard ~20 minutes).

5.3.8 CalTrack detects calcium transient responses to pharmacological agents Levosimendan and Isoproterenol in adult cardiomyocytes

Figure 5.10 illustrates the results of CalTrack analysis for WT adult guinea pig cardiomyocytes at baseline (n = 79) and after treatment (n = 96) with 10 μM of the calcium sensitizer Levosimendan [301]. Normalised mean calcium transients from 0.5 Hz paced cells (Figure 5.10A) and calcium decays (Figure 5.10B) that were obtained after Levosimendan treatment increased F_{max}/F_0 ($p = 0.0022$) (Figure 5.10C), and reduced tau ($p = 1.9 \times 10^{-14}$) (Figure 5.10D). $T50_{on}$ was not statistically significantly altered by Levosimendan (Figure 5.10E), but T_{on} was shortened ($p = 0.026$) (Figure 5.10F). Levosimendan accelerated $T50_{off}$ ($p = 2.4 \times 10^{-9}$; Figure 5.10G) and T_{off} ($p = 0.023$; Figure 5.10H) and reduced CD ($p = 0.0034$; Figure 5.10I). Drug-induced changes in fluorescence identified by CalTrack are consistent with prior studies in guinea pig cardiomyocytes [283] and pharmacologic activities of Levosimendan. Levosimendan binds troponin C and increases calcium affinity, which underlies its positive inotropic effects [302, 303] and also potently inhibits phosphodiesterase activity [304], thereby augmenting protein kinase A (PKA)

and cAMP effects that increase cellular relaxation rates [305] and promote lusitropy.

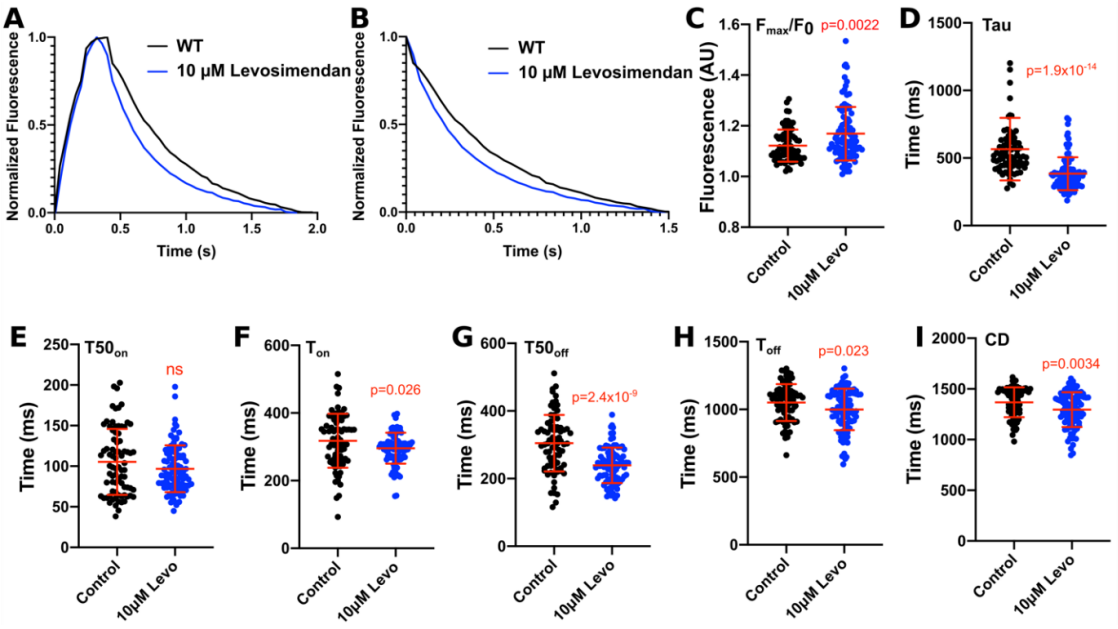

Figure 5.10. CalTrack defines calcium transient changes caused by the application of Levosimendan (Levo) in paced (0.5 Hz) adult guinea pig cardiomyocytes. A-B: Normalised mean calcium transients (A) and mean calcium decays (B) from control (n = 79) or Levo 10 μM (n = 96) treated guinea pig cardiomyocytes. C-I: F_{max}/F_0, tau, $T50_{on}$, T_{on}, $T50_{off}$, T_{off}, and CD in control and under Levo as assessed by CalTrack. Data presented as mean and standard deviation. Statistical analysis performed by a two-tailed Student's t-test or by nonparametric Mann-Whitney test with a significance cut-off of p > 0.05.

CalTrack also detected the effects of the β-adrenergic agonist Isoproterenol on 1 Hz paced WT iPSC-CMs (Figure 5.11). In comparison to untreated cells, isoproterenol increased calcium kinetics, showing both a more rapid increase in normalised calcium fluorescence and significantly reduced tau, T_{on}, and $T50_{off}$, consistent with previously reported data [306].

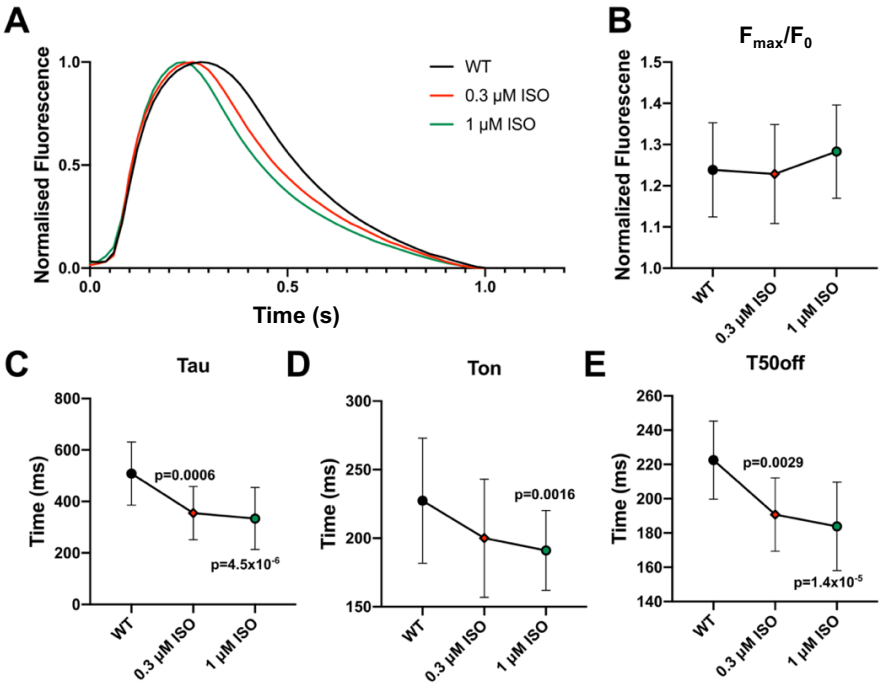

Figure 5.11. Effect of Isoproterenol (ISO) treatment on WT iPSC cardiomyocytes. A: Normalised fluorescent calcium transients for untreated wild type (n = 34) at 0.3 μM (n = 38) and 1 μM ISO (n = 71). B: F_{max}/F_0, tau, T_{on}, and $T50_{off}$ under ISO against WT. Data presented as mean and standard deviation. Statistical analysis performed by one-way ANOVA with post-hoc multiple comparisons Sidak correction or non-parametric Kruskal-Wallis with a Dunn's multiple comparisons correction, with a significance cut-off of p<0.05.

5.3.9 CalTrack detects abnormal calcium transients in guinea pig cardiomyocytes expressing the Tnni3$^{R145G/+}$ hypertrophic cardiomyopathy variant

A comparison of calcium homeostasis in 0.5 Hz paced adult WT (n=47) and *Tnni3*$^{R145G/+}$ (n=88) guinea pig cardiomyocytes is reported in Figure 5.12. In comparison to WT cardiomyocytes, the average calcium transients (Figure 5.12A) and decay traces (Figure 5.12B) indicated that *Tnni3*$^{R145G/+}$ did not

significantly alter F_{max}/F_0 (Figure 5.12C), but significantly prolonged tau ($p = 3.9 \times 10^{-11}$) and caused faster $T50_{on}$ ($p = 0.033$; Figure 5.12E). T_{on} was slowed in *TnnI3*$^{R145G/+}$ guinea pig cardiomyocytes (vs. WT, $p = 4.9 \times 10^{-8}$; Figure 5.12F). $T50_{off}$ ($p = 6.4 \times 10^{-9}$; Figure 5.12G) and T_{off} ($p = 5.0 \times 10^{-15}$; Figure 5.12H) were longer in *TnnI3*$^{R145G/+}$ guinea pig cardiomyocytes and CD was prolonged ($p = 5.9 \times 10^{-20}$; Figure 5.12I).

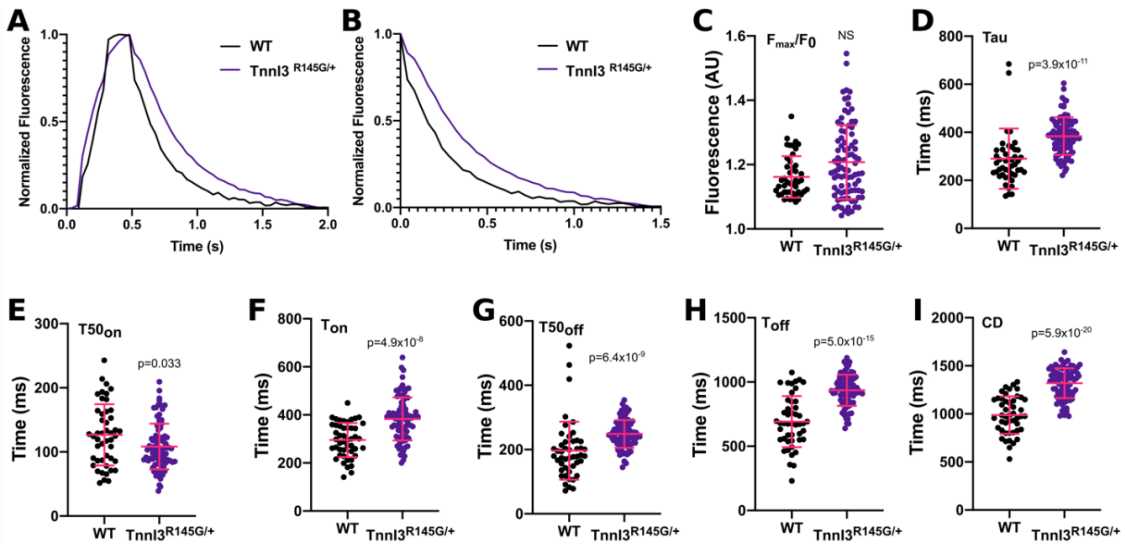

Figure 5.12. CalTrack defines calcium transient changes caused by the TnnI3$^{R145G/+}$ HCM variant in paced (0.5 Hz) adult guinea pig cardiomyocytes. A-B: Normalised mean calcium transients (A) and calcium decays (B) from WT (n = 47) or TnnI3$^{R145G/+}$ (n = 88) guinea pig cardiomyocytes. C-I: F_{max}/F_0, tau, $T50_{on}$, T_{on}, $T50_{off}$, T_{off}, and CD in control and under TnnI3$^{R145G/+}$ as assessed by CalTrack. Data presented as mean and standard deviation. Statistical analysis performed by a two-tailed Student's t-test or by nonparametric Mann-Whitney test with a significance cut-off of p > 0.05.

5.3.10 CalTrack detects basal and drug-induced calcium changes in iPSC-CMs with TNNI3$^{R21C/+}$ hypertrophic cardiomyopathy variant

CalTrack was used to assess the calcium transients from isogenic iPSC-CMs with and without an endogenous heterozygous pathogenic troponin I variant (*TNNI3*$^{R21C/+}$) that causes HCM [294]. A founder *TNNI3*$^{R21C/+}$ mutation in South Lebanon causes malignant HCM with sudden cardiac death, which often precedes hypertrophy [307], likely due to abnormal calcium handling and disruption of PKA-mediated phosphorylation of its N-terminal molecular switch [294, 308].

1 Hz paced cells treated with and without Mavacamten [309], an allosteric myosin ATPase inhibitor [81] that improves relaxation deficits associated with HCM thick filament variants [9, 10, 50, 86] and also influences calcium via unknown mechanisms [283], were studied. Using CalTrack outputs for the mean calcium transient in each cell analysed (excel file), an average transient at baseline and for each perturbation (Figure 5.13) was defined. Mutant iPSC-CMs had increased T_{50off}, T_{off}, and tau at baseline, which is consistent with previous work in a knock-in mouse model carrying the R21C variant [310] that exhibits marked diastolic insufficiency and slowed myofilament relaxation.

TNNI3$^{R21C/+}$ iPSC-CMs were not statistically different from WT iPSC-CMs when assaying F_{max}/F_0 at baseline, (Figure 5.13B), while Mavacamten further reduced F_{max}/F_0 at each dose (Figure 5.13C). Other calcium parameters that were abnormal in *TNNI3*$^{R21C/+}$ were reversed by treatment with 0.3 μM Mavacamten, including prolonged tau (vs. WT, $p = 0.001$, Figure 5.13D; normalised in Figure 5.13E) and significantly faster $T50_{on}$ (vs. WT, $p = 3x10^{-8}$; Figure 5.13F; normalised in Figure 5.13G).

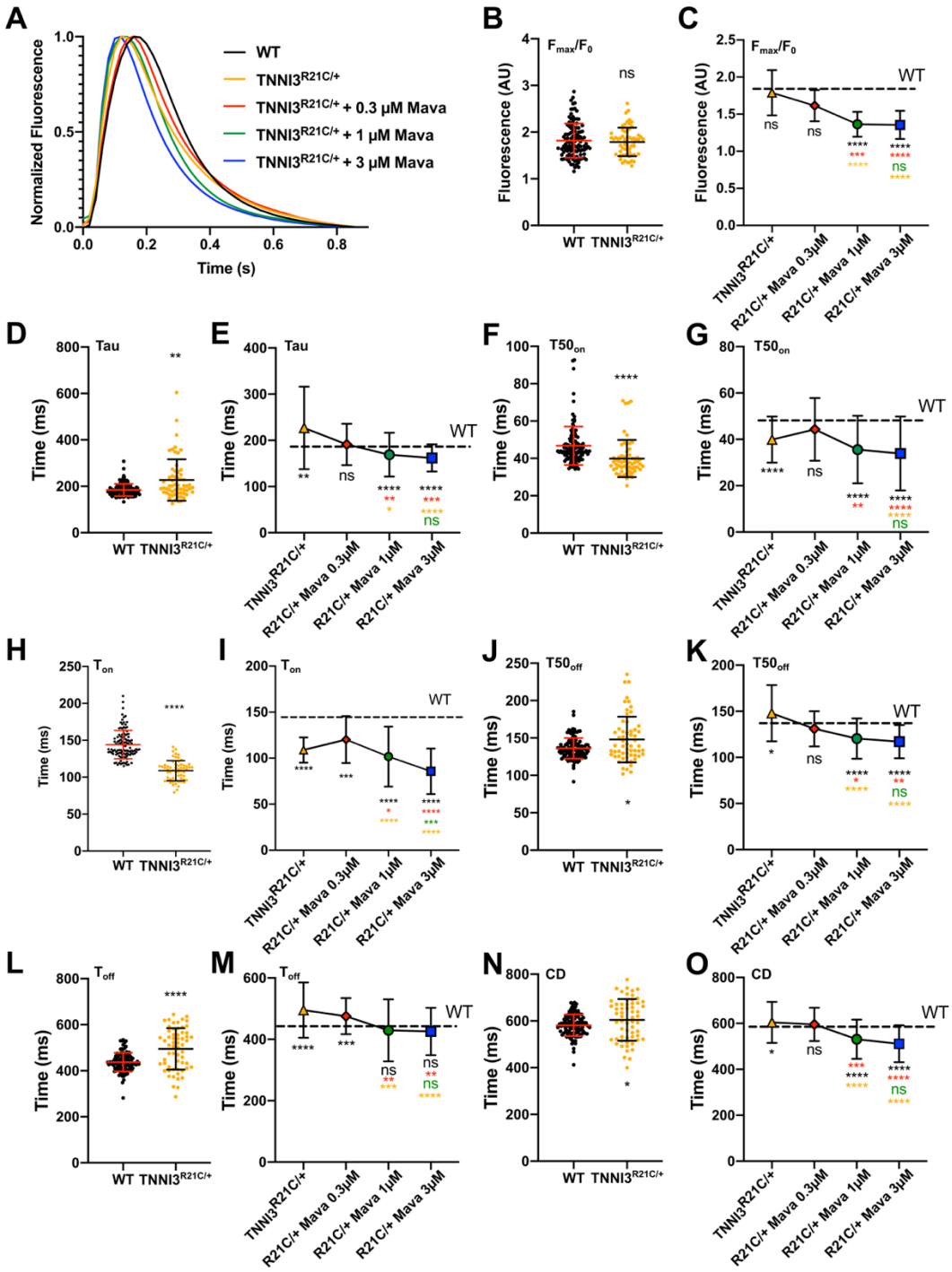

Figure 5.13. CalTrack defines calcium phenotypes and drug responses in paced iPSC-CMs harbouring the HCM TNNI3$^{R21C/+}$ variant. A: Averaged calcium transient traces of WT (n = 113) and TNNI3$^{R21C/+}$ (n = 60) cardiomyocytes with 0.3 µM (n = 40), 1 µM (n = 59), and 3 µM Mavacamten (Mava) (n = 92). B-O: F_{max}/F_0, tau, T50on, Ton, T50off, Toff, and CD in WT and TNNI3$^{R21C/+}$ and related dose-response to Mava. Data presented as mean and standard deviation. Colour of significance denotation defines

*the treatment group compared. Statistical analysis performed by non-parametric Kruskal-Wallis with post-hoc Dunn's correction for multiple comparisons. Significances are denoted on each panel where * p < 0.05, ** p < 0.01, *** p < 0.005, **** p < 0.0001.*

TNNI3$^{R21C/+}$ also had faster T_{on} (vs. WT, $p < 2.2x10^{-16}$, Figure 5.13H) and dose-dependently accelerated by Mavacamten (Figure 5.13I) while prolonged $T50_{off}$ (vs. WT, p = 0.044; Figure 5.13J) was normalised (Figure 5.13K). T_{off} was longer ($p = 1.7x10^{-5}$) (Figure 5.13L) and dose-dependently corrected by Mavacamten (Figure 5.13M). CD was longer in *TNNI3*$^{R21C/+}$ iPSC-CMs when compared to WT (p = 0.035, Figure 5.13N) but was dose-dependently shortened by Mavacamten (Figure 5.13O). CalTrack identified that 8% of *TNNI3*$^{R21C/+}$ iPSC-CMs displayed delayed after depolarisations (n = 60), in comparison to 0.9% in WT iPSC-CMs (n = 113).

The effects of increasing Mavacamten dose on WT iPSC-CMs is shown in more detail in Figure 5.14. F_{max}/F_0 was increased by 3 μM Mavacamten treatment whereas $T50_{on}$ and T_{on} were dose-dependently reduced by Mavacamten treatment (Figure 5.14A-C). $T50_{off}$ decreased at 1 μM and 3 μM doses (p = 0.023 and p = 0.0045 respectively; Figure 5.14D). At 3 μM Mavacamten there was an accelerated decay in tau (p = 0.0018; Figure 5.14E), an accelerated T_{off} at 3 μM (p = 0.024; Figure 5.14E) and decreased CD (p = 0.000019; Figure 5.14G).

The altered calcium phenotype of *TNNI3*$^{R21C/+}$ is mirrored in the contractile phenotype as assessed by SarcTrack [288]. Specifically, *TNNI3*$^{R21C/+}$ cardiomyocytes experience a significantly larger sarcomere shortening (p =

3.6x10^{-8}, Figure 5.15A) and prolonged relaxation (p = 1.0x10^{-15}, Figure 5.15C) compared to WT, which is normalised by 3 µM Mavacamten (Figure 5.15B&D).

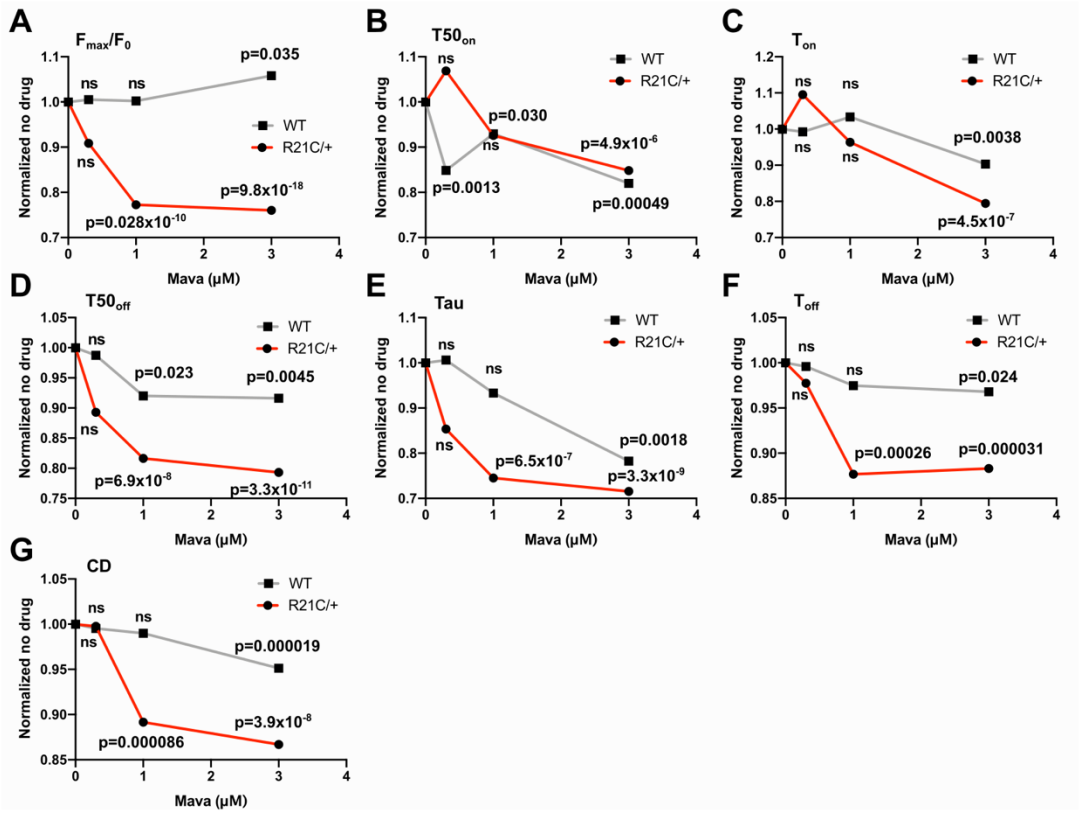

Figure 5.14. Effect of Mavacamten (Mava) treatment on the TNNI3 variant R21C and WT, each normalised to their respective control (0 µM point). Calcium parameters for WT (n = 82), WT + 0.3 µM Mava (n = 88), WT + 1 µM Mava (n = 90), WT + 3 µM Mava (n = 85), TNNI3$^{R21C/+}$ (n = 60), TNNI3$^{R21C/+}$ + 0.3 µM Mava (n = 40), TNNI3$^{R21C/+}$ + 1 µM Mava (n = 59), TNNI3$^{R21C/+}$ + 3 µM Mava (n = 92). A-G: Comparison of Mava effects in WT and R21C for the parameters F_{max}/F_0, T50on, Ton, T50off, tau, Toff, and CD. Data presented as mean and standard deviation. Statistical analysis performed by non-parametric Kruskal-Wallis with Dunn's correction for multiple comparisons, with a significance cut-off of p<0.05.

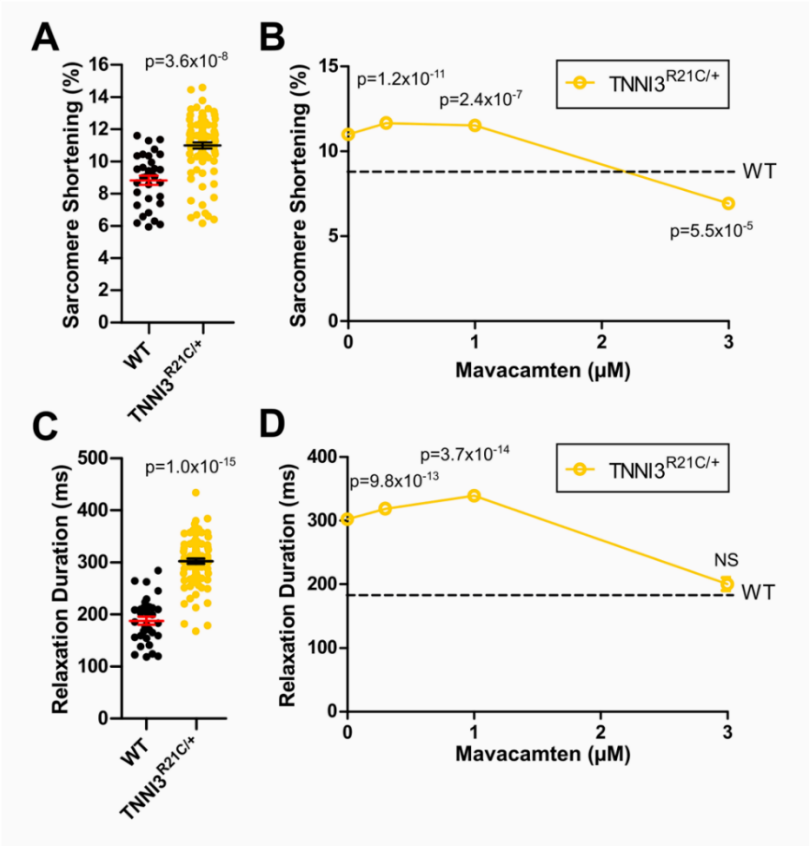

Figure 5.15. Mavacamten (Mava) corrects contractile changes caused by the TNNI3$^{R21C/+}$ variant in 1 Hz paced iPSC-CMs, assessed by SarcTrack analysis. A: Sarcomeric shortening measured in WT (n = 33) and TnnI3$^{R21C/+}$ (n = 89) iPSC-CMs. B: Mava treatment of TNNI3$^{R21C/+}$ iPSC-CMs at 0.3 μM (n = 127),1 μM (n = 51) and 3 μM (n = 60). C: Relaxation duration increased in TNNI3$^{R21C/+}$ iPSC-CMs when compared to WT iPSC-CMs. D: Mava application at 0.3 μM (n = 127), 1 μM (n = 51), and 3 μM (n = 60) showed dose-dependent correction of relaxational abnormalities in the TNNI3$^{R21C/+}$ iPSC-CMs. Data presented as mean and standard deviation; statistical significances are denoted against WT. Students t-test were used in A and C with a significance cut off of p < 0.05. One-way ANOVA was employed to compare all Mava treatments against WT in B and D with a post-hoc Sidak correction for multiple comparisons with a significance cut-off of p < 0.05.

5.4 Discussion

CalTrack is a novel high throughput automated analysis pipeline that capitalises on advanced imaging capacities and high frame rate acquisitions using fluorescent microscopy. This study demonstrates that CalTrack provides a robust assessment of calcium transients in multiple cellular formats. This extends to quantitative ratiometric analysis of calcium concentrations within cells when data is acquired at high temporal resolution (>1000 data points per second). Harnessing rapid screening technologies to visualise and image multiple cells in single fields of view, CalTrack acquires and automatedly and rapidly analyses data in high throughput.

Quantitative assessment of calcium transients by CalTrack can be used in computational investigations into the pathogenic mechanisms underlying cardiovascular conditions and their modulation under therapeutic interventions [22, 157], as I will demonstrate in the next chapters. Computational modelling and simulation of cardiac pathophysiology can then be used to augment experimental datasets provided by CalTrack to enable a mechanism-driven understanding of cellular phenotypes [22, 157], thereby providing a platform for testing hypotheses in human cardiomyocytes as alternatives to animal models [31], so as to characterise physiologic and pathologic processes at baseline and in response to interventions.

Contemporary open-source software for analysing calcium transients focuses on neuronal cell types [311-315] and characterise irregular traces generated by neurons. While these platforms have some utility in cardiomyocytes, they are cumbersome for use in this system, and cannot run automatedly. These issues limit high volume acquisition of cellular calcium transients and require significantly longer analysis times. Some laboratories overcome these issues

through custom scripts, which typically lack automation, have variable parameter definitions, or limited parameter extraction precluding cross-study comparisons [316-321]. By contrast, software automation eliminates manual user input and associated user error/bias, thereby providing calcium transient data in a defined, standardised way that can be compared between cells and experimental conditions.

While CalTrack is easily deployable for analysis across a variety of cardiac cells within a range of experimental systems, the platform has limitations. Analytical accuracy is compromised at low acquisition rates because of the rapid kinetics of the calcium transients generated in cardiomyocytes. This effect is independent of the software used for analysis. CalTrack uses interpolation to measure parameters smaller than the acquisition window, yet the acquisition frequency dictates accuracy, especially in parameters related to the start and fast phase of the transient. This may underlie the measurement difference of $T50_{on}$ in WT human iPSC-CMs (~50 ms, acquired at 50 FPS) compared with WT guinea pig cardiomyocytes (~100 ms, acquired at 25 FPS). Nevertheless, CalTrack enables comparative analyses for lower frame rate data, where the findings using CalTrack are complimentary to previous findings generated using the same experimental data set that had been analysed with manual user-driven analysis and previously reported [283]. Importantly, individual transient registration may be perturbed with extremely high frame rate data, as over-sampling reduces the prominence of point-to-point differences, from which the start of a calcium transient is defined. CalTrack data acquired at 1000 FPS is downsampled to 100 FPS solely to identify the start of the calcium transients and the raw 1000 FPS data is then

used for parametric analyses. Therefore, high frequency data acquired by line scanning or by the use of a photo multiplier tube can also be robustly and rapidly analysed by CalTrack. As with many platforms, high data noise may limit the accuracy of the algorithm in fitting key parameters, but this is largely overcome by the trace averaging used in CalTrack. Indeed, almost identical analysis fidelity of values were obtained with CalTrack and the IonOptix IonWizard software (Figure 5.9). When needed, CalTrack also provides the end user the ability to check fitting fidelity for all steps of the analysis process, so that data quality control standards can be identified. Notably, CalTrack can also be used to automatedly analyse data obtained using a ratiometric calcium indicator such as Fura-2.

The utility of CalTrack to define perturbations in components of calcium homeostasis in adult guinea pig cardiomyocytes and human iPSC-CMs is demonstrated here. Levosimendan, an agent with inotropic effects due to troponin C sensitisation [322], and potent phosphodiesterase inhibition [304] which stabilizes PKA, increases F_{max}/F_0, accelerates calcium decay, and accelerates the time to peak calcium which manifested as shorter CDs in guinea pig cardiomyocytes similar to human myocardium [305]. iPSC-CMs treated with the β-adrenergic agonist Isoproterenol activated calcium transients, due to PKA-dependent increases in L-type calcium channel activity [323], release of sarcoplasmic reticulum calcium by phosphorylation of phospholamban [324], and ryanodine receptor activity [325].

CalTrack robustly detected differences in mutated sarcomeric thin filament proteins. Two pathogenic HCM variants in *TNNI3* both had prolonged tau and longer T_{off} times. CalTrack also identified an 8-fold higher frequency of delayed

afterdepolarisations in *TNNI3*$^{R21C/+}$ iPSC-CMs when compared to WT iPSC-CMs. These findings result in decreased cellular relaxation, as assessed by SarcTrack in *TNNI3*$^{R21C/+}$ iPSC-CMs, which often manifest as diastolic abnormalities in HCM hearts [15, 283], and may promote after depolarisations and arrhythmias that contribute to sudden cardiac death [307]. The *TnnI3*$^{R145G/+}$ variant had a longer T_{on} while the *TNNI3*$^{R21C/+}$ variant had a shorter T_{on}. These findings are significant and are mirrored in the respective contractility profile of each variant [15]. Notably, these data also show that the allosteric myosin ATPase modulator Mavacamten, which corrects the contractile abnormalities in HCM thick filament variants, normalised tau and T_{off} in *TNNI3*$^{R21C/+}$ iPSC-CMs albeit with a dose-dependent reduced F_{max}/F_0, time to peak, and CD. As such, Mavacamten treatment may salvage some of the diastolic insufficiency caused by HCM mutations that are concomitant with increased lengths of calcium decays. These findings support recent studies [87] suggesting that Mavacamten influences calcium cycling with potential therapeutic efficacy in addition to its established effects on myosin ATPase [81, 87].

Dual functional assessment of sarcomere contraction and calcium transients in cardiomyocytes represents the potential for future development and combination of SarcTrack with CalTrack, thereby enabling wide-spread analyses using calcium-sarcomeric shortening loops (Figure 5.16). This can be achieved by combining the use of endogenous genetically encoded green fluorescent protein (GFP) tag on titin [297] with the red spectrum RGECO calcium fluorophore.

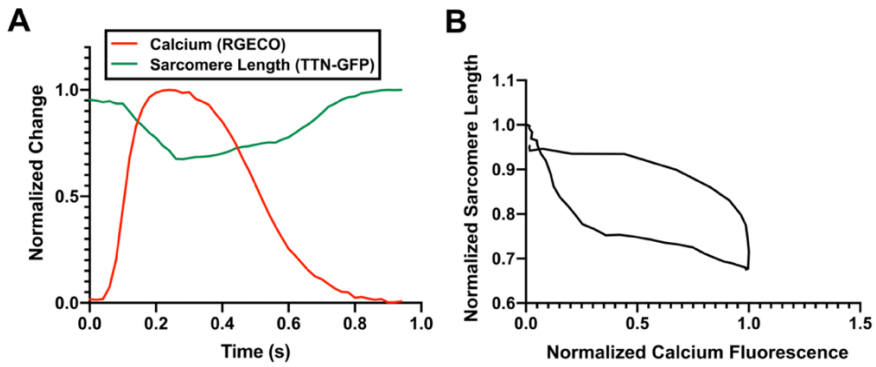

Figure 5.16: Simultaneous acquisition of sarcomeric motion and calcium fluorescence to illustrate the potential of CalTrack in conjunction with simultaneous sarcomere tracking. A: Average normalised calcium and sarcomere length. B: Sarcomere length-calcium loop.

Altogether, CalTrack has demonstrated applicability as a rapid automated calcium transient analysis platform for a wide variety of cardiomyocyte constructs and sources. CalTrack provides calcium amplitude and temporal parameters from single or multiple adult or iPSC-CMs within a field of view and can analyse previously extracted data from proprietary equipment. The algorithm provides high fidelity measurements, limited by the quality of data input (e.g., acquisition rate of image stacks and noise) and is easily adopted and applied on local computers with rapid automated data processing rates. This open-source tool may therefore advance assessments and understanding of calcium transients across multiple experimental cardiovascular fields. This is partially proven by the use of CalTrack-enabled data analysis to inform the computational investigations presented in the next chapters of this thesis.

6 Human-based modelling and simulation of myosin sequestration changes due to pathogenic variants and Mavacamten

In this chapter I propose an extension of the human electromechanical cellular model described in Chapter 4 of this thesis and in [33] to incorporate a phenomenological representation of myosin sequestration and release between the super relaxed state SRX and the disordered relaxed state DRX. This is used to investigate the influence of these conformations on cardiomyocyte contractility and relaxation in response to pathogenic variants and the allosteric modulator of myosin ATPase activity Mavacamten. In the next chapter I exploit the model generated here to conduct a computational investigation of HCM mutation-specific disease mechanisms and their responses to pharmacological therapy.

6.1 Introduction

As reviewed in Section 2.1.3, a new state of myosin that regulates contractile function by tuning myosin head availability was recently observed in myocardium [48]. This myosin state was termed SRX where myosin heads are sequestered away from the actin thin filament. Broadly, myosin SRX exists in a balance with the disordered relaxed state DRX which defines myosins that are available to drive contraction. Certain HCM variants decrease myosin SRX

thereby increasing the DRX myosin heads that are able to interact with actin and drive the clinical hypercontractile phenotype [8]. Mavacamten has been shown to re-stabilise myosin SRX and reverse the cellular hallmarks of HCM [9].

Given the important role played by SRX and myosin availability in modulating cardiac contractility, I generated a computational model that allows interrogation of how disease- or drug-induced changes in the myosin DRX:SRX ratio alter contractile function. I hypothesised that the sequestration and release of myosin heads by SRX could be phenomenologically modelled through a modulation of crossbridge availability. This enabled the investigation of varying the number of functionally accessible myosin heads on cardiac electromechanical function, without the complexity of a full characterisation of SRX dynamics. The latter approach could potentially be more accurate, but it would also require experimental data not currently available. Instead, I extended my framework for modelling and simulation of human ventricular electromechanics [33] to include the explicit dependency of crossbridge formation on the myosin DRX:SRX ratio. I then conducted a simulation study to evaluate the impact of changes in the DRX:SRX ratio on biomarkers of cellular mechanical function. I calibrated the newly generated model with experimental data on cardiac contractility under a pathogenic β-myosin heavy chain variant and the allosteric modulator of myosin ATPase activity Mavacamten. The proposed model is based on two key assumptions supported by strong evidence: 1) changes in myosin DRX:SRX ratio modulate the number of functionally accessible myosin heads for interaction with actin;

2) Mavacamten acts through a shift in myosin DRX:SRX ratio biasing SRX formation [9, 50].

6.2 Methods

6.2.1 Model construction

The electromechanical model constructed in this thesis (Chapter 4) makes use of the Land model of cardiac contraction [152] to simulate thin filament activation and crossbridge cycling (Figure 6.1A&B). This model does not explicitly consider the DRX and SRX myosin states, but it is parametrised so that it correctly accounts for the fact that only a small fraction of myosin molecules is estimated to be involved in sarcomere force production in a cardiac cycle. Here I modify the Land model so that it can simulate scenarios (diseases or drug intervention) where the DRX:SRX ratio deviates from its control value. A new parameter, R, is introduced into the model to account for deviations from the control DRX:SRX ratio. R represents the ratio $(DRX:SRX)/(DRX:SRX)_{control}$. In human myocardium $(DRX:SRX)_{control}$ can be roughly considered to be 30:70 with the majority of myosins in the SRX state [9, 52]. In the model proposed here, R acts by modulating the transitions between the U and W states (Figure 6.1B&C). This means that the state variable W, representing crossbridges in the pre-powerstroke state, now depends on both the U state (the actin binding sites available for crossbridge formation due to calcium activation) and R, which describes myosin heads functionally available for interaction with actin (only myosin in DRX can do so). The new parameter R modulates transition rates as follows

$$\frac{dW}{dt} = k_{uw} * f_1(R) * U - k_{wu} * f_2(R) * W - k_{ws} * W - \gamma_{wu} * W$$

where $f_1(R)$ and $f_2(R)$ are functions to be determined so that the output tension replicates the desired behaviour when compared to experimental data. In steady-state conditions, when $\frac{dW}{dt} = 0$, the relationship between the steady-state occupancies and transition rates will be

$$0 = k_{uw} * f_1(R) * U - k_{wu} * f_2(R) * W - k_{ws} * W$$

as no distortion (γ_{wu}) is present in steady-state, and therefore

$$\left(\frac{W}{U}\right)_{ss} = \frac{k_{uw} * f_1(R)}{k_{wu} * f_2(R) + k_{ws}}$$

The system will therefore reach a steady-state configuration determined by $f_1(R)$ and $f_2(R)$. In particular, depending on R, the ratio $\left(\frac{W}{U}\right)_{ss}$ will be shifted towards the U or the W state in line with the hypothesis that changing the availability of myosin heads that can interact with actin will affect how many crossbridges can enter in the pre-powerstroke state W. When $f_1(R) = f_2(R) = 1$, the original system is recovered (including the steady-state configuration). I therefore impose the constraint that $f_1(1) = f_2(1) = 1$, so that $R = 1$ represents the control condition where (DRX:SRX)=(DRX:SRX)$_{control}$. Note that $R \to 0$ as $\mathrm{DRX} \to 0$ (no interaction with actin), which implies $f_1(0) = 0$ (no crossbridges in pre-power state W). Moreover, $f_1(R)$ must be strictly

monotonic increasing in R to signify a gradual increased transition to the pre-powerstroke state W. Similarly, $R \to \infty$ ($R \gg 1$) as $\mathrm{SRX} \to 0$ (no crossbridges in super relaxed state, so all contribute to force production). Therefore, $f_2(R \gg 1) \to 0$, increasing the $\left(\frac{W}{U}\right)_{ss}$ ratio, where $f_2(R)$ must be strictly monotonic decreasing in R to signify a gradual increased number of crossbridges remaining in the pre-power state W. Finally, both $f_1(R)$ and $f_2(R)$ must be strictly positive in the range of considered values of R for compatibility conditions in the crossbridge cycling model (positive transition rates).

Based on these conditions, I chose the functions $f_1(R)$ and $f_2(R)$ to be of the form $f_i(R) = R^n$. This choice was further supported by the fact that a similar modulation is already implemented in the model for B to U state transitions (the transitions between blocked and unblocked myosin binding sites on actin that depend on how much calcium is bound to troponin), and it provides results consistent with the expected effect of DRX:SRX ratio modulation on contractile function, as shown in the next section. Specifically, I chose $f_1(R) = R^{\frac{1}{8}}$ and $f_2(R) = R^{-3}$ when $R < 1$, and $f_1(R) = R^{\frac{1}{8}}$ and $f_2(R) = R^{-2}$ when $R > 1$.

To further support this choice, I also studied the impact on the modulation of cardiac contractility of variations in the exponent parameters n of the $f_i(R)$ functions. n was varied in the range [1/8 1/2] for $f_1(R)$ and in [-3 -2] for $f_2(R)$.

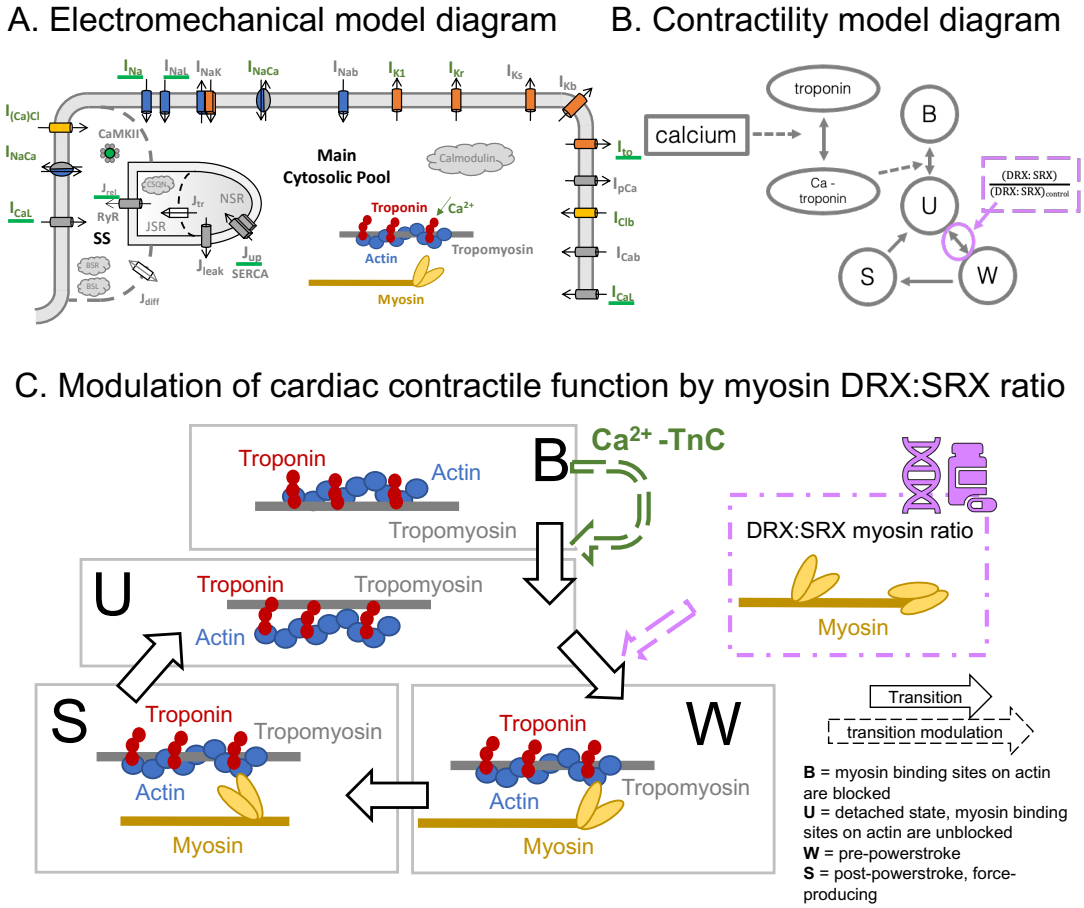

Figure 6.1. Human-based biophysical electromechanical model. A: Schematic representation of the ionic currents, calcium dynamics, and contractile properties considered. B: Diagram of the active tension model (redrawn from [152]) with changes highlighted in pink indicating the new model parameter R. C: Representation of cardiac muscle proteins' function in a cardiac cycle and correspondence with the in-silico active tension model state variables.

As mentioned, R represents the ratio $(DRX:SRX)/(DRX:SRX)_{control}$ with $(DRX:SRX)_{control}$ ~ 30:70. To determine reasonable ranges of variation of R, I made the following assumptions. I hypothesised that at least 10% of myosins may always be in the DRX state. It was indeed shown [9] that in squirrel during torpor when the heart rate reaches ~6bpm, the DRX population is always at

least ~10%. Also, not all the myosins may be recruited in the DRX state during muscle activation, but a proportion of them (~20%) may remain in the SRX state (there is no evidence to the best of our knowledge of reported DRX:SRX larger than 80:20). Therefore, I have chosen to test R values in the range [0.25 to 9]. R<1 represents a shift towards SRX with respect to the control ratio. Allowing R to vary in [0.25 1] enables the investigation of different Mavacamten concentrations. At the same time, varying R in [1 9] allows me to test the effect of HCM mutations that destabilise SRX.

6.2.2 Model calibration

Simulations to calibrate suitable responses to R were conducted with the human ventricular electromechanical model presented in [33] and Chapter 4. Two different protocols were simulated to obtain isometric twitch tension in intact cardiomyocytes and the steady-state tension-calcium relationship in skinned cardiomyocytes. Twitch tension is elicited in-silico by the stimulus current that triggers an AP through the excitation-contraction coupling process. The steady-state tension calcium curve is obtained by using fixed calcium values as input of the contractility model parametrised for skinned cardiomyocytes [152]. The tension produced by the cell quickly reaches a steady-state value that is saved and plotted with respect to the corresponding calcium value. From these two protocols the relevant biomarkers were computed. The steady-state calcium-tension curve was fitted to a Hill equation. From this, maximal tension, calcium sensitivity of force production, and Hill coefficient were estimated. From the twitch tension, time to 50% contraction, time to peak, time 50 and 90% decay, total duration, tension baseline and

amplitude were computed. The model was paced at 1Hz until the steady-state was observed. Tension biomarkers were computed for the chosen formulations of $f_1(R)$ and $f_2(R)$ and for the ones obtained by varying the n parameter. The optimal $f_1(R)$ and $f_2(R)$ were chosen because of their ability to replicate similar amounts of change in contractility in response to specific R changes with respect to experimental data. In particular, the target was to replicate the observed ~25-30% decrease in maximal tension under 0.5 μM Mavacamten in human myocardium [326], and the ~40% increase in contractility under an increase in DRX of 17% due to the pathogenic *MYH7*$^{R403Q/+}$ mutation observed in hiPSC-CMs [9]. These data were used to constrain $f_1(R)$ and $f_2(R)$.

Throughout this study, I focused on the Mavacamten 0.5 μM concentration because of data availability in human myocardium at that concentration [326] and because this is close to the IC50 value of 0.3 μM for inhibiting myosin ATPase activity in biochemical assays using murine and bovine myosin [81], and plasma levels that effectively relieved left ventricular outflow tract obstruction in human clinical trial data [88], as done in [326]. I also evaluated how the contractile response obtained with this formulation compared to experimental evidence from animal studies. Since interspecies differences are critical in the translation of findings from pre-clinical models to human cells, I decided to focus the study on human experimental data to maximise the relevance of the models' predictions in human cells. Animals and humans exhibit significant pathophysiological differences, and these may limit the predictive power of animal models. I therefore used the experimental data

collected in other species only as a qualitative comparison against the model outputs.

From the comparison with experimental data under 0.5 and 1 μM Mavacamten, and given the chosen formulation of crossbridge modulation by R, I was able to estimate an approximate dose response curve of Mavacamten so that R values could be approximated and derived from Mavacamten concentrations through the following Hill equation:

$$R = \frac{1}{1 + \left(\frac{[Mava]}{IC50}\right)^{n}}$$

where IC50 represents the Mavacamten concentration that leads to R = 0.5 and n is the Hill coefficient.

6.3 Results

The following combinations of $f_1(R) = R^{\frac{1}{8}}$ and $f_2(R) = R^{-3}$ if $R < 1$, and $f_1(R) = R^{\frac{1}{8}}$ and $f_2(R) = R^{-2}$ if $R > 1$ were selected as the optimal formulations to describe changes in contractile function by the modulation of crossbridge availability, as presented in Figure 6.2. This figure illustrates the modulation of cellular contractility by crossbridge availability under the chosen mathematical formulation. Compared to the control scenario where R = 1, twitch tension peak and duration both decreased when R<1 and increased for R>1. Calcium sensitivity of force production decreased for R<1. Minimal changes in the Hill coefficient were also observed for R<1 whereas the reduction in tension was significant. Opposite behaviour was observed for R>1. In particular, I highlight

the twitch (Figure 6.2A) and steady-state (Figure 6.2B) tension biomarker values for specific R values of 0.5, 0.8, and 1.3. The value of R = 1.3 mimics the experimentally observed increase in DRX:SRX ratio for the pathogenic *MYH7*$^{R403Q/+}$ mutation [9]. The values of 0.5 and 0.8 were not prescribed *a priori*, but represent optimal values for the simultaneous replication of multiple modes of action of Mavacamten in human myocardium at relevant clinical doses, as explained next.

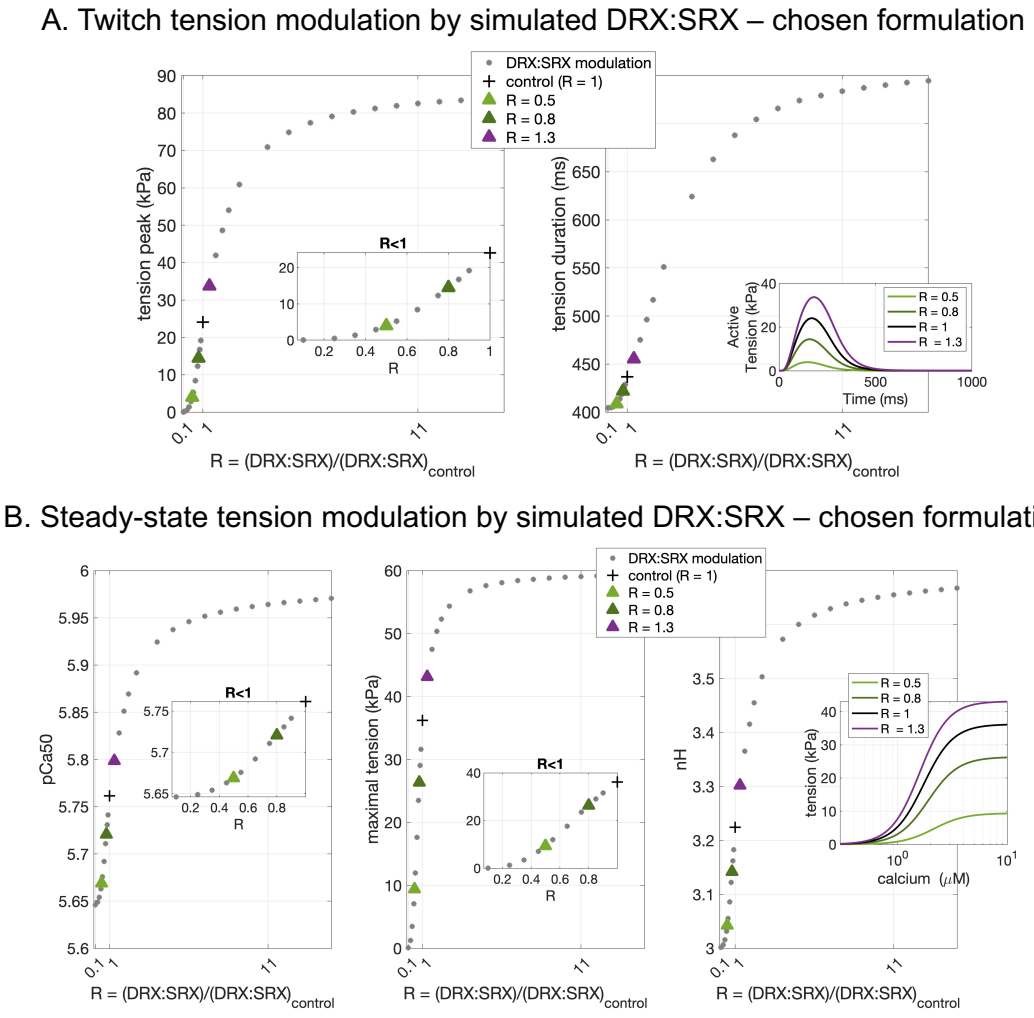

Figure 6.2. Computational evaluation of the impact of changes in the DRX:SRX ratio (on x axis) on healthy cardiac mechanical function for the chosen mathematical

formulation of $f_1(R) = R^{\frac{1}{8}}$ and $f_2(R) = R^{-3}$ if $R < 1$, and $f_1(R) = R^{\frac{1}{8}}$ and $f_2(R) = R^{-2}$ if $R > 1$. A: Twitch tension biomarkers: tension peak and duration. B: Steady-state tension biomarkers: calcium sensitivity of tension production (pCa50), maximal tension, and Hill coefficient of the calcium-tension relationship (nH).

The proposed model predicted a ~40% increase in contractility for R = 1.3 (Figure 6.2B, central panel). It was also able to recover for R = 0.8 the ~30% decrease in maximal tension observed in human myocardium [326] under exposure to a Mavacamten concentration of 0.5 μM (Figure 6.2B, central panel and inset).

Further details on the simulated response of ventricular cardiomyocytes to Mavacamten are provided in Figure 6.3. Under 0.5 μM Mavacamten (obtained for R = 0.8) both experiments [326] and simulations predicted a decrease in calcium sensitivity of force production (Figure 6.3A) of similar magnitude (~0.05 units in simulations and ~0.1 units in experiments). I selected R = 0.5 to represent 1 μM Mavacamten, as for this value the proposed model predicted a reduction in maximal tension similar to the ~70% reduction observed in animal experiments under 1 μM Mavacamten [81] (Figure 6.3A). It was also reported that additional inhibition of myosin ATPase activity by Mavacamten beyond 1 μM is minimal [81], similarly to our model predictions for R < 0.5 (Figure 6.3A&B).

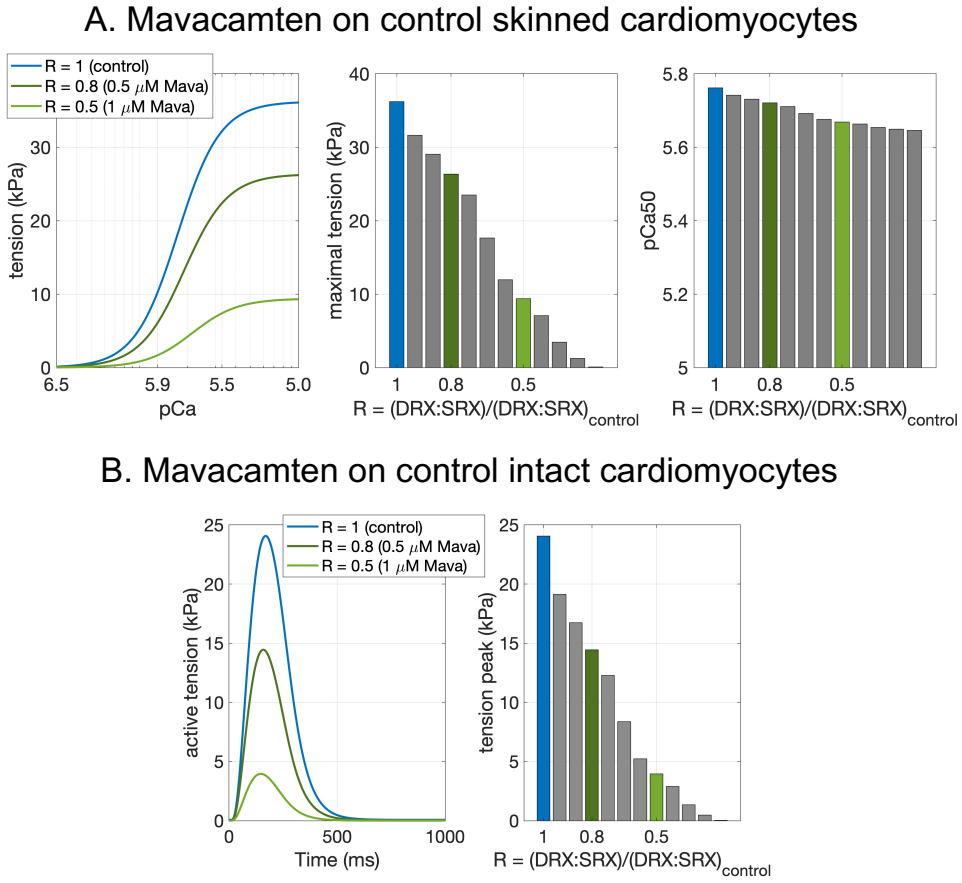

Figure 6.3. Simulation of Mavacamten's action as a reduction in the DRX:SRX ratio (R<1). A: Skinned cardiomyocytes. B: Twitch tension response to Mavacamten. C: Estimated dose-response curve of Mavacamten.

The dose-dependent response to Mavacamten for simulated twitch tension in intact adult human cardiomyocyte (Figure 6.3B) showed the same trend of

reduced contractility that was observed in sarcomere shortening in intact mouse cardiomyocytes [81].

Given the agreement between simulations and experiments at specific R values and Mavacamten concentrations, I used their correspondence to estimate the IC50 and Hill coefficient values of the Hill curve between the model parameter R and Mavacamten concentrations (Figure 6.3C). Specifically, by considering that drug concentrations equal to 0, 0.5, and 1 μM correspond to R equal to 1, 0.8, and 0.5, IC50 resulted in 1 μM and Hill coefficient in 1.9.

For the chosen optimal formulation, I also report in Figure 6.4 the effect of modulating R on the time evolution of the state variables U and W of the Land model. As illustrated in the figure, decreasing values of R (as induced, for example, by increasing Mavacamten concentrations) have the effect of promoting the U state occupancy against the W state, meaning that fewer crossbridges would move from the detached to the weakly bound state, reducing tension production. Moreover, the relaxation of the W state is faster for smaller R values, as expected when fewer myosins are bound to actin.

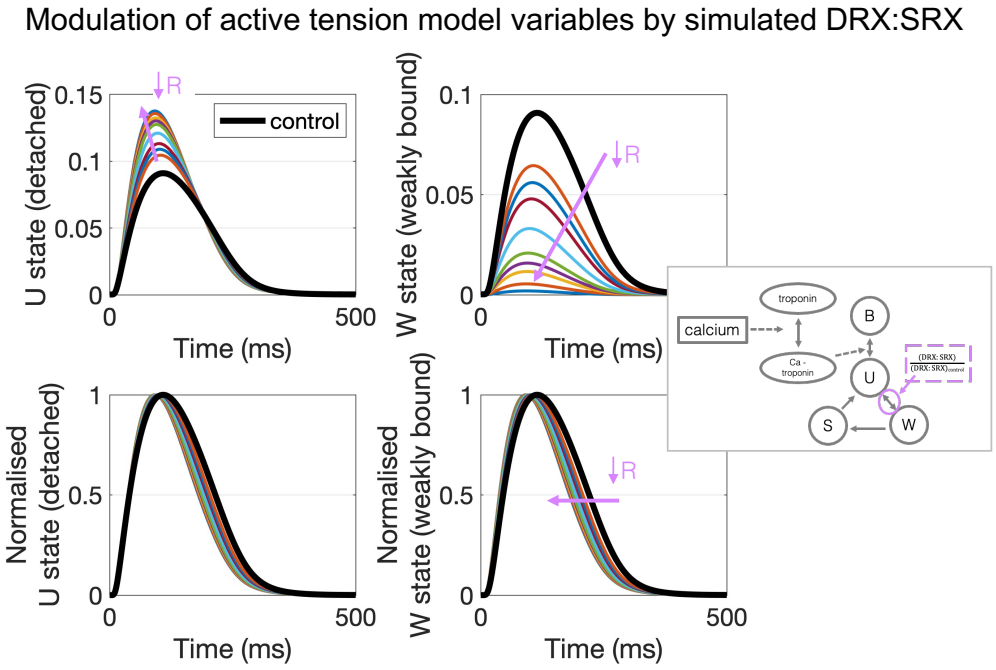

Figure 6.4. Model parameter R (representing the myosin ratio (DRX:SRX)/(DRX:SRX)$_{control}$) modulates the time course of model variables U and W, the unblocked myosin binding sites on actin with no crossbridges bound and the bound crossbridges in the pre-powerstroke state.

Finally, to further support the choice of the optimal formulation presented above, and to estimate the impact on the modulation of cardiac contractility of perturbations in the exponent parameter n in $f_1(R)$ and $f_2(R)$, I report a comparison of the effects of the different n values on twitch tension peak and duration (Figure 6.5A), maximal steady-state tension, calcium sensitivity of force production pCa50, and Hill coefficient nH of the calcium-tension relationship (Figure 6.5B). Figure 6.5 illustrates the results obtained with the chosen formulation of $f_1(R) = R^{\frac{1}{8}}$ and $f_2(R) = R^{-3}$ if $R < 1$, and $f_1(R) = R^{\frac{1}{8}}$ and $f_2(R) = R^{-2}$ if $R > 1$, and with the following $f_1(R)$ and $f_2(R)$ obtained by varying the n value:

1) $f_1(R) = R^{\frac{1}{2}}$ and $f_2(R) = R^{-3}$

2) $f_1(R) = R^{\frac{1}{4}}$ and $f_2(R) = R^{-3}$

3) $f_1(R) = R^{\frac{1}{8}}$ and $f_2(R) = R^{-3}$

4) $f_1(R) = R^{\frac{1}{8}}$ and $f_2(R) = R^{-2}$

Overall, these formulations displayed a similar modulation of twitch and steady-state tension (Figure 6.5) with plateaus at both very small and very large R values compatible with the fact that myosin motors are a finite number and tension cannot increase or decrease beyond certain levels.

A. Twitch tension modulation by simulated DRX:SRX – comparison

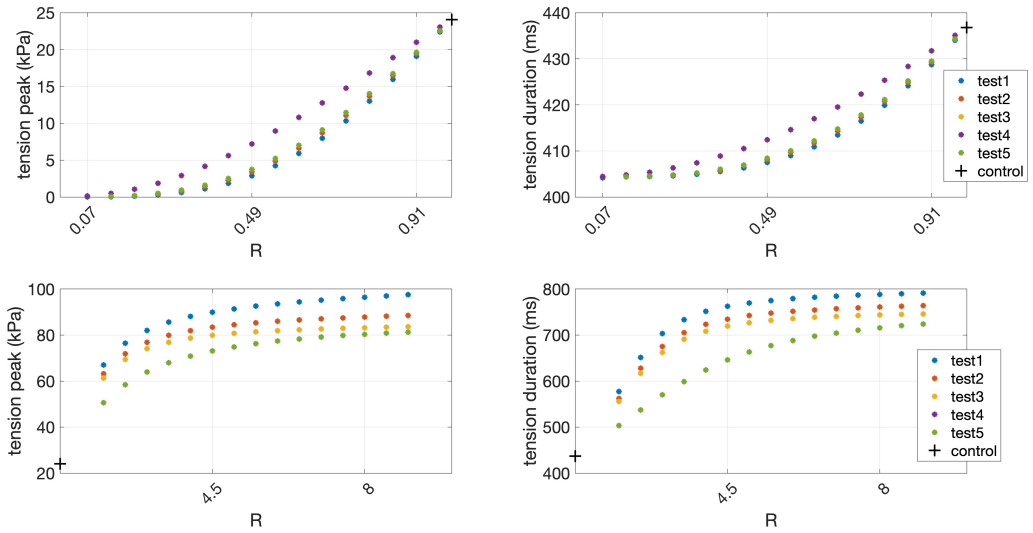

B. Steady-state tension modulation by simulated DRX:SRX – comparison

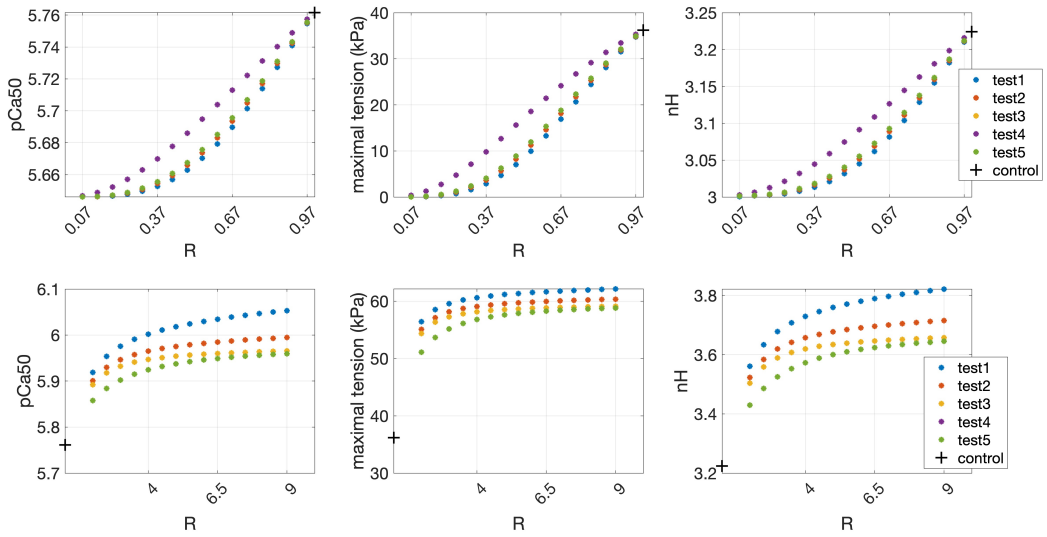

Figure 6.5. Comparison of different $f_1(R)$ and $f_2(R)$ formulations on parameters of the twitch tension (A) and steady-state tension-calcium curve (B). R varies in 0.07-9. First rows of A and B: R varied in 0.07-1. Second rows of A and B: R varied in 1-9. In test1 $f_1(R) = R^{\frac{1}{2}}$ and $f_2(R) = R^{-3}$; in test2 $f_1(R) = R^{\frac{1}{4}}$ and $f_2(R) = R^{-3}$; in test3: $f_1(R) = R^{\frac{1}{8}}$ and $f_2(R) = R^{-3}$; in test 4 $f_1(R) = R^{\frac{1}{8}}$ and $f_2(R) = R^{-2}$. Test5 is the chosen optimal formulation of $f_1(R) = R^{\frac{1}{8}}$ and $f_2(R) = R^{-3}$ if $R < 1$, and $f_1(R) = R^{\frac{1}{8}}$ and $f_2(R) = R^{-2}$ if $R > 1$.

For 1 < R < 5, $f_2(R)$ has a stronger effect, compared to $f_1(R)$, in determining the twitch tension peak and duration, with larger powers of R leading to higher biomarker values. On the contrary, for R > 5, $f_1(R)$ determines the twitch tension peak and duration with again larger powers leading to higher values (Figure 6.5A, second row). For 1 < R < 5, a smaller power of R in $f_2(R)$ leads to a more gradual increase in twitch tension peak and duration. Indeed, the optimal formulation has the smaller power of R in $f_2(R)$, and it allows the recovery of the increase in tension peak observed in the experimental data for R = 1.3, as reported above.

Similar modulation by the powers of R in $f_1(R)$ and $f_2(R)$ are observed for the steady-state biomarkers of the calcium-tension curve under R > 1 (Figure 6.5B, second row).

For R < 1, test1, test2, test3 (and the optimal formulation, which is equal to test3 for R < 1) lead to a similar modulation of all the twitch and steady-state biomarkers (Figure 6.5A, first row; Figure 6.5B, first row). This means that it is the power of R in $f_2(R)$ that determines their trend (and not $f_1(R)$), with higher powers leading to more pronounced reductions in biomarker values. In this regard, test1, test2, and test3 provide a modulation of contractility similar to the optimal formulation, and all allow replication of the reduction in maximal tension observed under 0.5 and 1 μM Mavacamten, as explained above for the optimal formulation.

6.4 Discussion

The destabilisation of the myosin energy-conserving state SRX is known to promote contractile and metabolic abnormalities and can cause adverse

clinical outcomes in HCM patients. Pharmacological treatment with Mavacamten can re-stabilise myosin SRX and correct the cellular hallmarks of HCM [9].

In this study, I generated a computational model that allows interrogation of how disease- or drug-induced changes in the myosin DRX:SRX ratio alter contractile function. This was achieved phenomenologically through a modulation of crossbridge availability by the myosin ratio DRX:SRX. The resulting model was calibrated with experimental data on sarcomere shortening under a pathogenic β-myosin heavy chain variant and the allosteric modulator of myosin ATPase activity Mavacamten.

I showed how the availability of myosin heads strongly modulates cellular contractility in terms of twitch tension peak and duration, and steady-state maximal tension and calcium sensitivity of force production. Particularly, the reduction in maximal tension observed under 0.5 μM Mavacamten in human myocardium and the reduction in maximal tension at ≥1 μM Mavacamten in animal experiments were replicated by my model for $(DRX:SRX)/(DRX:SRX)_{control} = 0.8$ and $(DRX:SRX)/(DRX:SRX)_{control} \leq 0.5$, respectively. Furthermore, the increase in sarcomere shortening under the β-myosin heavy chain mutation *MYH7*$^{R403Q/+}$ observed experimentally could be replicated by our model in terms of active tension peak. The modulation of tension generation by crossbridges availability in simulated human adult cardiomyocytes corroborates the experimental results previously obtained in different systems on the reduction of maximal force production [50, 81, 326, 327] and provides evidence to confirm the proposed effect of myosin sequestration and release by SRX on crossbridges availability [9, 50].

The model constructed and calibrated here is further evaluated in the next chapter where it is used to build HCM mutation-specific populations of human adult ventricular myocytes, and to evaluate their response to the pharmacological treatment Mavacamten.

The development of a translationally-relevant model of Mavacamten's action within a cell (easily adaptable to other sarcomeric therapies) in the context of disease-specific mechanisms represent an important tool in drug development where human-relevant models are needed to improve efficacy assessments. Together with computational models of genetic mutations, it has the potential to unravel mechanistic explanations of drug action in specific HCM pathophysiology. This approach holds both preclinical and clinical potential towards the development and delivery of personalised therapy, as further shown and discussed in the next chapter.

7 Human-based computational and experimental investigations of disease mechanisms and pharmacological action in mutation-specific hypertrophic cardiomyopathy

In this chapter I describe an experimentally-informed computational investigation of HCM mutation-specific disease mechanisms and their responses to pharmacological therapy. This study focuses on three heterozygous pathogenic missense variants: the *MYH7*$^{R403Q/+}$, the *TNNT2*$^{R92Q/+}$, and *TNNI3*$^{R21C/+}$ in β-myosin heavy chain, troponin T, and troponin I, respectively. After the introductory section (Section 7.1), in Section 7.2, I describe the experimental and computational methodology adopted for this study. Section 7.3 is divided in three main subsections, one for each of the mutations investigated. In each subsection I first present the experimental and clinical data on the specific mutation, then the modelling and simulation approach to investigate its pathophysiology, and finally its simulated response to the pharmacological treatment Mavacamten. Finally, in subsection 7.3.4, I illustrate a comparison of simulated Mavacamten's efficacy on the three different mutations in the context of mutation-specific pathophysiology.

7.1 Introduction

As reviewed in Chapter 2, HCM is a genetically and clinically highly heterogeneous disorder that can lead to atrial fibrillation, sudden cardiac death, and heart failure [54]. Pharmacological therapy plays a key role in the clinical management of HCM, but to date there are no therapies that specifically target disease mechanisms [79]. Mavacamten is the first drug developed to target HCM pathophysiology, with demonstrated efficacy for obstructive HCM [79, 81]. However, the exact mechanisms that govern Mavacamten's cellular effects are incompletely understood, and a deeper understanding is needed to guide effective and safe patient-specific therapy, as well as to facilitate the development of further novel pharmacological therapies for sarcomeric cardiomyopathies.

The overall goal of the study presented in this chapter is to characterise (experimentally and computationally) the pathophysiology of specific HCM-causing mutations, and then assess their responses to Mavacamten treatment. Unravelling mechanistic explanations of drug action in specific HCM pathophysiology holds both preclinical and clinical potential towards the development and delivery of personalised therapy. This study aims to address the following research questions: (i) What are the key mutation-specific mechanisms responsible for the observed disease cellular phenotypes? (ii) Is the proposed mechanism of action of Mavacamten effective in reversing HCM mutation-specific phenotypes?

I adopt a human-based multiscale approach where drug-induced subcellular changes are linked to cellular biomarkers of cardiac electromechanical function in the context of disease specific remodelling. This has the potential to mechanistically-guide the identification of the patients that will benefit the

most from specific pharmaceutical interventions, and those that may be at higher risk of developing an adverse reaction.

This study focuses on the three heterozygous pathogenic missense variants *MYH7*$^{R403Q/+}$, *TNNT2*$^{R92Q/+}$, and *TNNI3*$^{R21C/+}$. This choice was based on data availability and on the fact that these three mutations well represent typical cellular features of HCM including direct or indirect myofilament calcium sensitisation and destabilisation of the myosin super relaxed state. Therefore, the results generated through this study are expected to improve the understanding of disease pathways in HCM beyond the three specific mutations studied here and will be useful in informing the design of novel disease-specific pharmacological interventions.

7.2 Methods

7.2.1 Experimental characterisation of mutation-specific hypertrophic cardiomyopathy cellular phenotypes

The collection of data presented in this chapter provides a comprehensive description of the current understanding of the mutations under investigation and is used to inform the computational studies presented in the next sections. The experimental data used in this thesis chapter were collected at Toepfer Lab (University of Oxford) by Dr Christopher Toepfer, Dr Yiangos Psaras, and Manuel Schmid M.D., and part of the data presented here has been previously published [9, 34]. I contributed to the analysis of the calcium transient data. Experiments assessed myosin conformations, sarcomere function, and calcium transients in hiPSC-CMs through fluorescent ATP binding assays of

myosin, direct sarcomere tracking, and fluorescence calcium imaging. This combination of dynamic measurements provides key insights into cardiomyocyte pathophysiology in HCM and can inform the therapeutic efficacy and safety of pharmacological compounds. Furthermore, the use of hiPSC-CMs offers the opportunity to generate disease- and patient-specific genotypes, and despite the immaturity of their phenotypes in comparison to adult cardiomyocytes, hiPSC-CMs remain instrumental to providing a human relevant experimental system for cardiovascular research [103, 328, 329].

Details of experimental procedures can be found in Chapter 5 of this thesis and in [9, 34, 330]. Briefly, for calcium data acquisition, the heterozygous pathogenic missense variants *MYH7*$^{R403Q/+}$, *TNNT2*$^{R92Q/+}$, and *TNNI3*$^{R21C/+}$ were introduced using CRISPR/Cas9. Targeted hiPSC subclones were sequenced to confirm the mutant genotype, differentiated into hiPSC-CMs via Wnt pathway modulation, and plated in a 2D assay plate. Details on viral transduction of hiPSC-CMs with RGECO for calcium transient acquisition are reported in Chapter 5. For the acquisition of sarcomere shortening data, fluorescent tags on sarcomere proteins were introduced into isogenic hiPSC-CMs with and without the three variants (generated as described above). For this, GFP (green fluorescent protein) was introduced onto the Z-disc protein titin (TTN-GFP) in hiPSCs as described in [330]. Cells were treated with dimethylsulfoxide (DMSO) or Mavacamten 0.3-3 µM. Mant-ATP assays and analyses were conducted as described in [9] to estimate the abundance of myosins in the super relaxed state SRX and the disordered relaxed state DRX from the double-exponential decay pattern of the fluorescent ATP analogue Mant-ATP chased with nonfluorescent ATP.

To analyse the hiPSC-CMs sarcomere and calcium data, two recently developed rapid phenotyping assays, SarcTrack [330] and CalTrack (Chapter 5 and [34]), were used and provided characterisation of the contractile and calcium profile of isogenic hiPSC-CMs, with and without the three endogenous heterozygous pathogenic variants that cause HCM**.** Statistical analyses were performed as described in Chapter 5.

Literature data has also been reviewed and included to provide additional information on mutation-induced subcellular and cellular primary and secondary remodelling as well as clinical data from mutation-specific patient cohorts.

7.2.2 The in-silico population of human models approach to investigate mutation-specific hypertrophic cardiomyopathy pathophysiology

The computational study presented in this chapter is informed by the experimental hiPSC-CM data obtained as described in the previous section. Although hiPSC-CMs provide an unprecedented opportunity to investigate cardiac pathophysiology, their highly variable structural and functional immaturity with respect to adult cardiomyocytes remains a concern for clinical translation. For this reason, here I present a computational approach to augment and explain experimental data from hiPSC-CMs through in-silico modelling and simulation of human adult cardiomyocytes. As reviewed in Chapter 3, human-based modelling and simulation provides a human-relevant platform to test hypotheses, elucidate mechanisms, and make predictions. In combination with hiPSC-CMs experiments, they represent a step forward in explaining genotype-phenotype relationships in HCM.

This computational approach makes use of in-silico populations of healthy and mutant human cardiomyocytes. These are generated from the single-cell baseline model described in detail in Chapter 4 and then extended in Chapter 6 to model myosin sequestration changes by pathogenic variants and Mavacamten's action.

For the control population of healthy human adult ventricular myocytes, an initial population of 2,000 electromechanical models was created to account for cell-to-cell variability due to different expression levels of the main ion channels/pumps/exchangers [177] and different levels of protein kinase A (PKA)-mediated phosphorylation [331], a main endpoint of the β-adrenergic signalling cascade. This was achieved by sampling the following model parameters: fast and late sodium (GNa and GNaL), transient outward potassium (Gto), rapid and slow delayed rectifier potassium (GKr and GKs), inward rectifier potassium (GK1), sodium-calcium exchanger (GNCX), sodium-potassium pump (GNaK), and the L-type calcium (GCaL) conductances, the sarcoplasmic reticulum calcium release flux (Jrel), the calcium uptake via SERCA (Jrel), calcium sensitivity of SERCA (due to PKA-mediated phosphorylation of phospholamban), intracellular sodium affinity of the sodium-potassium pump (due to PKA-mediated phosphorylation of phospholemman), calcium sensitivity of myofilament (due to PKA-mediated phosphorylation of troponin I), crossbridge cycling rates Kuw, Kws (due to PKA-mediated phosphorylation of myosin binding protein C). Parameters were varied in the range [50-200]% of their baseline value with the Latin Hypercube Sampling technique, apart from the calcium sensitivity of SERCA and intracellular sodium affinity of the sodium-potassium pump, which were varied

in the range [70-130]% of their baseline value based on experimental data [332, 333] and their significant effect on simulated currents. The population of 2,000 models was constructed from the baseline endocardial cell version of the ToR-ORd+Land model [33], as modified in Chapter 6, stimulated at 1Hz pacing for 200 beats. The last 10 beats were saved and then the last beat was used to calibrate the population based on AP, calcium transient (CaT) and active tension data. The following biomarkers were computed and compared with experimental data: AP duration at 40%, 50%, and 90% of repolarisation (APD40, APD50, and APD90); AP triangulation (Tri90-40); maximum upstroke velocity (dV/dtMAX); peak voltage (Vpeak); resting membrane potential (RMP); CaT duration at 50% and 90% decay (CTD50 and CTD90); CaT amplitude (CaT Ampl); Ta duration at 50% and 95% decay (T50off and T95off). Models with biomarkers within experimental ranges were accepted in the calibrated population. Experimental AP recordings from [135, 231], CaT recordings from [58] and active tension recordings from [226-228] were used for calibration as reported in Chapter 4.

From the initial population of 2,000 biophysically-detailed electromechanical models of human adult cardiomyocytes, 348 passed calibration. Figure 7.1 graphically describes the constructed control population. It shows the AP, CaT, and active tension traces of the accepted models (Figure 7.1A) and the histograms of the distribution of the models' biomarkers across the range of allowed values (Figure 7.1B). Accepted models cover most of the experimental range for almost all biomarkers meaning that the constructed population accurately represents physiological variability. The quantification of the correlation between parameters varied in the population (Figure 7.1C) and the

AP, CaT, and active tension biomarkers used for calibration are reported in Figure 7.1D by means of partial correlation coefficients.

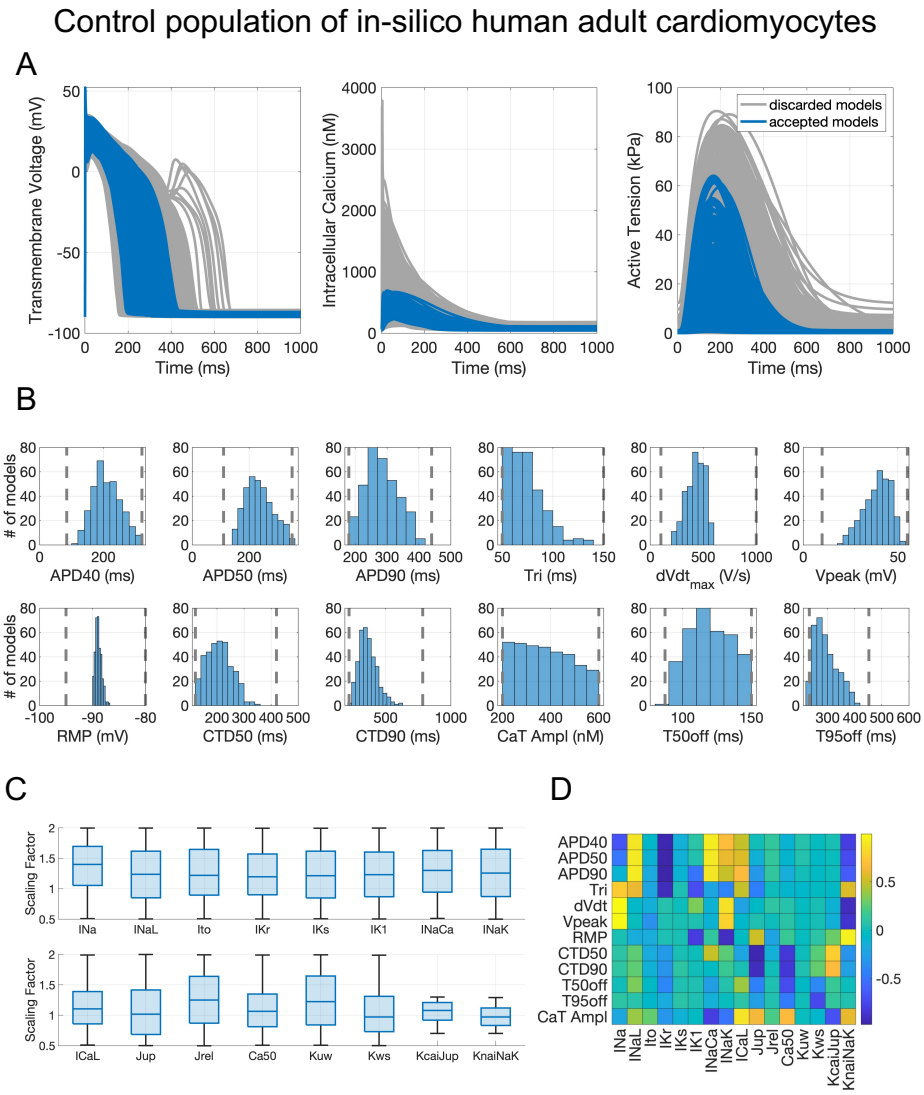

Figure 7.1. Experimentally-calibrated population of control (healthy) human ventricular electromechanical cell models. A: AP, CaT, and active tension traces for cell models accepted in the final control calibrated population (blue) and discarded ones (grey). Initial population of 2,000 models. B: AP, CaT, and active tension biomarker distributions for the 348 models accepted in the control population across the range of allowed values (black dashed lines). Y axes show the number of models for each of the bins. C: Distribution of scaling factors for accepted models' parameters

(KcaiJup and KnaiNaK have been varied in the range [0.7 1.3] of their baseline values whereas the other variables have been varied across the range [0.5 2]). D: Sensitivity analysis for the calibrated population of models, quantifying the correlation between parameters varied in the populations and the AP, CaT, and tension biomarkers used for calibration. The colour scale represents the partial correlation coefficients.

Well-known and previously reported [182] correlations between electrophysiology model parameters and model output are preserved in this population such as between AP duration (APD) and repolarising currents and between voltage peak/upstroke velocity and inward currents. Importantly, we note the role of two contractility model parameters in modulating both electrophysiology and contractility outputs. Calcium sensitivity Ca50 negatively correlated with both calcium and tension duration and positively correlated with calcium amplitude (lower Ca50 values indicate higher calcium sensitivity), and the crossbridge cycling rate Kws is negatively correlated to tension duration. Of note, variations in the sodium sensitivity of the sodium potassium pump KnaiNaK, varied here to represent varying levels of phospholemman phosphorylation, were associated with changes in both the depolarisation and repolarisation of the AP as well as in setting the value of the resting membrane potential.

From the control population, I then constructed three different populations specific to the *MYH7*$^{R403Q/+}$, *TNNT2*$^{R92Q/+}$, and *TNNI3*$^{R21C/+}$ variants. This was achieved, as described in detail in the next sections, by applying a mutation-specific contractile remodelling on the control population, as informed by the experimental data.

7.2.3 Human in-silico trials of Mavacamten

For each mutant population, after characterising the pathophysiological mechanisms underlying its cellular phenotype, I tested its response to the pharmacological therapy Mavacamten. In particular, I compared the populations' responses to 0.5 μM Mavacamten and evaluated the drug efficacy in the context of disease remodelling. I focused on the 0.5 μM Mavacamten because of the availability of data in human myocardium at that concentration [326], and because it lies close to the IC50 value of 0.3 μM for inhibiting myosin ATPase activity in biochemical assays using murine and bovine myosin [81], and registered plasma levels that effectively relieved left ventricular outflow tract obstruction in human clinical trial data [88], as explained before. After drug application I evaluated twitch tension biomarkers and assessed whether they were rescued by the drug.

7.3 Insights into mutation-specific pathophysiological mechanisms and their modulation of Mavacamten's efficacy

7.3.1 The pathogenic β-myosin heavy chain variant MYH7$^{R403Q/+}$

7.3.1.1 Clinical and experimental data

MYH7 mutations were the first to be linked to familial HCM and have been traditionally associated with moderate to severe hypertrophy, high disease penetrance and variable prognosis [334], although phenotypic variability is high. For example, the *MYH7*^{R403Q} mutation is associated with severe disease expression and high penetrance, severe hypertrophy, and high rates of sudden death, whereas the *MYH7*^{V606M} mutation is associated with a less severe

prognosis [334]. While initial in-vitro studies supported the hypothesis that the observed severe phenotype in the *MYH7*^{R403Q} patients was due to a variable decrease in the motor function of myosin, subsequent in-vitro and in-vivo analyses reported that the R403Q mutation leads to a gain in function (as reviewed in [335]). More recent basic science research provided remarkable insights on the molecular mechanisms of disease pathogenesis for *MYH7* mutations showing how they cause hypercontractility by increasing the number of functionally accessible myosin heads [9, 336, 337]. It was shown that they disrupt the physiological balance of myosins in the super relaxed and disordered relaxed state (Figure 7.2) altering cardiomyocyte contraction, relaxation, and metabolism. This is associated with high risks for heart failure and atrial fibrillation [9].

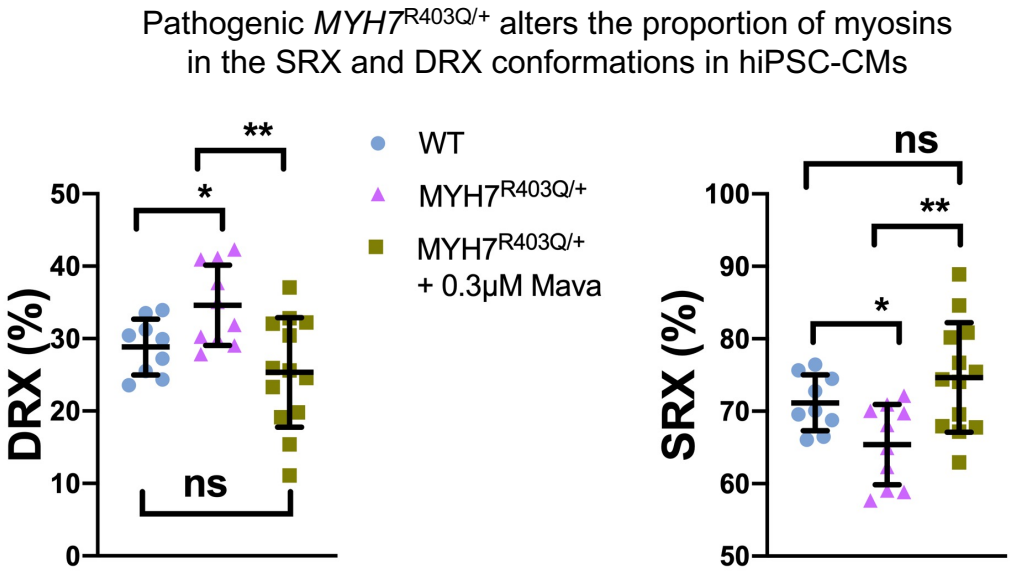

Figure 7.2. Altered proportion of myosins in the SRX and DRX conformations in MYH7$^{R403Q/+}$ hiPSC-CMs and normalisation by Mavacamten. Data from [9].

Experimental data from Dr Christopher Toepfer Lab (used in this thesis) revealed that, hiPSC-CMs harbouring the *MYH7*$^{R403Q/+}$ variant, exhibit increased contractility and prolonged relaxation times when compared to control (Figure 7.3A, first column).

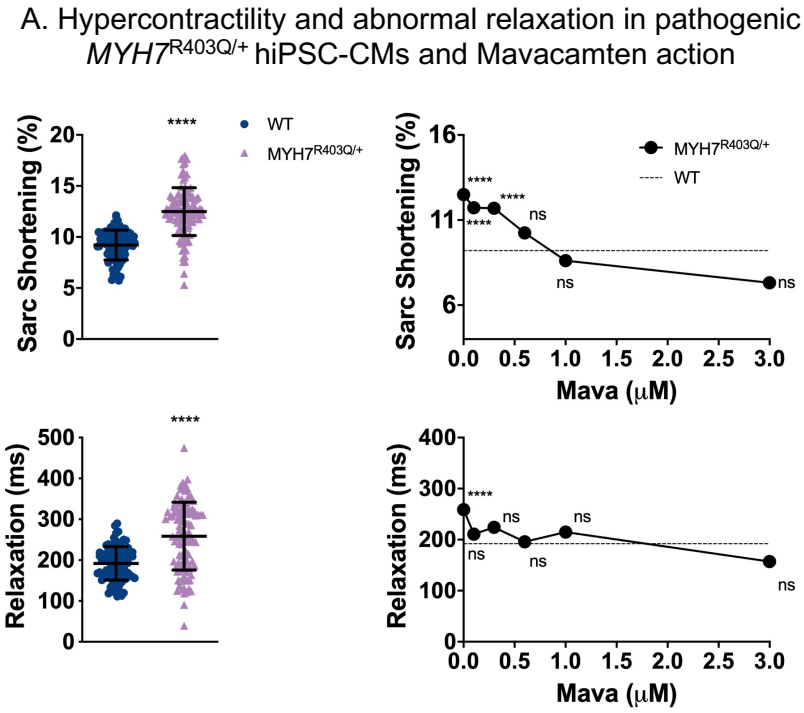

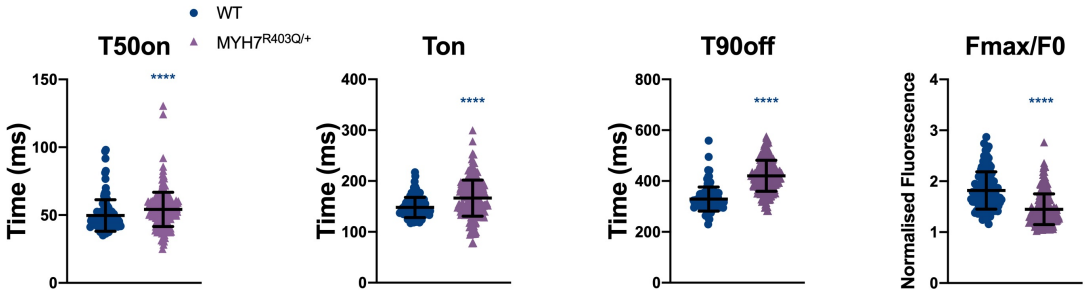

Figure 7.3. Contractile and calcium phenotype of pathogenic MYH7$^{R403Q/+}$ hiPSC-CMs. A: Hypercontractility and abnormal relaxation (first column) in pathogenic MYH7$^{R403Q/+}$ and their response to Mavacamten (second column), data previously published in [9]. B: Prolonged calcium rise and decay in pathogenic MYH7$^{R403Q/+}$.

T50on: time to 50% calcium rise, Ton: time to calcium peak, T90off: time to 90% calcium decay, Fmax/F0: ratio between peak and baseline fluorescence.

Mavacamten treatment corrected the cellular phenotype of the *MYH7*$^{R403Q/+}$ hiPSC-CMs at low doses (Figure 7.3A, second column). As shown in [9], under *MYH7*$^{R403Q/+}$ the amount of myosin in DRX is in fact significantly increased and can be normalised by 0.3 μM Mavacamten (Figure 7.2).

When I analysed the calcium phenotype of the *MYH7*$^{R403Q/+}$ variant (Figure 7.3B), experimental results showed that calcium transients are characterised by prolonged times for calcium rise (time to 50% contraction, T50on, and time to peak, Ton) and decay (time to 90% decay, T90off) in comparison to control. The ratio between fluorescence peak and baseline was lower in *MYH7*$^{R403Q/+}$ compared to control.

7.3.1.2 Computational characterisation of pathophysiological mechanisms

To investigate the mechanisms behind the observed cellular phenotype of the pathogenic β-myosin heavy chain *MYH7*$^{R403Q/+}$ variant, I constructed a *MYH7*$^{R403Q/+}$ population. To achieve this, I introduced a remodelling of R = 1.3 in the control population described in the Section 7.2.2, as consistent with the experimental data [9]. I then compared the mechanical behaviour of the two populations and evaluated their differences against experimental control and *MYH7*$^{R403Q/+}$ hiPSC-CM data. To be able to fully capture the *MYH7*$^{R403Q/+}$ phenotype, in particular the mutation-induced changes in relaxation, I tested the hypothesis that a positive feedback from crossbridge cycling to thin filament activation could explain the significant prolongation in relaxation

observed in the cells carrying the mutation. Specifically, I considered a slower calcium unbinding from troponin triggered by the larger amount of crossbridge cycling, as a myosin-based contribution to thin filament cooperativity.

Figure 7.4A illustrates the changes in tension waveform (for a representative model of the population) and Figure 7.4B in contractility (tension amplitude, TaAmpl) and relaxation (time to 90% decay, T90off) biomarkers that follow from R = 1.3 in the simulated population of 348 human adult cardiomyocytes. A median increase in contractility of ~40% and a median increase in relaxation time of 4% is observed (Figure 7.4B).

While the mutation-induced percentage change in contractility was similar between simulation and experiments, the prolongation of relaxation in simulated cardiomyocytes was only minimal compared to the significant ~35% prolongation observed in hiPSC-CMs. For this reason, I hypothesised that the significant prolongation observed experimentally could be explained by a positive feedback mechanism from crossbridge cycling to thin filament cooperative activation. According to this hypothesis, when a larger amount of crossbridges are cycling, thin filament activation is favoured and slows the release of calcium from troponin, which can significantly prolong tension relaxation. This hypothesis was tested in my model by downscaling the calcium unbinding rate by 60%. These simulations represent a proof of concept for this hypothesised mechanism and, as shown in figure 7.4A&B, can replicate the significant prolongation in tension relaxation if slower calcium unbinding from troponin is considered in the model together with the primary mutation-induced effect on crossbridges availability. As shown in Figure 7.4C, the myosin-based contribution to thin filament activation changes the steady-

state tension-calcium relationship increasing activation at low calcium, as expected.

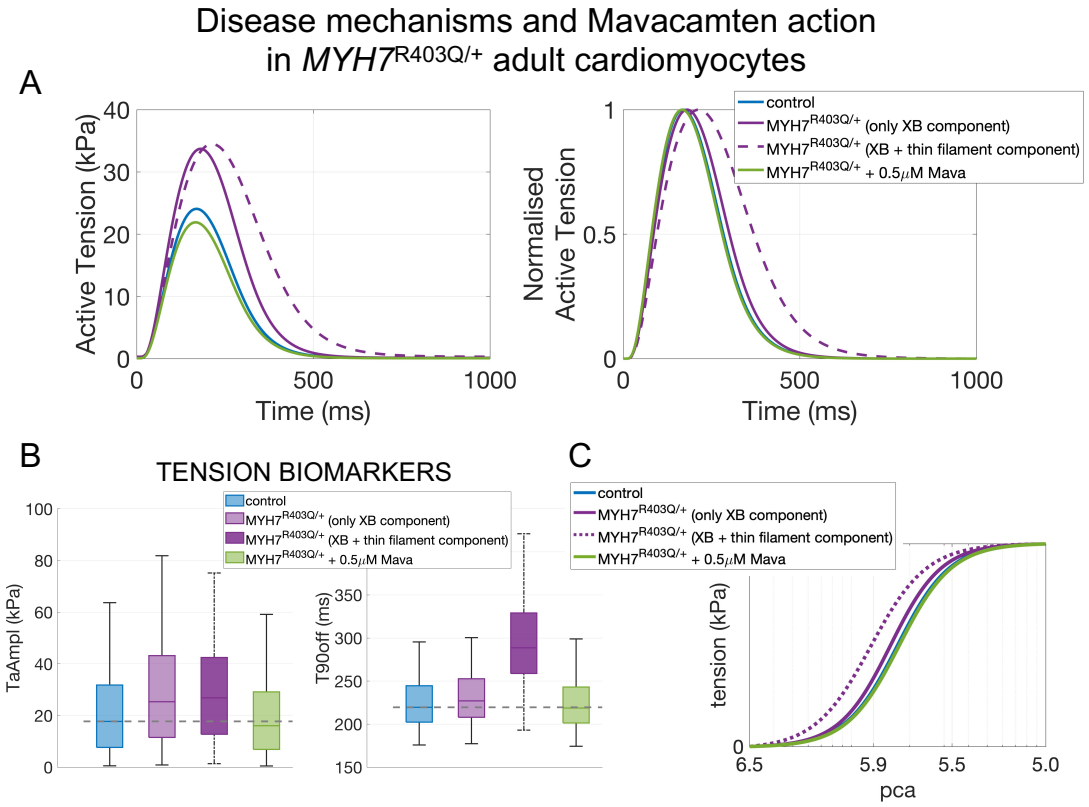

Figure 7.4. Simulation of pathogenic mechanisms in MYH7$^{R403Q/+}$ adult cardiomyocytes and their response to Mavacamten. A&B: Twitch tension response to an experimentally observed increase of myosin DRX:SRX ratio under MYH7$^{R403Q/+}$. Higher DRX:SRX can contribute to the disease phenotype through a 'XB component', i.e. crossbridge availability (solid purple line), and also through a feedback mechanism that involves the thin filament (dashed purple line). The latter is key to explaining diastolic dysfunction in the MYH7$^{R403Q/+}$ variant and modulates the steady-state calcium-tension curve (C). Simulated Mavacamten corrected the hypercontractility and impaired relaxation in MYH7$^{R403Q/+}$ (green) as also shown by the tension biomarkers (tension amplitude and time to 90% decay) reported in panel B.

7.3.1.3 Response to Mavacamten

I simulated the administration of 0.5 μM Mavacamten on the *MYH7*$^{R403Q/+}$ population, evaluated the contractile response to the simulated drug intervention, and compared this to experimental data [9]. The simulation of 0.5 μM Mavacamten was achieved by considering a value of R = 0.8, as extrapolated from the analysis presented in the previous chapter. This was applied in addition to the remodelling induced by the mutation.

Simulated Mavacamten treatment was able to rescue both the hypercontractility and impaired relaxation due to the pathogenic β-myosin heavy chain variant *MYH7*$^{R403Q/+}$ (Figure 7.4A-C, green) in agreement with experiments (Figure 7.3A). This is explained in-silico by Mavacamten's direct effect on crossbridge availability which directly suppresses tension and indirectly deactivates the positive feedback mechanism on thin filament activation. In fact, under Mavacamten, the amount of crossbridge cycling is brought back to normal, and this is sufficient to normalise the myosin-based contribution to thin filament activation thereby restoring cardiac relaxation.

7.3.2 The pathogenic troponin T variant TNNT2$^{R92Q/+}$

7.3.2.1 Clinical and experimental data

TNNT2 mutations are less common than *MYH7* mutations but potentially more dangerous because of malignant arrhythmias. They typically display a mild left ventricular hypertrophy, however *TNNT2* mutation carriers experience higher incidences of premature sudden death [338-340]. In patients who died suddenly and had genetic HCM, those that carried variants in the *TNNT2* gene were on average younger, had less hypertrophy and less fibrosis, but had more

myocardial disarray than those without *TNNT2* mutations [340]. More recently, two studies in a larger number of families carrying *TNNT2* mutations (20 families and 12 mutations [341], and 21 families and 6 different mutations [342]) showed that ventricular hypertrophy is uncommon in children and adolescents and it is absent on echo in an important minority of adult patients, however most adult carriers have an abnormal electrocardiogram [341].

Depending on the specific variant in *TNNT2* the clinical and prognostic profiles varied, with risk significantly higher in the *TNNT2*$^{R92Q/+}$ variant than in other patients [342]. The *TNNT2*$^{R92Q/+}$ mutation has been studied in several model systems [15, 343-346], including feline, rat, rabbit, guinea pig, and transgenic mouse models. However, interspecies differences have often complicated the interpretation of the results and highlighted the need for human-relevant systems. Particularly, disease presentation in mice, a widely studied system, depends on the myosin heavy chain isoform expressed [347]. Mice express alpha MHC in adulthood whereas humans express predominantly beta MHC. Clippinger et al. [14] adopted a human approach to study *TNNT2*^{R92Q} by engineering iPSC-CMs homozygous for the *TNNT2*$^{R92Q/R92Q}$ mutation. They showed that *TNNT2*$^{R92Q/R92Q}$ leads to increased force, power, and contraction speed, reduced intracellular calcium transients, shorter APD, and reduced inward calcium currents compared to wild-type cardiomyocytes. Myosin detachment kinetics or calcium binding affinity of troponin were not affected in their system. They were able to identify the initial biophysical insult of *TNNT2*$^{R92Q/R92Q}$ as increased thin filament activation due to the repositioning of tropomyosin along the thin filament. This can reduce the tropomyosin population in the more inhibitory blocked state while the population of the

closed state is increased, enhancing thin filament activation [14]. Consistent with this, Robinson et al. [348] reported the direct effects of HCM-causing R92Q mutation in troponin T on thin filament calcium affinity. They showed that this HCM causing mutation increases calcium affinity of reconstituted thin filaments and that this change is mediated without altering the calcium affinity of the isolated troponin, in agreement with [14]. They also explained that, since the R92Q mutation in troponin T is present in the extended T1 N-terminal tail of troponin I, it is not predicted to interact directly with the other 2 troponin subunits, and the indirect effect on calcium affinity of the thin filament could happen via altered cooperative activation due to disrupted interactions between the troponin T1 and tropomyosin [348].

Robinson et al. [15] examined the R92Q mutation in troponin T within guinea pig cardiomyocytes transfected with human recombinant troponin T delivered by adenovirus and provided evidence that altered calcium buffering can be directly attributed to the primary effect of the mutation on myofilament calcium affinity. This was because of the short-term transfection model used. They showed that the presence of the calcium-sensitising R92Q mutation doubled the calcium buffering of the myofilaments and had a profound effect on calcium handling. The increased calcium buffering and altered calcium handling is compatible with the increased myofilament peak calcium and delayed release revealed by myofilament-restricted calcium indicators in [283]. They suggested that the increased myofilament calcium affinity directly correlated with increased microdomain calcium.

Experimental data from Dr Christopher Toepfer Lab (used in this thesis) revealed that hiPSC-CMs harbouring the *TNNT2*$^{R92Q/+}$ pathogenic variant

exhibit increased contractility and prolonged relaxation times when compared to control (Figure 7.5A, first column).

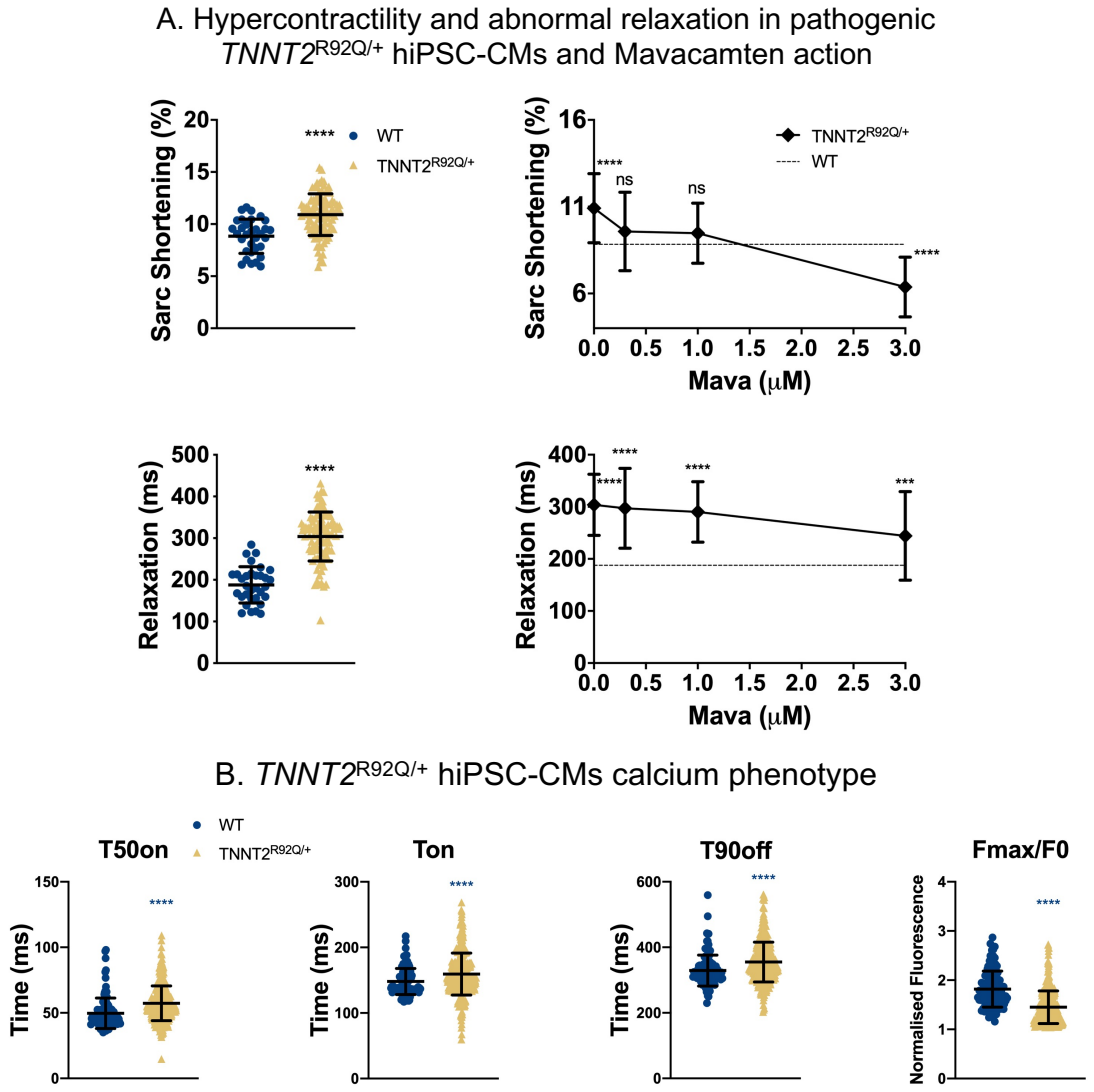

Figure 7.5. Contractile and calcium phenotype of pathogenic TNNT2$^{R92Q/+}$ hiPSC-CMs. A: Hypercontractility and abnormal relaxation (first column) in pathogenic TNNT2$^{R92Q/+}$ and their response to Mavacamten (second column). B: Prolonged calcium rise and decay in pathogenic TNNT2$^{R92Q/+}$. T50on: time to 50% calcium rise, Ton: time to calcium peak, T90off: time to 90% calcium decay, Fmax/F0: ratio between peak and baseline fluorescence.

The hypercontractility of the *TNNT2*$^{R92Q/+}$ variant was corrected at low doses, but the relaxation time was not corrected dose-dependently by Mavacamten (Figure 7.5A, second column). The calcium phenotype of the *TNNT2*$^{R92Q/+}$ variant is reported in Figure 7.5B. The *TNNT2*$^{R92Q/+}$ mutation exhibited prolonged times for calcium rise (time to 50% contraction, T50on, and time to peak, Ton) and decay (time to 90% decay, T90off) in comparison to control. The ratio between fluorescence peak and baseline was lower in *TNNT2*$^{R92Q/+}$ mutations compared to control.

7.3.2.2 Computational characterisation of pathophysiological mechanisms

My investigation of the mechanisms behind the observed cellular phenotype of the pathogenic troponin T *TNNT2*$^{R92Q/+}$ mutation was guided by the findings reported in [14, 15, 283] on abnormal tropomyosin positioning and altered calcium buffering, as described in the previous section.

To estimate the relative contribution of both abnormal tropomyosin positioning and altered calcium buffering on the observed contractile phenotype in *TNNT2*$^{R92Q/+}$, I conducted a sensitivity analysis where the reverse rate constant that defines K_B (for tropomyosin positioning) in our baseline mechanical model and the parameter Ca50 that regulates calcium buffering by myofilaments were varied one at a time. K_B represents the equilibrium constant between the blocked and closed tropomyosin states [14]. Specifically, the reverse rate constant that defines K_B was varied in the range [0.4 - 0.85] x baseline value and Ca50 was varied in the range [0.6 - 0.85] x baseline value. From this analysis, an average remodelling in the two model parameters, leading to an increase in contractility in the baseline electromechanical model similar to

experimental data, was determined as representative of the average remodelling under *TNNT2*$^{R92Q/+}$. I applied the average remodelling to the control healthy population described in Section 7.2.2 to study the pathophysiological consequences of this mutant remodelling in the context of physiological electromechanical variability.

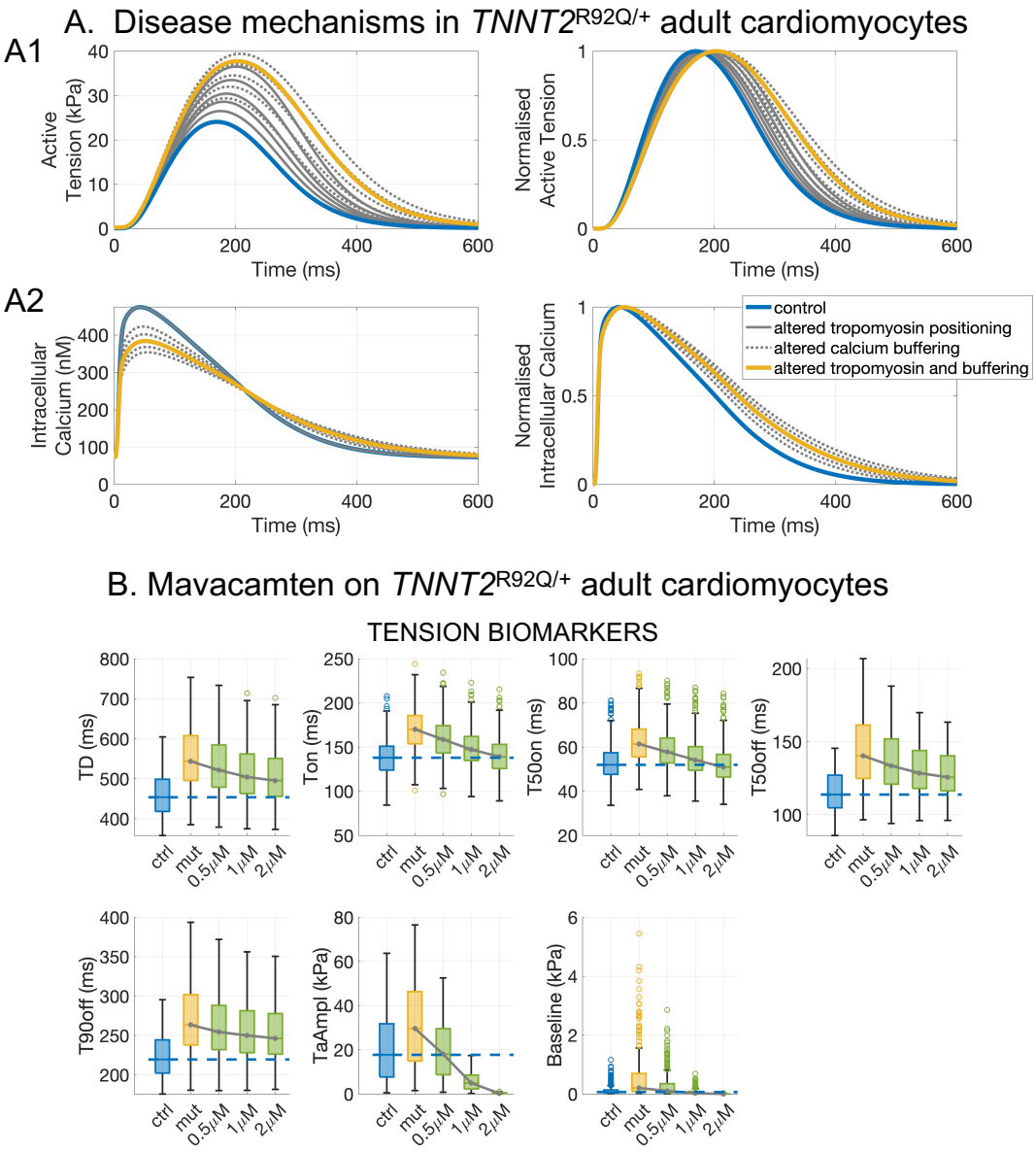

Figure 7.6. Simulation of pathogenic mechanisms in TNNT2$^{R92Q/+}$ *adult cardiomyocytes and their responses to Mavacamten. A1&A2: Comparison of the*

effects of abnormal tropomyosin positioning and increased calcium buffering on active tension (A1) and intracellular calcium (A2). Altered tropomyosin (solid grey lines) is achieved by scaling the reverse rate constant that defines K_B in the range [0.4 - 0.85] x baseline value. Altered calcium buffering (dotted grey lines) is achieved by scaling the Ca50 parameter in the range [0.6 - 0.85] x baseline value. Yellow lines represent the chosen average remodelling in the two model parameters, leading to an increase in contractility in the baseline electromechanical model similar to experimental data. B: Simulated contractile response of TNNT2$^{R92Q/+}$ to 0.5, 1, and 2 μM *Mavacamten.*

Figure 7.6A illustrates the effect of the *TNNT2*$^{R92Q/+}$-induced alteration in tropomyosin positioning and calcium buffering on simulated active tension (Figure 7.6A1) and intracellular calcium (Figure 7.6A2).

As previously shown by Clippinger et al. [14], these results confirm that the alteration of tropomyosin positioning alone can account for the hypercontractility that is observed experimentally (Figure 7.5A). However, to capture an impaired relaxation as an additional component of the phenotype, an increase in calcium buffering due to the indirect mutation-induced sensitisation of myofilaments [15, 283, 348] had to be considered in our simulations. Both altered tropomyosin positioning and calcium buffering contributed to increased tension amplitude, whereas impaired relaxation was predominantly induced by increased calcium buffering which also slowed the decay of the CaT and lowered its amplitude (Figure 7.6A2). The impaired tension relaxation observed here correlates with the hypercontracted sarcomere length of guinea pig cardiomyocytes under the R92Q mutation in troponin T reported in [15, 283]. The abnormalities observed in CaT (Figure 7.6A2) are compatible with the experimental hiPSC-CM calcium data (Figure

7.5B). Clippinger et al. [14] also observed a lower calcium transient amplitude. A prolonged cytosolic calcium transient decay was also observed in [15, 283], although the calcium amplitude was unchanged. Such a discrepancy between animal and hiPSC-CM data may be explained by the additional calcium handling remodelling observed in animal studies that may not be present in hiPSC-CMs due to their immature phenotype.

From the sensitivity results on the relative contribution of tropomyosin positioning and calcium buffering in determining abnormal calcium and contractility under *TNNT2*$^{R92Q/+}$ (Figure 7.6A), I selected an average mutant remodelling (Ca50 x 0.7, and rate constant that defines K_B x 0.8) consistent with the reported increase in contractility under this mutation, and applied it to the control population to generate a *TNNT2*$^{R92Q/+}$ population. The tension kinetics biomarkers and tension amplitude and baseline of the *TNNT2*$^{R92Q/+}$ population are compared to control biomarker values in Figure 7.6B. We observe a significant prolongation in all kinetics biomarkers and an increase in tension peak and baseline.

7.3.2.3 Response to Mavacamten

I simulated the contractile response of the *TNNT2*$^{R92Q/+}$ population to 0.5, 1, and 2 μM Mavacamten (corresponding to R = 0.8, 0.5, and 0.2), according to the estimated dose-response curve.

A dose-dependent decrease in tension amplitude, baseline and all kinetics biomarkers were observed in the simulated response of *TNNT2*$^{R92Q/+}$ adult cardiomyocytes to increasing doses of Mavacamten (Figure 7.6B). However, while tension amplitude was significantly reduced and restored to control

values at 0.5 μM Mavacamten, this drug intervention was unable to recover the impaired relaxation, as consistent with the hiPSC-CM experimental data (Figure 7.5A).

7.3.3 The pathogenic troponin I variant TNNI3$^{R21C/+}$

7.3.3.1 Clinical and experimental data

Penetrance of *TNNI3* mutations is highly heterogeneous, ranging major disease-related complications to mild symptoms. These can include severe restrictive physiology, severe biventricular hypertrophy and marked apical hypertrophy [349]. In particular, the *TNNI3*$^{R21C/+}$ mutation has been reported to cause malignant HCM with early sudden cardiac death even in the absence of hypertrophy [307]. *TNNI3*$^{R21C/+}$ is the only identified HCM-associated mutation located at the cardiac-specific N terminus of cardiac troponin I and since it was first reported [350] it has been the subject of several in vitro and in vivo studies. Wang et al. [294] and Dweck et al. [310] reported that this mutation prevented PKA-mediated phosphorylation in transgenic mice, and adult heterozygous and homozygous mutant mice developed a remarkable degree of cardiac hypertrophy and fibrosis. Isolated cardiac myocytes from mutant mice older than 12 months of age displayed significantly delayed calcium transient decay and relaxation [310]. It was also shown by Cheng et al. [351] that the R21C mutation in troponin I increases calcium binding of cardiac troponin and the affinity of cardiac troponin C for cardiac troponin I in solution, showing increases in the calcium sensitivity of myofibril tension development, and also prolonged early slow phase of relaxation. PKA mediated reductions in the

affinity of cardiac troponin C for cardiac troponin I and in the calcium sensitivity of tension is blunted in the R21C variant [351].

Experimental data from Dr Christopher Toepfer Lab (used in this thesis) revealed that hiPSC-CMs harbouring *TNNI3*$^{R21C/+}$ pathogenic variant exhibit increased contractility and prolonged relaxation times when compared to control (Figure 7.7A, first column). In *TNNI3*$^{R21C/+}$ hiPSC-CMs hypercontractility and prolonged relaxation were corrected only at the highest tested dose (Figure 7.7A, second column).

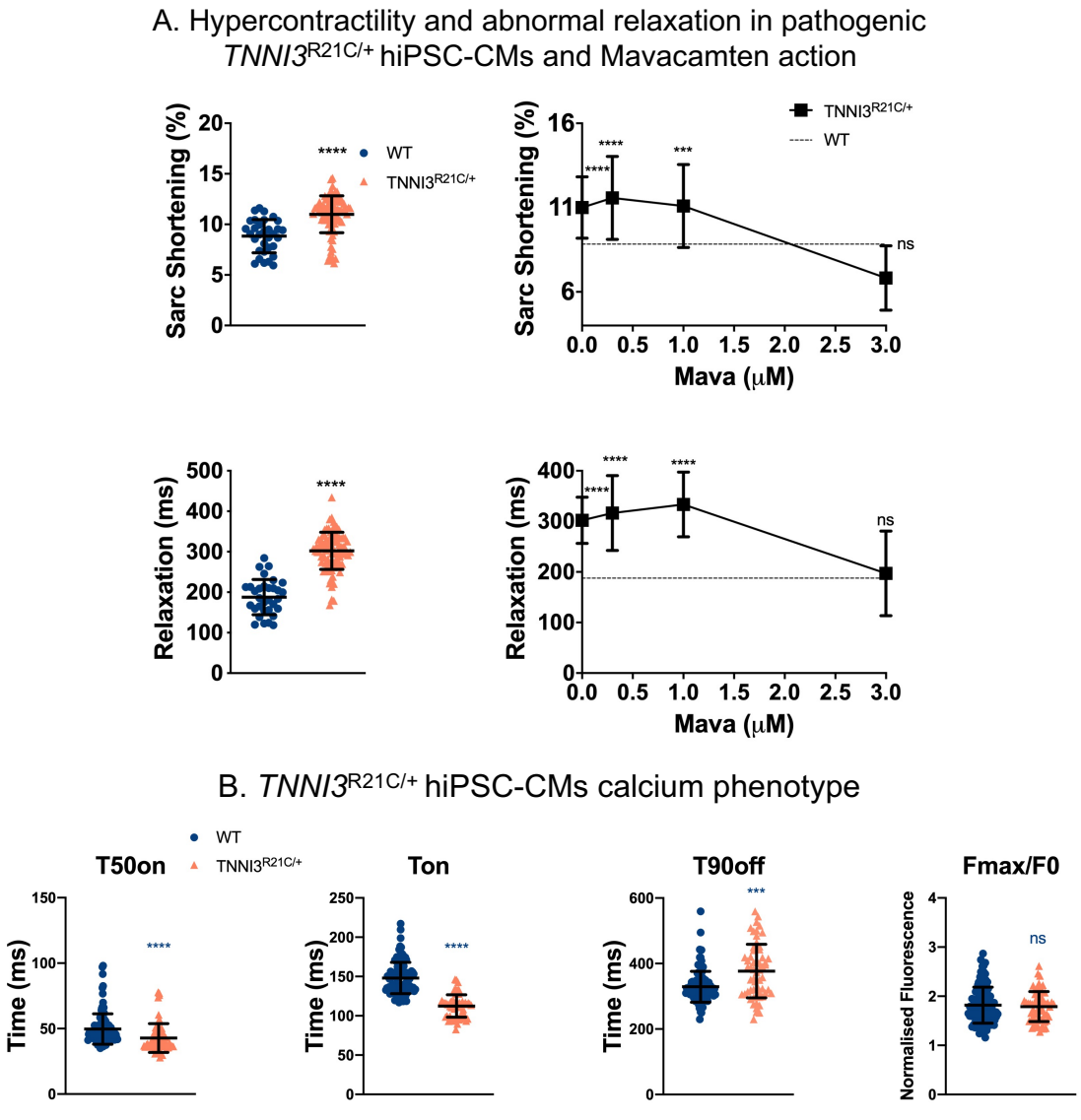

Figure 7.7. Contractile and calcium phenotype of pathogenic TNNI3$^{R21C/+}$ hiPSC-CMs. A: Hypercontractility and abnormal relaxation (first column) in pathogenic TNNI3$^{R21C/+}$ and their response to Mavacamten (second column). B: Shorter calcium rise and prolonged decay in pathogenic TNNI3$^{R21C/+}$. T50on: time to 50% calcium rise, Ton: time to calcium peak, T90off: time to 90% calcium decay, Fmax/F0: ratio between peak and baseline fluorescence. Data previously published in [34].

Thus, while Mavacamten could rescue the increased contractility for all three mutations and therefore independently of the genotype, its effectiveness in reversing the impaired relaxation seemingly depended on the underlying genetic defect.

The calcium phenotype of the *TNNI3*$^{R21C/+}$ variant is reported in Figure 7.7B. Interestingly the *TNNI3*$^{R21C/+}$ mutation share the same prolonged calcium transient decay as the *MYH7*$^{R403Q/+}$ and *TNNT2*$^{R92Q/+}$ mutations, but it also experiences a shorter time to peak (Ton) and time to 50% contraction (T50on). The ratio between fluorescence peak and baseline was not altered in *TNNI3*$^{R21C/+}$.

7.3.3.2 Computational characterisation of pathophysiological mechanisms

The investigation of the pathogenic mechanisms in *TNNI3*$^{R21C/+}$ is guided by the biophysical evidence presented in [351]. I hypothesised that the observed cellular phenotype of accelerated calcium rise and decelerated decay, hypercontractility, and prolonged relaxation (illustrated in the previous section and Figure 7.7) could be caused by altered calcium-troponin C interactions and tested this hypothesis computationally. Similar to the troponin T mutation, I have first conducted a sensitivity analysis to determine how model

parameters related to calcium-troponin binding affected the rise and decay of calcium transients. Specifically, I considered the Ca50 parameter that describes the binding of calcium to troponin and the unbinding rate of calcium from troponin (koff). Ca50 was varied in the range [0.5 - 0.7] x baseline value, and koff was varied in the range [0.4 - 0.6] x baseline value.

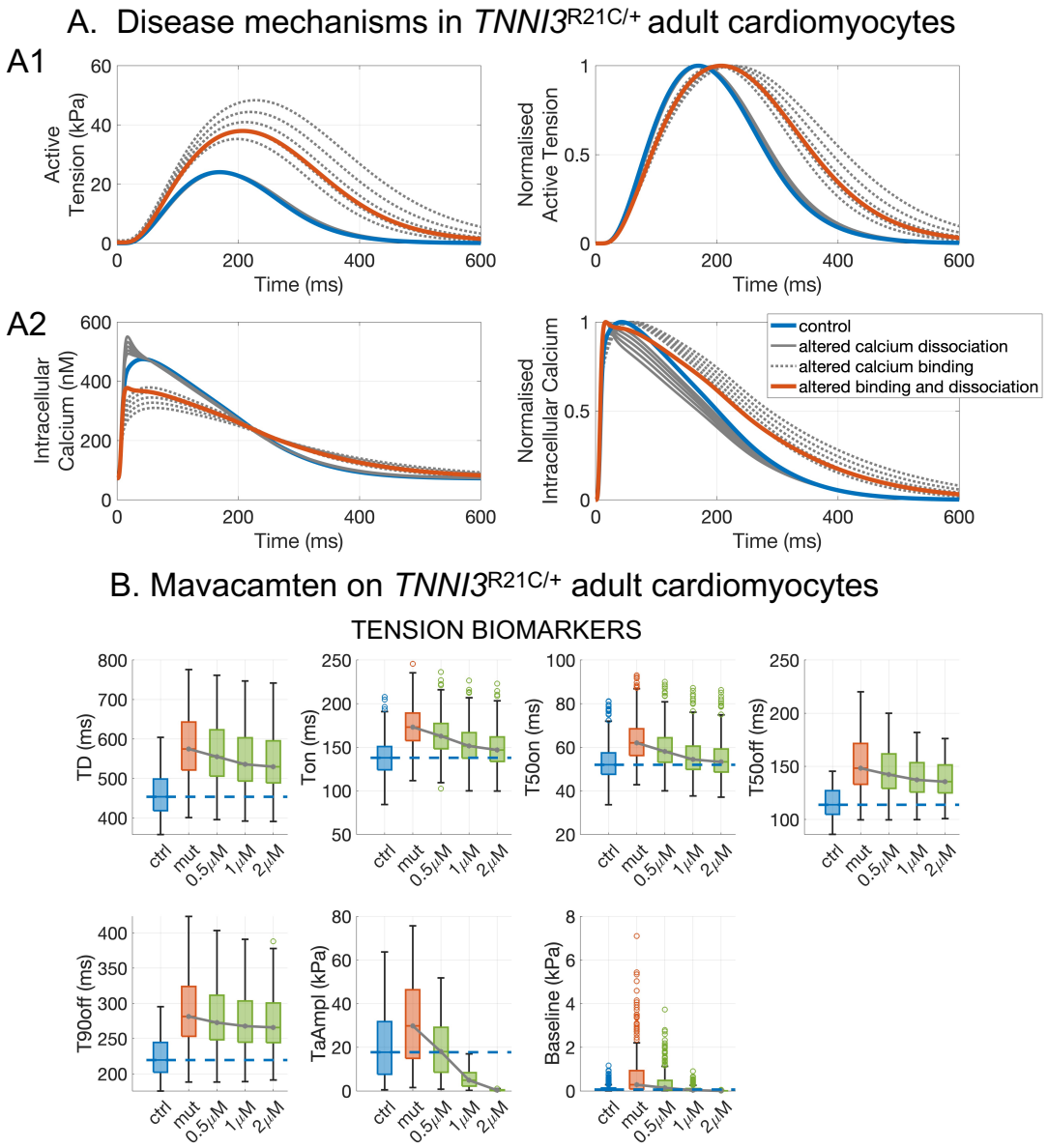

Figure 7.8. Simulation of pathogenic mechanisms in TNNI3$^{R21C/+}$ adult cardiomyocytes and response to Mavacamten. A1&A2: Comparison of the effects of abnormal calcium

binding and dissociation from troponin on active tension (A1) and intracellular calcium (A2). Altered calcium dissociation (solid grey lines) is achieved by scaling the koff parameter in the range [0.4 - 0.6] x baseline value. Altered calcium binding (dotted grey lines) is achieved by scaling the parameter Ca50 in the range [0.5 - 0.7] x baseline value. Red lines represent the chosen average remodelling in the two model parameters, leading to an increase in contractility in the baseline electromechanical model similar to experimental data. B: Simulated contractile response of TNNI3$^{R21C/+}$ to 0.5, 1, and 2 μM *Mavacamten.*

An average remodelling, leading to changes in calcium and contractility similar to those observed experimentally, was determined and applied to the control population described in Section 7.2.2 to study the pathophysiological consequences of the *TNNI3*$^{R21C/+}$ mutation in the context of physiologically relevant electromechanical variability.

Figure 7.8A illustrates the effect of the *TNNI3*$^{R21C/+}$-induced alteration in calcium binding/dissociation from troponin on simulated active tension (Figure 7.8A1) and intracellular calcium (Figure 7.8A2). As previously shown by Cheng et al. [351], our results confirm that abnormal calcium-troponin interactions can lead to the experimentally observed calcium and contractile phenotype.

In particular, to be able to fully capture the calcium phenotype of faster rise and slower decay (Figure 7.7B), both calcium binding and dissociation from troponin had to be taken into account (Figure 7.8A2). This increased myofilament calcium sensitivity in-silico led to the hypercontractile and slowed relaxation phenotype that had been observed experimentally (Figure 7.7A). Similar to the troponin T variant, an average remodelling of calcium binding

(Ca50 x 0.65) and dissociation (koff x 0.5) from troponin under *TNNI3*$^{R21C/+}$ was chosen so that it replicates the increase in contractility observed experimentally, and was then applied to the control population to construct the *TNNI3*$^{R21C/+}$ population. The tension kinetics biomarkers and tension amplitude and baseline of the *TNNI3*$^{R21C/+}$ population are compared to control biomarker values in Figure 7.8B. We observe a prolongation in all kinetics biomarkers and an increase in tension peak and baseline.

7.3.3.3 Response to Mavacamten

I simulated the contractile response of the *TNNI3*$^{R21C/+}$ population to 0.5, 1, and 2 μM Mavacamten (corresponding to R = 0.8, 0.5, and 0.2), according to the estimated dose-response curve.

This led to a dose-dependent decrease in tension amplitude, baseline and all kinetics biomarkers (Figure 7.8B). Normalisation of sarcomere shortening in hiPSC-CMs was only observed at the highest Mavacamten dose, while 0.5 and 1 μM Mavacamten did not produce a significant effect. This discrepancy with simulation results could be attributed to the variability in the stoichiometry of drug to target, i.e. the amount of drug per myosin molecule may vary depending on the amount of myosin present in the dish, thereby affecting the effective drug dose in a given dish. This may explain why we observe an effect of Mavacamten only from the 1 μM concentration in *TNNI3*$^{R21C/+}$ experiments.

As per the troponin T mutation, while simulated tension amplitude was significantly reduced and restored to control values already at 0.5 μM Mavacamten, this drug intervention was unable to recover the impaired relaxation, as shown in the hiPSC-CM experimental data (Figure 7.7A).

7.3.4 Comparison of Mavacamten's efficacy on MYH7$^{R403Q/+}$ TNNT2$^{R92Q/+}$ and TNNI3$^{R21C/+}$ variants.

Finally, I compared the efficacy of 0.5 μM Mavacamten on the three different variants (Figure 7.9A) and explained the results in the context of mutation-specific remodelling. The simulations showed that while Mavacamten was highly effective in rescuing both the hypercontractility and impaired relaxation due to the pathogenic *MYH7*$^{R403Q/+}$ mutation, it could only correct some aspects of the disease phenotypes of *TNNT2*$^{R92Q/+}$ and *TNNI3*$^{R21C/+}$. Particularly, by reducing the number of available myosin heads that interact with actin, Mavacamten could reduce contractility (tension amplitude or sarcomere shortening) significantly and independently to the source of the hypercontractility. In *MYH7*$^{R403Q/+}$ higher crossbridge recruitment is mediated by a destabilisation of the SRX state; in *TNNT2*$^{R92Q/+}$ the observed hypercontractility is a combination of altered tropomyosin positioning and indirect calcium sensitisation of the myofilament; and in *TNNI3*$^{R21C/+}$ higher calcium affinity of troponin mediates increased calcium buffering and hypercontractility.

The results presented in this chapter show that Mavacamten's mode of action is highly effective in correcting the abnormal crossbridge recruitment in all these mutations despite being generated through different pathways. On the contrary, in the simulations, Mavacamten could only correct diastolic dysfunction when this was driven by increased levels of crossbridge cycling and subsequent myosin-based contribution to thin filament activation, as observed for the *MYH7*$^{R403Q/+}$ mutation. This drug intervention could not fully correct the diastolic insufficiency that is caused by a direct or indirect calcium

sensitization of myofilaments which is particularly deleterious for diastolic dysfunction (Figure 7.9B).

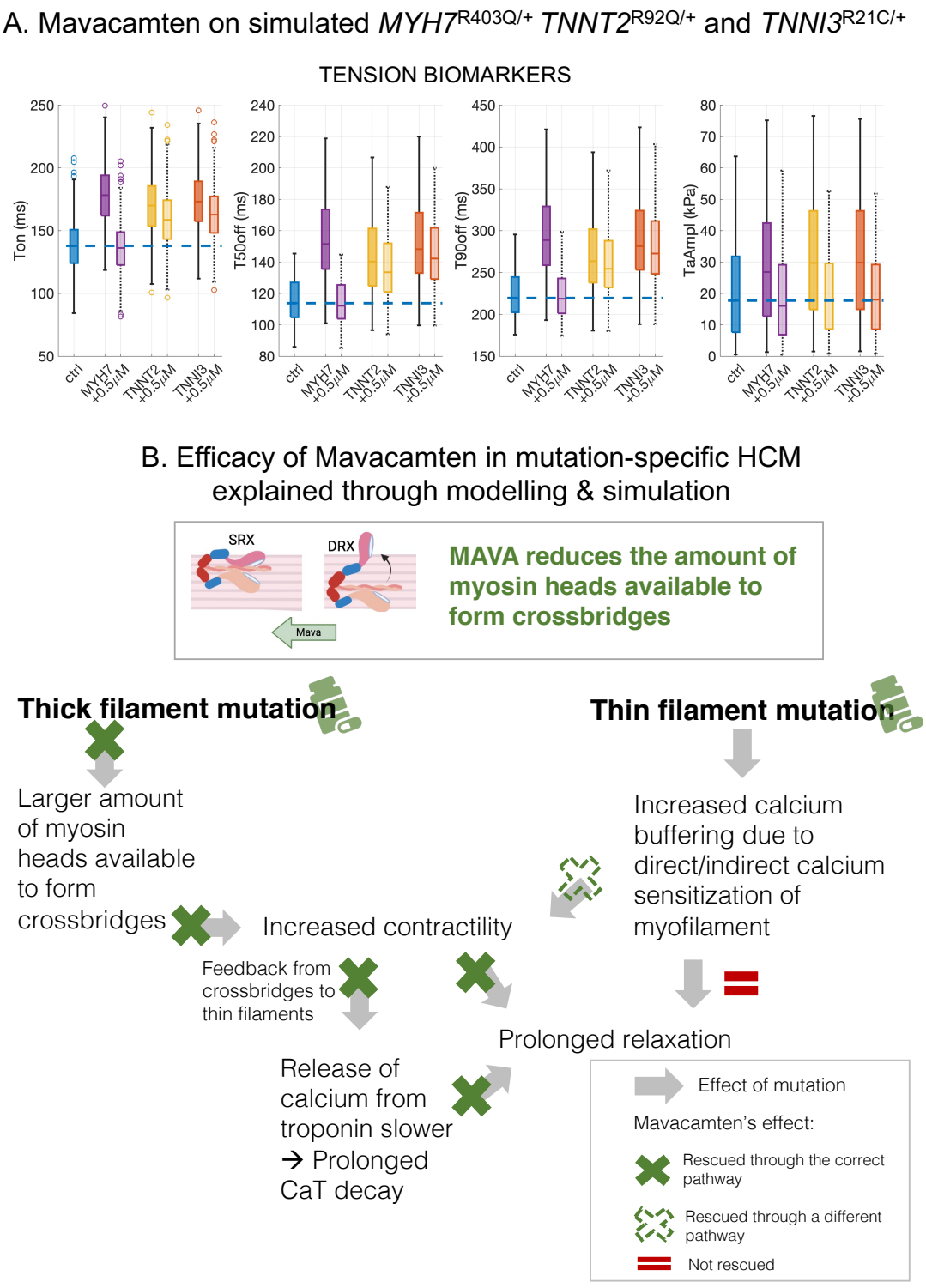

Figure 7.9. Mavacamten's efficacy A: Comparison of Mavacamten's efficacy on simulated control, MYH7$^{R403Q/+}$, TNNT2$^{R92Q/+}$, and TNNI3$^{R21C/+}$ cardiomyocytes.

Tension biomarkers are reported for each mutation before and after application of 0.5 μM Mavacamten (R = 0.8). B: Proposed explanation for the differential efficacy of Mavacamten based on disease pathways. Mavacamten's mode of action is reported at the top of panel B (myosin SRX/DRX diagram reproduced from [47], under Open Access Licence). Mutation-induced effects on cardiac contractility and relaxation are reported in grey. Mavacamten-induced effects on mutant cardiac contractility and relaxation are reported in green/red.

7.4 Discussion

In this thesis chapter, I present an experimentally-informed computational characterisation of the *MYH7*$^{R403Q/+}$, *TNNT2*$^{R92Q/+}$, and *TNNI3*$^{R21C/+}$ HCM-causing mutations' pathophysiology and their response to the pharmacological action of Mavacamten. Through a human-based multiscale approach, where drug-induced subcellular changes are linked to cellular biomarkers of cardiac electromechanical function, I identify the key mutation-specific mechanisms responsible for the observed disease phenotypes and evaluate the efficacy of Mavacamten in mutation-specific HCM.

I present a collection of novel and published data that comprehensively describe the current understanding of the mutations under investigation. Particularly, the hiPSC-CM experimental results presented here show that all three mutations exhibit very similar contractile profiles, quantified as sarcomere shortening and relaxation times. However, their contractile response under Mavacamten depend on the specific genotypes. The three mutations also share a similar calcium transient phenotype characterised by prolonged time to calcium rise and decay, except for the *TNNI3*$^{R21C/+}$ mutation that experiences a faster calcium rise.

I hypothesised that the *MYH7*$^{R403Q/+}$, *TNNT2*$^{R92Q/+}$, and *TNNI3*$^{R21C/+}$ mutations do not share the same pathogenic mechanisms and the similar phenotypes of hypercontractility and diastolic dysfunction may derive from abnormal crossbridge recruitment due different underlying disease pathways, explaining the different responses to Mavacamten. Particularly, based on biophysical evidence, I hypothesised that pathogenic mechanisms involve myosin SRX destabilisation for the thick filament variant [9], whereas abnormal myofilament calcium sensitivity may be critical for thin filament variants [14, 15, 351]. I use human modelling and simulations to test this hypothesis and explain Mavacamten's efficacy in the context of mutation-specific remodelling.

This study demonstrates how similar HCM phenotypes can be generated through different pathways with profound effects on the efficacy of the pharmacological intervention Mavacamten. Specifically, I found that: (i) the regulation of crossbridge availability by SRX under mutation or Mavacamten significantly modulates cellular contractility, independently of underlying mechanisms, with minimal effect on cellular relaxation; (ii) diastolic dysfunction under unstable SRX is explained by a positive crossbridge-based contribution to thin filament activation that favours prolonged calcium binding to troponin and can be reversed by Mavacamten; (iii) direct and indirect myofilament calcium sensitisation is a key determinant of impaired myofilament relaxation and Mavacamten has limited efficacy on it.

The successful integration of biophysically detailed information on human cardiac pathophysiology in computational modelling and simulation frameworks facilitates and augments basic science investigations of cardiac function and disease mechanisms [19-23, 121, 145, 157]. Such tools have

been particularly helpful for the evaluation of the cardiac safety and efficacy of new or existing therapeutic interventions through human in-silico drug trials [27, 29, 33, 207]. Here, I integrated experimental findings of calcium and sarcomere shortening obtained in hiPSC-CMs into the modelling and simulation framework of ventricular electromechanics presented in Chapter 4 and 6 to provide a mechanistic link between biophysically-detailed descriptions of thin filament kinetics and crossbridge cycling, affected by sarcomeric HCM mutations, and cellular electrophysiology in adult human cardiomyocytes. This model provides extended capabilities to concurrently investigate and replicate action potential, calcium dynamics and force generation features, in line with experimental data [33].

hiPSC-CMs can capture patient-specific genotype-phenotype relationships and recapitulate expected pharmacological responses [329], thus providing an unprecedented opportunity to investigate human cardiac pathophysiology and drug action . However, their highly variable structural and functional immaturity with respect to adult cardiomyocytes remains a concern for clinical translation. For this reason, I here augmented and explained experimental data from hiPSC-CMs through in-silico models of human adult cardiomyocytes. In combination with hiPSC-CM experiments, they represent a step forward in explaining genotype-phenotype relationships in HCM and hold great preclinical and translational potential.

As illustrated in Chapter 6, to be able to simulate different pathogenic mechanisms and the pharmacological action of Mavacamten, I first developed and embedded a model of myosin sequestration and release by SRX in the computational model of cardiomyocyte electromechanical function presented

in Chapter 4 [33]. Here, I used the generated model to further investigate the pathogenic mechanism of the *MYH7*$^{R403Q/+}$ mutation. It was recently shown that the primary mode by which this mutation causes hypercontractility is by decreasing the SRX population and increasing the number of heads functionally available for interaction with actin [9, 50, 337]. I generated a control and *MYH7*$^{R403Q/+}$ population of cardiomyocytes to account for cell-to-cell physiological variability in model predictions. When the same change in myosin SRX as observed in hiPSC-CM experiments was integrated in the control population to generate the *MYH7*$^{R403Q/+}$ cardiomyocytes, the expected increase in cellular contractility as quantified through active tension peak was observed. This further proves that even in the context of underlying electrophysiological and contractile variability a reduction in the SRX population generates hypercontraction by increasing the amount of crossbridge cycling.

The associated prolongation in relaxation was only minimal in our simulations in disagreement with experiments [9]. However, the observed prolongation was recovered by considering a crossbridge-based feedback mechanism to thin filament activation. Specifically, by considering a slower calcium unbinding from troponin triggered by the larger amount of crossbridges cycling. It was previously shown that calcium binding to troponin is dependent on active tension generated by attached crossbridges [352, 353], and unbinding of calcium from troponin C is known to be essential for thin filament deactivation and a significant determinant of relaxation [354]. The results presented here suggest that higher crossbridge cycling is not a significant determinant of diastolic dysfunction per se, but it can trigger secondary mechanisms that

prevent myofilament relaxation by prolonging thin filament activation. Upon Mavacamten application, whose effect was here simulated as a shift in DRX:SRX towards SRX, the amount of crossbridge cycling was brought back to normal terminating the induced thin filament activation, thereby promoting relaxation. Simulation results are in agreement with the experimental data showing that Mavacamten effectively correct the hypercontractility and diastolic dysfunction observed under thick filament mutations [9, 10, 81, 355]. In particular, the simulations support the effectiveness of the drug Mavacamten in normalising cardiac contractility. This is demonstrated through my simulations of the think filament mutation *MYH7*$^{R403Q/+}$ but also the thin filament mutations *TNNT2*$^{R92Q/+}$ and *TNNI3*$^{R21C/+}$ despite the differences in the underlying pathophysiology. In other words, reducing the amount of crossbridge cycling by myosin sequestration in SRX is a potent mechanism that can correct altered crossbridge recruitment generated through different pathways. This is in agreement with the reported efficacy of this drug in clinical trials for obstructive HCM that is observed independently of patient genotype [79]. However, simulations also showed that to salvage diastolic dysfunction a more tuned pharmacological intervention should be adopted that takes into account patients' genotype. In fact, while Mavacamten could rescue the impaired relaxation of *MYH7*$^{R403Q/+}$ by targeting its underlying pathophysiological mechanism (i.e. larger availability of crossbridges), it could not entirely rescue the diastolic dysfunction caused by thin filament mutations that directly or indirectly sensitise the thin filament to calcium. The shortening of relaxation under Mavacamten for these mutations was only partial. This is in agreement with the hiPSC-CM data presented in this thesis.

This study also showed that both thin filament mutations considered in this thesis alter calcium sensitivity of myofilaments. This is however achieved through different mechanisms. The *TNNT2*$^{R92Q/+}$ mutation is structurally distant from the calcium binding sites in the troponin complex, therefore it is thought that it sensitises myofilament calcium binding via alterations to cooperative communication [348]. Indeed, the calcium affinity of the troponin complex is not altered by the mutation [14, 348]. The *TNNT2*$^{R92Q/+}$ mutation has been studied in several model systems [15, 343-346], yet interspecies differences have often complicated the interpretation of the results. Using a humanised system, Clippinger et al. [14] identified the initial biophysical insult of *TNNT2*$^{R92Q/+}$ in the increased thin filament activation due to repositioning of tropomyosin along the thin filament. This can reduce the tropomyosin population in the more inhibitory blocked state while the population of the closed state is increased, enhancing thin filament activation. The simulation results presented here agree with [14] in that the hypercontractility observed in *TNNT2*$^{R92Q/+}$ can be ascribed to abnormal tropomyosin positioning along the thin filament. However, this study also showed that indirect calcium sensitisation of myofilament is a key determinant of observed diastolic dysfunction and calcium transient abnormalities [15, 283]. Myofilament calcium sensitivity was here identified as the most important contributor to impaired myofilament relaxation. Previously, increased myofilament calcium has been observed in in-vitro studies with recombinant mutant proteins, HCM mouse models, and in human cardiac tissue obtained from HCM patients [60-62, 348]. It is recognised as an important cellular hallmark of HCM that alters force development and myofilament relaxation. Enhanced myofilament calcium

sensitivity was also shown to be a mechanism for pause-dependent calcium-triggered arrhythmias [356].

The *TNNI3*$^{R21C/+}$ hiPSC-CMs exhibited faster calcium transient rises and prolonged transient decays, with hypercontractility and impaired relaxation. This study showed that the calcium transient abnormalities are primary consequences of abnormal calcium binding to troponin C. Previous reports showed that the *TNNI3*$^{R21C/+}$ mutation increases calcium binding of cardiac troponin and the affinity of cardiac troponin C for cardiac troponin I in solution, increases the calcium sensitivity of myofibril tension development, and also prolongs relaxation [351]. Simulation results confirmed that the abnormal calcium transient phenotype observed in hiPSC-CMs could be ascribed to altered calcium-troponin binding. Interestingly, I found that to be able to fully capture the observed calcium phenotype (both the faster calcium rise and slower decay), not only the binding properties of calcium to troponin had to be affected but also the kinetics of the troponin buffer, in particular the unbinding rate of calcium from troponin. Altered binding and dissociation of calcium generated higher calcium buffering in-silico, thus causing higher crossbridge recruitment and hypercontraction. Tension relaxation was also prolonged, and calcium sensitivity of force production increased, in agreement with experiments [351]. Hence, this work suggests that the disease phenotype observed in *TNNI3*$^{R21C/+}$ hiPSC-CMs is caused by a multifactorial remodelling of binding and dissociation of calcium from troponin, as a primary consequence of the mutation, leading to altered contractility and relaxation.

The study on HCM pathophysiology conducted in this thesis is focused on the earliest stages of the disease and aims at unravelling the alterations that

appear first, decoupling them from compensatory responses that may develop at later stages. Elucidating the primary changes induced by sarcomeric mutations associated with HCM in human adult cardiomyocytes can explain the chain of events that lead to chronic phenotypes. This information is particularly relevant for the development of effective pharmacological interventions. In this regard, the use of hiPSC-CMs is a great advantage, as they provide a model to unravel early human pathophysiology in a dish [357, 358], overcoming the limitation of poor availability of heart-tissue samples, particularly at early stages of disease development, but also in the chronic stages. Long term effects of HCM mutations have been reported and studied in patient myectomy samples. These have shown profound contractile and electrophysiological abnormalities [58, 82, 359]. It was proposed that sarcomeric mutations may cause a primary sustained increase in intracellular calcium with multiple mechanisms triggering a complex remodeling process involving alterations of calcium/calmodulin kinase II (CaMKII). Increased phosphorylation of CaMKII downstream targets may be responsible for the abnormalities observed in HCM cardiomyocytes and further contribute to abnormal calcium handling, thus setting up a vicious cycle [58]. I here showed that calcium abnormalities, although triggered by different mechanisms, are common in different mutations and may account for the sustained increase in intracellular calcium that drives remodelling. Also, the hypercontractile phenotype observed in the computational and experimental models of early disease pathogenesis presented in this thesis may drive hypertrophic remodelling. It was proposed that cellular tension alters mechanosensitive signalling pathways in cardiomyocytes, and alterations in

tension correlate with the hypertrophic response [360, 361]. This study also provides mutation-specific explanations for the reported diastolic dysfunction, another well-known hallmark of HCM.

Mavacamten is the first pharmacological intervention specifically developed to target HCM pathophysiology. In preclinical and clinical studies, treatment with Mavacamten was highly effective and improved exercise capacity, left ventricular outflow tract obstruction, New York Heart Association functional class, and health status in patients with obstructive HCM [79]. An extensive characterisation of the effects of Mavacamten on human myocardium is yet to be performed, and the exact mechanisms through which it restores contractile function remain to be fully understood. Available evidence shows that Mavacamten consistently reduces maximal force production [50, 81, 326, 327, 355]. Recent evidence also supports the positive impact of Mavacamten on diastolic function [326, 327]. However, compared to force reduction, the effect of Mavacamten on myocardial relaxation is less clear, and different mechanisms may be involved. Awinda et al. [326] reported faster cross-bridge detachment under Mavacamten. The simulations presented here and previous studies [87, 283] suggest that the improvement of relaxation under Mavacamten could be mediated by thin filament dynamics. In this study, Mavacamten action has been modelled according to the most established hypothesis that this drug stabilises the SRX and reduces the number of myosin heads that can interact with actin. I have not considered other proposed mechanisms of action, such as a faster crossbridge detachment [326] or a direct effect of Mavacamten on myofilament calcium sensitivity [87]. I nevertheless was able to report most of the changes in cardiac cellular

contractility and relaxation observed experimentally under Mavacamten action. Not considering those aspects may explain why the simulations did not show the potential beneficial effect on thin filament mutations shown in [87], where a partial reversal of the increased calcium sensitivity due to thin filament mutation was reported. They also showed a correction of altered calcium flux at the myofilaments by Mavacamten. However, this seems to disagree with the hiPSC-CM data reported in this thesis, showing the persistence of sarcomere relaxation abnormalities under Mavacamten. This simulation study supports the hiPSC-CM findings and attributes the impaired relaxation to myofilament calcium sensitisation. This cannot be corrected by Mavacamten unless considering a direct effect of the drug on calcium sensitivity. Differences between the experimental systems can also explain the discrepancies.

Finally, I acknowledge that the developed phenomenological model of myosins sequestration and release by SRX, as they occur under thick filament mutations or Mavacamten's action, do not account for the full complexity of the system and its related dynamics. Previous studies have developed more detailed models of myosin SRX or OFF state [141, 154], although they did not provide a coupled description of human contractility and electrophysiology as in the model presented here. Despite the simplifications, the model constructed in this thesis allowed the simulation and modulation of cardiac contraction by crossbridge availability in the context of human ventricular electromechanical function. The extended capability of this model to concurrently investigate and replicate action potential, calcium dynamics and force generation features, in line with experimental data will be key for future

investigations involving multiscale chronic contractile and electrophysiological remodelling from the cell to organ level.

In conclusion, this study showcases the potential of combining stem cell technology with mechanistic modelling to unearth direct mechanistic explanations of phenotypes driven by different HCM mutations, which can then be used to evaluate pharmacological efficacy for personalised therapy. Unearthing mechanistic pathways in mutation-specific HCM is key to develop effective therapies for a wide variety of mutations. It allows for an efficacy-informed segregation of patients in optimal therapy choice and the design of clinical trials, maximising trial success while minimising patient risk and the elevated costs associated to trial failure due to limited efficacy.

8 Conclusions

8.1 Summary of the thesis

Drug safety and efficacy varies widely across the population. Predicting drug-induced effects on cardiac function, including potentially lethal arrhythmias and heart failure, is especially complex. Lack of efficacy and cardiotoxicity are major reasons for which a drug does not proceed to clinic or is withdrawn from the market. Therefore, they represent both a safety and a pre-clinical development efficiency concern.

The safety and therapeutic efficacy of pharmacological interventions are modulated by several factors including genetic background, disease, gender, age, and lifestyle. The need for a human-relevant approach that provides mechanistic predictions and an understanding of drug safety and efficacy in the context of inter-subject variability is evident.

Human-based computational methodologies have already begun to prove their potential in this regard. This has been possible thanks to the last six decades of research that led to the integration of biophysically detailed information on human cardiac pathophysiology into human-relevant computational modelling and simulation frameworks. At the basic science level, this has facilitated and augmented mechanistic investigations of cardiac function and disease, paving the way for a new era of personalised care in cardiovascular medicine. Population- and patient-specific cardiac modelling and simulation offer the

opportunity to define the optimal therapy choice for each individual patient, which can be extended to patient populations.

This approach is especially relevant for the development and administration of pharmacological therapies in inherited cardiomyopathies, for which a mechanistic understanding of drug action and its modulation by cardiac pathophysiology are still largely unknown. HCM, a common inherited cardiomyopathy, is an emblematic example where pharmacological treatment is often required, yet it is based on the empirical use of drugs that do not target disease pathophysiology. Despite accumulating evidence showing that HCM pathophysiology and response to treatment depend on the underlying genotype, the use of this information in clinical decision making is still limited. Thus, defining key mechanisms in genetic cardiomyopathies due to specific genetic mutations would provide essential insights for the development and administration of novel effective pharmacological interventions that are patient specific.

This thesis addressed the challenges mentioned above, by reviewing the relevant literature, and investigating cardiac electromechanical alterations caused by drugs and HCM. This was achieved through the development of novel human-based computational methodologies. First, a novel in-silico human electromechanical ventricular modelling and simulation framework was developed. Mechanistic simulations were conducted to assess drug-induced pro-arrhythmia and inotropic risk in healthy cardiac function. Next, a novel software tool was developed to provide automated high-throughput analysis of calcium transients in cardiomyocytes. This was used to phenotype primary and

induced pluripotent stem cell-derived cardiomyocytes under pharmacological action and HCM variants. Then, the modelling and simulation framework was extended to include representation of myosin super relaxed and disordered relaxed states. This was used to investigate the influence of these conformations on cardiomyocyte contractility and relaxation in response to pathogenic variants and the pharmacological compound Mavacamten. Finally, a computational investigation into the pathophysiology of three different HCM-causing mutations and their response to Mavacamten was conducted.

These computational methodologies enabled mechanistic investigations that contribute towards a better understanding of how cardiac electromechanical substrates are affected by disease and pharmacological action.

8.2 Key contributions and main findings

The first main contribution of this thesis is the development of a novel in-silico human electromechanical ventricular modelling and simulation framework that provides extended capabilities to concurrently simulate transmurally-heterogenous action potentials, calcium dynamics, and force generation features, in line with experimental data. Mechanistic simulations with the novel framework enabled the prediction of inotropic responses of different multichannel action reference compounds. This work provides a human-based platform for the simultaneous mechanistic assessment of electrophysiological and contractile effects of drug action in human cardiac function, thus addressing an unmet need in preclinical drug development. This work was published in [33].

The second main contribution of this thesis is the development of the freely available software CalTrack for the analysis of cellular calcium transients from many cellular formats in an automated, un-biased, and rapid way. Investigating how calcium transients change dynamically within cardiac cells is key to understanding cardiomyocyte physiology, pathology, and the therapeutic efficacy and safety of pharmacological therapies. CalTrack addresses an unmet need for higher throughput calcium screening assays, and was developed with the aim of providing the cardiac biology community a critical resource for accelerating experimentation in physiology, pathology, and therapeutic screening. CalTrack also facilitates the availability of large quantities of high-quality data needed for computational studies into cardiac pathophysiology and drug action. This work was published in [34], where I share first authorship with Dr Yiangos Psaras. My contribution to this work is related to: (i) the development of the mathematical basis of CalTrack, (ii) the experimental data analysis with CalTrack and statistical analysis with Prism software, and (iii) the design and the writing of the journal publication.

The third main contribution of this thesis is the identification of key mutation-specific mechanisms responsible for the HCM cellular phenotypes of three different genetic mutations: *MYH7*$^{R403Q/+}$, *TNNT2*$^{R92Q/+}$, and *TNNI3*$^{R21C/+}$, in β-myosin heavy chain, troponin T, and troponin I, respectively. By using mechanistic modelling and simulation, in this thesis I demonstrated that the shared phenotypes of hypercontractility and diastolic dysfunction is likely derived from abnormal crossbridge recruitment due to different underlying disease pathways. Particularly, in *MYH7*$^{R403Q/+}$ hypercontractility was driven by the increased number of crossbridges cycling due to the reduced myosin

population in SRX. Diastolic dysfunction under unstable SRX was instead explained by a positive crossbridge-based contribution to thin filament activation that favoured prolonged calcium binding to troponin. This study also suggested that both thin filament mutations altered calcium sensitivity of myofilaments. The hypercontractility observed in *TNNT2*$^{R92Q/+}$ could be ascribed to abnormal tropomyosin positioning along the thin filament, but indirect calcium sensitisation of the myofilament was the key determinant of the observed diastolic dysfunction and calcium transient abnormalities. The disease phenotype in *TNNI3*$^{R21C/+}$ was caused by a multifactorial remodelling of binding and dissociation of calcium from troponin, as a primary consequence of the mutation, leading to altered contractility and relaxation.

The mechanistic explanations of disease pathways in specific HCM pathophysiology unravelled in this thesis can therefore contribute towards the development and delivery of personalised therapies, where a patient's genotype can be used to guide therapeutic targeting.

The final contribution of this thesis is the mechanistic explanation of Mavacamten's efficacy in mutation-specific HCM cardiomyocytes. The exact mechanisms that govern the cellular effects of Mavacamten, a promising novel drug developed to target HCM pathophysiology, are incompletely understood, and a deeper understanding is needed to guide effective and safe patient-specific therapy. In this thesis, Mavacamten's action was simulated as a modulation of crossbridge availability by the myosin ratio DRX:SRX. The regulation of crossbridge availability by SRX under Mavacamten significantly modulated cellular contractility, independently of the underlying mechanisms, with minimal effects on cellular relaxation. This confirmed the beneficial effect

of Mavacamten observed in clinical trials for obstructive HCM. The diastolic dysfunction under unstable SRX could be reversed by Mavacamten through a reduction of crossbridges cycling. However, Mavacamten had limited efficacy on restoring the increased myofilament calcium sensitivity that was directly or indirectly modulated by thin filament mutations. Simulations suggested that a more targeted approach should be adopted to address thin filament mutation pathophysiology.

These findings contribute towards a better identification of those patients who will benefit the most from specific pharmaceutical interventions. Moreover, the development of a translationally-relevant model of Mavacamten's action in the context of disease-specific mechanisms can be an important tool in drug development, where human-relevant models are needed to improve efficacy assessments.

8.3 Future Directions

This thesis presents novel computational methodologies to investigate the complex interplay between the electrical and mechanical activity of cardiac function in health and HCM, and its modulation by drug action.

The study on HCM pathophysiology conducted in this thesis was focused on the earliest stages of the disease. However, long term effects of HCM mutations [58, 82], including profound contractile and electrophysiological abnormalities, have also been reported and studied in patient myectomy samples. I plan to expand the study presented here to investigate the relationship between the reported long-term remodelling and the mutation-specific disease pathways identified in this thesis. The goal of this study will

be to elucidate the key contributions to long-term remodelling and effective targets that, if pharmacologically modulated, would rescue the profound alterations of electromechanical function observed in HCM cardiomyocytes from patient myectomy samples. This will be achieved through the simulation of distinct time points during disease development, from the early to the chronic phase, to inform on the progression of electromechanical abnormalities in HCM, as done in [145] for post-myocardial infarction. This study will specifically focus on the role of increased myofilament calcium sensitivity and diastolic calcium, which can be caused by different mutations as highlighted in this thesis, on chronic electrophysiological remodelling and arrhythmogenesis.

I also plan to expand the computational investigation on the efficacy of Mavacamten in mutation-specific HCM to conduct whole-heart simulations and explain the clinical outcome of this pharmacological therapy. This study will exploit the computational framework developed in our group for the simulation of clinical electrocardiograms and pressure-volume loops [145, 192] using patient-specific anatomical models, in which I will integrate the HCM cellular models developed in this thesis. Here, simulated clinical output of disease-specific treatments will be evaluated against clinical endpoints. Specifically, I am interested in studying how unstable myosin SRX and altered myofilament calcium sensitivity translate into clinically relevant biomarkers of cardiac function and if pharmacological therapy can restore clinical phenotypes. This study will inform the identification of electromechanical signatures underlying a positive response to treatment in distinct patient subgroups. This will contribute to a mechanistic segregation of patients to inform optimal therapy choice and clinical trial design.

Appendix I. Summary table for comparisons of currently available software for calcium transient assessments

Table A.1. Comparisons of currently available software for calcium transient assessments.

Method	Measurement parameters	Advantages	Limitations	Aimed at	Ref.
SIMA	Extraction of Ca^{2+} traces only	Motion correction, optional manual ROI editing	Parameter analysis dependent on external packages	Two-photon imaging of neuronal Ca^{2+}	Kaifosh et.al [311]
FluoroSNNAP	Peak magnitude, inter-peak interval, baseline, time to 50% peak, decay time, cell-to-cell synchronisation	Can analyse single cells and temporal network patterns	Manual input for ROI selection required	Neuronal Ca^{2+} / irregular Ca^{2+} characterisation	Patel et.al. [312]
NeuroCa	Peak magnitude, inter-peak interval, frequency, cell-to-cell propagation mapping	Baseline drift correction		Neuronal Ca^{2+} / irregular Ca^{2+} characterisation	Jang et.al. [313]
PeakCaller	Frequency, time to peak, time to baseline, synchronisation index, peak location, normalised peak height	Versatility of peak character, detrend facility	No inbuilt trace extraction from video microscopy, dependent on user for peak recognition	Neuronal Ca^{2+} / irregular Ca^{2+} characterisation	Artimovich et.al. [314]
ClampFit	Any temporal and magnitude parameter defined by the user, decay constant	Versatility of application	Intensive manual input, no automation	Electrophysiology traces, irregular trace characterisation	Commercial source

Excel-based analysis	Decay constant, absolute Ca^{2+} concentration, baseline, peak magnitude		Intensive manual input, requirement of Visual Basic for Applications	Cardiac Ca^{2+} / regular Ca^{2+} characterisation	Greensmith et.al. [320]
CytoSeer	Frequency, peak magnitude, normalised area under the curve, duration of 25%, 50%, 75% and 90% of peak magnitude, time to peak and 50% decay	Baseline drift correction, separation of sub-cellular compartment transients, filtering of non-excitable cells and aberrant traces	Manual input for thresholding, proprietary	Cardiac Ca^{2+} / regular Ca^{2+} characterisation	Cerignoli et.al. [317] and McKeithan et.al. [316]
AxoGraph	Any temporal and magnitude parameter defined by the user	Graphical interface	No automation, manual measurement of all parameters individually	Any trace in graph form	Commercial source
Automated contractility/ Ca^{2+} MATLAB code	Ca^{2+} trace extraction, unspecified Ca^{2+} temporal parameters, temporal correlation to contractile profile	Additional contractility assessment, user-friendly interface, open source, applicable to single/multiple cells	Independent calcium analysis unavailable	Cardiac contractility & Ca^{2+}, standard Ca^{2+} characterisation	Huebsch et al. [318]
MATLAB code	Diastolic and systolic calcium values, amplitude, relaxation time, shape analysis	Open source, automated cell segmentation, signal and shape analysis	Limited number of calcium parameters, no arrhythmic Ca^{2+} waves analysis	Quantitative analysis, relationships between Ca^{2+} signalling and cell morphology characterisation	Amanfu et al. [321]
IonOptix IonWizard & MultiCell HTS	Trace acquisition, measurement of baseline, including multiple parametric outputs.	Enables filtering and transient averaging, high throughput with MultiCell HTS	Proprietary, software only available with equipment	Cardiac Ca^{2+} / regular Ca^{2+} characterisation	Commercial source
MATLAB ISA	Peak fluorescent signal	Robust, tuneable cell segmentation	No Ca^{2+} characterisation	Non-excitable cells / irregular Ca^{2+} patterns	Wong et.al. [319]

Bibliography

1. Stevens, J.L. and T.K. Baker, *The future of drug safety testing: expanding the view and narrowing the focus.* Drug Discov Today, 2009. **14**(3-4): p. 162-7.
2. Laverty, H., et al., *How can we improve our understanding of cardiovascular safety liabilities to develop safer medicines?* Br J Pharmacol, 2011. **163**(4): p. 675-93.
3. Onakpoya, I.J., C.J. Heneghan, and J.K. Aronson, *Post-marketing withdrawal of anti-obesity medicinal products because of adverse drug reactions: a systematic review.* BMC Med, 2016. **14**(1): p. 191.
4. Ferdinandy, P., et al., *Definition of hidden drug cardiotoxicity: paradigm change in cardiac safety testing and its clinical implications.* Eur Heart J, 2019. **40**(22): p. 1771-1777.
5. Gintant, G.A., *Preclinical Torsades-de-Pointes screens: advantages and limitations of surrogate and direct approaches in evaluating proarrhythmic risk.* Pharmacol Ther, 2008. **119**(2): p. 199-209.
6. Mellor, H.R., et al., *Cardiotoxicity associated with targeting kinase pathways in cancer.* Toxicol Sci, 2011. **120**(1): p. 14-32.
7. Cecchi, F., B. Tomberli, and I. Olivotto, *Clinical and molecular classification of cardiomyopathies.* Glob Cardiol Sci Pract, 2012. **2012**(1): p. 4.
8. Spudich, J.A., *Three perspectives on the molecular basis of hypercontractility caused by hypertrophic cardiomyopathy mutations.* Pflugers Arch, 2019. **471**(5): p. 701-717.
9. Toepfer, C.N., et al., *Myosin Sequestration Regulates Sarcomere Function, Cardiomyocyte Energetics, and Metabolism, Informing the Pathogenesis of Hypertrophic Cardiomyopathy.* Circulation, 2020. **141**(10): p. 828-842.
10. Toepfer, C.N., et al., *Hypertrophic cardiomyopathy mutations in MYBPC3 dysregulate myosin.* Sci. Transl. Med., 2019. **11**(eaat199).
11. Hastings, R., et al., *Combination of Whole Genome Sequencing, Linkage, and Functional Studies Implicates a Missense Mutation in Titin as a Cause of Autosomal Dominant Cardiomyopathy With Features of Left Ventricular Noncompaction.* Circ Cardiovasc Genet, 2016. **9**(5): p. 426-435.
12. Jiang, H., et al., *Functional analysis of a gene-edited mouse model to gain insights into the disease mechanisms of a titin missense variant.* Basic Res Cardiol, 2021. **116**(1): p. 14.
13. McNamara, J.W., et al., *MYBPC3 mutations are associated with a reduced super-relaxed state in patients with hypertrophic cardiomyopathy.* PLoS One, 2017. **12**(6): p. e0180064.
14. Clippinger, S.R., et al., *Mechanical dysfunction of the sarcomere induced by a pathogenic mutation in troponin T drives cellular adaptation.* J Gen Physiol, 2021. **153**(5).
15. Robinson, P., et al., *Hypertrophic cardiomyopathy mutations increase myofilament Ca(2+) buffering, alter intracellular Ca(2+) handling, and stimulate Ca(2+)-dependent signaling.* J Biol Chem, 2018. **293**(27): p. 10487-10499.
16. Tardiff, J.C., et al., *Targets for therapy in sarcomeric cardiomyopathies.* Cardiovasc Res, 2015. **105**(4): p. 457-70.

17. Ommen, S.R., et al., *2020 AHA/ACC Guideline for the Diagnosis and Treatment of Patients With Hypertrophic Cardiomyopathy: A Report of the American College of Cardiology/American Heart Association Joint Committee on Clinical Practice Guidelines.* J Am Coll Cardiol, 2020. **76**(25): p. e159-e240.
18. Wijnker, P.J.M. and J. van der Velden, *Mutation-specific pathology and treatment of hypertrophic cardiomyopathy in patients, mouse models and human engineered heart tissue.* Biochim Biophys Acta Mol Basis Dis, 2020. **1866**(8): p. 165774.
19. Clancy, C.E. and Y. Rudy, *Linking a genetic defect to its cellular phenotype in a cardiac arrhythmia.* Nature, 1999. **400**(6744): p. 566-9.
20. Pueyo, E., et al., *Characterization of QT interval adaptation to RR interval changes and its use as a risk-stratifier of arrhythmic mortality in amiodarone-treated survivors of acute myocardial infarction.* IEEE Trans Biomed Eng, 2004. **51**(9): p. 1511-20.
21. Xie, Y., et al., *Slow [Na]i Changes and Positive Feedback Between Membrane Potential and [Ca]i Underlie Intermittent Early Afterdepolarizations and Arrhythmias.* Circ Arrhythm Electrophysiol, 2015. **8**(6): p. 1472-80.
22. Paci, M., et al., *Phenotypic variability in LQT3 human induced pluripotent stem cell-derived cardiomyocytes and their response to antiarrhythmic pharmacologic therapy: An in silico approach.* Heart Rhythm, 2017. **14**(11): p. 1704-1712.
23. Zhou, X., et al., *Investigating the Complex Arrhythmic Phenotype Caused by the Gain-of-Function Mutation KCNQ1-G229D.* Front Physiol, 2019. **10**: p. 259.
24. Sarkar, A.X. and E.A. Sobie, *Quantification of repolarization reserve to understand interpatient variability in the response to proarrhythmic drugs: a computational analysis.* Heart Rhythm, 2011. **8**(11): p. 1749-55.
25. Grandi, E. and M.M. Maleckar, *Anti-arrhythmic strategies for atrial fibrillation: The role of computational modeling in discovery, development, and optimization.* Pharmacol Ther, 2016. **168**: p. 126-142.
26. Yang, P.C., et al., *In silico prediction of drug therapy in catecholaminergic polymorphic ventricular tachycardia.* J Physiol, 2016. **594**(3): p. 567-93.
27. Passini, E., et al., *Human In Silico Drug Trials Demonstrate Higher Accuracy than Animal Models in Predicting Clinical Pro-Arrhythmic Cardiotoxicity.* Front Physiol, 2017. **8**: p. 668.
28. Viceconti, M., et al., *In silico trials: Verification, validation and uncertainty quantification of predictive models used in the regulatory evaluation of biomedical products.* Methods, 2021. **185**: p. 120-127.
29. Yang, P.C., et al., *A Computational Pipeline to Predict Cardiotoxicity: From the Atom to the Rhythm.* Circ Res, 2020. **126**(8): p. 947-964.
30. Zeigler, A.C., et al., *Network model-based screen for FDA-approved drugs affecting cardiac fibrosis.* CPT Pharmacometrics Syst Pharmacol, 2021. **10**(4): p. 377-388.
31. Rodriguez, B., et al., *Human-based approaches to pharmacology and cardiology: an interdisciplinary and intersectorial workshop.* Europace, 2016. **18**(9): p. 1287-98.
32. Corral-Acero, J., et al., *The 'Digital Twin' to enable the vision of precision cardiology.* Eur Heart J, 2020. **41**(48): p. 4556-4564.
33. Margara, F., et al., *In-silico human electro-mechanical ventricular modelling and simulation for drug-induced pro-arrhythmia and inotropic risk assessment.* Prog Biophys Mol Biol, 2021. **159**: p. 58-74.
34. Psaras, Y., et al., *CaITrack: High Throughput Automated Calcium Transient Analysis in Cardiomyocytes.* Circ Res, 2021.

35. Calvert, J.W. and D.J. Lefer, *Chapter 6 - Overview of Cardiac Muscle Physiology*, in *Muscle*, J.A. Hill and E.N. Olson, Editors. 2012, Academic Press: Boston/Waltham. p. 57-66.
36. Schwarzwald, C.C., J.D. Bonagura, and W.W. Muir, *Chapter 3 - The Cardiovascular System*, in *Equine Anesthesia (Second Edition)*, W.W. Muir and J.A.E. Hubbell, Editors. 2009, W.B. Saunders: Saint Louis. p. 37-100.
37. Thiriet, M., *Cardiac Pump: An Introduction*, in *PanVascular Medicine*, P. Lanzer, Editor. 2015, Springer Berlin Heidelberg: Berlin, Heidelberg. p. 345-412.
38. Franzone, P.C., L.F. Pavarino, and S. Scacchi, *Mathematical cardiac electrophysiology.* 2014.
39. Bers, D.M., *Cardiac excitation-contraction coupling.* Nature, 2002. **415**(6868): p. 198-205.
40. Grant, A.O., *Cardiac ion channels.* Circ Arrhythm Electrophysiol, 2009. **2**(2): p. 185-94.
41. Ravens, U. and E. Cerbai, *Role of potassium currents in cardiac arrhythmias.* Europace, 2008. **10**(10): p. 1133-7.
42. Sun, Y.B. and M. Irving, *The molecular basis of the steep force-calcium relation in heart muscle.* J Mol Cell Cardiol, 2010. **48**(5): p. 859-65.
43. Gerdes, A.M., *Chapter 5 - Cardiomyocyte Ultrastructure*, in *Muscle*, J.A. Hill and E.N. Olson, Editors. 2012, Academic Press: Boston/Waltham. p. 47-55.
44. Gordon, A.M., E. Homsher, and M. Regnier, *Regulation of contraction in striated muscle.* Physiol Rev, 2000. **80**(2): p. 853-924.
45. Spudich, J.A., *Hypertrophic and dilated cardiomyopathy: four decades of basic research on muscle lead to potential therapeutic approaches to these devastating genetic diseases.* Biophys J, 2014. **106**(6): p. 1236-49.
46. Sequeira, V., et al., *The physiological role of cardiac cytoskeleton and its alterations in heart failure.* Biochim Biophys Acta, 2014. **1838**(2): p. 700-22.
47. Schmid, M. and C.N. Toepfer, *Cardiac myosin super relaxation (SRX): a perspective on fundamental biology, human disease and therapeutics.* Biol Open, 2021. **10**(2).
48. Hooijman, P., M.A. Stewart, and R. Cooke, *A new state of cardiac myosin with very slow ATP turnover: a potential cardioprotective mechanism in the heart.* Biophys J, 2011. **100**(8): p. 1969-76.
49. Fusi, L., Z. Huang, and M. Irving, *The Conformation of Myosin Heads in Relaxed Skeletal Muscle: Implications for Myosin-Based Regulation.* Biophys J, 2015. **109**(4): p. 783-92.
50. Anderson, R.L., et al., *Deciphering the super relaxed state of human beta-cardiac myosin and the mode of action of mavacamten from myosin molecules to muscle fibers.* Proc Natl Acad Sci U S A, 2018. **115**(35): p. E8143-E8152.
51. Huxley, A.F., *Muscle structure and theories of contraction.* Prog Biophys Biophys Chem, 1957. **7**: p. 255-318.
52. Toepfer, C.N., et al., *Hypertrophic cardiomyopathy mutations in MYBPC3 dysregulate myosin.* Sci Transl Med, 2019. **11**(476).
53. Repetti, G.G., et al., *Novel Therapies for Prevention and Early Treatment of Cardiomyopathies.* Circ Res, 2019. **124**(11): p. 1536-1550.
54. Maron, B.J. and M.S. Maron, *Hypertrophic cardiomyopathy.* Lancet, 2013. **381**(9862): p. 242-55.
55. Authors/Task Force, m., et al., *2014 ESC Guidelines on diagnosis and management of hypertrophic cardiomyopathy: the Task Force for the Diagnosis and Management of Hypertrophic Cardiomyopathy of the European Society of Cardiology (ESC).* Eur Heart J, 2014. **35**(39): p. 2733-79.
56. Ho, C.Y., et al., *Genotype and Lifetime Burden of Disease in Hypertrophic Cardiomyopathy: Insights from the Sarcomeric Human Cardiomyopathy Registry (SHaRe).* Circulation, 2018. **138**(14): p. 1387-1398.

57. Pelliccia, F., B.J. Gersh, and P.G. Camici, *Gaps in Evidence for Risk Stratification for Sudden Cardiac Death in Hypertrophic Cardiomyopathy.* Circulation, 2021. **143**(2): p. 101-103.
58. Coppini, R., et al., *Late sodium current inhibition reverses electromechanical dysfunction in human hypertrophic cardiomyopathy.* Circulation, 2013. **127**(5): p. 575-84.
59. Robinson, P., et al., *Alterations in thin filament regulation induced by a human cardiac troponin T mutant that causes dilated cardiomyopathy are distinct from those induced by troponin T mutants that cause hypertrophic cardiomyopathy.* J Biol Chem, 2002. **277**(43): p. 40710-6.
60. Baudenbacher, F., et al., *Myofilament Ca2+ sensitization causes susceptibility to cardiac arrhythmia in mice.* J Clin Invest, 2008. **118**(12): p. 3893-903.
61. Fraysse, B., et al., *Increased myofilament Ca2+ sensitivity and diastolic dysfunction as early consequences of Mybpc3 mutation in heterozygous knock-in mice.* J Mol Cell Cardiol, 2012. **52**(6): p. 1299-307.
62. Sequeira, V., et al., *Perturbed length-dependent activation in human hypertrophic cardiomyopathy with missense sarcomeric gene mutations.* Circ Res, 2013. **112**(11): p. 1491-505.
63. Witjas-Paalberends, E.R., et al., *Gene-specific increase in the energetic cost of contraction in hypertrophic cardiomyopathy caused by thick filament mutations.* Cardiovasc Res, 2014. **103**(2): p. 248-57.
64. Teare, D., *Asymmetrical hypertrophy of the heart in young adults.* Br Heart J, 1958. **20**(1): p. 1-8.
65. Geisterfer-Lowrance, A.A., et al., *A molecular basis for familial hypertrophic cardiomyopathy: a beta cardiac myosin heavy chain gene missense mutation.* Cell, 1990. **62**(5): p. 999-1006.
66. Carrier, L., et al., *Mapping of a novel gene for familial hypertrophic cardiomyopathy to chromosome 11.* Nat Genet, 1993. **4**(3): p. 311-3.
67. Watkins, H., et al., *Mutations in the cardiac myosin binding protein-C gene on chromosome 11 cause familial hypertrophic cardiomyopathy.* Nat Genet, 1995. **11**(4): p. 434-7.
68. Poetter, K., et al., *Mutations in either the essential or regulatory light chains of myosin are associated with a rare myopathy in human heart and skeletal muscle.* Nat Genet, 1996. **13**(1): p. 63-9.
69. Kimura, A., et al., *Mutations in the cardiac troponin I gene associated with hypertrophic cardiomyopathy.* Nat Genet, 1997. **16**(4): p. 379-82.
70. Olson, T.M., et al., *Inherited and de novo mutations in the cardiac actin gene cause hypertrophic cardiomyopathy.* J Mol Cell Cardiol, 2000. **32**(9): p. 1687-94.
71. Landstrom, A.P. and M.J. Ackerman, *Mutation type is not clinically useful in predicting prognosis in hypertrophic cardiomyopathy.* Circulation, 2010. **122**(23): p. 2441-9; discussion 2450.
72. Repetti, G.G., et al., *Discordant clinical features of identical hypertrophic cardiomyopathy twins.* Proc Natl Acad Sci U S A, 2021. **118**(10).
73. Lopes, L.R., M.S. Rahman, and P.M. Elliott, *A systematic review and meta-analysis of genotype-phenotype associations in patients with hypertrophic cardiomyopathy caused by sarcomeric protein mutations.* Heart, 2013. **99**(24): p. 1800-11.
74. Sedaghat-Hamedani, F., et al., *Clinical outcomes associated with sarcomere mutations in hypertrophic cardiomyopathy: a meta-analysis on 7675 individuals.* Clin Res Cardiol, 2018. **107**(1): p. 30-41.
75. Coppini, R., et al., *Clinical phenotype and outcome of hypertrophic cardiomyopathy associated with thin-filament gene mutations.* J Am Coll Cardiol, 2014. **64**(24): p. 2589-2600.

76. Maurizi, N., et al., *Long-term Outcomes of Pediatric-Onset Hypertrophic Cardiomyopathy and Age-Specific Risk Factors for Lethal Arrhythmic Events.* JAMA Cardiol, 2018. **3**(6): p. 520-525.
77. Ho, C.Y., et al., *Diltiazem treatment for pre-clinical hypertrophic cardiomyopathy sarcomere mutation carriers: a pilot randomized trial to modify disease expression.* JACC Heart Fail, 2015. **3**(2): p. 180-8.
78. Penicka, M., et al., *The effects of candesartan on left ventricular hypertrophy and function in nonobstructive hypertrophic cardiomyopathy: a pilot, randomized study.* J Mol Diagn, 2009. **11**(1): p. 35-41.
79. Olivotto, I., et al., *Mavacamten for treatment of symptomatic obstructive hypertrophic cardiomyopathy (EXPLORER-HCM): a randomised, double-blind, placebo-controlled, phase 3 trial.* Lancet, 2020. **396**(10253): p. 759-769.
80. Argiro, A., et al., *Emerging Medical Treatment for Hypertrophic Cardiomyopathy.* J Clin Med, 2021. **10**(5).
81. Green, E.M., et al., *A small-molecule inhibitor of sarcomere contractility suppresses hypertrophic cardiomyopathy in mice.* Science, 2016. **351**(6273): p. 617-21.
82. Coppini, R., et al., *Electrophysiological and Contractile Effects of Disopyramide in Patients With Obstructive Hypertrophic Cardiomyopathy: A Translational Study.* JACC: Basic to Translational Science, 2019. **4**(7): p. 795-813.
83. Coppini, R., et al., *Ranolazine Prevents Phenotype Development in a Mouse Model of Hypertrophic Cardiomyopathy.* Circ Heart Fail, 2017. **10**(3).
84. Abozguia, K., et al., *Metabolic modulator perhexiline corrects energy deficiency and improves exercise capacity in symptomatic hypertrophic cardiomyopathy.* Circulation, 2010. **122**(16): p. 1562-9.
85. Kawas, R.F., et al., *A small-molecule modulator of cardiac myosin acts on multiple stages of the myosin chemomechanical cycle.* J Biol Chem, 2017. **292**(40): p. 16571-16577.
86. Rohde, J.A., et al., *Mavacamten stabilizes an autoinhibited state of two-headed cardiac myosin.* Proc Natl Acad Sci U S A, 2018. **115**(32): p. E7486-E7494.
87. Sparrow, A.J., et al., *Mavacamten rescues increased myofilament calcium sensitivity and dysregulation of Ca(2+) flux caused by thin filament hypertrophic cardiomyopathy mutations.* Am J Physiol Heart Circ Physiol, 2020. **318**(3): p. H715-H722.
88. Heitner, S.B., et al., *Mavacamten Treatment for Obstructive Hypertrophic Cardiomyopathy: A Clinical Trial.* Ann Intern Med, 2019. **170**(11): p. 741-748.
89. Saberi, S., et al., *Mavacamten Favorably Impacts Cardiac Structure in Obstructive Hypertrophic Cardiomyopathy: EXPLORER-HCM Cardiac Magnetic Resonance Substudy Analysis.* Circulation, 2021. **143**(6): p. 606-608.
90. Ho, C.Y., et al., *Evaluation of Mavacamten in Symptomatic Patients With Nonobstructive Hypertrophic Cardiomyopathy.* J Am Coll Cardiol, 2020. **75**(21): p. 2649-2660.
91. Harrison, R.K., *Phase II and phase III failures: 2013-2015.* Nat Rev Drug Discov, 2016. **15**(12): p. 817-818.
92. Mamoshina, P., B. Rodriguez, and A. Bueno-Orovio, *Toward a broader view of mechanisms of drug cardiotoxicity.* Cell Rep Med, 2021. **2**(3): p. 100216.
93. Food and H.H.S. Drug Administration, *International Conference on Harmonisation; guidance on E14 Clinical Evaluation of QT/QTc Interval Prolongation and Proarrhythmic Potential for Non-Antiarrhythmic Drugs; availability. Notice.* Fed Regist, 2005. **70**(202): p. 61134-5.
94. Food and H.H.S. Drug Administration, *International Conference on Harmonisation; guidance on S7B Nonclinical Evaluation of the Potential for*

Delayed Ventricular Repolarization (QT Interval Prolongation) by Human Pharmaceuticals; availability. Notice. Fed Regist, 2005. **70**(202): p. 61133-4.
95. Stockbridge, N., et al., *Dealing with global safety issues : was the response to QT-liability of non-cardiac drugs well coordinated?* Drug Saf, 2013. **36**(3): p. 167-82.
96. Rampe, D. and A.M. Brown, *A history of the role of the hERG channel in cardiac risk assessment.* J Pharmacol Toxicol Methods, 2013. **68**(1): p. 13-22.
97. Vargas, H.M., et al., *Time for a Fully Integrated Nonclinical-Clinical Risk Assessment to Streamline QT Prolongation Liability Determinations: A Pharma Industry Perspective.* Clin Pharmacol Ther, 2021. **109**(2): p. 310-318.
98. Fermini, B., et al., *A New Perspective in the Field of Cardiac Safety Testing through the Comprehensive In Vitro Proarrhythmia Assay Paradigm.* J Biomol Screen, 2016. **21**(1): p. 1-11.
99. Sager, P.T., et al., *Rechanneling the cardiac proarrhythmia safety paradigm: a meeting report from the Cardiac Safety Research Consortium.* Am Heart J, 2014. **167**(3): p. 292-300.
100. Takahashi, K., et al., *Induction of pluripotent stem cells from adult human fibroblasts by defined factors.* Cell, 2007. **131**(5): p. 861-72.
101. Chen, I.Y., E. Matsa, and J.C. Wu, *Induced pluripotent stem cells: at the heart of cardiovascular precision medicine.* Nat Rev Cardiol, 2016. **13**(6): p. 333-49.
102. Lu, H.R., et al., *Application of optical action potentials in human induced pluripotent stem cells-derived cardiomyocytes to predict drug-induced cardiac arrhythmias.* J Pharmacol Toxicol Methods, 2017. **87**: p. 53-67.
103. Lu, H.R., et al., *High Throughput Measurement of Ca++ Dynamics in Human Stem Cell-Derived Cardiomyocytes by Kinetic Image Cytometery: A Cardiac Risk Assessment Characterization Using a Large Panel of Cardioactive and Inactive Compounds.* Toxicol Sci, 2015. **148**(2): p. 503-16.
104. Pointon, A., et al., *Assessment of cardiomyocyte contraction in human-induced pluripotent stem cell-derived cardiomyocytes.* Toxicol Sci, 2015. **144**(2): p. 227-37.
105. Knollmann, B.C., *Induced pluripotent stem cell-derived cardiomyocytes: boutique science or valuable arrhythmia model?* Circ Res, 2013. **112**(6): p. 969-76; discussion 976.
106. Sarazan, R.D., et al., *Cardiovascular function in nonclinical drug safety assessment: current issues and opportunities.* Int J Toxicol, 2011. **30**(3): p. 272-86.
107. Guo, L., Z. Dong, and H. Guthrie, *Validation of a guinea pig Langendorff heart model for assessing potential cardiovascular liability of drug candidates.* J Pharmacol Toxicol Methods, 2009. **60**(2): p. 130-51.
108. Markert, M., et al., *The value added by measuring myocardial contractility 'in vivo' in safety pharmacological profiling of drug candidates.* J Pharmacol Toxicol Methods, 2007. **56**(2): p. 203-11.
109. Butler, L., et al., *Enhanced characterization of contractility in cardiomyocytes during early drug safety assessment.* Toxicol Sci, 2015. **145**(2): p. 396-406.
110. Harmer, A.R., et al., *Validation of an in vitro contractility assay using canine ventricular myocytes.* Toxicol Appl Pharmacol, 2012. **260**(2): p. 162-72.
111. Abi-Gerges, N., et al., *Multiparametric Mechanistic Profiling of Inotropic Drugs in Adult Human Primary Cardiomyocytes.* Sci Rep, 2020. **10**(1): p. 7692.
112. Nguyen, N., et al., *Adult Human Primary Cardiomyocyte-Based Model for the Simultaneous Prediction of Drug-Induced Inotropic and Pro-arrhythmia Risk.* Front Physiol, 2017. **8**: p. 1073.
113. Hayakawa, T., et al., *Image-based evaluation of contraction-relaxation kinetics of human-induced pluripotent stem cell-derived cardiomyocytes: Correlation and complementarity with extracellular electrophysiology.* J Mol Cell Cardiol, 2014. **77**: p. 178-91.

114. Scott, C.W., et al., *An impedance-based cellular assay using human iPSC-derived cardiomyocytes to quantify modulators of cardiac contractility.* Toxicol Sci, 2014. **142**(2): p. 331-8.
115. Sirenko, O., et al., *Assessment of beating parameters in human induced pluripotent stem cells enables quantitative in vitro screening for cardiotoxicity.* Toxicol Appl Pharmacol, 2013. **273**(3): p. 500-7.
116. Franconi, F. and I. Campesi, *Pharmacogenomics, pharmacokinetics and pharmacodynamics: interaction with biological differences between men and women.* Br J Pharmacol, 2014. **171**(3): p. 580-94.
117. Tamargo, J., et al., *Gender differences in the effects of cardiovascular drugs.* Eur Heart J Cardiovasc Pharmacother, 2017. **3**(3): p. 163-182.
118. Archibald, K., et al., *Better science for safer medicines: the human imperative.* J R Soc Med, 2018. **111**(12): p. 433-438.
119. Passini, E., et al., *The virtual assay software for human in silico drug trials to augment drug cardiac testing.* Journal of Computational Science, 2020: p. 101202.
120. Morrison, T.M., et al., *Advancing Regulatory Science With Computational Modeling for Medical Devices at the FDA's Office of Science and Engineering Laboratories.* Front Med (Lausanne), 2018. **5**: p. 241.
121. Noble, D., *Successes and failures in modeling heart cell electrophysiology.* Heart Rhythm, 2011. **8**(11): p. 1798-803.
122. Niederer, S.A., J. Lumens, and N.A. Trayanova, *Computational models in cardiology.* Nat Rev Cardiol, 2019. **16**(2): p. 100-111.
123. Hodgkin, A.L. and A.F. Huxley, *A quantitative description of membrane current and its application to conduction and excitation in nerve.* J Physiol, 1952. **117**(4): p. 500-44.
124. Noble, D., *A modification of the Hodgkin--Huxley equations applicable to Purkinje fibre action and pace-maker potentials.* J Physiol, 1962. **160**: p. 317-52.
125. Deck, K.A. and W. Trautwein, *Ionic Currents in Cardiac Excitation.* Pflugers Arch Gesamte Physiol Menschen Tiere, 1964. **280**: p. 63-80.
126. McAllister, R.E., D. Noble, and R.W. Tsien, *Reconstruction of the electrical activity of cardiac Purkinje fibres.* J Physiol, 1975. **251**(1): p. 1-59.
127. Beeler, G.W. and H. Reuter, *Reconstruction of the action potential of ventricular myocardial fibres.* J Physiol, 1977. **268**(1): p. 177-210.
128. DiFrancesco, D. and D. Noble, *A model of cardiac electrical activity incorporating ionic pumps and concentration changes.* Philos Trans R Soc Lond B Biol Sci, 1985. **307**(1133): p. 353-98.
129. DiFrancesco, D., *A new interpretation of the pace-maker current in calf Purkinje fibres.* J Physiol, 1981. **314**: p. 359-76.
130. Noble, D., A. Garny, and P.J. Noble, *How the Hodgkin-Huxley equations inspired the Cardiac Physiome Project.* J Physiol, 2012. **590**(11): p. 2613-28.
131. Earm, Y.E. and D. Noble, *A model of the single atrial cell: relation between calcium current and calcium release.* Proc R Soc Lond B Biol Sci, 1990. **240**(1297): p. 83-96.
132. ten Tusscher, K.H. and A.V. Panfilov, *Alternans and spiral breakup in a human ventricular tissue model.* Am J Physiol Heart Circ Physiol, 2006. **291**(3): p. H1088-100.
133. Grandi, E., F.S. Pasqualini, and D.M. Bers, *A novel computational model of the human ventricular action potential and Ca transient.* J Mol Cell Cardiol, 2010. **48**(1): p. 112-21.
134. Carro, J., et al., *A human ventricular cell model for investigation of cardiac arrhythmias under hyperkalaemic conditions.* Philosophical Transactions of the Royal Society A: Mathematical, Physical and Engineering Sciences, 2011. **369**(1954): p. 4205-4232.

135. O'Hara, T., et al., *Simulation of the undiseased human cardiac ventricular action potential: Model formulation and experimental validation.* PLoS Computational Biology, 2011. **7**(5).
136. Tomek, J., et al., *Development, calibration, and validation of a novel human ventricular myocyte model in health, disease, and drug block.* Elife, 2019. **8**.
137. Quarteroni, A., et al., *Integrated Heart—Coupling multiscale and multiphysics models for the simulation of the cardiac function.* Computer Methods in Applied Mechanics and Engineering, 2017. **314**: p. 345-407.
138. Niederer, S.A., K.S. Campbell, and S.G. Campbell, *A short history of the development of mathematical models of cardiac mechanics.* J Mol Cell Cardiol, 2019. **127**: p. 11-19.
139. Trayanova, N.A. and J.J. Rice, *Cardiac electromechanical models: from cell to organ.* Front Physiol, 2011. **2**: p. 43.
140. McKillop, D.F. and M.A. Geeves, *Regulation of the interaction between actin and myosin subfragment 1: evidence for three states of the thin filament.* Biophysical Journal, 1993. **65**(2): p. 693-701.
141. Campbell, K.S., P.M.L. Janssen, and S.G. Campbell, *Force-Dependent Recruitment from the Myosin Off State Contributes to Length-Dependent Activation.* Biophys J, 2018. **115**(3): p. 543-553.
142. Lyon, A., et al., *Differentiating the effects of beta-adrenergic stimulation and stretch on calcium and force dynamics using a novel electromechanical cardiomyocyte model.* Am J Physiol Heart Circ Physiol, 2020. **319**(3): p. H519-H530.
143. Lumens, J., et al., *Differentiating Electromechanical From Non-Electrical Substrates of Mechanical Discoordination to Identify Responders to Cardiac Resynchronization Therapy.* Circ Cardiovasc Imaging, 2015. **8**(9): p. e003744.
144. Lewalle, A., et al., *Balance of Active, Passive, and Anatomical Cardiac Properties in Doxorubicin-Induced Heart Failure.* Biophys J, 2019. **117**(12): p. 2337-2348.
145. Wang, Z.J., et al., *Human biventricular electromechanical simulations on the progression of electrocardiographic and mechanical abnormalities in post-myocardial infarction.* Europace, 2021. **23**(Supplement_1): p. i143-i152.
146. Hill, A.V., *The heat of shortening and the dynamic constants of muscle.* Proceedings of the Royal Society of London. Series B - Biological Sciences, 1938. **126**(843): p. 136-195.
147. Rice, J.J., R.L. Winslow, and W.C. Hunter, *Comparison of putative cooperative mechanisms in cardiac muscle: length dependence and dynamic responses.* Am J Physiol, 1999. **276**(5): p. H1734-54.
148. Rice, J.J., et al., *Approximate model of cooperative activation and crossbridge cycling in cardiac muscle using ordinary differential equations.* Biophys J, 2008. **95**(5): p. 2368-90.
149. Campbell, S.G., et al., *Coupling of adjacent tropomyosins enhances cross-bridge-mediated cooperative activation in a markov model of the cardiac thin filament.* Biophys J, 2010. **98**(10): p. 2254-64.
150. Land, S., et al., *An analysis of deformation-dependent electromechanical coupling in the mouse heart.* J Physiol, 2012. **590**(18): p. 4553-69.
151. Mijailovich, S.M., et al., *Modeling the Actin.myosin ATPase Cross-Bridge Cycle for Skeletal and Cardiac Muscle Myosin Isoforms.* Biophysical Journal, 2017. **112**(5): p. 984-996.
152. Land, S., et al., *A model of cardiac contraction based on novel measurements of tension development in human cardiomyocytes.* J Mol Cell Cardiol, 2017. **106**: p. 68-83.
153. Balakina-Vikulova, N.A., et al., *Mechano-calcium and mechano-electric feedbacks in the human cardiomyocyte analyzed in a mathematical model.* J Physiol Sci, 2020. **70**(1): p. 12.

154. Mijailovich, S.M., et al., *Multiscale modeling of twitch contractions in cardiac trabeculae.* J Gen Physiol, 2021. **153**(3).
155. Carusi, A., K. Burrage, and B. Rodríguez, *Bridging experiments, models and simulations: An integrative approach to validation in computational cardiac electrophysiology.* American Journal of Physiology - Heart and Circulatory Physiology, 2012. **303**(2): p. H144-H155.
156. Pueyo, E., et al., *Experimentally-Based Computational Investigation into Beat-To-Beat Variability in Ventricular Repolarization and Its Response to Ionic Current Inhibition.* PLoS One, 2016. **11**(3): p. e0151461.
157. Passini, E., et al., *Mechanisms of pro-arrhythmic abnormalities in ventricular repolarisation and anti-arrhythmic therapies in human hypertrophic cardiomyopathy.* J Mol Cell Cardiol, 2016. **96**: p. 72-81.
158. Dutta, S., et al., *Electrophysiological properties of computational human ventricular cell action potential models under acute ischemic conditions.* Progress in Biophysics and Molecular Biology, 2017. **129**: p. 40-52.
159. Trovato, C., et al., *Human Purkinje in silico model enables mechanistic investigations into automaticity and pro-arrhythmic abnormalities.* J Mol Cell Cardiol, 2020. **142**: p. 24-38.
160. Martinez-Navarro, H., et al., *High arrhythmic risk in antero-septal acute myocardial ischemia is explained by increased transmural reentry occurrence.* Sci Rep, 2019. **9**(1): p. 16803.
161. Arevalo, H.J., et al., *Arrhythmia risk stratification of patients after myocardial infarction using personalized heart models.* Nat Commun, 2016. **7**: p. 11437.
162. Zemzemi, N., et al., *Computational assessment of drug-induced effects on the electrocardiogram: from ion channel to body surface potentials.* Br J Pharmacol, 2013. **168**(3): p. 718-33.
163. Bukhari, H.A., et al., *Characterization of T Wave Amplitude, Duration and Morphology Changes During Hemodialysis: Relationship with Serum Electrolyte Levels and Heart Rate.* IEEE Trans Biomed Eng, 2020. **PP**.
164. Palmieri, F., et al., *Monitoring blood potassium concentration in hemodialysis patients by quantifying T-wave morphology dynamics.* Sci Rep, 2021. **11**(1): p. 3883.
165. Taggart, P., et al., *Emerging evidence for a mechanistic link between low-frequency oscillation of ventricular repolarization measured from the electrocardiogram T-wave vector and arrhythmia.* Europace, 2021.
166. Niederer, S.A., et al., *Length-dependent tension in the failing heart and the efficacy of cardiac resynchronization therapy.* Cardiovasc Res, 2011. **89**(2): p. 336-43.
167. Campbell, K.S., B.S. Chrisman, and S.G. Campbell, *Multiscale Modeling of Cardiovascular Function Predicts That the End-Systolic Pressure Volume Relationship Can Be Targeted via Multiple Therapeutic Strategies.* Front Physiol, 2020. **11**: p. 1043.
168. Leon, L.J. and B.M. Horacek, *Computer model of excitation and recovery in the anisotropic myocardium. III. Arrhythmogenic conditions in the simplified left ventricle.* J Electrocardiol, 1991. **24**(1): p. 33-41.
169. Clayton, R.H., et al., *Models of cardiac tissue electrophysiology: progress, challenges and open questions.* Prog Biophys Mol Biol, 2011. **104**(1-3): p. 22-48.
170. Holzapfel, G.A. and R.W. Ogden, *Constitutive modelling of passive myocardium: a structurally based framework for material characterization.* Philos Trans A Math Phys Eng Sci, 2009. **367**(1902): p. 3445-75.
171. Augustin, C.M., et al., *Anatomically accurate high resolution modeling of human whole heart electromechanics: A strongly scalable algebraic multigrid solver method for nonlinear deformation.* J Comput Phys, 2016. **305**: p. 622-646.

172. Levrero-Florencio, F., et al., *Sensitivity analysis of a strongly-coupled human-based electromechanical cardiac model: Effect of mechanical parameters on physiologically relevant biomarkers.* Computer Methods in Applied Mechanics and Engineering, 2020. **361**.
173. Rodero, C., et al., *Linking statistical shape models and simulated function in the healthy adult human heart.* PLoS Comput Biol, 2021. **17**(4): p. e1008851.
174. Eriksson, T.S.E., et al., *Influence of myocardial fiber/sheet orientations on left ventricular mechanical contraction.* Mathematics and Mechanics of Solids, 2013. **18**(6): p. 592-606.
175. Jeyaraj, D., et al., *Circadian rhythms govern cardiac repolarization and arrhythmogenesis.* Nature, 2012. **483**(7387): p. 96-9.
176. Herraiz-Martinez, A., et al., *Ageing is associated with deterioration of calcium homeostasis in isolated human right atrial myocytes.* Cardiovasc Res, 2015. **106**(1): p. 76-86.
177. Muszkiewicz, A., et al., *Variability in cardiac electrophysiology: Using experimentally-calibrated populations of models to move beyond the single virtual physiological human paradigm.* Prog Biophys Mol Biol, 2016. **120**(1-3): p. 115-27.
178. Ni, H., S. Morotti, and E. Grandi, *A Heart for Diversity: Simulating Variability in Cardiac Arrhythmia Research.* Front Physiol, 2018. **9**: p. 958.
179. Sarkar, A.X., D.J. Christini, and E.A. Sobie, *Exploiting mathematical models to illuminate electrophysiological variability between individuals.* J Physiol, 2012. **590**(11): p. 2555-67.
180. Romero, L., et al., *Impact of ionic current variability on human ventricular cellular electrophysiology.* Am J Physiol Heart Circ Physiol, 2009. **297**(4): p. H1436-45.
181. Mora, M.T., et al., *Sensitivity analysis revealing the effect of modulating ionic mechanisms on calcium dynamics in simulated human heart failure.* PLoS One, 2017. **12**(11): p. e0187739.
182. Britton, O.J., et al., *Experimentally calibrated population of models predicts and explains intersubject variability in cardiac cellular electrophysiology.* Proc Natl Acad Sci U S A, 2013. **110**(23): p. E2098-105.
183. Lawson, B.A.J., et al., *Unlocking data sets by calibrating populations of models to data density: A study in atrial electrophysiology.* Sci Adv, 2018. **4**(1): p. e1701676.
184. Passini, E., et al., *Drug-induced shortening of the electromechanical window is an effective biomarker for in silico prediction of clinical risk of arrhythmias.* Br J Pharmacol, 2019. **176**(19): p. 3819-3833.
185. Zhou, X., et al., *Blinded In Silico Drug Trial Reveals the Minimum Set of Ion Channels for Torsades de Pointes Risk Assessment.* Front Pharmacol, 2019. **10**: p. 1643.
186. Groenendaal, W., et al., *Cell-specific cardiac electrophysiology models.* PLoS Comput Biol, 2015. **11**(4): p. e1004242.
187. Syed, Z., et al., *Atrial cell action potential parameter fitting using genetic algorithms.* Med Biol Eng Comput, 2005. **43**(5): p. 561-71.
188. Antman, E.M. and J. Loscalzo, *Precision medicine in cardiology.* Nat Rev Cardiol, 2016. **13**(10): p. 591-602.
189. Morris, P.D., et al., *"Virtual" (Computed) Fractional Flow Reserve: Current Challenges and Limitations.* JACC Cardiovasc Interv, 2015. **8**(8): p. 1009-1017.
190. Xi, J., et al., *The estimation of patient-specific cardiac diastolic functions from clinical measurements.* Med Image Anal, 2013. **17**(2): p. 133-46.
191. Prakosa, A., et al., *Personalized virtual-heart technology for guiding the ablation of infarct-related ventricular tachycardia.* Nat Biomed Eng, 2018. **2**(10): p. 732-740.

192. Lyon, A., et al., *Electrocardiogram phenotypes in hypertrophic cardiomyopathy caused by distinct mechanisms: apico-basal repolarization gradients vs. Purkinje-myocardial coupling abnormalities.* Europace, 2018. **20**(suppl_3): p. iii102-iii112.
193. Aboelkassem, Y., et al., *Multiscale Models of Cardiac Muscle Biophysics and Tissue Remodeling in Hypertrophic Cardiomyopathies.* Curr Opin Biomed Eng, 2019. **11**: p. 35-44.
194. Campbell, S.G. and A.D. McCulloch, *Multi-scale computational models of familial hypertrophic cardiomyopathy: genotype to phenotype.* J R Soc Interface, 2011. **8**(64): p. 1550-61.
195. Doh, C.Y., et al., *The HCM-causing Y235S cMyBPC mutation accelerates contractile function by altering C1 domain structure.* Biochimica et Biophysica Acta (BBA) - Molecular Basis of Disease, 2019. **1865**(3): p. 661-677.
196. Cheng, Y., et al., *Effects of Cardiac Troponin I Mutation P83S on Contractile Properties and the Modulation by PKA-Mediated Phosphorylation.* J Phys Chem B, 2016. **120**(33): p. 8238-53.
197. Vera, C.D., et al., *Myosin motor domains carrying mutations implicated in early or late onset hypertrophic cardiomyopathy have similar properties.* J Biol Chem, 2019. **294**(46): p. 17451-17462.
198. Sewanan, L.R., et al., *Predicting Effects of Tropomyosin Mutations on Cardiac Muscle Contraction through Myofilament Modeling.* Frontiers in Physiology, 2016. **7**(473).
199. Mijailovich, S.M., et al., *The effect of variable troponin C mutation thin filament incorporation on cardiac muscle twitch contractions.* J Mol Cell Cardiol, 2021. **155**: p. 112-124.
200. Zile, M.A. and N.A. Trayanova, *Myofilament protein dynamics modulate EAD formation in human hypertrophic cardiomyopathy.* Prog Biophys Mol Biol, 2017. **130**(Pt B): p. 418-428.
201. Prondzynski, M., et al., *Disease modeling of a mutation in alpha-actinin 2 guides clinical therapy in hypertrophic cardiomyopathy.* EMBO Mol Med, 2019. **11**(12): p. e11115.
202. Lyon, A., et al., *Distinct ECG Phenotypes Identified in Hypertrophic Cardiomyopathy Using Machine Learning Associate With Arrhythmic Risk Markers.* Front Physiol, 2018. **9**: p. 213.
203. Davies, M.R., et al., *Recent developments in using mechanistic cardiac modelling for drug safety evaluation.* Drug Discov Today, 2016. **21**(6): p. 924-38.
204. Perissinotti, L.L., et al., *Determinants of Isoform-Specific Gating Kinetics of hERG1 Channel: Combined Experimental and Simulation Study.* Front Physiol, 2018. **9**: p. 207.
205. DeMarco, K.R., et al., *Digging into Lipid Membrane Permeation for Cardiac Ion Channel Blocker d-Sotalol with All-Atom Simulations.* Front Pharmacol, 2018. **9**: p. 26.
206. Moreno, J.D., et al., *A computational model to predict the effects of class I anti-arrhythmic drugs on ventricular rhythms.* Sci Transl Med, 2011. **3**(98): p. 98ra83.
207. Lancaster, M.C. and E.A. Sobie, *Improved Prediction of Drug-Induced Torsades de Pointes Through Simulations of Dynamics and Machine Learning Algorithms.* Clin Pharmacol Ther, 2016. **100**(4): p. 371-9.
208. Mirams, G.R., et al., *Simulation of multiple ion channel block provides improved early prediction of compounds' clinical torsadogenic risk.* Cardiovasc Res, 2011. **91**(1): p. 53-61.
209. Martinez-Navarro, H., et al., *Electrophysiological and anatomical factors determine arrhythmic risk in acute myocardial ischaemia and its modulation by sodium current availability.* Interface Focus, 2021. **11**(1): p. 20190124.

210. Britton, O.J., et al., *Quantitative Comparison of Effects of Dofetilide, Sotalol, Quinidine, and Verapamil between Human Ex vivo Trabeculae and In silico Ventricular Models Incorporating Inter-Individual Action Potential Variability.* Front Physiol, 2017. **8**: p. 597.
211. Paci, M., et al., *All-Optical Electrophysiology Refines Populations of In Silico Human iPSC-CMs for Drug Evaluation.* Biophys J, 2020. **118**(10): p. 2596-2611.
212. Morotti, S. and E. Grandi, *Logistic regression analysis of populations of electrophysiological models to assess proarrythmic risk.* MethodsX, 2017. **4**: p. 25-34.
213. Gong, J.Q.X. and E.A. Sobie, *Population-based mechanistic modeling allows for quantitative predictions of drug responses across cell types.* NPJ Syst Biol Appl, 2018. **4**: p. 11.
214. Grabowska, M.E., et al., *Computational model of cardiomyocyte apoptosis identifies mechanisms of tyrosine kinase inhibitor-induced cardiotoxicity.* J Mol Cell Cardiol, 2021. **155**: p. 66-77.
215. Vicente, J., et al., *Electrocardiographic Biomarkers for Detection of Drug-Induced Late Sodium Current Block.* PLoS One, 2016. **11**(12): p. e0163619.
216. Jie, X., B. Rodriguez, and E. Pueyo, *Torsadogenic Drug-induced Increased Short-term Variability of JT-area.* Comput Cardiol (2010), 2010. **2010**: p. 353-356.
217. Colman, M.A., et al., *Trigger vs. Substrate: Multi-Dimensional Modulation of QT-Prolongation Associated Arrhythmic Dynamics by a hERG Channel Activator.* Frontiers in Physiology, 2017. **8**: p. 757.
218. Delaunois, A., et al., *Applying the CiPA approach to evaluate cardiac proarrhythmia risk of some antimalarials used off-label in the first wave of COVID-19.* Clin Transl Sci, 2021.
219. Varshneya, M., et al., *Investigational Treatments for COVID-19 may Increase Ventricular Arrhythmia Risk Through Drug Interactions.* CPT Pharmacometrics Syst Pharmacol, 2021. **10**(2): p. 100-107.
220. Yarov-Yarovoy, V., T.W. Allen, and C.E. Clancy, *Computational Models for Predictive Cardiac Ion Channel Pharmacology.* Drug Discov Today Dis Models, 2014. **14**: p. 3-10.
221. Timmermann, V., et al., *An integrative appraisal of mechano-electric feedback mechanisms in the heart.* Progress in Biophysics and Molecular Biology, 2017. **130**: p. 404-417.
222. Negroni, J.A., et al., *beta-adrenergic effects on cardiac myofilaments and contraction in an integrated rabbit ventricular myocyte model.* J Mol Cell Cardiol, 2015. **81**: p. 162-75.
223. Khokhlova, A., et al., *Transmural cellular heterogeneity in myocardial electromechanics.* Journal of Physiological Sciences, 2018. **68**(4): p. 387-413.
224. Campbell, S.G., et al., *Effect of transmurally heterogeneous myocyte excitation-contraction coupling on canine left ventricular electromechanics.* Exp Physiol, 2009. **94**(5): p. 541-52.
225. Lou, Q., et al., *Transmural heterogeneity and remodeling of ventricular excitation- contraction coupling in human heart failure.* Circulation, 2011. **123**(17): p. 1881-1890.
226. Mulieri, L.A., et al., *Altered myocardial force-frequency relation in human heart failure.* Circulation, 1992. **85**(5): p. 1743-1750.
227. Pieske, B., et al., *Diminished post-rest potentiation of contractile force in human dilated cardiomyopathy: Functional evidence for alterations in intracellular Ca2+ handling.* Journal of Clinical Investigation, 1996. **98**(3): p. 764-776.

228. Rossman, E.I., et al., *Abnormal frequency-dependent responses represent the pathophysiologic signature of contractile failure in human myocardium.* Journal of Molecular and Cellular Cardiology, 2004. **36**(1): p. 33-42.
229. Demer, L.L. and F.C. Yin, *Passive biaxial mechanical properties of isolated canine myocardium.* The Journal of Physiology, 1983. **339**(1): p. 615-630.
230. Yin, F.C.P., et al., *Quantification of the mechanical properties of noncontracting canine myocardium under simultaneous biaxial loading.* Journal of Biomechanics, 1987. **20**(6): p. 577-589.
231. Britton, O.J., et al., *The Electrogenic Na(+)/K(+) Pump Is a Key Determinant of Repolarization Abnormality Susceptibility in Human Ventricular Cardiomyocytes: A Population-Based Simulation Study.* Front Physiol, 2017. **8**: p. 278.
232. Haynes, P., et al., *Transmural heterogeneity of cellular level power output is reduced in human heart failure.* Journal of Molecular and Cellular Cardiology, 2014. **72**: p. 1-8.
233. Page, G., et al., *Human ex-vivo action potential model for pro-arrhythmia risk assessment.* Journal of Pharmacological and Toxicological Methods, 2016. **81**: p. 183-195.
234. Schmidt, U., et al., *Contribution of abnormal sarcoplasmic reticulum ATPase activity to systolic and diastolic dysfunction in human heart failure.* Journal of Molecular and Cellular Cardiology, 1998. **30**(10): p. 1929-1937.
235. Vahl, C.F., et al., *Myocardial length-force relationship in end stage dilated cardiomyopathy and normal human myocardium: Analysis of intact and skinned left ventricular trabeculae obtained during 11 heart transplantations.* Basic Research in Cardiology, 1997. **92**(4): p. 261-270.
236. Holubarsch, C., et al., *Shortening versus isometric contractions in isolated human failing and non-failing left ventricular myocardium: Dependency of external work and force on muscle length, heart rate and inotropic stimulation.* Cardiovascular Research, 1998. **37**(1): p. 46-57.
237. Guo, D., et al., *Electrophysiological properties of HBI-3000: A new antiarrhythmic agent with multiple-channel blocking properties in human ventricular myocytes.* Journal of Cardiovascular Pharmacology, 2011. **57**(1): p. 79-85.
238. Dutta, S., et al., *Early afterdepolarizations promote transmural reentry in ischemic human ventricles with reduced repolarization reserve.* Prog Biophys Mol Biol, 2016. **120**(1-3): p. 236-48.
239. Kramer, J., et al., *MICE models: Superior to the HERG model in predicting torsade de pointes.* Scientific Reports, 2013. **3**.
240. Crumb, W.J., et al., *An evaluation of 30 clinical drugs against the comprehensive in vitro proarrhythmia assay (CiPA) proposed ion channel panel.* Journal of Pharmacological and Toxicological Methods, 2016. **81**: p. 251-262.
241. Ritchie, R.H., et al., *Attenuation of the Negative Inotropic Effects of Metoprolol at Short Cycle Lengths in Humans. Comparison With Sotalol and Verapamil.* Journal of the American College of Cardiology, 2006. **48**(6): p. 1234-1241.
242. Johannesen, L., et al., *Differentiating drug-induced multichannel block on the electrocardiogram: Randomized study of dofetilide, quinidine, ranolazine, and verapamil.* Clinical Pharmacology and Therapeutics, 2014. **96**(5): p. 549-558.
243. Woosley, R. and K. Romer, 1999.
244. Santiago, A., et al., *Fully coupled fluid-electro-mechanical model of the human heart for supercomputers.* International Journal for Numerical Methods in Biomedical Engineering, 2018. **34**(12).
245. King, N.M., et al., *Mouse intact cardiac myocyte mechanics: cross-bridge and titin-based stress in unactivated cells.* J Gen Physiol, 2011. **137**(1): p. 81-91.

246. Boukens, B.J., et al., *Transmural APD gradient synchronizes repolarization in the human left ventricular wall.* Cardiovascular Research, 2015. **108**(1): p. 188-196.
247. Cordeiro, J.M., et al., *Transmural heterogeneity of calcium activity and mechanical function in the canine left ventricle.* American Journal of Physiology - Heart and Circulatory Physiology, 2004. **286**(4 55-4): p. H1471-H1479.
248. De Cicco, M., et al., *Pharmacokinetic and pharmacodynamic effects of high-dose continuous intravenous verapamil infusion: Clinical experience in the intensive care unit.* Critical Care Medicine, 1999. **27**(2): p. 332-339.
249. Hoffmeister, H.M., A. Hepp, and L. Seipel, *Negative inotropic effect of class-i-antiarrhythmic drugs: Comparison of flecainide with disopyramide and quinidine.* European Heart Journal, 1987. **8**(7): p. 1126-1132.
250. Piacentino Iii, V., et al., *Cellular basis of abnormal calcium transients of failing human ventricular myocytes.* Circulation Research, 2003. **92**(6): p. 651-658.
251. Høydal, M.A., et al., *Human cardiomyocyte calcium handling and transverse tubules in mid-stage of post-myocardial-infarction heart failure.* ESC Heart Failure, 2018. **5**(3): p. 332-342.
252. Yue, L., et al., *Transient outward and delayed rectifier currents in canine atrium: Properties and role of isolation methods.* American Journal of Physiology - Heart and Circulatory Physiology, 1996. **270**(6 39-6): p. H2157-H2168.
253. Voigt, N., et al., *Methods for isolating atrial cells from large mammals and humans.* Journal of Molecular and Cellular Cardiology, 2015. **86**: p. 187-198.
254. Perel, P., et al., *Comparison of treatment effects between animal experiments and clinical trials: Systematic review.* British Medical Journal, 2007. **334**(7586): p. 197-200.
255. Ji, Y.C., R.A. Gray, and F.H. Fenton, *Implementation of contraction to electrophysiological ventricular myocyte models, and their quantitative characterization via post-extrasystolic potentiation.* PLoS ONE, 2015. **10**(8).
256. Li, G.-R., et al., *Transmural heterogeneity of action potentials andI to1 in myocytes isolated from the human right ventricle.* American Journal of Physiology-Heart and Circulatory Physiology, 1998. **275**(2): p. H369-H377.
257. Gaborit, N., et al., *Regional and tissue specific transcript signatures of ion channel genes in the non-diseased human heart.* Journal of Physiology, 2007. **582**(2): p. 675-693.
258. Stelzer, J.E., et al., *Transmural variation in myosin heavy chain isoform expression modulates the timing of myocardial force generation in porcine left ventricle.* Journal of Physiology, 2008. **586**(21): p. 5203-5214.
259. Van Der Velden, J., et al., *Transmural heterogeneity of myofilament function and sarcomeric protein phosphorylation in remodeled myocardium of pigs with a recent myocardial infarction.* Front Physiol, 2011. **2**.
260. Taggart, P., et al., *Transmural repolarisation in the left ventricle in humans during normoxia and ischaemia.* Cardiovascular Research, 2001. **50**(3): p. 454-462.
261. Khokhlova, A., et al., *The effects of load on transmural differences in contraction of isolated mouse ventricular cardiomyocytes.* Journal of Molecular and Cellular Cardiology, 2018. **114**: p. 276-287.
262. Khokhlova, A., et al., *The Effects of Mechanical Preload on Transmural Differences in Mechano-Calcium-Electric Feedback in Single Cardiomyocytes: Experiments and Mathematical Models.* Frontiers in Physiology, 2020. **11**.
263. Wan, X., et al., *Molecular correlates of repolarization alternans in cardiac myocytes.* Journal of Molecular and Cellular Cardiology, 2005. **39**(3): p. 419-428.

264. De Simone, G., et al., *Midwall left ventricular mechanics: An independent predictor of cardiovascular risk in arterial hypertension.* Circulation, 1996. **93**(2): p. 259-265.
265. Wachtell, K., et al., *In-treatment midwall and endocardial fractional shortening predict cardiovascular outcome in hypertensive patients with preserved baseline systolic ventricular function: The Losartan Intervention for Endpoint reduction study.* Journal of Hypertension, 2010. **28**(7): p. 1541-1546.
266. Wang, H., et al., *Computational Investigation of Transmural Differences in Left Ventricular Contractility.* Journal of Biomechanical Engineering, 2016. **138**(11).
267. Khokhlova, A., et al., *Effects of cellular electromechanical coupling on functional heterogeneity in a one-dimensional tissue model of the myocardium.* Computers in Biology and Medicine, 2017. **84**: p. 147-155.
268. Vaverka, J., et al., *Effect of Transmural Differences in Excitation-Contraction Delay and Contraction Velocity on Left Ventricle Isovolumic Contraction: A Simulation Study.* BioMed Research International, 2018. **2018**.
269. Dusturia, N., et al., *Effect of myocardial heterogeneity on ventricular electro-mechanical responses: A computational study.* BioMedical Engineering Online, 2019. **18**(1).
270. Reiser, P.J., et al., *Human cardiac myosin heavy chain isoforms in fetal and failing adult atria and ventricles.* American Journal of Physiology - Heart and Circulatory Physiology, 2001. **280**(4 49-4): p. H1814-H1820.
271. Carnes, C.A., T.P. Geisbuhler, and P.J. Reiser, *Age-dependent changes in contraction and regional myocardial myosin heavy chain isoform expression in rats.* Journal of Applied Physiology, 2004. **97**(1): p. 446-453.
272. Li, Z., et al., *Assessment of an In Silico Mechanistic Model for Proarrhythmia Risk Prediction Under the CiPA Initiative.* Clinical Pharmacology and Therapeutics, 2019. **105**(2): p. 466-475.
273. Tande, P.M. and H. Refsum, *Class III Antiarrhythmic Action Linked with Positive Inotropy: Acute Electrophysiological and Inotropic Effects of Amiodarone in Vitro.* Pharmacology & Toxicology, 1990. **66**(1): p. 18-22.
274. Li, Z., et al., *General Principles for the Validation of Proarrhythmia Risk Prediction Models: An Extension of the CiPA In Silico Strategy.* Clinical Pharmacology and Therapeutics, 2020. **107**(1): p. 102-111.
275. Amerini, S., A. Giotti, and A. Mugelli, *Effect of verapamil and diltiazem on calcium-dependent electrical activity in cardiac Purkinje fibres.* British Journal of Pharmacology, 1985. **85**(1): p. 89-96.
276. Kimura, S., et al., *Verapamil diminishes action potential changes during metabolic inhibition by blocking ATP-regulated potassium currents.* Circulation Research, 1992. **71**(1): p. 87-95.
277. Lei, C.L., et al., *Tailoring mathematical models to stem-cell derived cardiomyocyte lines can improve predictions of drug-induced changes to their electrophysiology.* Frontiers in Physiology, 2017. **8**(DEC).
278. de Tombe, P.P. and H.E.D.J. ter Keurs, *Cardiac muscle mechanics: Sarcomere length matters.* Journal of Molecular and Cellular Cardiology, 2016. **91**: p. 148-150.
279. Paredes, R.M., et al., *Chemical calcium indicators.* Methods, 2008. **46**(3): p. 143-51.
280. Lock, J.T., I. Parker, and I.F. Smith, *A comparison of fluorescent Ca(2)(+) indicators for imaging local Ca(2)(+) signals in cultured cells.* Cell Calcium, 2015. **58**(6): p. 638-48.
281. Kaestner, L., et al., *Genetically encoded Ca2+ indicators in cardiac myocytes.* Circ Res, 2014. **114**(10): p. 1623-39.
282. Chen, T.W., et al., *Ultrasensitive fluorescent proteins for imaging neuronal activity.* Nature, 2013. **499**(7458): p. 295-300.

283. Sparrow, A.J., et al., *Measurement of Myofilament-Localized Calcium Dynamics in Adult Cardiomyocytes and the Effect of Hypertrophic Cardiomyopathy Mutations.* Circ Res, 2019. **124**(8): p. 1228-1239.
284. Broyles, C.N., P. Robinson, and M.J. Daniels, *Fluorescent, Bioluminescent, and Optogenetic Approaches to Study Excitable Physiology in the Single Cardiomyocyte.* Cells, 2018. **7**(6).
285. Lou, Q., A. Janardhan, and I.R. Efimov, *Remodeling of calcium handling in human heart failure.* Adv Exp Med Biol, 2012. **740**: p. 1145-74.
286. Richardson, C.D., et al., *Enhancing homology-directed genome editing by catalytically active and inactive CRISPR-Cas9 using asymmetric donor DNA.* Nat Biotechnol, 2016. **34**(3): p. 339-44.
287. Sala, L., et al., *MUSCLEMOTION: A Versatile Open Software Tool to Quantify Cardiomyocyte and Cardiac Muscle Contraction In Vitro and In Vivo.* Circ Res, 2018. **122**(3): p. e5-e16.
288. Toepfer, C.N., et al., *SarcTrack: An Adaptable Software Tool for Efficient Large-Scale Analysis of Sarcomere Function in hiPSC-Cardiomyocytes.* Circ Res, 2019.
289. Lundy, S.D., et al., *Structural and functional maturation of cardiomyocytes derived from human pluripotent stem cells.* Stem Cells Dev, 2013. **22**(14): p. 1991-2002.
290. Werley, C.A., et al., *Geometry-dependent functional changes in iPSC-derived cardiomyocytes probed by functional imaging and RNA sequencing.* PLoS One, 2017. **12**(3): p. e0172671.
291. Saleem, U., et al., *Force and Calcium Transients Analysis in Human Engineered Heart Tissues Reveals Positive Force-Frequency Relation at Physiological Frequency.* Stem Cell Reports, 2020. **14**(2): p. 312-324.
292. Linkert, M., et al., *Metadata matters: access to image data in the real world.* J Cell Biol, 2010. **189**(5): p. 777-82.
293. Marr, D. and E. Hildreth, *Theory of edge detection.* Proc R Soc Lond B Biol Sci, 1980. **207**(1167): p. 187-217.
294. Wang, Y., et al., *Generation and functional characterization of knock-in mice harboring the cardiac troponin I-R21C mutation associated with hypertrophic cardiomyopathy.* J Biol Chem, 2012. **287**(3): p. 2156-67.
295. Mali, P., et al., *RNA-guided human genome engineering via Cas9.* Science (New York, N.Y.), 2013. **339**(6121): p. 823-826.
296. Hendel, A., et al., *Chemically modified guide RNAs enhance CRISPR-Cas genome editing in human primary cells.* Nature biotechnology, 2015. **33**(9): p. 985-989.
297. Sharma, A., et al., *CRISPR/Cas9-Mediated Fluorescent Tagging of Endogenous Proteins in Human Pluripotent Stem Cells.* Current protocols in human genetics, 2018. **96**: p. 21.11.1-21.11.20.
298. Sharma, A., et al., *Differentiation and Contractile Analysis of GFP-Sarcomere Reporter hiPSC-Cardiomyocytes.* Curr Protoc Hum Genet, 2018. **96**: p. 21 12 1-21 12 12.
299. Nakai, J., M. Ohkura, and K. Imoto, *A high signal-to-noise Ca(2+) probe composed of a single green fluorescent protein.* Nat Biotechnol, 2001. **19**(2): p. 137-41.
300. Arking, D.E., et al., *Genetic association study of QT interval highlights role for calcium signaling pathways in myocardial repolarization.* Nat Genet, 2014. **46**(8): p. 826-36.
301. De Luca, L., et al., *Evidence-based use of levosimendan in different clinical settings.* Eur Heart J, 2006. **27**(16): p. 1908-20.
302. Haikala, H., et al., *Cardiac troponin C as a target protein for a novel calcium sensitizing drug, levosimendan.* J Mol Cell Cardiol, 1995. **27**(9): p. 1859-66.

303. Katz, A.M., *Regulation of myocardial contractility 1958-1983: an odyssey.* J Am Coll Cardiol, 1983. **1**(1): p. 42-51.
304. Orstavik, O., et al., *Inhibition of phosphodiesterase-3 by levosimendan is sufficient to account for its inotropic effect in failing human heart.* Br J Pharmacol, 2014. **171**(23): p. 5169-81.
305. Hasenfuss, G., et al., *Influence of the novel inotropic agent levosimendan on isometric tension and calcium cycling in failing human myocardium.* Circulation, 1998. **98**(20): p. 2141-7.
306. Novak, A., et al., *Functional abnormalities in iPSC-derived cardiomyocytes generated from CPVT1 and CPVT2 patients carrying ryanodine or calsequestrin mutations.* J Cell Mol Med, 2015. **19**(8): p. 2006-18.
307. Fahed, A.C., et al., *Founder Mutation in N Terminus of Cardiac Troponin I Causes Malignant Hypertrophic Cardiomyopathy.* Circ Genom Precis Med, 2020. **13**(5): p. 444-452.
308. Gomes, A.V., K. Harada, and J.D. Potter, *A mutation in the N-terminus of troponin I that is associated with hypertrophic cardiomyopathy affects the Ca(2+)-sensitivity, phosphorylation kinetics and proteolytic susceptibility of troponin.* J Mol Cell Cardiol, 2005. **39**(5): p. 754-65.
309. Alamo, L., et al., *Lessons from a tarantula: new insights into myosin interacting-heads motif evolution and its implications on disease.* Biophys Rev, 2018. **10**(5): p. 1465-1477.
310. Dweck, D., et al., *Long term ablation of protein kinase A (PKA)-mediated cardiac troponin I phosphorylation leads to excitation-contraction uncoupling and diastolic dysfunction in a knock-in mouse model of hypertrophic cardiomyopathy.* J Biol Chem, 2014. **289**(33): p. 23097-23111.
311. Kaifosh, P., et al., *SIMA: Python software for analysis of dynamic fluorescence imaging data.* Front Neuroinform, 2014. **8**: p. 80.
312. Patel, T.P., et al., *Automated quantification of neuronal networks and single-cell calcium dynamics using calcium imaging.* J Neurosci Methods, 2015. **243**: p. 26-38.
313. Jang, M.J. and Y. Nam, *NeuroCa: integrated framework for systematic analysis of spatiotemporal neuronal activity patterns from large-scale optical recording data.* Neurophotonics, 2015. **2**(3): p. 035003.
314. Artimovich, E., et al., *PeakCaller: an automated graphical interface for the quantification of intracellular calcium obtained by high-content screening.* BMC Neurosci, 2017. **18**(1): p. 72.
315. Mackay, L., et al., *Systematic Characterization of Dynamic Parameters of Intracellular Calcium Signals.* Front Physiol, 2016. **7**: p. 525.
316. McKeithan, W.L., et al., *An Automated Platform for Assessment of Congenital and Drug-Induced Arrhythmia with hiPSC-Derived Cardiomyocytes.* Front Physiol, 2017. **8**: p. 766.
317. Cerignoli, F., et al., *High throughput measurement of Ca(2)(+) dynamics for drug risk assessment in human stem cell-derived cardiomyocytes by kinetic image cytometry.* J Pharmacol Toxicol Methods, 2012. **66**(3): p. 246-56.
318. Huebsch, N., et al., *Automated Video-Based Analysis of Contractility and Calcium Flux in Human-Induced Pluripotent Stem Cell-Derived Cardiomyocytes Cultured over Different Spatial Scales.* Tissue Eng Part C Methods, 2015. **21**(5): p. 467-79.
319. Wong, L.C., et al., *Fully-automated image processing software to analyze calcium traces in populations of single cells.* Cell Calcium, 2010. **48**(5): p. 270-4.
320. Greensmith, D.J., *Ca analysis: an Excel based program for the analysis of intracellular calcium transients including multiple, simultaneous regression analysis.* Comput Methods Programs Biomed, 2014. **113**(1): p. 241-50.

321. Amanfu, R.K., J.B. Muller, and J.J. Saucerman, *Automated image analysis of cardiac myocyte Ca2+ dynamics.* Annu Int Conf IEEE Eng Med Biol Soc, 2011. **2011**: p. 4661-4.
322. Pollesello, P., et al., *Binding of a new Ca2+ sensitizer, levosimendan, to recombinant human cardiac troponin C. A molecular modelling, fluorescence probe, and proton nuclear magnetic resonance study.* J Biol Chem, 1994. **269**(46): p. 28584-90.
323. Ginsburg, K.S. and D.M. Bers, *Modulation of excitation-contraction coupling by isoproterenol in cardiomyocytes with controlled SR Ca2+ load and Ca2+ current trigger.* J Physiol, 2004. **556**(Pt 2): p. 463-80.
324. Lindemann, J.P., et al., *beta-Adrenergic stimulation of phospholamban phosphorylation and Ca2+-ATPase activity in guinea pig ventricles.* J Biol Chem, 1983. **258**(1): p. 464-71.
325. Yoshida, A., et al., *Phosphorylation of ryanodine receptors in rat myocytes during beta-adrenergic stimulation.* J Biochem, 1992. **111**(2): p. 186-90.
326. Awinda, P.O., et al., *Effects of mavacamten on Ca(2+) sensitivity of contraction as sarcomere length varied in human myocardium.* Br J Pharmacol, 2020. **177**(24): p. 5609-5621.
327. Sewanan, L.R., S. Shen, and S.G. Campbell, *Mavacamten preserves length-dependent contractility and improves diastolic function in human engineered heart tissue.* Am J Physiol Heart Circ Physiol, 2021. **320**(3): p. H1112-H1123.
328. Yang, X. and T. Papoian, *Moving beyond the comprehensive in vitro proarrhythmia assay: Use of human-induced pluripotent stem cell-derived cardiomyocytes to assess contractile effects associated with drug-induced structural cardiotoxicity.* J Appl Toxicol, 2018. **38**(9): p. 1166-1176.
329. Wu, H., et al., *Modelling diastolic dysfunction in induced pluripotent stem cell-derived cardiomyocytes from hypertrophic cardiomyopathy patients.* Eur Heart J, 2019. **40**(45): p. 3685-3695.
330. Toepfer, C.N., et al., *SarcTrack.* Circ Res, 2019. **124**(8): p. 1172-1183.
331. Clark, J.A., J.D. Weiss, and S.G. Campbell, *A Microwell Cell Capture Device Reveals Variable Response to Dobutamine in Isolated Cardiomyocytes.* Biophys J, 2019. **117**(7): p. 1258-1268.
332. Schwinger, R.H., et al., *Reduced Ca(2+)-sensitivity of SERCA 2a in failing human myocardium due to reduced serin-16 phospholamban phosphorylation.* J Mol Cell Cardiol, 1999. **31**(3): p. 479-91.
333. Despa, S., et al., *Phospholemman-phosphorylation mediates the beta-adrenergic effects on Na/K pump function in cardiac myocytes.* Circ Res, 2005. **97**(3): p. 252-9.
334. Watkins, H., et al., *Characteristics and prognostic implications of myosin missense mutations in familial hypertrophic cardiomyopathy.* N Engl J Med, 1992. **326**(17): p. 1108-14.
335. Tardiff, J.C., *Sarcomeric proteins and familial hypertrophic cardiomyopathy: linking mutations in structural proteins to complex cardiovascular phenotypes.* Heart Fail Rev, 2005. **10**(3): p. 237-48.
336. Adhikari, A.S., et al., *beta-Cardiac myosin hypertrophic cardiomyopathy mutations release sequestered heads and increase enzymatic activity.* Nat Commun, 2019. **10**(1): p. 2685.
337. Sarkar, S.S., et al., *The hypertrophic cardiomyopathy mutations R403Q and R663H increase the number of myosin heads available to interact with actin.* Sci Adv, 2020. **6**(14): p. eaax0069.
338. Watkins, H., et al., *Mutations in the genes for cardiac troponin T and alpha-tropomyosin in hypertrophic cardiomyopathy.* N Engl J Med, 1995. **332**(16): p. 1058-64.
339. Moolman, J.C., et al., *Sudden death due to troponin T mutations.* J Am Coll Cardiol, 1997. **29**(3): p. 549-55.

340. Varnava, A.M., et al., *Hypertrophic cardiomyopathy: histopathological features of sudden death in cardiac troponin T disease.* Circulation, 2001. **104**(12): p. 1380-4.
341. Pasquale, F., et al., *Long-term outcomes in hypertrophic cardiomyopathy caused by mutations in the cardiac troponin T gene.* Circ Cardiovasc Genet, 2012. **5**(1): p. 10-7.
342. Ripoll-Vera, T., et al., *Clinical and Prognostic Profiles of Cardiomyopathies Caused by Mutations in the Troponin T Gene.* Rev Esp Cardiol (Engl Ed), 2016. **69**(2): p. 149-58.
343. Marian, A.J., et al., *Expression of a mutant (Arg92Gln) human cardiac troponin T, known to cause hypertrophic cardiomyopathy, impairs adult cardiac myocyte contractility.* Circ Res, 1997. **81**(1): p. 76-85.
344. Rust, E.M., F.P. Albayya, and J.M. Metzger, *Identification of a contractile deficit in adult cardiac myocytes expressing hypertrophic cardiomyopathy-associated mutant troponin T proteins.* J Clin Invest, 1999. **103**(10): p. 1459-67.
345. Tardiff, J.C., et al., *Cardiac troponin T mutations result in allele-specific phenotypes in a mouse model for hypertrophic cardiomyopathy.* J Clin Invest, 1999. **104**(4): p. 469-81.
346. Ferrantini, C., et al., *Pathogenesis of Hypertrophic Cardiomyopathy is Mutation Rather Than Disease Specific: A Comparison of the Cardiac Troponin T E163R and R92Q Mouse Models.* J Am Heart Assoc, 2017. **6**(7).
347. Ford, S.J., et al., *Effects of R92 mutations in mouse cardiac troponin T are influenced by changes in myosin heavy chain isoform.* J Mol Cell Cardiol, 2012. **53**(4): p. 542-51.
348. Robinson, P., et al., *Dilated and hypertrophic cardiomyopathy mutations in troponin and alpha-tropomyosin have opposing effects on the calcium affinity of cardiac thin filaments.* Circ Res, 2007. **101**(12): p. 1266-73.
349. Mogensen, J., et al., *Frequency and clinical expression of cardiac troponin I mutations in 748 consecutive families with hypertrophic cardiomyopathy.* J Am Coll Cardiol, 2004. **44**(12): p. 2315-25.
350. Arad, M., et al., *Gene mutations in apical hypertrophic cardiomyopathy.* Circulation, 2005. **112**(18): p. 2805-11.
351. Cheng, Y., et al., *Troponin I Mutations R146G and R21C Alter Cardiac Troponin Function, Contractile Properties, and Modulation by Protein Kinase A (PKA)-mediated Phosphorylation.* J Biol Chem, 2015. **290**(46): p. 27749-66.
352. Hofmann, P.A. and F. Fuchs, *Effect of length and cross-bridge attachment on Ca2+ binding to cardiac troponin C.* Am J Physiol, 1987. **253**(1 Pt 1): p. C90-6.
353. Hofmann, P.A. and F. Fuchs, *Evidence for a force-dependent component of calcium binding to cardiac troponin C.* Am J Physiol, 1987. **253**(4 Pt 1): p. C541-6.
354. Biesiadecki, B.J., et al., *Tri-modal regulation of cardiac muscle relaxation; intracellular calcium decline, thin filament deactivation, and cross-bridge cycling kinetics.* Biophys Rev, 2014. **6**(3-4): p. 273-289.
355. Mamidi, R., et al., *Impact of the Myosin Modulator Mavacamten on Force Generation and Cross-Bridge Behavior in a Murine Model of Hypercontractility.* J Am Heart Assoc, 2018. **7**(17): p. e009627.
356. Schober, T., et al., *Myofilament Ca sensitization increases cytosolic Ca binding affinity, alters intracellular Ca homeostasis, and causes pause-dependent Ca-triggered arrhythmia.* Circ Res, 2012. **111**(2): p. 170-9.
357. Buikema, J.W. and S.M. Wu, *Untangling the Biology of Genetic Cardiomyopathies with Pluripotent Stem Cell Disease Models.* Curr Cardiol Rep, 2017. **19**(4): p. 30.

358. Sewanan, L.R. and S.G. Campbell, *Modelling sarcomeric cardiomyopathies with human cardiomyocytes derived from induced pluripotent stem cells.* J Physiol, 2020. **598**(14): p. 2909-2922.
359. Ferrantini, C., et al., *Late sodium current inhibitors to treat exercise-induced obstruction in hypertrophic cardiomyopathy: an in vitro study in human myocardium.* Br J Pharmacol, 2018. **175**(13): p. 2635-2652.
360. Davis, J., et al., *A Tension-Based Model Distinguishes Hypertrophic versus Dilated Cardiomyopathy.* Cell, 2016. **165**(5): p. 1147-1159.
361. Saucerman, J.J., et al., *Mechanical regulation of gene expression in cardiac myocytes and fibroblasts.* Nat Rev Cardiol, 2019. **16**(6): p. 361-378.